frontiers | Research Topics

# Computational biomechanics for ventricle-arterial dysfunction and remodeling in heart failure, volume II

**Edited by**
Yunlong Huo, Shaun Gregory and Shengzhang Wang

**Published in**
Frontiers in Physiology

ISSN 1664-8714
ISBN 978-2-83251-119-0
DOI 10.3389/978-2-83251-119-0

## About Frontiers

Frontiers is more than just an open access publisher of scholarly articles: it is a pioneering approach to the world of academia, radically improving the way scholarly research is managed. The grand vision of Frontiers is a world where all people have an equal opportunity to seek, share and generate knowledge. Frontiers provides immediate and permanent online open access to all its publications, but this alone is not enough to realize our grand goals.

## Frontiers journal series

The Frontiers journal series is a multi-tier and interdisciplinary set of open-access, online journals, promising a paradigm shift from the current review, selection and dissemination processes in academic publishing. All Frontiers journals are driven by researchers for researchers; therefore, they constitute a service to the scholarly community. At the same time, the *Frontiers journal series* operates on a revolutionary invention, the tiered publishing system, initially addressing specific communities of scholars, and gradually climbing up to broader public understanding, thus serving the interests of the lay society, too.

## Dedication to quality

Each Frontiers article is a landmark of the highest quality, thanks to genuinely collaborative interactions between authors and review editors, who include some of the world's best academicians. Research must be certified by peers before entering a stream of knowledge that may eventually reach the public - and shape society; therefore, Frontiers only applies the most rigorous and unbiased reviews. Frontiers revolutionizes research publishing by freely delivering the most outstanding research, evaluated with no bias from both the academic and social point of view. By applying the most advanced information technologies, Frontiers is catapulting scholarly publishing into a new generation.

## What are Frontiers Research Topics?

Frontiers Research Topics are very popular trademarks of the *Frontiers journals series*: they are collections of at least ten articles, all centered on a particular subject. With their unique mix of varied contributions from Original Research to Review Articles, Frontiers Research Topics unify the most influential researchers, the latest key findings and historical advances in a hot research area.

Find out more on how to host your own Frontiers Research Topic or contribute to one as an author by contacting the Frontiers editorial office: frontiersin.org/about/contact

# Computational biomechanics for ventricle-arterial dysfunction and remodeling in heart failure, volume II

**Topic editors**

Yunlong Huo — Shanghai Jiao Tong University, China
Shaun Gregory — Monash University, Australia
Shengzhang Wang — Fudan University, China

**Citation**

Huo, Y., Gregory, S., Wang, S., eds. (2023). *Computational biomechanics for ventricle-arterial dysfunction and remodeling in heart failure, volume II*. Lausanne: Frontiers Media SA. doi: 10.3389/978-2-83251-119-0

*The authors declare that the research was conducted in the absence of any commercial or financial relationships that could be construed as a potential conflict of interest.*

# Table of contents

frontiers | Frontiers in Physiology

TYPE Editorial
PUBLISHED 08 December 2022
DOI 10.3389/fphys.2022.1100037



OPEN ACCESS

EDITED AND REVIEWED BY
Raimond L. Winslow,
Northeastern University, United States

*CORRESPONDENCE
Yunlong Huo,
huoyunlong@sjtu.edu.cn
Shaun D. Gregory,
shaun.gregory1@gmail.com

SPECIALTY SECTION
This article was submitted to Computational Physiology and Medicine, a section of the journal Frontiers in Physiology

RECEIVED 16 November 2022
ACCEPTED 28 November 2022
PUBLISHED 08 December 2022

CITATION
Huo Y and Gregory SD (2022), Editorial: Computational biomechanics for ventricle-arterial dysfunction and remodeling in heart failure, Volume II. *Front. Physiol.* 13:1100037. doi: 10.3389/fphys.2022.1100037



# Editorial: Computational biomechanics for ventricle-arterial dysfunction and remodeling in heart failure, Volume II

Yunlong Huo[1,2]* and Shaun D. Gregory[3]*

[1]Institute of Mechanobiology and Medical Engineering, School of Life Sciences and Biotechnology, Shanghai Jiao Tong University, Shanghai, China, [2]PKU-HKUST Shenzhen-Hong Kong Institution, Shenzhen, Guangdong, China, [3]Cardio-Respiratory Engineering and Technology Laboratory, Department of Mechanical and Aerospace Engineering, Monash University, Melbourne, VIC, Australia

KEYWORDS

**computational biomechanics, heart failiure, hemodynamics, FFR = fractional flow reserve, soft tissue mechanical properties**

Editorial on the Research Topic
Computational biomechanics for ventricle-arterial dysfunction and remodeling in heart failure, Volume II

## Introduction

Interactions between the left ventricle (LV) and systemic circulation, and between the right ventricle (RV) and the pulmonary circulation are key determinants of cardiac and cardiovascular function. The global performance of LV-arterial coupling (e.g., the ratio of effective arterial elastance, time-varying pressure-flow relations, and effects of wave reflections) has been applied to many clinical scenarios such as aging, hypertension, heart failure (HF), and dilated cardiomyopathy. The global approach, however, has significant limitations in heart failure with preserved ejection fraction (HFpEF), although it can provide useful information regarding the mechanical efficiency and performance in heart failure with reduced ejection fraction (HFrEF). This approach is also less informative in the study of RV dysfunction and its coupling with the pulmonary circulation in HF. With the development of simulation-based biomechanics in recent years, it is required to demonstrate accurate analysis of local ventricle-arterial functions and remodeling in health and disease, particularly in the progression of HF.

This Research Topic in computational biomechanics was conceived to improve our understanding and treatment of cardiac and cardiovascular dysfunction and their coupling abnormalities associated with the occurrence and development of HFpEF or

HFrEF. There is a total of 12 published articles (11 original research and 1 brief research report) relevant to basic and clinical studies covering: 1) cardiac stress and strain analysis using computational models; 2) hemodynamics in systemic/pulmonary circulations or coronary circulation; 3) advanced biomechanics models of LV/RV-arterial coupling and remodeling; 4) computational models based on bio-imaging measurements in patients of HF; 5) machine learning methods to enhance the accuracy of computational biomechanics; and 6) computational models to aid in the development of medical devices for treatment of HF. Here, we briefly summarize the contributions from the 12 publications.

## Computational simulation of heart valves and cardiovascular devices

Computational analysis of the native cardiovascular system, and devices that are used to treat the diseased native cardiovascular system, is regularly conducted to enhance our understanding of patient anatomy and blood flow dynamics (Neidlin et al., 2021; Vatani et al., 2022). This enhanced understanding can lead to improvements in patient management, better cardiovascular devices, and additional applications of existing devices. Modern cardiovascular computational simulations have progressed beyond simplified geometries to patient-specific models based on medical imaging, with some progressing further to statistical shape models based on larger cohorts of patient data (Goubergrits et al., 2022).

In this Research Topic, three-dimensional statistical shape models of healthy patients and those with varying degrees of tricuspid valve regurgitation were generated from cardiac MRI data (Orkild et al.). Those with tricuspid regurgitation demonstrated increased right ventricular free wall bulging, narrowing of the base, and blunting of the right ventricular apex. Compared with tricuspid regurgitation, aortic stenosis is even more common, with low-flow and low-gradient aortic stenosis (LFLG AS) being a commonly recognized sub-type with controversial management strategies due in part to a lack of biomechanics knowledge. To improve the knowledge of LFLG AS biomechanics, a patient-specific model using ECG-gated cardiac computed tomography was developed using a previously validated multi-scale, multi-physics computational heart model coupled with a virtual circulatory system and calibrated to clinically-measured parameters in this issue (Wisneski et al.). Progression of valvular disease may necessitate placement of a mechanical replacement valve, with minimally invasive transcatheter aortic valve replacement (TAVR) increasing in popularity. In this issue, a fluid-structure interaction model of TAVR was used to investigate blood flow dynamics, revealing variations in maximum leaflet stress, opening area, and low-velocity areas when leaflet geometries were altered (Liu et al.).

Cardiovascular modelling techniques can combine blood flow simulations with structural models (e.g. fluid-structure interaction models), lumped parameter modelling, and even *in-vivo* experiments. In this issue, a combination of cardiac electrical signals, blood pressure and echocardiography imaging from a pacing animal model was combined with a cardiac fluid-structure interaction model to demonstrate the influence of pacemaker location on cardiac outcome (Fan et al.). In another research topic, a combination of patient images *via* computed tomography and lumped parameter modelling was used in this issue to investigate the influence of atrial fibrillation and left atrial appendage occlusion on thrombosis in a simulated patient supported by a left ventricular assist device (Ghodrati-Misek et al.). Results obtained from the advanced contractile left-heart model revealed unfavorable left atrial flow dynamics during atrial fibrillation which was improved after left atrial appendage occlusion, which may reduce the potential for thrombus formation within the left atrium.

## Computational techniques for physiological assessments

Fractional flow reserve (FFR) is the Class Ia recommendation for guiding the decision to revascularize epicardial coronary stenoses by societal guidelines in Europe and United States (Knuuti et al., 2020; Writing Committee et al., 2022). Some practical restrictions limit the traditional wire-based FFR utilization, such as requiring drug-induced hyperemia, pressure drift of the pressure wire, and so on (Gong et al., 2020; Li et al., 2020; Gong et al., 2022). Multiple computational techniques have been developed to determine FFR based on computed tomography angiograms (CTA-FFR) (Taylor et al., 2013). The diagnostic accuracy of CTA-FFR, however, varied significantly across the spectrum of cardiovascular diseases (Cook et al., 2017). Hence, it is still required to improve the computational techniques. In this Research Topic, a method for calculating FFR based on steady-state geometric multiscale ($FFR_{SS}$) was proposed based on a coronary artery model segmented from a patient's coronary CTA images (Liu et al.). The diagnostic performance of $FFR_{SS}$ and traditional $FFR_{CT}$ was compared with the wire-based FFR. $FFR_{ss}$ showed similar accuracy to $FFR_{CT}$, but improved the calculation efficiency. Moreover, a fluid–structure interaction (FSI) algorithm with a physics-driven 3D–0D coupled mode was developed to improve the accuracy of CTA-FFR (Xi et al.). This method improved the diagnostic accuracy of CTA-FFR computation.

The coronary arterial trees include millions of blood vessels, most of them are small arterioles and pre-capillary vessels (Huo et al., 2009). An index of microcirculatory resistance (IMR) was proposed to quantify coronary microcirculatory dysfunction

(Fearon et al., 2003; Aarnoudse et al., 2004; Fearon et al., 2004). However, its application within clinical practice remains extremely limited due to a complex guide wire measurement under hyperemia (Ai et al., 2020). Coronary angiography-derived IMR (caIMR) has been proven to have high correlation and diagnostic accuracy with invasive wire-based IMR (Ai et al., 2020; Choi et al., 2021). In this Research Topic, caIMR >40 was shown to be an independent predictor of the combined events including cardiovascular death or heart failure readmission and hence a promising method for prognosis in STEMI patients (Duan et al.).

## Hemodynamics and vessel wall mechanics

Various abnormal hemodynamic parameters such as low wall shear stress (WSS), high oscillatory shear index (OSI), old blood volume fraction (OBVF), and old blood volume (OBV), have been proposed to investigate the occurrence and development of atherosclerosis (Huang et al., 2016; Fan et al., 2017; Feng et al., 2020). In this Research Topic, thrombosis risk was evaluated within occluded coronary arterial fistulas (CAF) with terminal aneurysms using untreated, aneurysm-reserved and aneurysm-removed numerical models (Jiang et al.). The OBV was found to be superior to the area of high OSI and low WSS in determining treatment type. On the other hand, competitive flow and anastomotic stenosis are two risk factors for poor instant patency of coronary artery bypass grafting (CABG) surgery (Fan et al., 2016; Fan et al., 2017). A 0D-3D coupled multiscale CABG model was developed to investigate anastomotic stenosis and competitive flow (Mao et al.). The graft flow waveform shape and flow fast Fourier transformation (FFT) ratio were found to predict the poor instant patency after CABG.

In vessel wall mechanics, wall tissue fatigue is a chronic failure process induced by repetitive loading and could impact plaque development under pulsatile blood pressure (Guo et al.). In this Research Topic, the relationship between fatigue and stenosis progression was investigated based on *in-vivo* intravascular ultrasound (IVUS) images and finite element models (Guo et al.). Stenosis progression was associated with the maximum stress amplitude, average stress amplitude and average strain amplitude.

In comparison with fine particle pollution (PM2.5), ultrafine particles (UFPs) (PM0.1) produce stronger chemical reactions given their small volume and large surface area (Li et al., 2021; Huo and Li). In this Research Topic, the change of cardiac function and peripheral hemodynamics was investigated in rats of myocardial infarction (MI) after long-term inhalation of ultrafine Zn particles (Huo and Li). The long-term inhalation of ultrafine zinc particles induced excessive accumulation of zinc in serum and tissue, which deteriorated cardiac and hemodynamic dysfunctions in MI rats.

In summary, this special edition incorporates novel cardiovascular modelling research into a single issue to advance the knowledge in cardiovascular disease, simulation techniques, medical devices, and more.

## Author contributions

YH and SG wrote the manuscript together.

## Conflict of interest

The authors declare that the research was conducted in the absence of any commercial or financial relationships that could be construed as a potential conflict of interest.

## Publisher's note



## References

Aarnoudse, W., Fearon, W. F., Manoharan, G., Geven, M., Van de Vosse, F., Rutten, M., et al. (2004). Epicardial stenosis severity does not affect minimal microcirculatory resistance. *Circulation* 110 (15), 2137–2142. doi:10.1161/01.CIR.0000143893.18451.0E

Ai, H., Feng, Y., Gong, Y., Zheng, B., Jin, Q., Zhang, H. P., et al. (2020). Coronary angiography-derived index of microvascular resistance. *Front. Physiol.* 11, 605356. doi:10.3389/fphys.2020.605356

Choi, K. H., Dai, N., Li, Y., Kim, J., Shin, D., Lee, S. H., et al. (2021). Functional coronary angiography-derived index of microcirculatory resistance in patients with ST-segment elevation myocardial infarction. *JACC. Cardiovasc. Interv.* 14 (15), 1670–1684. doi:10.1016/j.jcin.2021.05.027

Cook, C. M., Petraco, R., Shun-Shin, M. J., Ahmad, Y., Nijjer, S., Al-Lamee, R., et al. (2017). Diagnostic accuracy of computed tomography-derived fractional flow reserve : A systematic review. *JAMA Cardiol.* 2 (7), 803–810. doi:10.1001/jamacardio.2017.1314

Duan, Y., Wang, Y., Zhang, M., Li, Z., Chen, L., Miao, H., et al. (2022). Computational pressure-fluid dynamics applied to index of microcirculatory resistance, predicting the prognosis of drug-coated balloons compared with drug-eluting stents in STEMI patients. *Front. Physiol.* 13, 898659. doi:10.3389/fphys.2022.898659

Fan, T., Feng, Y., Feng, F., Yin, Z., Luo, D., Lu, Y., et al. (2017). A comparison of postoperative morphometric and hemodynamic changes between saphenous vein and left internal mammary artery grafts. *Physiol. Rep.* 5 (21), e13487. doi:10.14814/phy2.13487

Fan, T., Lu, Y., Gao, Y., Meng, J., Tan, W., Huo, Y., et al. (2016). Hemodynamics of left internal mammary artery bypass graft: Effect of anastomotic geometry,

coronary artery stenosis, and postoperative time. *J. Biomech.* 49 (5), 645–652. doi:10.1016/j.jbiomech.2016.01.031

Fearon, W. F., Aarnoudse, W., Pijls, N. H., De Bruyne, B., Balsam, L. B., Cooke, D. T., et al. (2004). Microvascular resistance is not influenced by epicardial coronary artery stenosis severity: Experimental validation. *Circulation* 109 (19), 2269–2272. doi:10.1161/01.CIR.0000128669.99355.CB

Fearon, W. F., Balsam, L. B., Farouque, H. M., Caffarelli, A. D., Robbins, R. C., Fitzgerald, P. J., et al. (2003). Novel index for invasively assessing the coronary microcirculation. *Circulation* 107 (25), 3129–3132. doi:10.1161/01.CIR.0000080700.98607.D1

Feng, Y., Liu, J., Fan, T., Zhang, W., Yin, X., Tan, Y. E., et al. (2020). Vertebral artery stenoses contribute to the development of diffuse plaques in the basilar artery. *Front. Bioeng. Biotechnol.* 8, 168. doi:10.3389/fbioe.2020.00168

Ghodrati-Misek, M., Schlöglhofer, T., Gross, C., Maurer, A., Zimpfer, D., Beitzke, D., et al. (2022). Left atrial appendage occlusion in ventricular assist device patients to decrease thromboembolic events: A computer simulation study. *Front. Physiol.* 13, 1010862. doi:10.3389/fphys.2022.1010862

Gong, Y., Feng, Y., Yi, T., Yang, F., Li, Y., Zhang, L., et al. (2020). Coronary angiography-derived diastolic pressure ratio. *Front. Bioeng. Biotechnol.* 8, 596401. doi:10.3389/fbioe.2020.596401

Gong, Y. J., Zheng, B., Yi, T. C., Yang, F., Hong, T., Liu, Z. P., et al. (2022). Coronary angiography-derived contrast fractional flow reserve. *Catheter. Cardiovasc. Interv.* 99 (3), 763–771. doi:10.1002/ccd.29558

Goubergrits, L., Vellguth, K., Obermeier, L., Schlief, A., Tautz, L., Bruening, J., et al. (2022). CT-based analysis of left ventricular hemodynamics using statistical shape modeling and computational fluid dynamics. *Front. Cardiovasc. Med.* 9.doi:10.3389/fcvm.2022.90190

Huang, X., Yin, X., Xu, Y., Jia, X., Li, J., Niu, P., et al. (2016). Morphometric and hemodynamic analysis of atherosclerotic progression in human carotid artery bifurcations. *Am. J. Physiol. Heart Circ. Physiol.* 310 (5), H639–H647. doi:10.1152/ajpheart.00464.2015

Huo, Y., Kaimovitz, B., Lanir, Y., Wischgoll, T., Hoffman, J. I., and Kassab, G. S. (2009). Biophysical model of the spatial heterogeneity of myocardial flow. *Biophys. J.* 96 (10), 4035–4043. doi:10.1016/j.bpj.2009.02.047

Knuuti, J., Wijns, W., Saraste, A., Capodanno, D., Barbato, E., Funck-Brentano, C., et al. (2020). 2019 ESC Guidelines for the diagnosis and management of chronic coronary syndromes. *Eur. Heart J.* 41 (3), 407–477. doi:10.1093/eurheartj/ehz425

Li, J., Gong, Y., Wang, W., Yang, Q., Liu, B., Lu, Y., et al. (2020). Accuracy of computational pressure-fluid dynamics applied to coronary angiography to derive fractional flow reserve: Flash FFR. *Cardiovasc. Res.* 116 (7), 1349–1356. doi:10.1093/cvr/cvz289

Li, L., Niu, P., Wang, X., Bing, F., Tan, W., and Huo, Y. (2021). Short-term inhalation of ultrafine zinc particles could alleviate cardiac dysfunctions in rats of myocardial infarction. *Front. Bioeng. Biotechnol.* 9, 646533. doi:10.3389/fbioe.2021.646533

Liu, J., Wang, X., Li, B., Huang, S., Sun, H., Zhang, L., et al. (2022a). Non-invasive quantification of fraction flow reserve based on steady-state geometric multiscale models. *Front. Physiol.* 13, 881826. doi:10.3389/fphys.2022.881826

Neidlin, M., Liao, S., Li, Z., Simpson, B., Kaye, D. M., Steinseifer, U., et al. (2021). Understanding the influence of left ventricular assist device inflow cannula alignment and the risk of intraventricular thrombosis. *Biomed. Eng. Online* 20 (1), 47. doi:10.1186/s12938-021-00884-6

Taylor, C. A., Fonte, T. A., and Min, J. K. (2013). Computational fluid dynamics applied to cardiac computed tomography for noninvasive quantification of fractional flow reserve scientific basis. *J. Am. Coll. Cardiol.* 61 (22), 2233–2241. doi:10.1016/j.jacc.2012.11.083

Vatani, A., Liao, S., Burrell, A. J. C., Carberry, J., Azimi, M., Steinseifer, U., et al. (2022). Improved drainage cannula design to reduce thrombosis in veno-arterial extracorporeal membrane oxygenation. *Asaio J.* 68 (2), 205–213. doi:10.1097/MAT.0000000000001440

Writing Committee, M., Lawton, J. S., Tamis-Holland, J. E., Bangalore, S., Bates, E. R., Beckie, T. M., et al. (2022). 2021 ACC/AHA/SCAI guideline for coronary artery revascularization: A report of the American college of cardiology/American heart association joint committee on clinical practice guidelines. *J. Am. Coll. Cardiol.* 79 (2), e21–e129.doi:10.1161/CIR.0000000000001039

frontiers in Physiology

ORIGINAL RESEARCH
published: 17 February 2022
doi: 10.3389/fphys.2022.843421

# Optimization of Left Ventricle Pace Maker Location Using Echo-Based Fluid-Structure Interaction Models

*Longling Fan[1,2], Jing Yao[3]*, Liang Wang[4], Di Xu[5] and Dalin Tang[4,6]**

*[1] Faculty of Science, Kunming University of Science and Technology, Kunming, China, [2] School of Mathematics, Southeast University, Nanjing, China, [3] Department of Ultrasound Medicine, Affiliated Drum Tower Hospital of Nanjing University Medical School, Nanjing, China, [4] School of Biological Science and Medical Engineering, Southeast University, Nanjing, China, [5] Department of Cardiology, First Affiliated Hospital of Nanjing Medical University, Nanjing, China, [6] Mathematical Sciences Department, Worcester Polytechnic Institute, Worcester, MA, United States*

OPEN ACCESS

**Edited by:**
*Yunlong Huo,*
*Shanghai Jiao Tong University, China*

**Reviewed by:**
*Yue Han,*
*Shanghai Jiao Tong University, China*
*Fan Tingting,*
*Capital Medical University, China*
*Anqiang Sun,*
*Beihang University, China*

***Correspondence:**
*Jing Yao*
*echoluyao@163.com*
*Dalin Tang*
*dtang@wpi.edu*

**Specialty section:**
*This article was submitted to Computational Physiology and Medicine, a section of the journal Frontiers in Physiology*

**Received:** *25 December 2021*
**Accepted:** *26 January 2022*
**Published:** *17 February 2022*

**Citation:**
*Fan L, Yao J, Wang L, Xu D and Tang D (2022) Optimization of Left Ventricle Pace Maker Location Using Echo-Based Fluid-Structure Interaction Models. Front. Physiol. 13:843421. doi: 10.3389/fphys.2022.843421*

**Introduction:** Cardiac pacing has been an effective treatment in the management of patients with bradyarrhythmia and tachyarrhythmia. Different pacemaker location has different responses, and pacemaker effectiveness to each individual can also be different. A novel image-based ventricle animal modeling approach was proposed to optimize ventricular pacemaker site for better cardiac outcome.

**Method:** One health female adult pig (weight 42.5 kg) was used to make a pacing animal model with different ventricle pacing locations. Ventricle surface electric signal, blood pressure and echo image were acquired 15 min after the pacemaker was implanted. Echo-based left ventricle fluid-structure interaction models were constructed to perform ventricle function analysis and investigate impact of pacemaker location on cardiac outcome. With the measured electric signal map from the pig associated with the actual pacemaker site, electric potential conduction of myocardium was modeled by material stiffening and softening in our model, with stiffening simulating contraction and softening simulating relaxation. Ventricle model without pacemaker (NP model) and three ventricle models with the following pacemaker locations were simulated: right ventricular apex (RVA model), posterior interventricular septum (PIVS model) and right ventricular outflow tract (RVOT model). Since higher peak flow velocity, flow shear stress (FSS), ventricle stress and strain are linked to better cardiac function, those data were collected for model comparisons.

**Results:** At the peak of filling, velocity magnitude, FSS, stress and strain for RVOT and PIVS models were 13%, 45%, 18%, 13% and 5%, 30%, 10%, 5% higher than NP model, respectively. At the peak of ejection, velocity magnitude, FSS, stress and strain for RVOT and PIVS models were 50%, 44%, 54%, 59% and 23%, 36%, 39%, 53% higher than NP model, respectively. RVA model had lower velocity, FSS, stress and

strain than NP model. RVOT model had higher peak flow velocity and stress/strain than PIVS model. It indicated RVOT pacemaker site may be the best location.

**Conclusion:** This preliminary study indicated that RVOT model had the best performance among the four models compared. This modeling approach could be used as "virtual surgery" to try various pacemaker locations and avoid risky and dangerous surgical experiments on real patients.

**Keywords: fluid-structure interaction model, pacemaker electrical conduction, fluid dynamic, ventricle material properties, ventricle mechanics**

## INTRODUCTION

Rapid development of cardiac pacing has recently become the only effective treatment for slow cardiac arrhythmia (Glikson et al., 2021). Between 2004 and 2014, 2.9 million patients received permanent pacemakers in the United States (Mohamed et al., 2019). China Ministry of Health Online Registration indicated that pacemaker implants were placed in 82779 patients in 2018, and the number has been increasing year by year (Liu, 2019). Right ventricular apex (RVA) has been the conventional location for pacemaker lead placement. However, RVA is a non-physiological agonist site that causes the electrical and mechanical origin and distribution patterns of the heart to be opposite to normal sinus rhythm, resulting in hemodynamic abnormalities and tissue remodeling (Kapa et al., 2010). The review by Tops et al. (2009) provided a contemporary overview of the available evidence on the detrimental effects of RVA pacing. Furthermore, clinical trials have shown that RVA pacing can cause electro-mechanical contraction of the left and right ventricles to be asynchronous. Long-term RVA pacing can cause cardiac histologic and electrical remodeling, abnormal myocardial contractile pattern, hemodynamic disorder, and ultimately cardiac insufficiency, there is also the risk of atrial fibrillation (AF) and heart failure (HF), which increases the rate of hospitalization and mortality (Manolis et al., 2008; Miranda et al., 2012; Alhous et al., 2015). So optimization of right ventricular pacing site becomes an important object of pacing electrophysiology. In recent years, the concept of physiological pacing has been proposed in the field of electrophysiological (Das and Kahali, 2016; Vijayaraman et al., 2017; Liu et al., 2021), and the study of the selection of pacing sites has received great attention (Coppola et al., 2015; Carpio et al., 2019; Zhu et al., 2020). The physiological pacing sites currently studied include the His bundle or para-His bundle (Kronborg et al., 2014; Sharma et al., 2020), the right ventricular inflow tract septum (Tsujii et al., 2016), the right ventricular outflow tract (RVOT) (Da Costa et al., 2013; Yao et al., 2013; Zou et al., 2015), Left bundle branch area (Das et al., 2020; Michalik et al., 2021), and so on. Here His indicates His bundle which is a collection of heart muscle cells specialized for electrical conduction. As part of the electrical conduction system of the heart, it transmits the electrical impulses from the atrioventricular node (located between the atria and the ventricles) to the point of the apex of the fascicular branches via the bundle branches. Studies have shown that the above-mentioned pacing site can increase cardiac output and improve cardiac function compared with conventional RVA pacing, but these sites have advantages and disadvantages in terms of operation technique, stability, pacing threshold, etc. (Erdogan and Hunuk, 2010; Singh et al., 2015; Alberti et al., 2017). Moreover, Individual differences in heart disease such as myocardial infarction, cardiomyopathy, valvular disease, etc., myocardial contraction/diastolic function, and myocardial thickness can influence the response of the pacemaker, thus could produce different cardiac functional responses.

The analysis of electrical, mechanical and flow fields in patients with pacemaker implantation has been a hot topic in the field of pacing electrophysiology, and most of these studies focus on electro-mechanical coupling. Usyk et al. (2012) established a three-dimensional biventricular electrical complex model that reflects the local myocardial mechanics of the ventricle, and completely simulated the entire cycle of the heart. Zhu et al. (2001) based on the constructed cardiac electrophysiological model and proposed an algorithm for calculating ECG based on single-cell action potential. Gurev et al. (2010) established a three-dimensional electrophysiological model of the rabbit ventricle and used it to analyze the three-dimensional distribution of ventricular fibril contraction delay and its dependence on loading conditions. Recent advances in computational modeling, methods and computer technology have made it possible for computer-simulated procedures to be used in clinical decision-making for specific patients. The feasibility to integrate computational modeling with clinical investigations in a clinical environment and to guide therapeutic treatment of cardiac arrhythmia and heart failure in real time for individual patients has been previously demonstrated (Chen et al., 2017). Lee et al. (2018) focus on the contribution of electrophysiology, mechanics, and circulatory computer models of the heart to understanding cardiac resynchronization therapy response. In our previous studies, we introduced patient-specific cardiac magnetic resonance (CMR)-based left ventricular/right ventricular (LV/RV) models with fluid-structure interactions (FSI) with various surgical design and potential applications (Tang et al., 2010, 2011, 2016; Huang et al., 2021). Echo-based 3D LV FSI models were introduced to perform ventricle mechanical analysis and investigate flow behaviors (Fan et al., 2018).

This paper will integrate echocardiography images, propagating dynamic electric potential on ventricle surface induced by pacemaker, and computational models with fluid-structure interactions (FSI) to perform myocardial function and intra-cardiac flow assessment. Ventricle model without

pacemaker (NP model) and three ventricle models with the following pacemaker locations were simulated: right ventricular apex (RVA model), posterior interventricular septum (PIVS model) and right ventricular outflow tract (RVOT model). The models will be used to evaluate the impact of pacemaker locations and optimize its placement.

# MATERIALS AND METHODS

## Animal Model Preparation

The animal study were approved by the Ethics Committee of the First Affiliated Hospital of Nanjing Medical University and all applicable institutional and governmental regulations concerning the ethical use of animals were followed. One health female adult pig weight 42.5kg was used to make pacing animal model under different ventricular pacing location. Health status was assessed before undergoing the experimental procedures. The pig was intubated and mechanically ventilated, and anesthesia was maintained using isoflurane. A 5-7cm left anterolateral thoracotomy was made in the fourth left intercostal space. After opening the chest, a transverse incision of approximately 2-3cm was made in the pericardial sac. Parietal pericardium was made with cotton 2-0 stitches to expose the ventricle and the left atrium. Epicardial pacing leads were fixed to following locations: right atrial appendage (RAA), right ventricular apex (RVA), posterior interventricular septum (PIVS), and right ventricular outflow tract (RVOT), and left ventricular lateral wall (LVL). The tip of RAA lead was connected to atrial terminals of Medtronic Dual Chamber Temporary cardiac pacemaker. Then RVA, PIVS, RVOT, and LVL lead was connected to the Ventricular pacing, respectively. **Figure 1** shows the positions of the pacemaker leads in the heart.

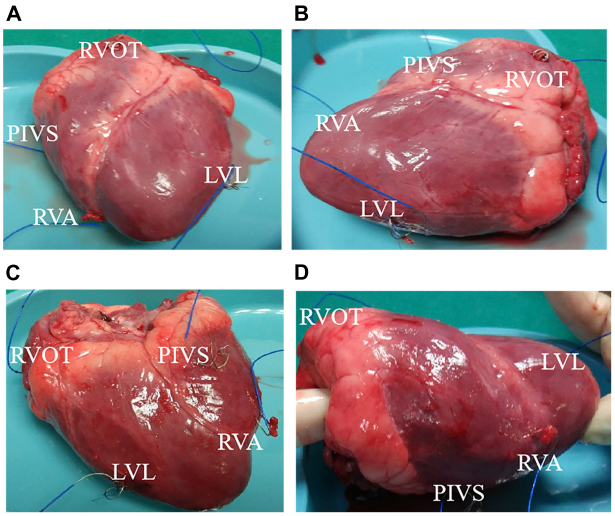


**FIGURE 1 |** The position of the pacemaker lead in the heart. **(A)** Front view of heart. **(B)** Left side view of heart. **(C)** Back view of heart. **(D)** Right side view of heart. RVA, right ventricular apex; PIVS, posterior interventricular septum; RVOT, right ventricular outflow tract; LVL, left ventricular lateral wall.

## 3D Echo Data Acquisition

Electric potential data recording and echocardiographic image acquisition were started 15 min after stabilization of pacing model. Real-time three-dimensional full-volume image of the apical 4-chamber view was obtained using an ultrasound machine (E9, GE Mechanical Systems, Milwaukee, Wisconsin), with TEE probe 6VT-D attaching to LV apex directly. Electrophysiological recorder records body surface 12-lead electrocardiogram and intracardiac electrogram. Meantime, the pressure gauge catheter was connected to the Medtronic Lifpark12 monitor. The left ventricular pressure curve was measured before and during the time period when the pacemaker was implanted. **Table 1** gives basic information including ventricular pacing location, pressure and volume data. We obtained the relationship between the different pacing interventions and the myocardial material function by analyzing the ultrasound images, volume data and cardiac chamber pressure data, determining the function of the myocardial analysis material corresponding to the specific pacing mode, and establishing the left ventricle under different pacing interventions. Three-dimensional FSI models were used to obtain left ventricle stress and strain, and flow velocity and shear stress in the heart chamber. Furthermore, the differences in these variables under different pacing models were analyzed to infer the optimal pacing model for optimal pacemaker implantation. **Figure 2** shows the *in vivo* Echo image, pressure curve and electrical signal conduction map, and ventricular partitioning under RVA pacing intervention. The compartment partitions were used to set material parameters to simulate the conduction of electrical signals.

## The Fluid-Structure Interaction Model of Left Ventricular

Blood flow in the left ventricle was assumed to be laminar, Newtonian, viscous and incompressible. The Navier-Stokes equations with arbitrary Lagrangian-Eulerian (ALE) formulation were used as the governing equations. To simplify the computational model, the cardiac cycle was split into two phases: (a) the filling phase (diastole) when the inlet was open, inlet blood pressure was prescribed (**Figure 2C**), blood flows into the LV, and the outlet was closed (by setting flow velocity to zero); (b) The ejection phase (systole) when inlet was closed, outlet was open, outlet pressure was prescribed, and blood was ejected out of the LV. Pressure conditions were prescribed at the mitral (inlet) and aortic (outlet) valves. When the inlet or outlet were closed, flow velocity was set to zero and pressure was left unspecified. When the inlet or outlet was open, blood pressure was prescribed and flow velocity was calculated by ADINA. No-slip boundary conditions and natural force boundary conditions were specified at all interfaces to couple fluid and structure models together (Tang et al., 2010, 2016). Navier-Stokes equation in ALE coordinate system and boundary conditions for fluid model were given:

$$\rho(\partial u/\partial t + ((u-u_g)\cdot\nabla)u) = -\nabla p + \mu\nabla^2 u \quad (1)$$

$$\nabla \cdot u = 0 \quad (2)$$

**TABLE 1 |** Ventricular pacing location and volume data.

| Pacemaker location | NP | | RVA | | RVOT | | PIVS | |
|---|---|---|---|---|---|---|---|---|
| Pressure (mmHg) | Min = 9 | Max = 102 | Min = 10 | Max = 119 | Min = 8 | Max = 90 | Min = 7 | Max = 83 |
| Echo Vol (ml) | Min = 26 | Max = 54 | Min = 27 | Max = 55 | Min = 25 | Max = 53 | Min = 24 | Max = 50 |
| Echo EF (%) | 51.85 | | 50.91 | | 52.83 | | 52.00 | |
| Model Vol (ml) | Min = 25.96 | Max = 54.01 | Min = 27.07 | Max = 54.96 | Min = 25.02 | Max = 53.04 | Min = 24.01 | Max = 49.98 |
| Model EF (%) | 51.93 | | 50.75 | | 52.83 | | 51.96 | |

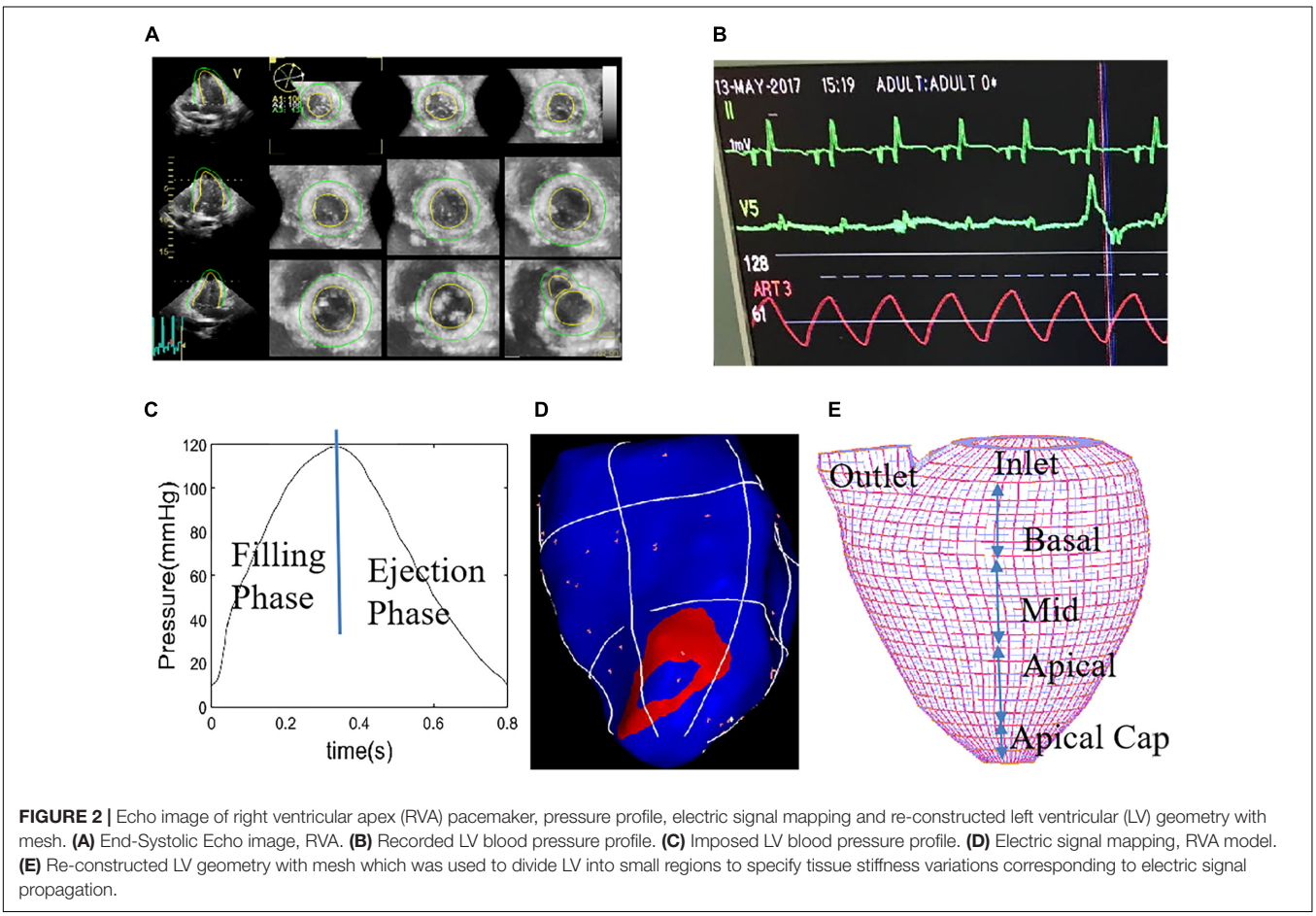


**FIGURE 2 |** Echo image of right ventricular apex (RVA) pacemaker, pressure profile, electric signal mapping and re-constructed left ventricular (LV) geometry with mesh. **(A)** End-Systolic Echo image, RVA. **(B)** Recorded LV blood pressure profile. **(C)** Imposed LV blood pressure profile. **(D)** Electric signal mapping, RVA model. **(E)** Re-constructed LV geometry with mesh which was used to divide LV into small regions to specify tissue stiffness variations corresponding to electric signal propagation.

$$u|_{\Gamma} = (\partial x/\partial t) \tag{3}$$

$$P|_{inlet} = p_{in}(t), \partial u/\partial n|_{inlet} = 0,\ u|_{outlet} = 0, \text{(filling phase)} \tag{4}$$

$$P|_{outlet} = p_{out}(t), \partial u/\partial n|_{outlet} = 0,\ u|_{inlet} = 0, \text{(ejection phase)} \tag{5}$$

$$\sigma_{ij} \cdot n_j|_{outwall} = 0 \tag{6}$$

$$\sigma^r_{ij} \cdot n^r_j\Big|_{interface} = \sigma^s_{ij} \cdot n^s_j\Big|_{interface} \tag{7}$$

where $\boldsymbol{u}$ and $\boldsymbol{p}$ are flow velocity and pressure, $\boldsymbol{u}_g$ is mesh velocity, $\mu$ is the viscosity of blood. $\Gamma$ stands for LV inner wall, $f_{\bullet,j}$ stands for derivative of $f$ with respect to the $j$th variable (or time t), $\sigma_r$ and $\sigma_s$ are fluid and structure stress tensors, and $\mathbf{n}^r$ and $\mathbf{n}^s$ are their outward normal directions, respectively.

The ventricle material tissue was assumed to be hyperelastic, anisotropic, homogeneous and nearly incompressible. The governing equations for the LV structure model were:

$$\rho v_{i,tt} = \sigma_{ij,j},\ i, j = 1, 2, 3; \text{ sum over } j, \tag{8}$$

$$\varepsilon_{ij} = \frac{1}{2}\left(v_{i,j} + v_{j,i} + v_{\alpha,i}\, v_{\alpha,j}\right),\ i, j, \alpha = 1, 2, 3, \tag{9}$$

where $\sigma$ is the stress tensor, $\varepsilon$ is the strain tensor, $\boldsymbol{v}$ is displacement, and $\rho$ is material density. The normal stress was assumed to

be zero on the outer (epicardial) LV surface and equal to the normal stress imposed by fluid forces on the inner (endocardial) LV surface as specified by Eq. (7). Fluid and structure were coupled through their interfaces. Fluid-structure interaction must satisfy the traction balance and compatibility conditions for displacement and velocity.

The nonlinear Mooney-Rivlin model was used to describe the nonlinear anisotropic material properties. The strain energy function for the anisotropic modified Mooney-Rivlin model is given:

$$W = c_1\,(I_1-3) + c_2\,(I_2-3) + D_1\left[exp\,(D_2\,(I_1-3))-1\right] + \frac{K_1}{K_2}\,[exp(I_4-1)^2-1] \quad (10)$$

where $I_1$ and $I_2$ are the first and second strain invariants given by,

$$I_1 = \sum C_{ii}, I_2 = \frac{1}{2}\left(I_1^2 - C_{ij}C_{ij}\right), I_4 = C_{ij}(n_f)_i(n_f)_j \quad (11)$$

$C = [C_{ij}] = X^TX$ is the right Cauchy-Green deformation tensor, $X = [X_{ij}] = [\partial x_i/\partial a_j]$, $(x_i)$ is the current position, $(a_i)$ is the original position, $\mathbf{n}_f$ is the fiber direction, $c_i$, $D_i$ and $K_i$ are material parameters chosen to match experimental measurements (Fan et al., 2018; Lee et al., 2018). With parameters properly chosen, it was shown that stress-strain curves derived from Eq. (10) agreed very well with the stress-strain curves from the anisotropic (transversely isotropic) strain-energy function with respect to the local fiber direction given in McCulloch et al. (1992):

$$W = \frac{C}{2}(e^Q-1) \quad (12)$$

$$Q = b_1E_{ff}^2 + b_2(E_{cc}^2 + E_{rr}^2 + E_{cr}^2 + E_{rc}^2) + b_3(E_{fc}^2 + E_{cf}^2 + E_{fr}^2 + E_{rf}^2) \quad (13)$$

where $E_{ff}$ is fiber strain, $E_{cc}$ is cross-fiber in-plane strain, $E_{rr}$ is radial strain, and $E_{cr}$, $E_{fr}$ and $E_{fc}$ are the shear components in their respective coordinate planes, C, $b_1$, $b_2$, and $b_3$ are parameters to be chosen to fit experimental data. For simplicity, we set $b_1$ = 0.8552, $b_2$ = 1.7005, $b_3$ = 0.7742 in Eq. (13) so that we can have a single parameter C for comparison. **Figure 3** gave material stress-stretch curves for a baseline model with RVA pacemaker. The least-squares method was used to find the equivalent Young's moduli (YM) for the material curves for easy comparison.

As patient-specific fiber orientation data was not available from these patients, we chose to construct a two-layer LV model and set fiber orientation angles using fiber angles given in Axel (2002). Fiber orientation angles were set at -60 degree and 80 degree for epicardium (outer layer) and endocardium (inner layer), respectively. Fiber orientation can be adjusted when patient-specific data becomes available (Tang et al., 2010).

## A Pre-shrink Process and Geometry-Fitting Technique for Mesh Generation

Under *in vivo* condition, ventricles are pressurized and the zero-stress ventricular geometries are unknown. In our model construction process, a pre-shrink process was applied to *in vivo* end-systolic ventricular geometries to generate the starting shape for the computational simulation (Fan et al., 2018). A geometry-fitting mesh generation technique was also used to generate mesh for our models (Tang et al., 2010). Mesh analysis was performed by decreasing mesh size by 10% (in each dimension) until solution differences were less than 2%. The mesh was then chosen for our simulations.

## Solution Methods and Data Collection for Statistical Analysis

The Echo-based anisotropic LV models were constructed for the four different pacing locations and the models were solved by ADINA (ADINA R&D, Watertown, MA, United States) using unstructured finite elements and the Newton-Raphson iteration method. The "Re-Start" feature in ADINA was used to adjust material parameters at each numerical time step to implement the potential conduction of myocardium. Flow velocity, flow shear stress (FSS) and stress/strain distributions were obtained for analysis. Because stress and strain are tensors, for simplicity, maximum principal stress (Stress-$P_1$) and strain (Strain-$P_1$) were used and referred to as stress and strain in this paper.

# RESULTS

It is common to use selected cut-surfaces and critical time points (begin-filling, peak velocity during filling, begin-ejection, peak velocity during ejection, etc.) to demonstrate and compare solution behaviors. For our modeling set-up, the time points for begin-filling and end-ejection are connection points of systole and diastole phases. The same is true for end-filling and before-ejection time points. This explanation should be helpful to understand why we mainly used end-filling and end-ejection in our comparative analyses.

## Simulating Electrical Signal Conduction by Echo-Based Fluid-Structure Interactions Ventricle Model

The atrial and ventricular contraction and relaxation are necessary conditions for the heart to achieve blood pumping and promote blood circulation, and the excitatory process of the cell membrane is the initiating factor that triggers the contractile response. On the one hand, myocardium is functionally a syncytium, and the excitability generated in any part of the myocardial cell membrane can not only spread along the entire cell membrane, but can also be transmitted to other cardiomyocyte through the disc, thereby causing excitation and contraction of the whole myocardial. On the other hand, when the ventricular myocardium is excited, the action potential expands from the site of excitation to the periphery, thereby affecting myocardial contraction. In our model, the mapping between material stiffness and ventricular electrical signals is quantified based

on data measured on pig implanted pacemakers, and the potential conduction of the myocardium is simulated by the softness of the material. **Figure 4** shows the electrical signal conduction diagram and the corresponding 3D reconstruction geometry model at different phases. The red region in **Figure 4E** is the stiffest part of the model material, corresponding to the red region of the myocardial electrical signal conduction at this time in **Figure 4A**. And along the direction of electrical signal conduction, the myocardial material is getting softer. LV myocardial material parameter values at different phases are given in **Table 2**. The myocardial material was stiffer, C in Eq. (13), the mean YM value for the fiber direction ($YM_f$) and the mean YM value for the circumferential direction of the fiber ($YM_c$) were higher.

## Right Ventricular Outflow Tract Pacing Has a Higher Maximum Velocity Value and Flow Shear Stress

The flow dynamics index is an important indicator for characterizing and evaluating cardiac function under pacing. FSS reflects the influence of flow on LV inner surface and ventricle valves. **Table 3** gives the maximum velocity values over the whole LV flow domain and the average FSS on LV inner surface at selected time points from the four models studied. Using the

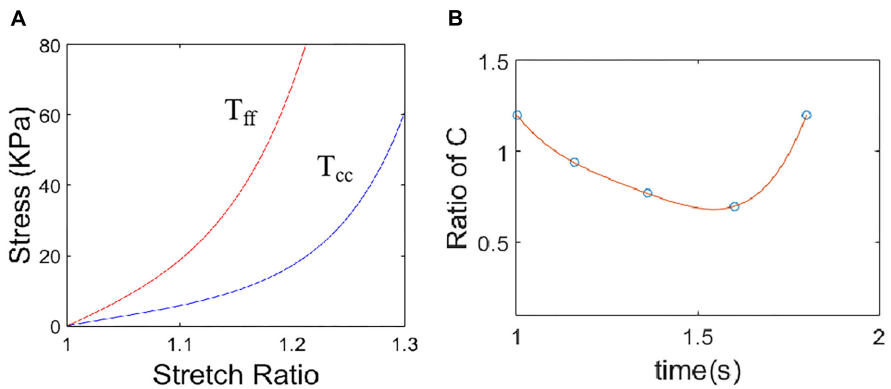


**FIGURE 3 |** Material stress-stretch curves for a baseline model with right ventricular apex (RVA) pacemaker. **(A)** Baseline material stress-stretch curves, $T_{ff}$: stress in fiber direction, $T_{cc}$: stress in circumferential direction of the fiber. **(B)** Stiffness variation in a cardiac cycle for a sample region of the model with RVA pacemaker. Stiffness variation was realized by adjust C values in Eq. (12).

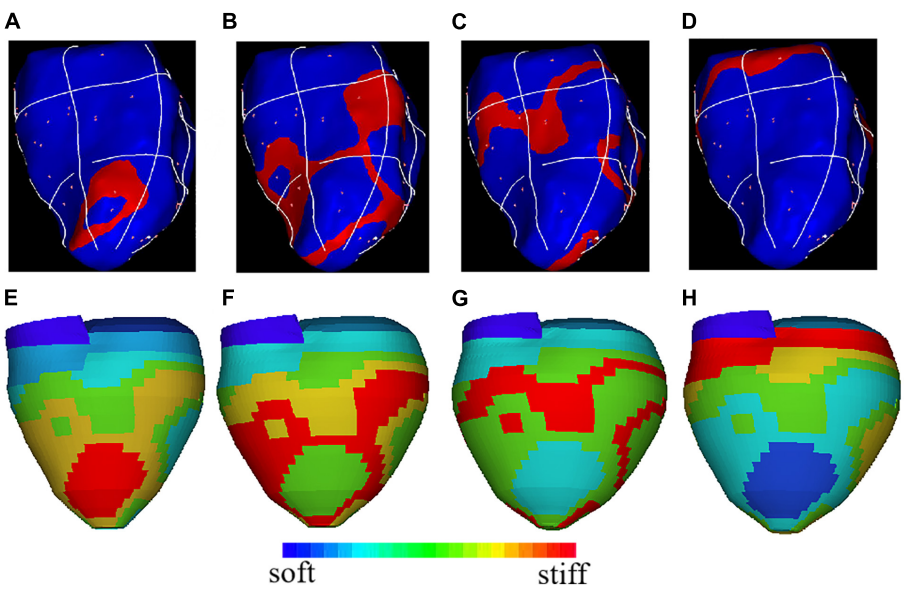


**FIGURE 4 |** The electrical signal conduction diagrams with right ventricular apex (RVA) pacemaker at different phases and the corresponding 3D geometry model showing regional stiffness variation. **(A)** Electric signal mapping during Phase 1; **(B)**. Electric signal mapping during Phase 2; **(C)**. Electric signal mapping during Phase 3; **(D)**. Electric signal mapping during Phase 4; **(E)**. Model stiffness mapping corresponding to **(A)**; **(F)**. Model stiffness mapping corresponding to **(B)**; **(G)**. Model stiffness mapping corresponding to **(C)**; **(H)**. Model stiffness mapping corresponding to **(D)**.

**TABLE 2 |** Material parameters from Right ventricular apex (RVA) model at different phases.

| | Phase 1 | | | Phase 2 | | |
|---|---|---|---|---|---|---|
| **Color** | **C(kPa)** | **$YM_f$(kPa)** | **$YM_c$(kPa)** | **C(kPa)** | **$YM_f$(kPa)** | **$YM_c$(kPa)** |
| Red | 21.65 | 622.4 | 215.2 | 18.76 | 539.4 | 186.5 |
| Yellow | 19.48 | 560.2 | 193.7 | 16.89 | 485.5 | 167.9 |
| Green | 17.32 | 497.9 | 172.2 | 15.01 | 431.5 | 149.2 |
| Cyan | 15.15 | 435.7 | 150.7 | 13.13 | 377.6 | 130.6 |
| Blue | 14.07 | 404.6 | 139.9 | 12.20 | 350.6 | 121.2 |
| Darkblue | 12.99 | 373.5 | 129.1 | 11.26 | 323.7 | 111.9 |
| | **Phase 3** | | | **Phase 4** | | |
| **Color** | **C(kPa)** | **$YM_f$(kPa)** | **$YM_c$(kPa)** | **C(kPa)** | **$YM_f$(kPa)** | **$YM_c$(kPa)** |
| Red | 15.59 | 448.1 | 155.0 | 20.93 | 601.7 | 208.1 |
| Yellow | 13.85 | 398.4 | 137.7 | 18.83 | 541.5 | 187.2 |
| Green | 12.99 | 373.5 | 129.1 | 17.79 | 511.4 | 176.8 |
| Cyan | 12.12 | 348.6 | 120.5 | 16.74 | 481.3 | 166.4 |
| Blue | 11.26 | 323.7 | 111.9 | 14.65 | 421.2 | 145.6 |
| Darkblue | 10.39 | 298.8 | 103.3 | 12.56 | 361.0 | 124.8 |

*$YM_f$: YM value for the fiber direction; $YM_c$: YM value for circumferential direction of the fiber.*

NP model as baseline, at the peak of filling, velocity magnitude for RVOT and PIVS pacing models were 13% and 5% higher than that of the NP, respectively. FSS for RVOT and PIVS pacing models were 45% and 30% higher than that of the NP, respectively. However, velocity magnitude and FSS for RVA were 4% and 9% lower than that of the NP, respectively. At the peak of ejection, velocity magnitude for RVOT and PIVS pacing models were 50% and 23% higher than that of the NP model, respectively. FSS for RVOT and PIVS pacing models were 44% and 36% higher than that of the NP, respectively. Moreover, RVOT pacing model has higher maximum velocity and FSS values. However, velocity magnitude and FSS for RVA were 6% and 6% lower than that of the NP, respectively. **Figure 5** gave flow velocity and FSS plots from the RVOT model. It should be noted that global FSS maxima occurred near the mitral and aortic valve area, as expected.

## Right Ventricular Outflow Tract Pacing Have Higher Stress and Strain

Because of different pacemakers, different pacing methods or parts, the electrical impulses emitted are different for myocardial activation sequence, and the effects on myocardial motion will be different. Therefore, studying the movement of left ventricular myocardium under different pacing conditions is of positive significance for the evaluation of artificial pacing therapy. Ventricle stress and strain are good measure about how stiff ventricle muscle is. It is of interest to calculate LV stress/strain conditions for comparisons. Comparison of average stress and strain values on LV inner contours of four models were given in **Table 4**. Using NP model as baseline, at the peak of filling, stress of PVOT and PIVS pacing models were 18% and 10% higher than that of NP model, respectively. Moreover, Strain of PVOT and PIVS models were 13% and 5% higher than that of NP model, respectively. Stress of RVA pacing model was 4% lower than that of NP model. Strain of RVA model close to that of NP model. At the peak of ejection, stress of RVOT and PIVS models were 54% and 39% higher than that of NP model, respectively. Moreover, strain of RVOT and PIVS pacing models were 59% and 53% higher than that of NP model, respectively. However, stress and strain of RVA pacing model were 6% and 18% lower than those of NP model, respectively. **Figure 6** gives the stress and strain distribution plots of RVOT model.

# DISCUSSION

Compared with other medical imaging methods, ultrasound medical imaging technology has many advantages. Currently, echocardiography is the main imaging modality for the assessment of LV structure and functions. Echocardiography does not have radiation and is a safe imaging mode. In most cases, it is non-invasive and will not cause harm to humans. In addition, echocardiography imaging equipment is more accessible and requires lower diagnostic costs. More importantly, echocardiography can image soft tissue and display the anatomy and real activity of the internal organs of the human body in real time. It has become the main means of cardiac function assessment and heart disease diagnosis in most major hospitals. Echocardiography can non-invasively examine any cross-sectional image of the heart and is often used to estimate left ventricular wall segment motion (Chamsi-Pasha et al., 2017). However, the use of echocardiography relies on the visual observation of the two-dimensional image by the examiner, and lacks quantitative description. The left ventricular wall function can only be estimated semi-quantitatively, and the local motion of the left ventricular wall cannot be observed and estimated. In recent years, two-dimensional ultrasound technology has been widely used to evaluate ventricular function, but the positioning of the image plane is still affected by the movement of the patient and the movement of the operator, and the analysis of ventricular function must rely on the assumption

**TABLE 3 |** Velocity and flow shear stress (FSS) mean values at different times from 4 pacing models.

| | Begin-filling | | Peak of filling | | Begin-ejection | | Peak of ejection | |
|---|---|---|---|---|---|---|---|---|
| | **Velocity (cm/s)** | **FSS (dyn/cm$^2$)** | **Velocity (cm/s)** | **FSS (dyn/cm$^2$)** | **Velocity (cm/s)** | **FSS (dyn/cm$^2$)** | **Velocity (cm/s)** | **FSS (dyn/cm$^2$)** |
| NP | 17.60 | 0.2142 | 293.1 | 4.572 | 59.87 | 2.796 | 109.9 | 3.359 |
| RVA | 17.01 | 0.1713 | 280.6 | 4.153 | 56.89 | 2.319 | 103.4 | 3.157 |
| RVOT | 29.08 | 0.4531 | 329.9 | 6.616 | 70.96 | 3.783 | 164.9 | 4.831 |
| PIVS | 22.51 | 0.3982 | 306.2 | 5.956 | 66.75 | 3.452 | 135.6 | 4.563 |

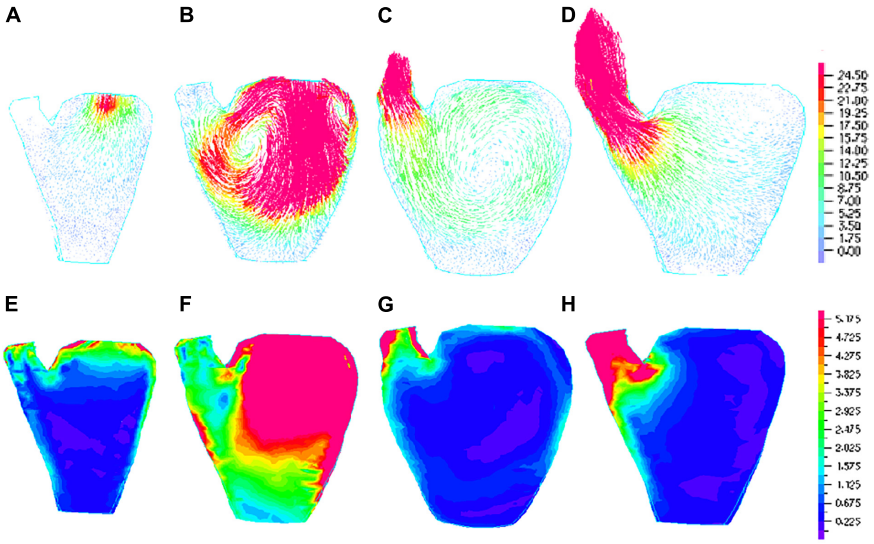


**FIGURE 5 |** Flow velocity and flow shear stress (FSS) plots of right ventricular outflow tract (RVOT) pacemaker model. **(A)** Velocity vector plot at begin-filling, $t$ = 1.28s, maximum velocity = 29.08cm/s, mitral valve opens, filling begins, aortic valve is closed; **(B)**. Velocity vector plot at the peak of filling, $t$ = 1.56s, maximum velocity = 329.9cm/s, mitral valve is open, aortic valve is closed; **(C)**. Velocity vector plot at begin-ejection, $t$ = 1.78s, aortic valve opens, ejection begins, mitral is closed, maximum velocity = 70.96cm/s; **(D)**. Velocity vector plot at $t$ = 2.06s, maximum velocity = 164.9 cm/s, aortic valve is open, mitral valve is closed; **(E)**. FSS band plot at begin-filling, $t$ = 1.28s, maximum = 10.87 dyn/cm$^2$; **(F)**. FSS band plot at the peak of filling, $t$ = 1.56s, maximum = 192.9dyn/cm$^2$; **(G)**. FSS band plot at begin-ejection, $t$ = 1.78s, maximum = 51.24dyn/cm$^2$; **(H)**. FSS band plot at peak of ejection, $t$ = 2.06s, maximum = 106.8dyn/cm$^2$.

**TABLE 4 |** Stress and strain mean values at different times from 4 pacing models.

| | Begin-filling | | Peak of filling | | Begin-ejection | | Peak of ejection | |
|---|---|---|---|---|---|---|---|---|
| | Stress (kPa) | Strain | Stress (kPa) | Strain | Stress (kPa) | Strain | Stress (kPa) | Strain |
| NP | 2.779 | 0.0882 | 81.21 | 0.5756 | 135.9 | 0.6979 | 33.46 | 0.4214 |
| RVA | 2.705 | 0.0760 | 77.94 | 0.5717 | 103.2 | 0.6312 | 31.47 | 0.3446 |
| RVOT | 4.285 | 0.1685 | 95.85 | 0.6475 | 168.4 | 0.8691 | 51.54 | 0.6684 |
| PIVS | 3.754 | 0.1502 | 89.36 | 0.6046 | 145.7 | 0.7617 | 46.67 | 0.6447 |

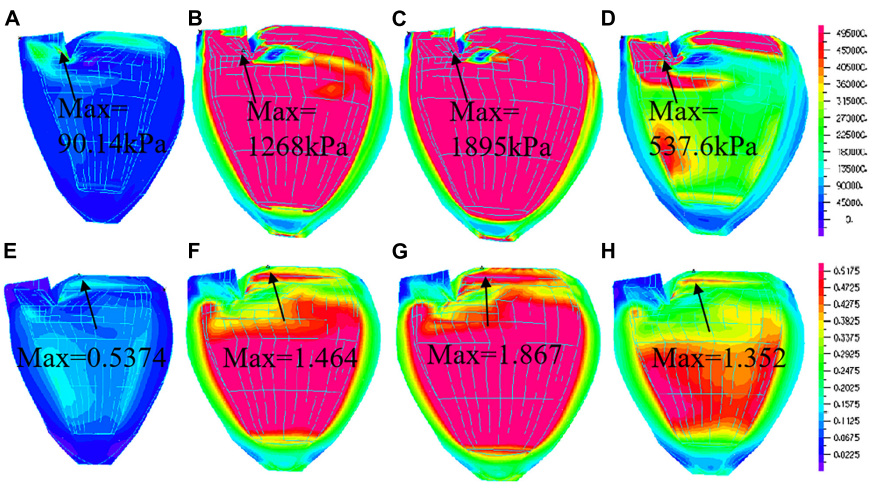


**FIGURE 6 |** Stress and Strain plots of right ventricular outflow tract (RVOT) model. **(A)** Stress distribution at begin-filling; **(B)**. Stress distribution at the peak of filling; **(C)**. Stress distribution at begin-ejection; **(D)**. Stress distribution at peak of ejection; **(E)**. Strain distribution at begin-filling; **(F)**. Strain distribution at peak of filling; **(G)**. Strain distribution at begin-ejection; **(H)**. Strain distribution at peak of ejection.

of cross-sectional information or ventricular geometry, so two-dimensional ultrasound has the limitations of its technology itself. In contrast, the three-dimensional model of the heart can not only provide clinical three-dimensional morphological information, but also provide an intuitive and effective judgment tool for determining the three-dimensional spatial location and pathological characteristics of the lesion. Therefore, the study of three-dimensional models of the heart has become a commonly used diagnostic tool in medical research for cardiovascular diseases.

Cardiac therapy is an important non-pharmacological treatment for patients with arrhythmia. However, while the cardiac pacing treatment saves the patient's life, how to obtain better pacing therapy to improve the cardiac function status and quality of life for the patients is a major problem that needs to be solved urgently in clinical cardiovascular disease. The pumping process of the heart involves three kinds of physiological activities: first, myocardial excitation, electrical activity, including cell membrane depolarization-repolarization periodicity, forming an electrocardiogram cycle, the physiological function of cardiac electrical activity dominates the periodic rhythm of the heart, heart electrical activity triggers myocardial mechanical motion, called excitation-contraction coupling. Second, myocardial relaxation, mechanical movement, including muscle fiber contraction-diastolic periodicity, the formation of cardiac cycle, myocardial mechanical movement caused by changes in the distribution of blood flow in the heart chamber, thereby achieving cardiac pumping function. Third, the distribution of blood flow field in the heart chamber is a category of hemodynamics. The distribution of myocardial mechanical motion and heart chamber flow field can indirectly reflect the state of cardiac electrical expansion. These three kinds of cardiac physiological activities complement each other and constitute an important part of the heart pumping blood. To date, a number of active cardiac mechanics models have been proposed for different uses. The most important application is to explore the relationship between electrical signaling and mechanical motion in the heart. Clinical trials have found that asynchronous electrical activation can cause filling and pumping dysfunction (Lee et al., 2018). This finding suggests a biomechanical effect of changes in cardiac activation sequence. In order to better understand the relationship between the electrical activation mode of the ventricle and the local sequence of mechanical strain. This paper introduces an echo-based left ventricular FSI simulation model to achieve cardiac pumping, and simulates myocardial electrical signal transmission by realizing myocardial mechanical motion and cardiac flow distribution. In this study, we not only quantitatively analyze the hemodynamic parameters, but also the advantages and disadvantages of the hemodynamic effects, combined with the movement of the left ventricular myocardium, and evaluate the effects of different pacing modes on cardiac function. Ventricle remodeling, disease development, tissue regeneration, patient recovery after surgery and many other cell biological activities are closely associated with ventricle mechanical conditions (Pagani et al., 2021).

With the development of technology and research, more and more evidences show that ventricular electrical activation sequence and ventricular contraction synchronization are important factors affecting cardiac function. The closer to the physiological state of cardiac pacing, the less the effect on long-term cardiac function. Physiological pacing is not only to ensure the atrial-ventricular sequence, but also to maintain the synchrony of biventricular electro-mechanical activity. At present, many studies tend to think that the direct His bundle pacing has the best effect (Kronborg et al., 2014; Sharma et al., 2015). The direct His bundle pacing contraction activation sequence is consistent with the normal sinus rhythm. The earliest contraction is the upper part of the ventricular septum, which is rapidly transmitted from the ventricular septum to the apex. And the left and right ventricle free wall, the outer side spread, and finally stopped at the same time on both sides of the ventricular base. In theory, His bundle is the best ventricular pacing site. For many years electro-physicists have been studying direct His bundle pacing in order to obtain normal or near normal ventricular activation sequences. Kronborg et al. (2014) showed that His or para-His pacing preserves LV ejection fraction and mechanical synchrony compared with RV septal pacing in patient with atrioventricular block and may be a future pacing strategy to prevent pacing-induced heart failure in selected pacemaker patients. Sharma et al. (2015) assessed the safety, feasibility, and success rates of His-bundle pacing in unselected patients without the use of a mapping catheter or a backup RV lead as compared to RVA pacing. However, the direct His bundle pacing has limited the operation and application of this kind of surgery because of the difficulty in surgery operation and the long operation time, high pacing threshold, potential damage or blocking of His bundle. Because of the location of the right ventricular septum near the His bundle, the proximal end of the ventricular septum is first contracted and excited, and rapidly spread to the left and right ventricles and apex through the interventricular septum, so that the left and right ventricular contraction activation is basically synchronized. The electrical activation synchrony of the left and right ventricles ensures that the simultaneous mechanical contraction of the biventricular, the ejection fraction is improved, the left ventricular diastolic filling time is increased, the mitral regurgitation is reduced, and get better acute and long-term hemodynamic effects. Da Costa et al. (2013) provided a comprehensive overview of RVOT pacing. Singh et al. (2015) assessed LV function and dyssynchrony in patients with RVOT pacing and conventional RVA pacing using equilibrium radionuclide angiography. Their results indicated RVOT pacing may lead to better preservation of LV function on longer follow-up. Yao et al. (2013) evaluated contractile patterns in the circumferential direction in patients with idiopathic frequent premature ventricular complexes form RVOT. The present study also shows RVOT pacing have better blood flow and myocardial motion.

Several limitations should be acknowledged in our modeling study: (a) only one health animal's data were used in this study. The pacemaker implant benefits may be different for each individual. A multi-animal or animal with cardiac arrhythmia study and should be conducted to help us draw more valid conclusions and further verify and confirm our

findings; (b) ventricle valve mechanics was not included. Valve mechanics plays an important role. However, including it requires considerable more data (valve morphology and material properties) and it remains to be our future modeling effort; (c) local ventricle deformation imaging data (by particle tracking) was not included. We are in need of patient-specific data such as fiber orientation, sarcomere length contraction rate, regional material properties, etc. Lack of such *in vivo* data and model construction cost are also considerations. (d) active contraction and expansion were modeled by material stiffening and softening without adjusting zero-stress ventricle geometries. (e) Further research needs to be done into options for alternative pacing methods, such as RVOT pacing, PVIS pacing, and how they correlate with long-term clinical outcomes.

## CONCLUSION

Patient-specific models of the cardiovascular system are a promising approach to personalized cardiovascular medicine. FSI models provide complete mechanical analysis including both flow forces and structural stress/strain conditions and fluid structure interaction. Correct ventricle flow characteristics and stress/strain calculations are of fundamental importance for many cardiovascular researches where mechanical forces play a role in disease initiation, progression and treatment strategy selections. The existence of alternatives to existing leads and pacing methods may permit improvement in long-term outcomes with chronic pacemaker therapy while also making therapies such as synchronous pacing available to a wider array of patients with clinical situations. Direct comparison studies between pacing options will be needed to better understand the electromechanical associations and how these correlates with long-term morbidity, mortality, and quality of life. Studies concentrating on the therapeutic benefits of existing experimental therapies will also allow for the development of parameters that may permit correlation of findings during acute animal studies with long-term clinical outcomes. The clinical value of the present model can be further assessed by testing its ability to predict cardiac functional alterations during cardiac resynchronization therapy and ultimately to help optimize the therapeutic protocol. Here we have made a first step toward this goal by defining the baseline model of a patient with dyssynchronous heart failure.

## DATA AVAILABILITY STATEMENT

The original contributions presented in the study are included in the article/supplementary material, further inquiries can be directed to the corresponding authors.

## ETHICS STATEMENT

The animal study was reviewed and approved by the Ethics Committee of the First Affiliated Hospital of Nanjing Medical University. Written informed consent was obtained from the owners for the participation of their animals in this study.

## AUTHOR CONTRIBUTIONS

JY and DX were collected the data. LF, LW, and DT were done computational modelling and results analysis. LF and DT wrote the manuscript. All authors contributed to manuscript revision, read, and approved the submitted version.

## FUNDING

This research was supported in part by National Sciences Foundation of China grants 11672001(JY), 81571691(JY), 81771844(JY) and Yunnan Fundamental Research Projects KKAE202107036 (LF).

## REFERENCES

Alberti, L., Pieragnoli, P., Ricciardi, G., and Padeletti, L. (2017). Hemodynamics of his bundle pacing. *J. Electrocardiol.* 50, 161–165. doi: 10.1016/j.jelectrocard.2016.10.007

Alhous, M. H., Small, G. R., Hannah, A., Hillis, G. S., Frenneaux, M., and Broadhurst, P. A. (2015). Right ventricular septal pacing as alternative for failed left ventricular lead implantation in cardiac resynchronization therapy candidates. *Europace* 17, 94–100. doi: 10.1093/europace/euu259

Axel, L. (2002). Biomechanical dynamics of the heart with MRI. *Annu. Rev. Biomed. Eng.* 4, 321–347. doi: 10.1146/annurev.bioeng.4.020702.153434

Carpio, E. F., Gomez, J. F., Sebastian, R., Lopez-Perez, A., Castellanos, E., and Almendral, J. (2019). Optimization of lead placement in the right ventricle during cardiac resynchronization therapy. a simulation study. *Front. Physiol.* 10:74. doi: 10.3389/fphys.2019.00074

Chamsi-Pasha, M. A., Sengupta, P. P., and Zoghbi, W. A. (2017). Handheld echocardiography: current state and future perspectives. *Circulation* 136, 2178–2188. doi: 10.1161/CIRCULATIONAHA.117.026622

Chen, Z., Niederer, S., Shanmugam, N., Sermesant, M., and Rinaldi, C. A. (2017). Cardiac computational modeling of ventricular tachycardia and cardiac resynchronization therapy: a clinical perspective. *Minerva Cardioangiol.* 65, 380–397. doi: 10.23736/S0026-4725.17.04362-6

Coppola, G., La Greca, C., Corrado, E., Ajello, L., Nogara, A., and Ciaramitaro, G. (2015). Selective pacing sites. *Minerva Cardioangiol.* 63, 151–160.

Da Costa, A., Gabriel, L., Romeyer-Bouchard, C., Géraldine, B., Gate-Martinet, A., and Laurence, B. (2013). Focus on right ventricular outflow tract septal pacing. *Arch. Cardiovasc. Dis.* 106, 394–403. doi: 10.1016/j.acvd.2012.08.005

Das, A., and Kahali, D. (2016). Physiological cardiac pacing: current status. *Indian Heart J.* 68, 552–558. doi: 10.1016/j.ihj.2016.03.033

Das, A., Islam, S. S., Pathak, S. K., Majumdar, I., Sharwar, S. A., and Saha, R. (2020). Left bundle branch area. A new site for physiological pacing: a pilot study. *Heart Vessels* 35, 1563–1572. doi: 10.1007/s00380-020-01623-y

Erdogan, O., and Hunuk, B. (2010). Right ventricular outflow tract pacing: an alternative, safe, and effective pacing site. *J. Long Term Effects Med. Implants* 20, 13–21. doi: 10.1615/jlongtermeffmedimplants.v20.i1.20

Fan, L. L., Yao, J., Yang, C., Tang, D., and Xu, D. (2018). Patient-Specific echo-based fluid-structure interaction modeling study of blood flow in the left ventricle with infarction and hypertension. *Comput. Model. Eng. Sci.* 114, 221–237. doi: 10.3970/cmes.2018.114.221

Glikson, M., Nielsen, J. C., Kronborg, M. B., Michowitz, Y., Auricchio, A., Barbash, I. M., et al. (2021). 2021 ESC Guidelines on cardiac pacing and cardiac resynchronization therapy. *Eur. Heart J.* 42, 3427–3520. doi: 10.1093/eurheartj/ehab364

Gurev, V., Constantino, J., Rice, J. J., and Trayanova, N. A. (2010). Distribution of electromechanical delay in the heart: insights from a three-dimensional electromechanical model. *Biophys. J.* 99, 745–754. doi: 10.1016/j.bpj.2010.05.028

Huang, X., Deng, L., Zuo, H., Yang, C., Song, Y., Lesperance, M., et al. (2021). Comparisons of simulation results between passive and active fluid structure interaction models for left ventricle in hypertrophic obstructive cardiomyopathy. *Biomed. Eng. Online* 20:9. doi: 10.1186/s12938-020-00838-4

Kapa, S., Bruce, C. J., Friedman, P. A., and Asirvatham, S. J. (2010). Advances in cardiac pacing: beyond the transvenous right ventricular apical lead. *Cardiovasc. Ther.* 28, 369–379. doi: 10.1111/j.1755-5922.2010.00157.x

Kronborg, M. B., Mortensen, P. T., Poulsen, S. H., Gerdes, J. C., Jensen, H. K., and Nielsen, J. C. (2014). His or para-His pacing preserves left ventricular function in atrioventricular block: a double-blind, randomized, crossover study. *Europace* 16, 1189–1196. doi: 10.1093/europace/euu011

Lee, A. W. C., Costa, C. M., Strocchi, M., Rinaldi, C. A., and Niederer, S. A. (2018). Computational modeling for cardiac resynchronization therapy. *J. Cardiovasc. Transl. Res.* 11, 92–108. doi: 10.1007/s12265-017-9779-4

Liu, H. S. (2019). More standardized, more progressive, more reasonable-Mainland China congenital heart disease intervention registration data sharing in 2018. *China Med. News* 34:16. doi: 10.3969/j.issn.1000-8039.2019.10.015

Liu, P., Wang, Q., Sun, H., Qin, X., and Zheng, Q. (2021). Left bundle branch pacing: current knowledge and future prospects. *Front. Cardiovasc. Med.* 8:630399. doi: 10.3389/fcvm.2021.630399

Manolis, A. S., Sakdlariou, D., and Andrikopoulos, G. K. (2008). Alternate site pacing in patients at risk for heart failure. *Angiology* 59(Suppl. 2), 97S–102S. doi: 10.1177/0003319708321479

McCulloch, A. D., Waldman, L., Rogers, J., and Guccione, J. M. (1992). Large-scale finite element analysis of the beating heart. *Crit. Rev. Biomed. Eng.* 20, 427–449.

Michalik, J., Dabrowska-Kugacka, A., Kosmalska, K., Moroz, R., Kot, A., and Lewicka, E. (2021). Hemodynamic effects of permanent his bundle pacing compared to right ventricular pacing assessed by two-dimensional speckle-tracking echocardiography. *Int. J. Environ. Res. Public Health* 18:11721. doi: 10.3390/ijerph182111721

Miranda, R. I., Nault, M., Simpson, C. S., Michael, K. A., Abdollah, H., Baranchuk, A., et al. (2012). The right ventricular septum presents the optimum site for maximal electrical separation during left ventricular pacing. *J. Cardiovasc. Electrophysiol.* 23, 370–374. doi: 10.1111/j.1540-8167.2011.02207.x

Mohamed, M. O., Sharma, P. S., Volgman, A. S., Bhardwaj, R., Kwok, C. S., Rashid, M., et al. (2019). Prevalence, outcomes, and costs according to patient frailty status for 2.9 million cardiac electronic device implantations in the United States. *Can. J. Cardiol.* 35, 1465–1474. doi: 10.1016/j.cjca.2019.07.632

Pagani, S., Dedè, L., Manzoni, A., and Quarteroni, A. (2021). Data integration for the numerical simulation of cardiac electrophysiology. *Pacing Clin. Electrophysiol.* 44, 726–736. doi: 10.1111/pace.14198

Sharma, P. S., Dandamudi, G., Naperkowski, A., Oren, J. W., Storm, R. H., Ellenbogen, K. A., et al. (2015). Permanent his-bundle pacing is feasible, safe, and superior to right ventricular pacing in routine clinical practice. *Heart Rhythm* 12, 305–312. doi: 10.1016/j.hrthm.2014.10.021

Sharma, P. S., Vijayaraman, P., and Ellenbogen, K. A. (2020). Permanent His bundle pacing: shaping the future of physiological ventricular pacing. *Nat. Rev. Cardiol.* 17, 22–36. doi: 10.1038/s41569-019-0224-z

Singh, H., Patel, C. D., Sharma, G., and Naik, N. (2015). Comparison of left ventricular systolic function and mechanical dyssynchrony using equilibrium radionuclide angiography in patients with right ventricular outflow tract versus right ventricular apical pacing: a prospective single-center study. *J. Nucl. Cardiol.* 22, 903–911. doi: 10.1007/s12350-014-0033-z

Tang, D., del Nido, P. J., Yang, C., Zuo, H., Huang, X. Y., Rathod, R. H., et al. (2016). Patient-specific MRI-based right ventricle models using different zero-load diastole and systole geometries for better cardiac stress and strain calculations and pulmonary valve replacement surgical outcome predictions. *PLoS One* 11:e0162986. doi: 10.1371/journal.pone.0162986

Tang, D., Yang, C., Geva, T., and del Nido, P. J. (2010). Image-Based patient-specific ventricle models with fluid-structure interaction for cardiac function assessment and surgical design optimization. *Prog. Pediatr. Cardiol.* 30, 51–62. doi: 10.1016/j.ppedcard.2010.09.007

Tang, D., Yang, C., Geva, T., Gaudette, G., and del Nido, P. J. (2011). Multi-physics MRI-based two-layer fluid-structure interaction anisotropic models of human right and left ventricles with different patch materials: cardiac function assessment and mechanical stress analysis. *Comput. Struct.* 89, 1059–1068. doi: 10.1016/j.compstruc.2010.12.012

Tops, L. F., Schalij, M. J., and Bax, J. J. (2009). The effects of right ventricular apical pacing on ventricular function and dyssynchrony implications for therapy. *J. Am. Coll. Cardiol.* 54, 764–776. doi: 10.1016/j.jacc.2009.06.006

Tsujii, N., Miyazaki, A., Sakaguchi, H., Kagisaki, K., Yamamoto, T., and Matsuoka, M. (2016). High incidence of dilated cardiomyopathy after right ventricular inlet pacing in patients with congenital complete atrioventricular block. *Circ. J.* 80, 1251–1258. doi: 10.1253/circj.CJ-15-1122

Usyk, T. P., Legrice, I. J., and Mcculloch, A. D. (2012). Computational model of three-dimensional cardiac electromechanics. *Comput. Vis. Sci.* 4, 249–257. doi: 10.1007/s00791-002-0081-9

Vijayaraman, P., Bordachar, P., and Ellenbogen, K. A. (2017). The continued search for physiological pacing: where are we now? *J. Am. Coll. Cardiol.* 69, 3099–3114. doi: 10.1016/j.jacc.2017.05.005

Yao, J., Yang, R., Xu, D., Zhuang, Y., Yong, Y., and Cao, K. (2013). Circumferential myocardial contraction patterns in patients with idiopathic frequent premature ventricular complexes from the right ventricular outflow tract. *Int. J. Cardiol.* 166, 166–172. doi: 10.1016/j.ijcard.2011.10.105

Zhu, H., Yin, B., and Zhu, D. (2001). Computing ECG based on action potential of single cardiac cell: some abnormal simulated ECES. *J. Biophys.* 1, 123–134.

Zhu, H., Zou, T., Zhong, Y., Yang, C., Ren, Y., and Wang, F. (2020). Prevention of non-response to cardiac resynchronization therapy: points to remember. *Heart Fail. Rev.* 25, 269–275. doi: 10.1007/s10741-019-09834-w

Zou, C., Song, J., Li, H., Huang, X., Liu, Y., and Zhao, C. (2015). Right ventricular outflow tract septal pacing is superior to right ventricular apical pacing. *J. Am. Heart Assoc.* 4:e001777. doi: 10.1161/JAHA.115.001777

**Conflict of Interest:** The authors declare that the research was conducted in the absence of any commercial or financial relationships that could be construed as a potential conflict of interest.

**Publisher's Note:** All claims expressed in this article are solely those of the authors and do not necessarily represent those of their affiliated organizations, or those of the publisher, the editors and the reviewers. Any product that may be evaluated in this article, or claim that may be made by its manufacturer, is not guaranteed or endorsed by the publisher.

frontiers | Frontiers in Physiology

BRIEF RESEARCH REPORT
published: 06 April 2022
doi: 10.3389/fphys.2022.848011

# Left Ventricle Biomechanics of Low-Flow, Low-Gradient Aortic Stenosis: A Patient-Specific Computational Model

*Andrew D. Wisneski[1], Yunjie Wang[2], Salvatore Cutugno[3], Salvatore Pasta[3], Ashley Stroh[4], Jiang Yao[5], Tom C. Nguyen[1], Vaikom S. Mahadevan[6] and Julius M. Guccione[1]**

[1]Department of Surgery, University of California, San Francisco, San Francisco, CA, United States, [2]Thornton Tomassetti Life Sciences, Santa Clara, CA, United States, [3]Department of Engineering, Viale Dell Scienze, Universita degli Studi di Palermo, Palermo, Italy, [4]CATIA, Dassault Systèmes, Wichita, KS, United States, [5]Simulia, Dassault Systèmes Simulia, Johnston, RI, United States., [6]Division of Cardiology, University of California, San Francisco, San Francisco, CA, United States

This study aimed to create an imaging-derived patient-specific computational model of low-flow, low-gradient (LFLG) aortic stenosis (AS) to obtain biomechanics data about the left ventricle. LFLG AS is now a commonly recognized sub-type of aortic stenosis. There remains much controversy over its management, and investigation into ventricular biomechanics may elucidate pathophysiology and better identify patients for valve replacement. ECG-gated cardiac computed tomography images from a patient with LFLG AS were obtained to provide patient-specific geometry for the computational model. Surfaces of the left atrium, left ventricle (LV), and outflow track were segmented. A previously validated multi-scale, multi-physics computational human heart model was adapted to the patient-specific geometry, yielding a model consisting of 91,000 solid elements. This model was coupled to a virtual circulatory system and calibrated to clinically measured parameters from echocardiography and cardiac catheterization data. The simulation replicated key physiologic parameters within 10% of their clinically measured values. Global LV systolic myocardial stress was 7.1 ± 1.8 kPa. Mean stress of the basal, middle, and apical segments were 7.7 ± 1.8 kPa, 9.1 ± 3.8 kPa, and 6.4 ± 0.4 kPa, respectively. This is the first patient-specific computational model of LFLG AS based on clinical imaging. Low myocardial stress correlated with low ejection fraction and eccentric LV remodeling. Further studies are needed to understand how alterations in LV biomechanics correlates with clinical outcomes of AS.

**Keywords: aortic stenosis, finite elememt method, myofiber stress, ventricular function, aortic stenosis, realistic simulation, ventricle-aortic coupling**

OPEN ACCESS

***Edited by:***
*Shengzhang Wang, Fudan University, China*

***Reviewed by:***
*Hao Gao, University of Glasgow, United Kingdom*
*Jiaqiu Wang, Queensland University of Technology, Australia*

****Correspondence:***
*Julius M. Guccione*
*Julius.Guccione@ucsf.edu*

***Specialty section:***
*This article was submitted to Computational Physiology and Medicine, a section of the journal Frontiers in Physiology*

***Received:*** *03 January 2022*
***Accepted:*** *11 March 2022*
***Published:*** *06 April 2022*

***Citation:***
*Wisneski AD, Wang Y, Cutugno S, Pasta S, Stroh A, Yao J, Nguyen TC, Mahadevan VS and Guccione JM (2022) Left Ventricle Biomechanics of Low-Flow, Low-Gradient Aortic Stenosis: A Patient-Specific Computational Model. Front. Physiol. 13:848011. doi: 10.3389/fphys.2022.848011*

## INTRODUCTION

Aortic stenosis (AS) is the most common acquired heart valve disease in the developed world (Lindman et al., 2013). With the advent of transcatheter aortic valve replacement (TAVR), there has been increased attention to better understanding AS pathophysiology and how to optimally select patients for aortic valve replacement. Low-flow, low-gradient (LFLG) AS, first described by Hachicha et al., is a disease characterized by low aortic valve area but, given ventricular dysfunction, an elevated

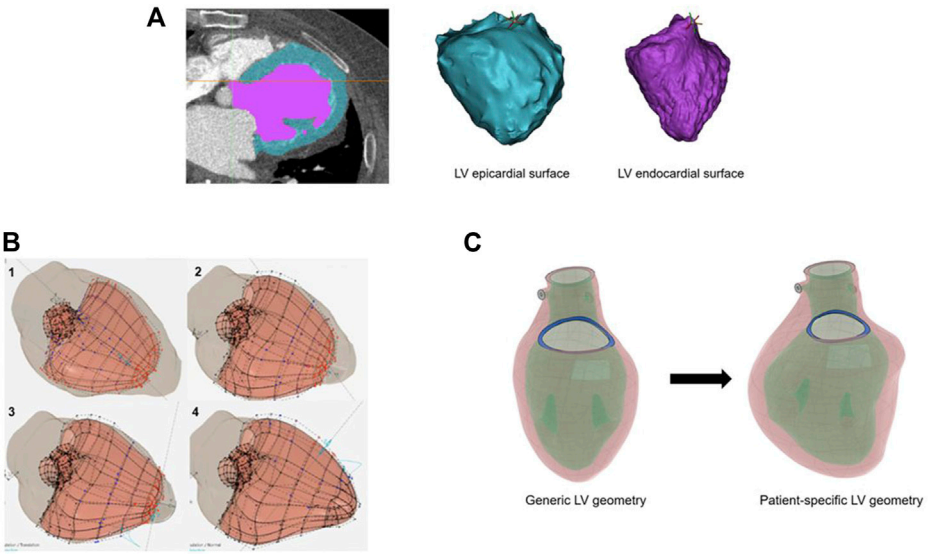


**FIGURE 1 | (A)** Image segmentation of the left ventricle from computed tomography imaging. The left ventricle (LV) wall is in blue, and the LV cavity is in purple. At right are the three-dimensional surfaces representing the LV epicardial and endocardial surface boundaries. **(B)** The CATIA™ software allows rapid alignment of the generic model (salmon-colored model) to patient-specific imaging surfaces (left ventricle shadow overlay shown in gray). Alignment of the generic epicardial surface to patient-specific epicardial surface: 1) initial overlay, 2) alignment of the basal segments, 3) mid-wall segments, 4) apical segments. **(C)** Overview of the generic left ventricle geometry transformed to patient-specific geometry after application of the Smart Geometry processing.

trans-valvular pressure gradient is lacking (Hachicha et al., 2007). It is estimated that up to 25% of all severe AS cases may be classified as LFLG (Hachicha et al., 2007; Pibarot and Dumesnil 2012; Clavel et al., 2016). This has raised challenges in the clinical management and diagnosis of patients suspected of having LFLG AS, with many diagnostic algorithms recommending dobutamine stress echocardiography to determine presence of LV contractile reserve (Pibarot and Dumesnil 2012; Pibarot and Clavel 2015; Clavel et al., 2016). Established evidence-based guidelines to determine diagnostic criteria for severe AS in presence of LFLG, and whom to select for aortic valve replacement, remains a topic of ongoing study (Nishimura et al., 2014).

The goal of aortic valve replacement, through TAVR or surgery, is to halt progression of and reverse pathologic left ventricle (LV) remodeling from chronic increased afterload of the stenotic aortic valve. We believe that a contemporary understanding of AS pathophysiology should encompass detailed analysis of ventricular function. Advancements in computational techniques and imaging have enabled creation of high-fidelity models of the human heart and LV (Sack et al., 2016; Sack et al. 2018a; Sack et al. 2020). We previously modeled aortic stenosis with a comprehensive human heart model to determine myocardial stress values in a non-LFLG AS case (Wisneski et al., 2020), with a model that was based on idealized ventricular geometry without any ventricular dysfunction. Detailed cardiac clinical imaging, and enhanced image processing techniques afford new opportunities to create patient-specific models to understand LV biomechanics.

We describe the first patient-specific computational model of the LV in a patient with LFLG AS. This model is derived from clinical cardiac computed tomography (CT) imaging which was obtained for TAVR planning purposes. While this study reports an initial case, this method should be scalable to permit greater numbers of patient-specific models to be generated. Future studies should correlate biomechanics data to disease severity, progression, and treatment outcomes.

# METHODS

## Clinical Case and Image Processing

A 68-year-old man with co-morbidities of hypertension, hyperlipidemia, diabetes mellitus, psoriatic arthritis, chronic kidney disease, and coronary artery disease with prior percutaneous coronary intervention developed progressive AS, limiting his functional status. From transthoracic echocardiography, the LV ejection fraction of 25% was measured and eccentric LV geometry was noted. The mean pressure gradient across the aortic valve was 15 mmHg with an estimated aortic valve area of 0.8 $cm^2$. LFLG AS was confirmed with dobutamine stress echocardiography. Coronary angiogram confirmed that his prior coronary stents were patent. The Society of Thoracic Surgeon's mortality score was 11% for isolated surgical aortic valve replacement, rendering this patient a high-risk operative candidate, thus he was considered for TAVR.

Images from the diastolic phase of the ECG-gated CT scan were used to provide geometry for the computational model (**Figure 1A**). CT scan slices were 0.625 mm contiguous axial slices acquired on a GE Lightspeed VCT scanner (GE Healthcare, Chicago, Illinois, United States). All CT images were anonymized prior to analysis for research purposes, done in accordance with the institutional review board.

Segmentation of the LV, left atrium, and the aortic root was performed with Mimics version 2.1 (Materialise, Leuven,

Belgium). Separate segmentation of the innermost surface of the LV chamber at the endocardium, and the outermost LV surface at the epicardium provided the LV wall geometry (**Figure 1A**).

## Computational Model

Our computational model platform, which has been described previously, provides realistic anatomy of the chambers and valves and accounts for multiple domains of cardiac function, including electrical activation, valve function and structure, myocardial material properties, myocardial microstructure and fiber orientation, and for blood flow (Carrick et al., 2012; Baillargeon et al., 2014; Sack et al., 2018a; Wisneski et al., 2021). The LV myocardium material model has been described in the aforementioned references. The ventricular model passive response uses the Holzapfel and Ogden anisotropic hyperelastic model (Holzapfel and Ogden 2009). The deviatoric response is governed by the following strain energy potential:

$$\Psi_{dev} = \frac{a}{2b}\exp\left[b\left(I_1 - 3\right)\right] + \sum_{i=f,s}\frac{a_i}{2b_i}\left\{\exp\left[b_i\left(\left(I_{4i} - 1\right)^2\right)\right] - 1\right\} + \frac{a_{fs}}{2b_{fs}}\Big[ \tag{1}$$

Eight material parameters $a$, $b$, $a_f$, $b_f$, $a_s$, $b_s$, $a_{fs}$, $b_{fs}$, and four strain invariants $I_1$, $I_{4f}$, $I_{4s}$, and $I_{8fs}$ define **Eq. 1**. For these simulations, $a$ = 3.354 kPa, $b$ = 7.08, $a_f$ = 2.501 kPa, while the remaining parameters were set to null. The strain invariants are derived from the isochoric right Cauchy-Green tensor:

$$\bar{C} = \bar{\mathbf{F}}^T\bar{\mathbf{F}} = J^{-2/3}C = J^{-2/3}\mathbf{F}^T\mathbf{F} \tag{2}$$

$F$ is the deformation gradient, J is the determinant of the deformation gradient, $J = \det(F)$ and $\bar{F}$ is the isochoric part of the deformation gradient where $\bar{F} = J^{-1/3}F$ and $\det(\bar{F}) = 1$. The strain invariants can now be defined as:

$$I_1 = tr\left(\bar{C}\right),\ I_{4f} = f_0 \cdot \left(\bar{C}f_0\right),\ I_{4s} = s_0 \cdot \left(\bar{C}s_0\right),\ I_{8fs} = f_0 \cdot \left(\bar{C}s_0\right) \tag{3}$$

Terms $f_0$ and $s_0$ are orthogonal vectors in the fiber and sheet direction in the reference configuration. The volumetric response is governed by:

$$\Psi_{vol} = \frac{1}{D}\left(\frac{\left(J^2 - 1\right)}{2} - \ln\left(J\right)\right) \tag{4}$$

Where $J$ is the third deformation gradient invariant, and $D$ is the multiple of the bulk modulus ($D = \frac{2}{K}$).

The active myocardial tissue response is represented as a time-varying elastance model (Guccione and McCulloch 1993; Guccione et al., 1993; Holzapfel and Ogden 2009; Carrick et al., 2012; Wenk et al., 2012; Genet et al., 2016; Sack et al., 2018b; Wisneski et al., 2020):

$$\sigma_{af}\left(t, E_{ff}\right) = \frac{T_{\max}}{2}\frac{Ca_0^2}{Ca_0^2 + ECa_{50}^2\left(E_{ff}\right)}\left(1 - \cos\left(\omega\left(t, E_{ff}\right)\right)\right) \tag{5}$$

With functions defined as:

$$ECa_{50}\left(E_{ff}\right) = \frac{Ca_{0\max}}{\sqrt{e^{B\left(l\left(E_{ff}\right)\right) - l_0} - 1}} \tag{6}$$

$$\omega\left(t, E_{ff}\right) = \pi\frac{t}{t_0}\ when\ 0 \le t < t_0 \tag{7a}$$

$$\omega\left(t, E_{ff}\right) = \pi\frac{t - t_0 + t_r\left(l\left(E_{ff}\right)\right)}{t_r}\ when\ t_0 \le t \le t_0 + t_r\left(l\left(E_{ff}\right)\right) \tag{7b}$$

$$\omega\left(t, E_{ff}\right) = 0\ when\ t > t_0 + t_r\left(l\left(E_{ff}\right)\right) \tag{7c}$$

$$t_r\left(l\right) = ml + b \tag{7d}$$

$$l\left(E_{ff}\right) = l_r\sqrt{2E_{ff} + 1} \tag{7e}$$

$T_{max}$ is the maximum allowable active tension and is multiplied by terms regulating calcium concentration and the time course of the contraction. These two terms are dependent on the sarcomere length $l$. Parameters were set as follows: $T_{\max}$ = 135.7 kPa, $Ca_0 = 4.35umol/l$, $Ca_{0\max} = 4.35\mu mol/l$, $m = 1.0489s\mu m^{-1}$, $b = -1.429s$, $B = 4.750\mu m^{-1}$, $l_0 = 1.58\mu m$. $l_r$ is the sarcomere length in the unloaded state, and was assumed to vary linearly from 1.78 μm at the endocardium to 1.91 μm at the epicardium.

The idealized geometry of the heart model was adapted to the patient-specific geometry with the aid of CATIA™ software (3D Systems, Johnston RI, United States) (**Figure 1B**). Groups of nodes representing the LV wall could be moved in sync to line up with surface geometry from image segmentation. This enabled efficient transformation from generic LV geometry to that of patient-specific geometry (**Figure 1C**). With the focus of this study being LV biomechanics, the LV was represented by a mesh of 91,000 individual solid elements, each consisting of a 10-noded tetrahedron bound by the surfaces obtained from the CT imaging segmentation (**Figure 2A**). Although portions of the left atrium and LV outflow tract were included in the model geometry, their primary purpose was to serve as boundary conditions for the LV model. The left atrium, LV outflow tract, and papillary muscles were excluded from biomechanical analysis. The LV was subdivided into 17 distinct segments in the basilar, mid-wall, and apical regions guided by the American Heart Association topographic classification system (Cerqueira et al., 2002).

The model was connected to a lumped-parameter virtual circulatory system for cardiac-cycle simulations run in Abaqus® FEA (Simulia, Johnston, RI, United States) (**Figure 2B**). AS was created by increasing the aortic valve resistance to generate a trans-valvular pressure gradient and elevated LV chamber pressures over the cardiac cycle (Wisneski et al., 2020). An iterative process was used to tune the model to the patient's circulatory system and LV physiology based on echocardiographic and catheterization data. Cardiac cycle simulations were run with automated adjustments to myocardial material properties and systemic vascular resistances/compliances, which permitted simulation results to optimally replicate patient-specific physiology. An acceptable steady state was achieved until further cycles produced <5% variation in chamber pressures compared to the prior cycle.

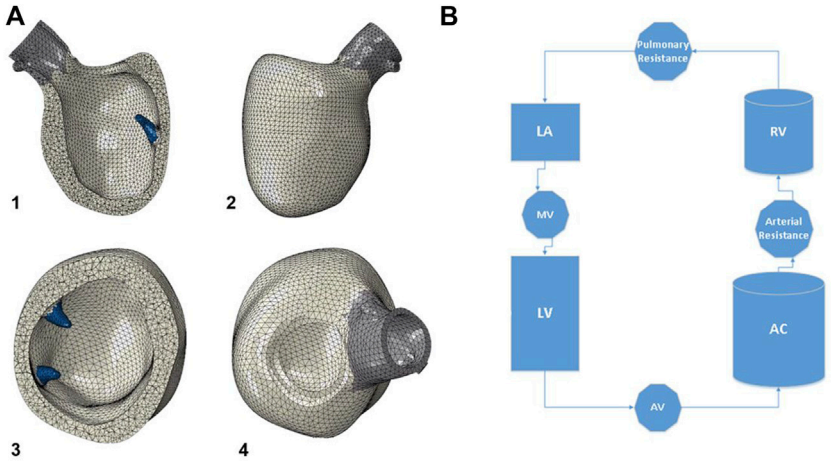


**FIGURE 2 | (A)** The model geometry is then meshed, with the left ventricle consisting of 91,000 ten-noded tetrahedral elements. The papillary muscles are shown in blue, and were excluded from biomechanical analysis of the left ventricle. 1) anterior cutaway, 2) short axis cutaway, 3) posterior view, 4) superior view. **(B)** Diagram of the circulatory model connected to the left ventricle for cardiac cycle simulations. Valves are assigned resistance values, and chambers are assigned elastances. LV: left ventricle, AV: aortic valve, AC: arterial chamber, RV: right ventricle, LA: left atrium, MV: mitral valve.

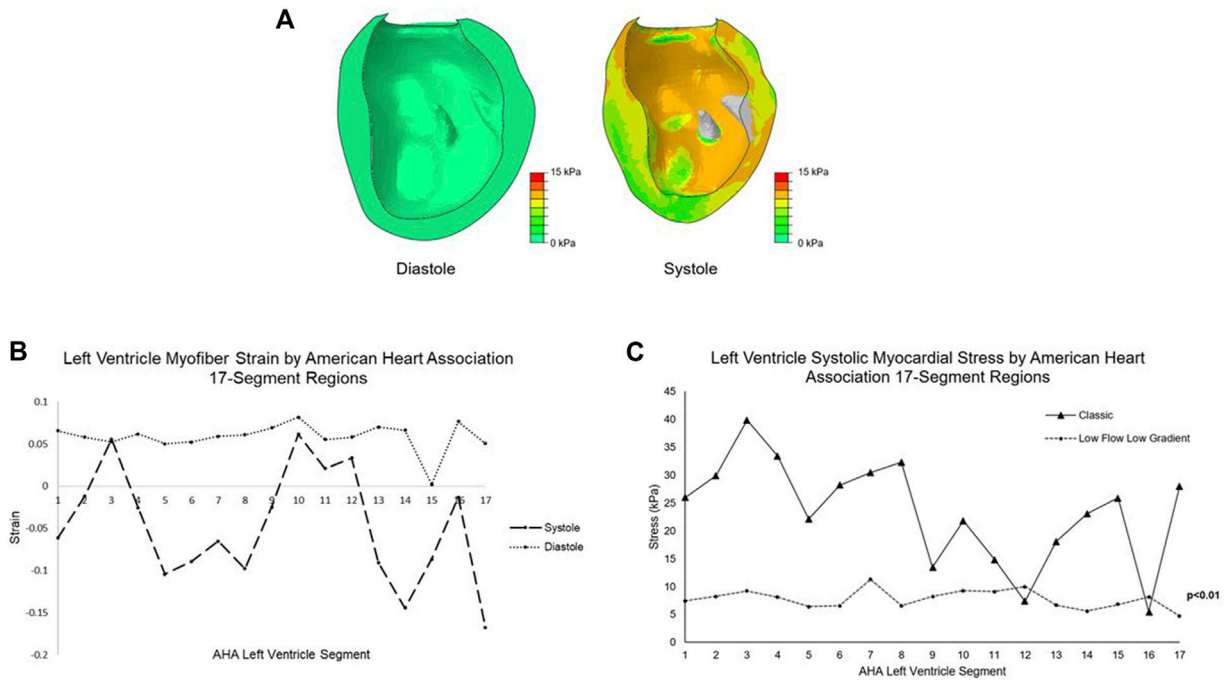


**FIGURE 3 | (A)** Color plots of the left ventricle myocardial stress (kPa) at end diastole and peak systole. The papillary muscles are excluded from biomechanical analysis. **(B)** Mean myofiber strain at diastole and systole for the LFLG model by American Heart Association 17-segment left ventricle classification system. **(C)** The mean systolic stress of each left ventricle segment by American Heart Association classification system for the LFLG model compared to the idealized left ventricle model with classic severe AS. Lower magnitude stress values and low variation among the segments are found in the LFLG model. Segments 1-6 represent the basal aspect, segments 7–12 the LV mid-wall, and 13–17 the apical region. LFLG: low-flow, low-gradient; LV, left ventricle; AS, aortic stenosis.

For the final model, the following system parameters were used: aortic valve resistance (AV) 5e− 9 MPa*s/mm$^3$, arterial resistance 1.35e+ 02 MPa*sec/mm$^3$, pulmonary vascular resistance 8e+ 0 MPa*sec/mm$^3$, mitral valve resistance 2e+ 0 MPa*sec/mm$^3$, arterial compliance (AC) 1.0e+ 07 mm$^3$/MPa, pulmonary compliance (PC) 7.99e+ 06 mm$^3$/MPa.

The results of LV stress (kPa) and strain along the direction of the myofibers were obtained at end-diastole and peak systole, and

**TABLE 1 |** Comparison of patient clinical parameters compared to simulation results.

| Physiologic parameter | Patient measured | Simulation result |
|---|---|---|
| LV ejection fraction | 25% | 23% |
| LV systolic pressure | 128 mmHg | 118 mmHg |
| LV diastolic pressure | 12 mmHg | 6 mmHg |
| Aortic systolic pressure | 116 mmHg | 109 mmHg |
| Aortic diastolic pressure | 45 mmHg | 50 mmHg |
| Mean pressure gradient across aortic valve | 15 mmHg | 17 mmHg |
| Peak pressure gradient across aortic valve | 25 mmHg | 23 mmHg |

*Abbreviations: LV, left ventricle.*

reported as mean ± standard deviation. The t-test was used for statistical comparison of continuous variables.

## RESULTS

Global LV peak systolic myocardial stress and strain were 7.1 ± 1.8 kPa and −0.07 ± 0.12; global LV end diastolic stress and strain were 0.24 ± 0.17 kPa and +0.07 ± 0.04 (**Figures 3A–C**). Further division by American Heart Association segment classification yielded mean basal region systolic stress of 7.7 ± 1.8 kPa, mean mid-wall region systolic stress of 9.1 ± 3.8 kPa, and mean apical region systolic stress of 6.4 ± 0.4 kPa. Myocardial systolic stress for each individual segment is plotted in **Figure 3C**. The patient-specific simulation achieved close correspondence to clinically measured parameters, listed in **Table 1**.

## DISCUSSION

This study describes the first patient-specific computational model of the LV in a patient with LFLG AS, and the biomechanics results of myocardial stress and strain. This model was based on imaging obtained for TAVR planning purposes, and the use of specialized software enabled a generic LV model to be rapidly adapted to patient-specific geometry and physiology. The ability to create accurate computational models of the LV in AS facilitates the study of "LV-aortic coupling", whereby aortic valve pathology is linked to LV function for a more complete understanding of the disease (Ikonomidis et al., 2019).

This model represents an advancement in computational investigations in two respects: 1) a patient-specific model of the LV can now be readily obtained from clinical imaging, rather than dedicated research-specific imaging, and 2) specialized software permitted efficient creation of a highly detailed mesh. Previously, weeks of effort were required for a single user to create highly detailed patient-specific ventricular geometry, whereas the CATIA™ software enabled it to be done by one user in approximately one and a half days. With this LV model having a high degree of detail represented by 91,000 elements, validated computational material properties and physiology, there is great potential to use clinical cardiac imaging for future studies of LV biomechanics in AS.

Our group previously published the myocardial stress associated with "classic" severe AS, where a mean transvalvular pressure gradient ≥40 mmHg exists, using a model of idealized LV geometry with normal LV function (Wisneski et al., 2020). Systolic stress of the LV was 16 ± 10 kPa. In contrast, systolic myocardial stress in the LFLG model is substantially reduced with a narrower standard deviation. We attribute this finding to the reduced LV function of the LFLG model, coupled with eccentric hypertrophy from pathologic remodeling. The globe-shaped ventricle creates a more uniform stress distribution. Breakdown of the classic AS LV model into the American Heart Association 17 segments demonstrated a relatively wider variation in segment stress with a range of 5.5–39.9 kPa as shown in **Figure 3C**. In the LFLG mode, the range across the LV segments is much narrower at 4.7–11.3 kPa. Comparison of LV segment mean systolic stresses yielded a significant difference with $p < 0.01$. The LFLG model's eccentric hypertrophy with a dilated ventricle may explain the pronounced difference in stress distribution among the two models.

A computational modeling study by Lee et al. on LV geometry after surgical ventricular restoration for systolic heart failure concluded that a more spherical ventricle shape reduced myocardial stress magnitude and produced a more uniform stress distribution (Lee et al., 2013). The eccentric geometry of the LV in our LFLG model resulted in a similar finding when the stress magnitudes and distribution were compared to those of the normal, more ellipsoidal LV geometry in the classic AS model. It could be theorized that future ventricular biomechanics analysis showing reduced stress range throughout the LV may serve as biomechanical evidence of remodeling with reduced LV function. We acknowledge that in-depth analysis is limited by a sample comparison of one representative model from these two sub-types of AS, and that greater numbers of patient-specific models will be required for more definitive conclusions to be drawn.

There is a growing body of literature addressing the complexity of diagnosing severe AS when LFLG or suspected LFLG is encountered. Although a patient may be thought to have LFLG AS, many studies have used stroke volume index to help differentiate true low-flow, low-gradient AS from normal flow, low-gradient AS (Hachicha et al., 2007; Herrmann et al., 2011; Adda et al., 2012; Pibarot and Dumesnil 2012). This has highlighted limitations in use of LV ejection fraction as a sole indicator of true LV function. Research has demonstrated alternative indicators of LV dysfunction can be present in patients whose ejection fraction remains in the normal range. Adda et al. assessed ventricular longitudinal strain by speckle-tracking echocardiography in a cohort of patients with severe AS and normal ejection fractions. They concluded that compared to patients with normal flow, low-gradient AS, patients with LFLG AS had more severe stenosis with lower mean aortic valve areas, higher systemic afterloads, and decreased LV function with reduced basal longitudinal strain (Adda et al., 2012).

Herrmann et al. found that patients with low-gradient severe AS had higher degrees of myocardial fibrosis and decreased longitudinal strain despite a preserved LV ejection fraction (Herrmann et al., 2011). Reliance on ejection fraction alone may miss subtle signs of LV dysfunction. Through further investigation with patient-specific models, we envision that biomechanics analysis will permit detection of the early signs of LV dysfunction.

A study by Shavik et al. applied computational simulation techniques to replicate the physiology of heart failure with preserved ejection fraction (HFpEF), whereby decreased longitudinal strain exists with a normal ejection fraction (Shavik et al., 2021). Through their framework, the variables of ventricular geometry, chamber size, blood pressure, and ventricular strains were altered based on sets of clinically measured patient-specific data. To adequately replicate HFpEF, the combination of depressed myocardial contractility coupled with increased afterload was required. While clinically distinct entities, LFLG AS and HFpEF may share some commonalities in the initial set of conditions that trigger the chronic pathologic remodeling.

Our results include strain along the direction of myofibers, a microscopic tissue-level organization of the myocardium. The differences between the LV segment strains at diastole and systole (**Figure 3B**) indicate the complex dynamics of ventricular contraction. This can be correlated to the known ventricular dysfunction this patient has, as several segments appear to contribute minimally to systolic LV contraction.

Myofiber orientation varies transmurally with a helix angle spanning $-60^{\circ}$ at the endocardium to $+60^{\circ}$ at the epicardium relative to the short axis of the heart (Walker et al., 2005; Carrick et al., 2012; Wenk et al., 2012; Genet et al., 2014; Genet et al., 2016; Sack et al., 2018b; Dabiri et al., 2018; Wisneski et al., 2020). Specialized imaging techniques such as diffusion-tensor and displacement encoding with stimulated echoes (DENSE) magnetic resonance imaging can be used to measure myofiber strain *in-vivo* (Bayer et al., 2012; Moulin et al., 2021). However, magnetic resonance imaging is more time consuming than CT imaging and is not routinely used for TAVR planning purposes. Computational models with myocardial material models accounting for myofiber orientation will be able to provide myofiber strain data throughout the LV. Myofiber strain should be differentiated from the strain reported in many clinical echocardiographic studies, such as global longitudinal strain, which describes deformation relative to the long axis of the heart. Reduced strain in LFLG AS, whether at the myofiber or global LV level, likely stems from the same mechanism of LV dysfunction.

The systolic stress and strain profile from the American Heart Association 17 segment classification can provide a unique biomechanical 'footprint' for a patient's LV, provide a snapshot of LV performance, and help to categorize a patient's disease severity in future investigations.

### Limitations

The study's main limitation is that it only encompasses a single patient, limiting our ability to draw broader conclusions on LV biomechanics for LFLG AS. Future studies with greater numbers of AS patients will need to correlate biomechanics results with the severity of AS and LV dysfunction. Greater numbers of patient-specific models for LFLG AS versus "classic" elevated gradient AS will need to be compared as well. For computational efficiency, the model encompassed only the left heart, omitting the right atrium and ventricle. However, this case of isolated AS did not involve right heart disease; future cases that have biventricular dysfunction or diseases that affect the right heart should be modeled with both ventricles. Additionally, clinically measured data (ejection fraction, LV and aortic pressures) are used to calibrate the model, and close correlation was achieved. A patient's physiology is expected to exhibit normal variation in daily life (i.e., heart rate, blood pressure) and thus we believe the model can yield useful data as long as the model results replicates key physiologic parameters within an acceptable range of the clinically measured values.

In our model, AS was created by increasing the aortic valve resistance parameter in the computational circulatory model, rather than creating a physical representation of calcium on the aortic valve restricting leaflet opening. Since our goal was to study the impact of AS on LV biomechanics, it was not necessary to create the physical representation of aortic stenosis, which permitted greater computational efficiency. This preliminary investigation demonstrates the feasibility of creating a patient-specific computational model from clinical cardiac imaging by modification of an existing LV model platform. There is great potential to generate biomechanics data to help elucidate the pathophysiology of LV dysfunction in AS.

## CONCLUSION

We describe the first patient-specific LV model in a case of LFLG aortic stenosis and the LV biomechanics results obtained. Compared to idealized LV geometry and normal ventricular function, reduced LV stress, an initial observation of globally reduced LV stress, was quantified. To translate patient-specific computational modeling to the clinical setting, future studies of larger AS populations should correlate biomechanics results with disease progression, ventricular dysfunction, and outcomes after aortic valve replacement. Data beyond traditional flow-derived metrics and ejection fraction should be incorporated into clinical assessment of AS and determination of who should receive aortic valve replacement. With the widespread adoption of TAVR, CT imaging obtained for pre-TAVR planning should yield abundant clinical imaging that can be used to create patient-specific models.

## DATA AVAILABILITY STATEMENT

The raw data supporting the conclusion of this article will be made available by the authors, without undue reservation.

## AUTHOR CONTRIBUTIONS

AW, JY, TN, VM and JG were involved in the conception, design of the study, and analysis of the results. SC and SP provided imaging analysis to create the model geometry; YW, JY and AS

were involved with running the computational model. AW, JY, SP, TN, VM and JG were involved in data analysis and clinical concepts of this study. All authors contributed to manuscript drafting, and have read and approved the submitted version.

## ACKNOWLEDGMENTS

The authors thank Pamela Derish in the Department of Surgery, University of California San Francisco for proofreading this manuscript.

## REFERENCES

Adda, J., Mielot, C., Giorgi, R., Cransac, F., Zirphile, X., Donal, E., et al. (2012). Low-flow, Low-Gradient Severe Aortic Stenosis Despite normal Ejection Fraction Is Associated with Severe Left Ventricular Dysfunction as Assessed by Speckle-Tracking Echocardiography: a Multicenter Study. *Circ. Cardiovasc. Imaging* 5 (1), 27–35. doi:10.1161/circimaging.111.967554

Baillargeon, B., Rebelo, N., Fox, D. D., Taylor, R. L., and Kuhl, E. (2014). The Living Heart Project: A Robust and Integrative Simulator for Human Heart Function. *Eur. J. Mech. A. Sol.* 48, 38–47. doi:10.1016/j.euromechsol.2014.04.001

Bayer, J. D., Blake, R. C., Plank, G., and Trayanova, N. A. (2012). A Novel Rule-Based Algorithm for Assigning Myocardial Fiber Orientation to Computational Heart Models. *Ann. Biomed. Eng.* 40 (10), 2243–2254. doi:10.1007/s10439-012-0593-5

Carrick, R., Ge, L., Lee, L. C., Zhang, Z., Mishra, R., Axel, L., et al. (2012). Patient-specific Finite Element-Based Analysis of Ventricular Myofiber Stress after Coapsys: Importance of Residual Stress. *Ann. Thorac. Surg.* 93 (6), 1964–1971. doi:10.1016/j.athoracsur.2012.03.001

Cerqueira, M. D., Weissman, N. J., Dilsizian, V., Jacobs, A. K., Kaul, S., Laskey, W. K., et al. (2002). Standardized Myocardial Segmentation and Nomenclature for Tomographic Imaging of the Heart. A Statement for Healthcare Professionals from the Cardiac Imaging Committee of the Council on Clinical Cardiology of the American Heart Association. *Circulation* 9 (4), 240–245. doi:10.1067/mnc.2002.123122

Clavel, M. A., Magne, J., and Pibarot, P. (2016). Low-gradient Aortic Stenosis. *Eur. Heart J.* 37 (34), 2645–2657. doi:10.1093/eurheartj/ehw096

Dabiri, Y., Sack, K. L., Shaul, S., Sengupta, P. P., and Guccione, J. M. (2018). Relationship of Transmural Variations in Myofiber Contractility to Left Ventricular Ejection Fraction: Implications for Modeling Heart Failure Phenotype with Preserved Ejection Fraction. *Front. Physiol.* 9, 1003. doi:10.3389/fphys.2018.01003

Genet, M., Lee, L. C., Nguyen, R., Haraldsson, H., Acevedo-Bolton, G., Zhang, Z., et al. (2014). "Distribution of normal Human Left Ventricular Myofiber Stress at End Diastole and End Systole: a Target for In Silico Design of Heart Failure Treatments." *J. Apply. Physiol. 1985* 117(2), 142–152.doi:10.1152/japplphysiol.00255.2014

Genet, M., Lee, L. C., Baillargeon, B., Guccione, J. M., and Kuhl, E. (2016). Modeling Pathologies of Diastolic and Systolic Heart Failure. *Ann. Biomed. Eng.* 44 (1), 112–127. doi:10.1007/s10439-015-1351-2

Guccione, J. M., and McCulloch, A. D. (1993). Mechanics of Active Contraction in Cardiac Muscle: Part I-Constitutive Relations for Fiber Stress that Describe Deactivation. *J. Biomech. Eng.* 115 (1), 72–81. doi:10.1115/1.2895473

Guccione, J. M., Waldman, L. K., and McCulloch, A. D. (1993). Mechanics of Active Contraction in Cardiac Muscle: Part II-Cylindrical Models of the Systolic Left Ventricle. *J. Biomech. Eng.* 115 (1), 82–90. doi:10.1115/1.2895474

Hachicha, Z., Dumesnil, J. G., Bogaty, P., and Pibarot, P. (2007). Paradoxical Low-Flow, Low-Gradient Severe Aortic Stenosis Despite Preserved Ejection Fraction Is Associated with Higher Afterload and Reduced Survival. *Circulation* 115 (22), 2856–2864. doi:10.1161/circulationaha.106.668681

Herrmann, S., Störk, S., Niemann, M., Lange, V., Strotmann, J. M., Frantz, S., et al. (2011). Low-gradient Aortic Valve Stenosis Myocardial Fibrosis and its Influence on Function and Outcome. *J. Am. Coll. Cardiol.* 58 (4), 402–412. doi:10.1016/j.jacc.2011.02.059

Holzapfel, G. A., and Ogden, R. W. (2009). Constitutive Modelling of Passive Myocardium: a Structurally Based Framework for Material Characterization. *Philos. Trans. A. Math. Phys. Eng. Sci.* 367, 3445–3475. doi:10.1098/rsta.2009.0091

Ikonomidis, I., Aboyans, V., Blacher, J., Brodmann, M., Brutsaert, D. L., Chirinos, J. A., et al. (2019). The Role of Ventricular-Arterial Coupling in Cardiac Disease and Heart Failure: Assessment, Clinical Implications and Therapeutic Interventions. A Consensus Document of the European Society of Cardiology Working Group on Aorta & Peripheral Vascular Diseases, European Association of Cardiovascular Imaging, and Heart Failure Association. *Eur. J. Heart Fail.* 21 (4), 402–424. doi:10.1002/ejhf.1436

Lee, L. C., Wenk, J. F., Zhong, L., Klepach, D., Zhang, Z., Ge, L., et al. (2013). Analysis of Patient-specific Surgical Ventricular Restoration: Importance of an Ellipsoidal Left Ventricular Geometry for Diastolic and Systolic Function. *J. Appl. Physiol.* 115 (1), 136–144. doi:10.1152/japplphysiol.00662.2012

Lindman, B. R., Bonow, R. O., and Otto, C. M. (2013). Current Management of Calcific Aortic Stenosis. *Circ. Res.* 113 (2), 223–237. doi:10.1161/circresaha.111.300084

Moulin, K., Croisille, P., Viallon, M., Verzhbinsky, I. A., Perotti, L. E., and Ennis, D. B. (2021). Myofiber Strain in Healthy Humans Using DENSE and cDTI. *Magn. Reson. Med.* 86 (1), 277–292. doi:10.1002/mrm.28724

Nishimura, R. A., Otto, C. M., Bonow, R. O., Carabello, B. A., Erwin, J. P., 3rd, Guyton, R. A., et al. (2014). 2014 AHA/ACC Guideline for the Management of Patients with Valvular Heart Disease: a Report of the American College of Cardiology/American Heart Association Task Force on Practice Guidelines. *Circulation* 129 (23), e521–643. doi:10.1161/CIR.0000000000000031

Pibarot, P., and Clavel, M.-A. (2015). Management of Paradoxical Low-Flow, Low-Gradient Aortic Stenosis: Need for an Integrated Approach, Including Assessment of Symptoms, Hypertension, and Stenosis Severity. *J. Am. Coll. Cardiol.* 65 (1), 67–71. doi:10.1016/j.jacc.2014.10.030

Pibarot, P., and Dumesnil, J. G. (2012). Low-flow, Low-Gradient Aortic Stenosis with normal and Depressed Left Ventricular Ejection Fraction. *J. Am. Coll. Cardiol.* 60 (19), 1845–1853. doi:10.1016/j.jacc.2012.06.051

Sack, K. L., Aliotta, E., Choy, J. S., Ennis, D. B., Davies, N. H., Franz, T., et al. (2020). Intra-myocardial Alginate Hydrogel Injection Acts as a Left Ventricular Mid-wall Constraint in Swine. *Acta Biomater.* 111, 170–180. doi:10.1016/j.actbio.2020.04.033

Sack, K. L., Aliotta, E., Ennis, D. B., Choy, J. S., Kassab, G. S., Guccione, J. M., et al. (2018). Construction and Validation of Subject-Specific Biventricular Finite-Element Models of Healthy and Failing Swine Hearts from High-Resolution DT-MRI. *Front. Physiol.* 9, 539. doi:10.3389/fphys.2018.00539

Sack, K. L., Baillargeon, B., Acevedo-Bolton, G., Genet, M., Rebelo, N., Kuhl, E., et al. (2016). Partial LVAD Restores Ventricular Outputs and Normalizes LV but Not RV Stress Distributions in the Acutely Failing Heart In Silico. *Int. J. Artif. Organs* 39 (8), 421–430. doi:10.5301/ijao.5000520

Sack, K. L., Dabiri, Y., Franz, T., Solomon, S. D., Burkhoff, D., and Guccione, J. M. (2018). Investigating the Role of Interventricular Interdependence in Development of Right Heart Dysfunction During LVAD Support: A Patient-Specific Methods-Based Approach. *Front. Physiol.* 9, 520. doi:10.3389/fphys.2018.00520

Shavik, S. M., Wall, S., Sundnes, J., Guccione, J. M., Sengupta, P., Solomon, S. D., et al. (2021). Computational Modeling Studies of the Roles of Left Ventricular Geometry, Afterload, and Muscle Contractility on Myocardial Strains in Heart Failure with Preserved Ejection Fraction. *J. Cardiovasc. Transl Res.* 14(6), 10130. doi:10.1007/s12265-021-10130-y

Walker, J. C., Ratcliffe, M. B., Zhang, P., Wallace, A. W., Fata, B., Hsu, E. W., et al. (2005). MRI-based Finite-Element Analysis of Left Ventricular Aneurysm. *Am. J. Physiol. Heart Circ. Physiol.* 289 (2), H692–H700. doi:10.1152/ajpheart.01226.2004

Wenk, J. F., Klepach, D., Lee, L. C., Zhang, Z., Ge, L., Tseng, E. E., et al. (2012). First Evidence of Depressed Contractility in the Border Zone of a Human Myocardial Infarction. *Ann. Thorac. Surg.* 93 (4), 1188–1193. doi:10.1016/j.athoracsur.2011.12.066

Wisneski, A. D., Cutugno, S., Stroh, A., Pasta, S., Yao, J., Mahadevan, V. S., et al. (2021). From Clinical Imaging to Patient-Specific Computational Model: Rapid Adaptation of the Living Heart Human Model to a Case of

Aortic Stenosis. *Lecture Notes Comp. Sci.* 12738, 373–381. doi:10.1007/978-3-030-78710-3_36

Wisneski, A. D., Wang, Y., Deuse, T., Hill, A. C., Pasta, S., Sack, K. L., et al. (2020). Impact of Aortic Stenosis on Myofiber Stress: Translational Application of Left Ventricle-Aortic Coupling Simulation. *Front. Physiol.* 11, 574211. doi:10.3389/fphys.2020.574211

**Conflict of Interest:** AS were employed by the company CATIA, Dassault Systèmes. JY were employed by company Simulia, Dassault Systèmes Simulia.

The remaining authors declare that the research was conducted in the absence of any commercial or financial relationships that could be construed as a potential conflict of interest.

**Publisher's Note:** All claims expressed in this article are solely those of the authors and do not necessarily represent those of their affiliated organizations, or those of the publisher, the editors and the reviewers. Any product that may be evaluated in this article, or claim that may be made by its manufacturer, is not guaranteed or endorsed by the publisher.

frontiers | Frontiers in Physiology

ORIGINAL RESEARCH
published: 12 April 2022
doi: 10.3389/fphys.2022.881826

# Non-Invasive Quantification of Fraction Flow Reserve Based on Steady-State Geometric Multiscale Models

*Jincheng Liu[1], Xue Wang[1], Bao Li[1], Suqin Huang[1], Hao Sun[1], Liyuan Zhang[1], Yutong Sun[2], Zhuo Liu[2], Jian Liu[2], Lihua Wang[3], Xi Zhao[4], Wenxin Wang[4], Mingzi Zhang[5] and Youjun Liu[1]**

[1]Faculty of Environment and Life, Beijing University of Technology, Beijing, China, [2]Cardiovascular Department, Peking University People's Hospital, Beijing, China, [3]Radiology Department, The Second Affiliated Hospital, Zhejiang University School of Medicine, Zhejiang, China, [4]Clinical and Technical Support, Philips Healthcare, Shanghai, China, [5]Depart of Biomedical Sciences, Macquarie Medical School, Macquarie University, Sydney, NSW, Australia

**Background:** The underuse of invasive fraction flow reserve (FFR) in clinical practice has motivated research towards its non-invasive prediction. The early attempts relied on solving the incompressible three-dimensional Navier–Stokes equations in segmented coronary arteries. However, transient boundary condition has a high resource intensity in terms of computational time. Herein, a method for calculating FFR based on steady-state geometric multiscale ($FFR_{SS}$) is proposed.

**Methods:** A total of 154 moderately stenotic vessels (40–80% diameter stenosis) from 136 patients with stable angina were included in this study to validate the clinical diagnostic performance of $FFR_{SS}$. The method was based on the coronary artery model segmented from the patient's coronary CTA image. The average pressure was used as the boundary condition for the inlet, and the microcirculation resistance calculated by the coronary flow was used as the boundary condition for the outlet to calculate the patient-specific coronary hyperemia. Then, the flow velocity and pressure distribution and the FFRss of each coronary artery branch were calculated to evaluate the degree of myocardial ischemia caused by coronary stenosis. Also, the $FFR_{SS}$ and $FFR_{CT}$ of all patients were calculated, and the clinically measured FFR was used as the "gold standard" to verify the diagnostic performance of $FFR_{SS}$ and to compare the correlation between $FFR_{SS}$ and $FFR_{CT}$.

**Results:** According to the $FFR_{SS}$ calculation results of all patients, $FFR_{SS}$ and FFR have a good correlation (r = 0.68, $p < 0.001$). Similarly, the correlation of $FFR_{SS}$ and $FFR_{CT}$ demonstrated an r of 0.75 (95%CI: 0.67–0.72) ($p < 0.001$). On receiver-operating characteristic analysis, the optimal $FFR_{SS}$ cut point for FFR≤0.80 was 0.80 (AUC:0.85 [95% confidence interval: 0.79 to 0.90]; overall accuracy:88.3%). The overall sensitivity, specificity, PPV, and NPV for $FFR_{SS}$ ≤0.80 versus FFR ≤0.80 was 68.18% (95% CI: 52.4–81.4), 93.64% (95% CI: 87.3–97.4), 82.9%, and 91.1%, respectively.

**Conclusion:** $FFR_{SS}$ is a reliable diagnostic index for myocardial ischemia. This method was similar to the closed-loop geometric multiscale calculation of FFR accuracy but improved the calculation efficiency. It also improved the clinical applicability of the non-

OPEN ACCESS

***Edited by:***
*Yunlong Huo,*
*Shanghai Jiao Tong University, China*

***Reviewed by:***
*Jianyong Huang,*
*Peking University, China*
*Yuan Feng,*
*Shanghai Jiao Tong University, China*

****Correspondence:***
*Youjun Liu*
*lyjlma@bjut.edu.cn*

***Specialty section:***
*This article was submitted to Computational Physiology and Medicine, a section of the journal Frontiers in Physiology*

***Received:*** *23 February 2022*
***Accepted:*** *24 March 2022*
***Published:*** *12 April 2022*

***Citation:***
*Liu J, Wang X, Li B, Huang S, Sun H, Zhang L, Sun Y, Liu Z, Liu J, Wang L, Zhao X, Wang W, Zhang M and Liu Y (2022) Non-Invasive Quantification of Fraction Flow Reserve Based on Steady-State Geometric Multiscale Models. Front. Physiol. 13:881826. doi: 10.3389/fphys.2022.881826*

invasive computational FFR model, helped the clinicians diagnose myocardial ischemia, and guided percutaneous coronary intervention.

**Keywords: coronary heart disease, fractional flow reserve, geometric multiscale, fast calculation of FFR, non-invasive diagnosis of myocardial ischemia**

## INTRODUCTION

Over the last 10 years, fractional flow reserve (FFR) has become a reference standard for the invasive assessment of coronary artery disease. Its measurement assesses the functional severity of coronary artery stenoses and the need for coronary revascularization (Pijls et al., 1996; Pijls, 2013). FFR is calculated by dividing the distal coronary pressure (Pd) by the proximal coronary pressure (Pa) during maximal hyperemia (Pijls et al., 1996) and the diagnostic threshold is 0.80. FFR carries a Class 1a recommendation for guiding revascularization in angiographically intermediate coronary stenoses in patients with stable angina (Fihn et al., 2012; Kolh et al., 2014; Knuuti et al., 2020). However, uptake of FFR in coronary catheter laboratories worldwide has remained low. Potential reasons for the low adoption rate of coronary physiology despite demonstrated clinical benefit of its use may include time consumption to perform FFR measurements, tries, no availability of adenosine, patient-related discomfort, contraindications, or lack of reimbursement (Hannawi et al., 2014; Gotberg et al., 2017).

The underuse of invasive FFR in clinical practice has motivated research towards non-invasive prediction of FFR. Most early attempts for non-invasive FFR prediction relied on solving the incompressible 3D Navier–Stokes equations in segmented coronary arteries (Taylor et al., 2013; Raissi et al., 2019; Liu et al., 2021). Due to the need to solve the fully coronary model, the time cost of its calculation is very high. There are also some simple computational FFR models: reduced-order physics such as 1D blood flow or lumped parameter models (Itu et al., 2012; Blanco et al., 2018; Boileau et al., 2018), and (2) purely data-driven approaches (Hae et al., 2018; Zreik et al., 2018). Despite the fast computation time of this model, it is only included for stenotic vessels and ignores the entire coronary hemodynamic environment. Therefore, considering the fully hemodynamic environment of the coronary artery and improving the calculation speed are the development of non-invasive prediction of FFR.

In this study, a non-invasive quantification of fraction flow reserve based on steady-state geometric multiscale models ($FFR_{SS}$) was developed. It was based on the coronary artery model segmented from the patient's coronary CTA image. The average pressure was used as the boundary condition for the inlet, while the microcirculation resistance calculated by the coronary flow was used as the boundary condition for the outlet. Thus, it could rapidly calculate the patient-specific coronary hyperemia. Also, the flow velocity and pressure distribution were calculated, and the FFRss of each branch of the coronary artery was computed to evaluate the degree of myocardial ischemia caused by coronary stenosis. $FFR_{SS}$ and $FFR_{CT}$ were calculated simultaneously for 136 patients. The clinically measured FFR was used as the gold standard to verify the diagnostic performance of $FFR_{SS}$, and the ability of $FFR_{SS}$ and $FFR_{CT}$ to evaluate myocardial ischemia was compared.

## METHODS AND MATERIALS

### Patient and Image Data

This study was approved by the institutional review board of Peking University People's Hospital and the Second Affiliated Hospital of Zhejiang University School of Medicine. All patients signed an informed consent. 136 coronary heart disease patients with 154 moderate-to-severe epicardial stenosis were retrospectively enrolled (between 2019 and 2021). The patient inclusion criteria were shown in **Figure 1**. Under the guidance of coronary angiography based on the Azurion 7M20 DSA system, all patients had undergone the FFR catheter surgery measurement with FFR system and Verrata Plus pressure guide wire (Philips Healthcare, Netherland). The period between the CTA examination and the cardiac catheterisation did not exceed 1 week. The Biomechanics Laboratory of Beijing University of Technology analyzed the anonymized data independently.

The coronary CTA images were obtained using of a dual-layer detector CT system (IQon, Philips Healthcare), with a matrix size of $512 \times 512$ and a slice of 0.625 mm thickness. Segmentation and 3D reconstruction of the coronary artery for each patient were performed using Mimics (Materialise, Leuven, Belgium), with the results being reviewed by two radiologists with 15 years of experience in cardiac CTA. Only arteries with a diameter bigger than or equal to 1 mm were retained in the reconstructed model for further computational fluid dynamics (CFD) analysis (Sankaran et al., 2016).

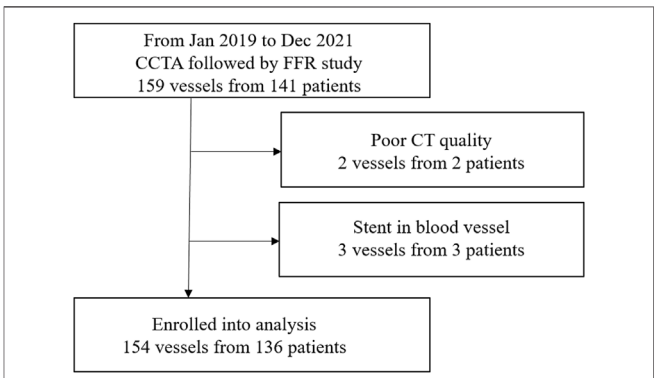


**FIGURE 1 |** Study enrolment.

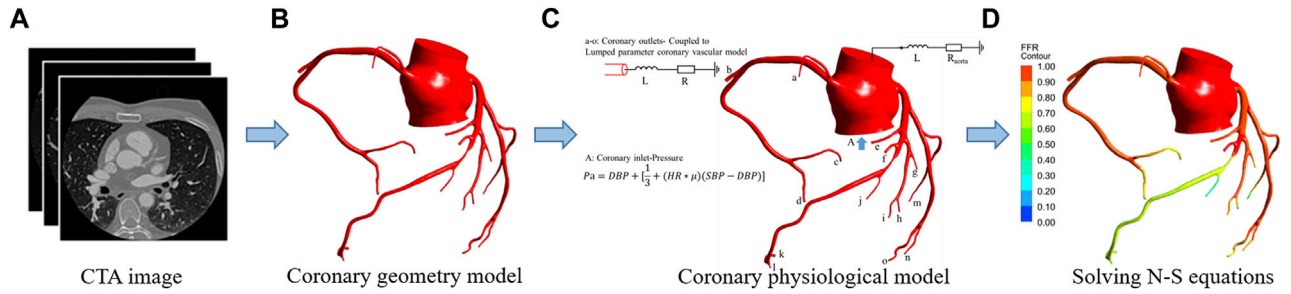


**FIGURE 2 |** $FFR_{SS}$ calculation flowchart. **(A)** CTA image. **(B)** Coronary geometry model. **(C)** Coronary physiological model. The 0D model stands for lumped parameter model (a–o) and is composed of resistance "R" and inductance "L." "R" represents the flow resistance of coronary branch vessels under the action of blood viscosity, obtained by the allometric scale rate. "L" The inertia of blood flow, for the branch of the coronary artery, the empirical parameter is 0.05. The 3D model represents the whole coronary model, and the blood vessels larger than 1 mm in diameter are completely preserved. The 3D model was obtained by reconstruction of coronary CTA images. Among them, in the 0D-3D coupling model, the input is the mean pressure calculated by the physiological formula, and the output is the 0D resistance boundary condition of the coronary artery. **(D)** Solved N-S equations.0D and 3D coupling diagram.

## The Establishment of Steady-State Geometric Multiscale Models

In a previous study, we proposed a closed-loop geometric multiscale model to compute FFR (Liu et al., 2021) non-invasively. Although the closed-loop model has improved computational accuracy, the clinical application is limited due to its superior computational speed and complexity in determining individualized parameters. In order to fulfill the needs of clinical FFR calculation, a steady-state-based model mimicking the closed-loop geometric multiscale model was proposed in this study. It replaced the transient state with steady-state boundary conditions to reduce the computation time, optimize the geometric multiscale module, and reduce the optimization of individual parameters.

The steady-state geometric multiscale model consists of lumped parameter model (LPM) (0D) and a coronary global three-dimensional (3D) model. LPM uses the circuit structure to simulate the microcirculation network downstream of the coronary artery, the resistance "R" to simulate the resistance of blood flow, and the inductance "L" to simulate the inertia of blood flow (Pietrabissa et al., 1996). The full-scale 3D model of the coronary artery preserves the real structure of the coronary artery instead of only stenotic vessels. The 0D part provides the outlet boundary conditions for the patient's 3D coronary model. As shown in **Figure 2C**, the details of the geometrical multiscale model of 0D and 3D coupling are described previously (Zhao et al., 2016; Li et al., 2020; Mao et al., 2020).

The inlet boundary condition of the coronary model is set to the aortic pressure, which could be equivalent to the mean pressure (Wilson et al., 2001) and calculated from the cuff pressure based on systolic blood pressure (SBP), diastolic blood pressure (DBP), and heart rate (HR) (Sharma et al., 2012) as follows:

$$Pa = DBP + \left[\frac{1}{3} + (HR*0.0012)(SBP - DBP)\right] \quad (1)$$

The outlet boundary condition of the branch of the coronary model is composed of microcirculation resistance. The microcirculatory resistance of the downstream branch of the coronary artery was termed as resistance "R," which could be estimated as follows:

$$R_{resting} = \frac{P}{Q} \quad (2)$$

where P is the aorta pressure, and Q is the flow rate of blood in the target coronary branch while resting. The latter can be estimated using Murray's Law (Murray, 1926) based on the patient's cardiac output (Opie, 2003). Since the FFR needs to be calculated in the hyperemia state, according to the assumption (Wilson et al., 1990; Sdringola et al., 2011; Taylor et al., 2013), the R_resting becomes 0.24 of the original in the hyperemia state:

$$R_{hyperemia} = 24\%*R_{resting} \quad (3)$$

Notably, in the computation model of $FFR_{SS}$ for the resistance of the outlet of the ascending aorta (**Figure 2C**) connected to the systemic circulation, the resistance is calculated based on the cardiac output (Opie, 2003):

$$R_{doa} = \frac{Pa}{co}*96\% \quad (4)$$

where Pa is the pressure at the aorta pressure, and CO is the cardiac output.

## 0D/3D Interface Processing

The model described in this study was similar to the 0D/3D coupling method (Zhao et al., 2016; Liu et al., 2021) of the previous closed-loop model and used specific interface conditions and coupling algorithms to establish the 0D-3D coupling model. The 3D model calculation of the whole coronary artery relies on the fluid calculation software ANSYS, while the calculation of the lumped parameter model relies on the FORTRAN program of the CFX junction box. The data transmission between them was completed by the CFX User CEL Function, and the specific geometric multiscale coupling model solution process is shown in **Figure 3**.

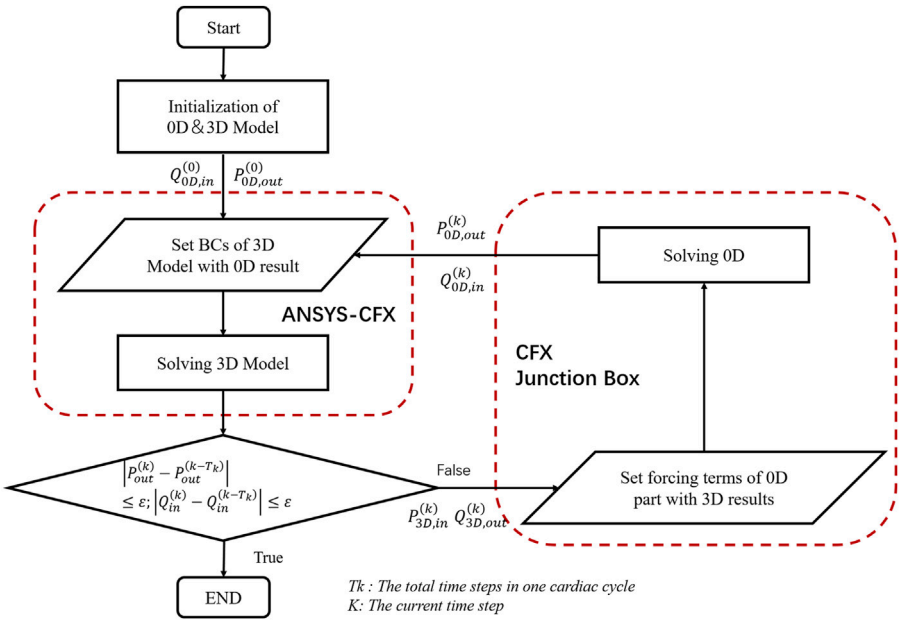


**FIGURE 3 |** The solution flow chart of the geometric multiscale coupled model. where Q_(0D,in) represents the flow of the entrance at the junction of the 0D model and the 3D model. P_(0D,out) represents the average pressure at the outlet at the junction of the 0D model and the 3D model. P_(3D,in) represents the mean pressure at the inlet calculated by the 3D model. Q_(3D,out) represents the outlet flow calculated in 3D, and BC is short for boundary conditions. The formula in the figure is the coupling judgment formula of the 3D and 0D models, where ε = 0.0001.

The above models were divided into tetrahedral meshes by the ANSYS ICEM CFD software. It was assumed that the vascular wall was rigid and impermeable without slippage, the blood material property was adiabatic and comprised of an incompressible viscous Newtonian fluid, and its flow was unsteady laminar flow. The density of blood flow was set to 1,050 kg/m3, and the viscosity of blood was set to 0.0035 Pa s (Deplano et al., 2001).

## Calculation Process of FFR

The specific steps of the steady-state geometric multiscale model include four processes: 1) Based on the coronary CTA image, a patient's accurate personalized epicardial coronary 3D model was established; 2) According to the segment 3D model, the boundary conditions of the inlet (mean pressure) and outlet (microcirculation resistance) were calculated, respectively; 3) The change in the coronary microcirculation resistance in the maximum hyperemia state was quantified, and 0D and 3D coupling was calculated; 4) The Navier–Stokes (N-S) equation of the intracoronary fluid was solved using the ANSYS software, the flow velocity and pressure in each coronary artery were obtained under the hyperemia state, and the $FFR_{SS}$ was calculated (**Figure 2**).

The specific steps of closed-loop geometric multi-scale calculation of $FFR_{CT}$ include five processes: 1) Based on the patient's coronary artery CTA image, the patient's accurate and personalized 3D model of the epicardial coronary artery and heart model is constructed. 2) According to the constructed three-dimensional model and based on the allometric scaling law, the branch flow of the coronary arteries and the coronary microcirculation resistance in the resting state (assuming that there is no stenosis) are determined. 3) A closed-loop 0D centralized parameter model is constructed to personalize the physiological parameters of the patients. 4) The change in the coronary microcirculation resistance under maximum hyperemia is quantified, and zero-dimensional and three-dimensional coupling calculations are performed. 5) The control equation (N-S) of the fluid in the coronary artery is solved using a calculation software to obtain the flow velocity and pressure in each blood vessel of the coronary artery under congestion, and FFRCT is calculated. The detailed of $FFR_{CT}$ calculation steps refer to previous studies (Liu et al., 2021).

In this study, we calculated the FFR of 134 cases based on the steady-state and closed-loop geometric multiscale model and compared the computational accuracy of $FFR_{SS}$ with clinical FFR and $FFR_{CT}$, respectively.

## Statistical Analysis

Data are summarized by descriptive statistics. Pearson correlation and linear regression analysis were performed to examine the relationship between FFR and $FFR_{SS}$ and $FFR_{CT}$, respectively. Agreement between the methods was assessed by Bland-Altman plots with corresponding 95% limits of agreement. The optimal cut-off values for $FFR_{SS}$ was computed based on maximizing the sum of sensitivity plus specificity. The sensitivity, specificity, accuracy, and area under the ROC curves (AUC) with 95% CI classification metrics were computed. Throughout this study, a *p*-value threshold of 0.05 was considered to infer statistically significant findings.

**TABLE 1 |** Basic characteristic form of enrolled patients.

| Characteristic | Data |
|---|---|
| Number of patients | 136 |
| Number of vessels | 154 |
| Ages(years) | 60 ± (10) |
| Male | 78 |
| Female | 58 |
| Systolic and diastolic blood pressure | 128 ± (10)/85 ± (9) |
| Heart rate | 72 ± (12.76) n/min |
| Cardiac output | 5.26 ± 2.6 L/min |
| Myocardial mass | 126 ± (34.08) g |
| Stenosis location | |
| Left artery descending (LAD) | 115 |
| Left circumflex artery (LCX) | 11 |
| Right coronary artery (RCA) | 28 |

# RESULTS

## Characteristics of the Patients

A total of 154 vessels in 136 patients (57% male, median age:60 years) were analyzed with stenosis severity of coronary lesions evaluated by CCTA and ICA ranging from 40 to 80% luminal narrowing. Invasive FFR interrogation assessed the presence of hemodynamically significant stenosis (FFR ≤0.80) in 154 vessels (28.57%, 44/154) of 136 patients. The clinical and demographics characteristics of the patients' population are summarized in **Table 1**.

## Relationships Between FFR, $FFR_{SS}$ and $FFR_{CT}$

The medians (interquartile range) of the FFR, $FFR_{CT}$ and $FFR_{SS}$ in this study were 0.81 (0.33–0.99), 0.85 (0.34–0.98), and 0.84 (0.26–0.99), respectively. A scatter plot between FFR and $FFR_{SS}$ is shown in **Figure 4A**, demonstrating moderate overall linear correlation between the 2 measures, with an r of 0.68 (95% confidence interval [CI]: 0.21–0.39) ($p < 0.001$). Similarly, the correlation of $FFR_{SS}$ and $FFR_{CT}$ demonstrated an r of 0.75 (95%CI: 0.67–0.72) ($p < 0.001$) (**Figure 4B**).

Bland-Altman plots for $FFR_{SS}$ are illustrated in **Figure 4C**. On average, $FFR_{SS}$ exceeded FFR by 0.03 (95% CI: −0.043 to −0.009). Most of the points in the figure are distributed within the 95% confidence interval, indicating that there is good agreement between FFR and $FFR_{SS}$. Similarly, Bland-Altman plots for $FFR_{SS}$ and $FFR_{CT}$ are illustrated in **Figure 4D**. $FR_{CT}$ exceeded $FFR_{SS}$ by 0.01 (95% CI: −0.001 to −0.029).

The formula for calculating relative error:

$$\text{Relative error} = \frac{Calculate\ FFR - Clinical\ FFR}{Clinical\ FFR} \quad (5)$$

The relative error between $FFR_{SS}$ and FFR is 0.11. The relative error between $FFR_{SS}$ and $FFR_{CT}$ is 0.067.

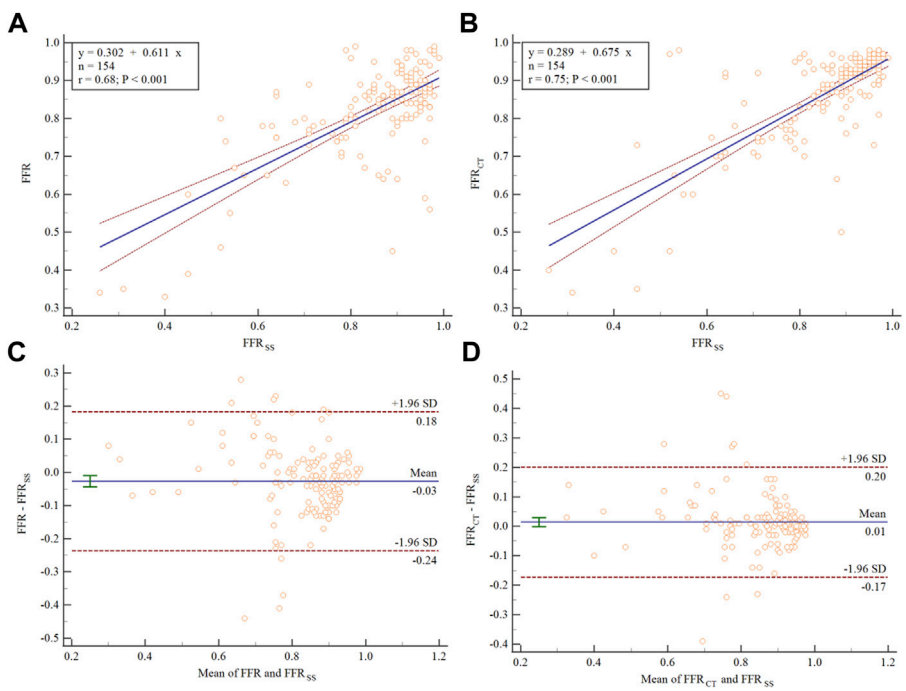


**FIGURE 4 |** Scatter plot and Bland–Altman analysis showing the correlation between FFR, $FFR_{SS}$, and $FFR_{CT}$. The dashed blue line represents the line of best fit. **(A)** The correlation between FFR and $FFR_{SS}$. **(B)** The correlation between $FFR_{CT}$ and $FFR_{SS}$. Bland–Altman plots of differences against the means are displayed for **(C)** $FFR_{SS}$ and **(D)** $FFR_{CT}$. The mean bias is represented by the solid blue line (with the 95% confidence interval represented by the dashed blue line).

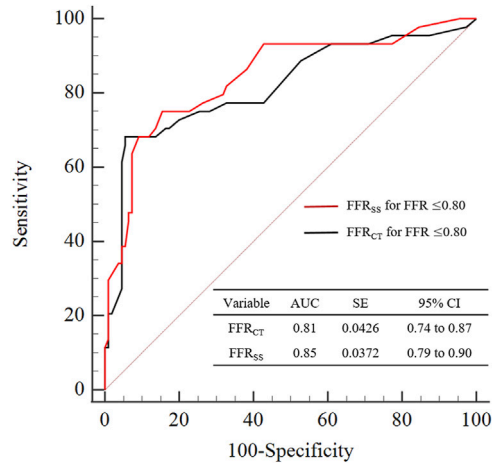


**FIGURE 5 |** Graphs show diagnostic performance of $FFR_{SS}$ and $FFR_{CT}$. The diagnostic performance of $FFR_{SS}$ and $FFR_{CT}$ was compared with clinical FFR≤0.80 as the criterion for the diagnosis of myocardial ischemia. It can be seen from the figure that the diagnostic performance of $FFR_{SS}$ and $FFR_{CT}$ is comparable, both have good diagnostic performance, and the variance is also close. AUC = area under receiver operating characteristics curve.

## Diagnostic Accuracy of $FFR_{SS}$

The diagnostic performance of $FFR_{SS}$ and $FFR_{CT}$ are assessed using clinically measured invasive FFR as the diagnostic criteria. The Youden index was 0.61 and the optimal cut-off was 0.80 for $FFR_{SS}$. The overall sensitivity, specificity, PPV, and NPV for $FFR_{SS}$ ≤ 0.80 versus FFR ≤ 0.80 was 68.18% (95% CI: 52.4–81.4), 93.64% (95% CI: 87.3–97.4), 82.9%, and 91.1%, respectively, with an overall diagnostic accuracy of 88.3%. Similarly, the overall sensitivity, specificity, PPV, and NPV for $FFR_{CT}$ ≤0.80 versus FFR ≤0.80 was 68.1% (95% CI: 52.4–81.4), 94.5% (95% CI: 88.5–98.0), 82.0%, and 89.5%, respectively, with an overall diagnostic accuracy of 87.6%.

According to the ROC receiver characteristic curve, the area under the curve of $FFR_{SS}$ and $FFR_{CT}$ are AUC = 85.7% (95%CI: [0.79–0.90]), AUC = 81.8% (95%CI: [0.74–0.87]), respectively. It suggesting that a good diagnostic performance is achieved of $FFR_{SS}$ as shown in **Figure 5**.

## Hemodynamic Results of Coronary Artery Stenosis

The $FFR_{SS}$ analysis of 6 representative patients was based on each narrowed vessel. We also list the clinical FFR, $FFR_{CT}$ and $FFR_{SS}$ of representative patients. The hemodynamic differences between $FFR_{CT}$ and $FFR_{SS}$ were compared based on clinically measured FFR (**Figure 6**). The stenosis of 6 representative patients stenosis was located in the anterior descending artery (LAD), and the degree of stenosis was 40–80%. It can be seen from the figure that the hemodynamic distribution calculated by $FFR_{SS}$ is basically consistent with that of $FFR_{CT}$.

# DISCUSSION

A rapid method for calculating FFR is proposed in this study. Based on the closed-loop geometric multiscale model for calculating FFR, the transient pressure boundary condition at the inlet was changed to a steady-state, and the model was optimized to ensure calculation accuracy. The inlet boundary condition improves computational efficiency. The diagnostic performance of $FFR_{SS}$ was validated by clinical FFR of 136 personalized patients. The $FFR_{CT}$ was calculated at the same time as the $FFR_{SS}$, and the myocardial ischemia assessment ability of the two calculated FFR methods was compared. The computational results showed that $FFR_{SS}$ was correlated and in agreement with both FFR and $FFR_{CT}$, with excellent diagnostic performance.

## Advantages of $FFR_{SS}$ Compared to $FFR_{CT}$

In the previous closed-loop geometric multiscale model (Liu et al., 2021), the physiological parameters of the patient had to be optimized to simulate the individualized physiological state, using transient periodic inlet boundary conditions. The $FFR_{SS}$ model adjusts the transient boundary condition of the inlet to a steady-state and replaces the transient pressure with the average pressure, which markedly improves the calculation efficiency. Then, the transient and steady-state pressure waveforms of the coronary arteries calculated by the geometric multiscale model were compared (**Figure 7**). $FFR_{SS}$ can replace $FFR_{CT}$ because the steady-state pressure and the transient average pressure are the same, resulting in the same calculation of FFR.

In addition, the $FFR_{SS}$ model saves the tedious process of optimizing the cardiac parameters of individual patients and replaces it with the average pressure, thereby improving the calculation efficiency and the clinical applicability of the model. The calculation time of $FFR_{CT}$ is usually 8–9 h, while the calculation time for $FFR_{SS}$ is only 20 min. Unlike other models that only consider stenotic vessels to calculate FFR (Itu et al., 2012; Itu et al., 2016; Zreik et al., 2018), the calculation model described in this study retains the complete coronary model, which can view the complete hemodynamic state of the coronary artery.

## The Selection of Inlet and Outlet Boundary Conditions

The inlet of the $FFR_{SS}$ model adopts the mean pressure calculated based on the "physiological formula," and the outlet adopts the microcirculation resistance model as the closed-loop geometric multiscale model. In a previous study, we presented a numerical investigation of the effects of the computational model's inlet and outlet boundary conditions on computed CT-FFR. The mean pressure calculated by the "physiological formula" differed from the real aortic pressure wave (Tosello et al., 2021). However, the calculation model was not sensitive to the boundary conditions of the inlet pressure, i.e., the true aortic pressure could be replaced by the mean pressure calculated by the "physiological formula." The findings revealed that distal boundary conditions (hyperemic vasodilation response of coronary micro-vessels) have a

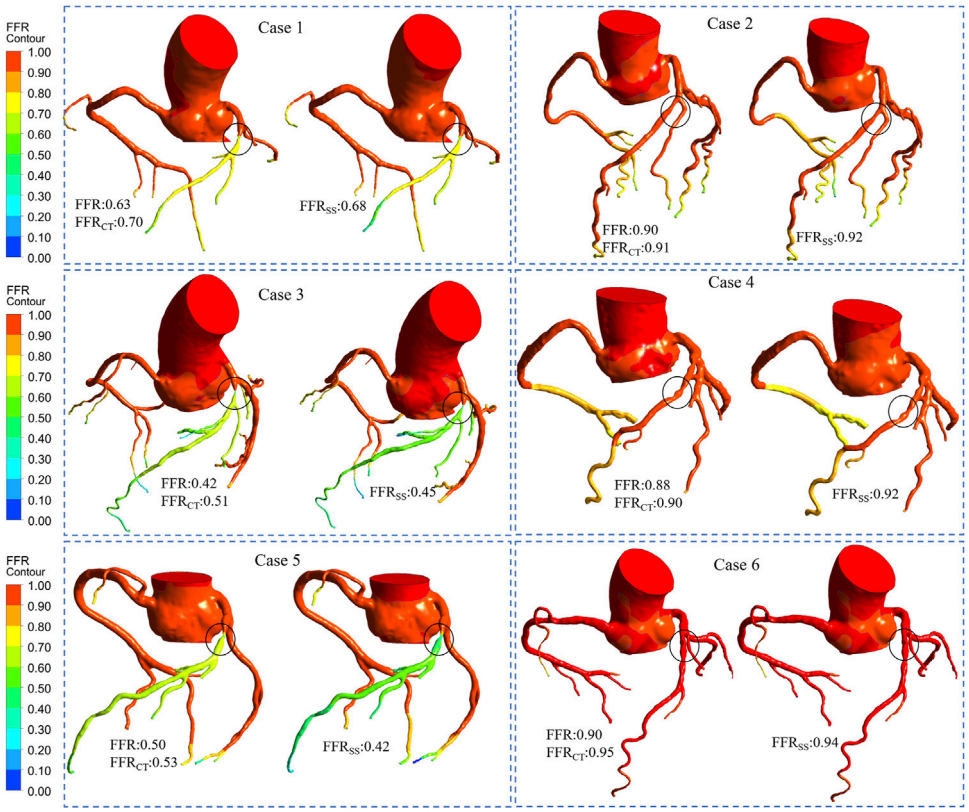


**FIGURE 6 |** Computed FFR contours for representative patients. Six representative patients had moderate stenosis of the left descending artery. Among them, cases 1, 3, and 5 were ischemia patients. Cases 2, 4, and 6 were non-ischemic patients. The FFR, $FFR_{CT}$, and $FFR_{SS}$ for each representative patient are listed separately. It can be seen from the figure that the contours of the calculation result of $FFR_{CT}$ is comparable to that of $FFR_{SS}$, and it have good consistency.

significant impact on FFR. Thus, improving the calculation accuracy of distal microcirculation resistance is the key to further improving the calculation of $FFR_{SS}$.

## Diagnostic Performance of $FFR_{SS}$

The calculation results show that compared to the closed-loop geometric multiscale model, the improved calculation model does not reduce the accuracy of calculating FFR. The accuracy of traditional $FFR_{CT}$ is 84.3% (Taylor et al., 2013), and that of $FFR_{CT}$ based on the closed-loop geometric multiscale model is 87.3% (Liu et al., 2021), which was similar to the 88.3% computational accuracy of $FFR_{SS}$ proposed in this study. Compared to the closed-loop geometric multiscale model, the $FFR_{SS}$ improves the computation speed, retaining the computation time within half an hour. Itu et al. proposed a non-invasive FFR calculation based on a neural network with an accuracy rate of 88.3% (Itu et al., 2016). Fredrik et al. (Fossan et al., 2021) proposed a non-invasive rapid calculation method of FFR based on an enhanced neural network, while the standard deviation of repeated FFR measurements was 0.018. However, the premise of improving the calculation speed in the above two studies was that only the coronary arteries in the stenotic segment are retained, and the other coronary arteries are ignored. The advantage of this study is that while improving the calculation speed, it retains the complete model and displays the hemodynamic positions of all coronary arteries, facilitating the diagnosis of myocardial ischemia.

## LIMITATIONS

CT-based non-invasive $FFR_{SS}$ calculations are very sensitive to image quality and segmentation models. $FFR_{SS}$ requires accurate anatomical models. Image artifacts, calcifications and improper registration may limit the accuracy of model calculations. Therefore, it is important to follow the protocol of high-quality image data and accurate description of the boundary of the lumen (Zarins et al., 2013).

Although the $FFR_{SS}$ computation model shortens the calculation time to less than half an hour, there is still some gap compared to the other simplified non-invasive methods for calculating FFR (Itu et al., 2016; Fossan et al., 2021), which does not meet the requirements of real-time FFR calculation. In the future studies, we will directly predict the coronary flow field through a neural network based on that calculated by the steady-state model $FFR_{SS}$, thereby improving the calculation speed.

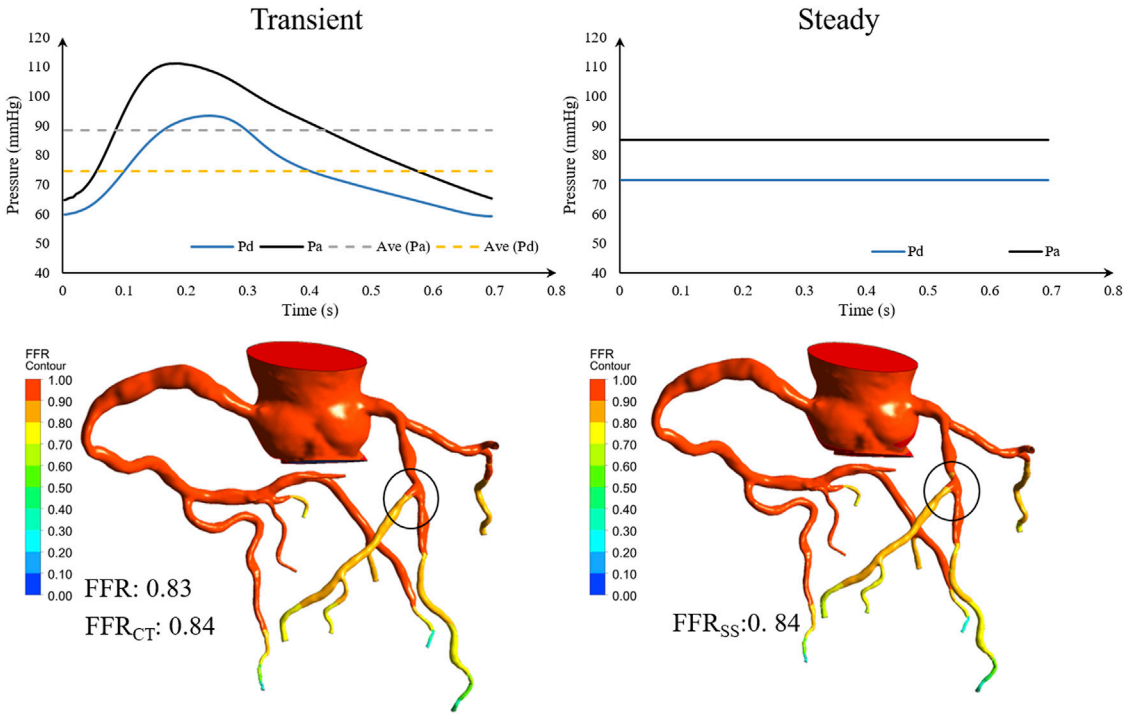


**FIGURE 7 |** Geometric multiscale solution for comparison of transient and steady-state pressure. Pa is the inlet pressure of the stenotic vessel, Pd is the outlet pressure, and Ave is the mean pressure.

## CONCLUSION

The present study proposed a steady-state-based geometric multiscale model to calculate FFR non-invasively and validate its accuracy with personalized clinical data from 136 cases. The calculation method has the same accuracy as the closed-loop geometric multiscale FFR computation but reduces the calculation time and exhibits a satisfactory diagnostic performance. This method improves the clinical applicability of the non-invasive computational FFR model, helps clinicians diagnose myocardial ischemia, and guides percutaneous coronary intervention (PCI) operations.

## DATA AVAILABILITY STATEMENT

The raw data supporting the conclusion of this article will be made available by the authors, without undue reservation.

## ETHICS STATEMENT

The studies involving human participants were reviewed and approved by the People's Hospital, Peking University Ethics Committee ;Human Research Ethics Committee of the Second Affiliated Hospital of Zhejiang University School of Medicine. The patients/participants provided their written informed consent to participate in this study. Written informed consent was obtained from the individual(s) for the publication of any potentially identifiable images or data included in this article.

## AUTHOR CONTRIBUTIONS

All authors were fully involved in the study. JL designed the research approach, analyzed results and write the article. XW, BL, SH and HS computational model. XZ and WW provides multi-scale technical assistance. LZ and MZ revised the manuscript. YS, ZL and LW provided assistance in the reconstruction of the coronary artery model and collected clinical data. JL provided theoretical support in the field of coronary arteries. YL was responsible for supervision.

## FUNDING

This study was supported by National Natural Science Foundation of China (11832003, 11772016), National Key Research and Development Program of China (2020YFC2004400, 2021YFA1000200), Zhejiang Science and Technology Plan major Project(2019C03084).

## REFERENCES


Blanco, P. J., Bulant, C. A., Müller, L. O., Talou, G. D. M., Bezerra, C. G., Lemos, P. A., et al. (2018). Author Correction: Comparison of 1D and 3D Models for the Estimation of Fractional Flow Reserve. *Sci. Rep.* 8, 17962. doi:10.1038/s41598-018-37078-5

Boileau, E., Pant, S., Roobottom, C., Sazonov, I., Deng, J., Xie, X., et al. (2018). Estimating the Accuracy of a Reduced-Order Model for the Calculation of Fractional Flow reserve (FFR). *Int. J. Numer. Method Biomed. Eng.* 34, e2908. doi:10.1002/cnm.2908

Deplano, V., Bertolotti, C., and Boiron, O. (2001). Numerical Simulations of Unsteady Flows in a Stenosed Coronary Bypass Graft. *Med. Biol. Eng. Comput.* 39, 488–499. doi:10.1007/bf02345372

Fihn, S. D., Gardin, J. M., Abrams, J., Berra, K., Blankenship, J. C., Dallas, A. P., et al. (2012). 2012 ACCF/AHA/ACP/AATS/PCNA/SCAI/STS Guideline for the Diagnosis and Management of Patients with Stable Ischemic Heart Disease: Executive Summary: A Report of the American College of Cardiology Foundation/American Heart Association Task Force on Practice Guidelines, and the American College of Physicians, American Association for Thoracic Surgery, Preventive Cardiovascular Nurses Association, Society for Cardiovascular Angiography and Interventions, and Society of Thoracic Surgeons. *J. Am. Coll. Cardiol.* 60, 2564–2603. doi:10.1016/j.jacc.2012.07.012

Fossan, F. E., Müller, L. O., Sturdy, J., Bråten, A. T., Jørgensen, A., Wiseth, R., et al. (2021). Machine Learning Augmented Reduced-Order Models for FFR-Prediction. *Comput. Methods Appl. Mech. Eng.* 384, 113892. doi:10.1016/j.cma.2021.113892

Götberg, M., Cook, C. M., Sen, S., Nijjer, S., Escaned, J., and Davies, J. E. (2017). The Evolving Future of Instantaneous Wave-free Ratio and Fractional Flow Reserve. *J. Am. Coll. Cardiol.* 70, 1379–1402. doi:10.1016/j.jacc.2017.07.770

Hae, H., Kang, S.-J., Kim, W.-J., Choi, S.-Y., Lee, J.-G., Bae, Y., et al. (2018). Machine Learning Assessment of Myocardial Ischemia Using Angiography: Development and Retrospective Validation. *Plos Med.* 15, e1002693. doi:10.1371/journal.pmed.1002693

Hannawi, B., Lam, W. W., Wang, S., and Younis, G. A. (2014). Current Use of Fractional Flow Reserve: A Nationwide Survey. *Tex. Heart Inst. J.* 41, 579–584. doi:10.14503/thij-13-3917

Itu, L., Rapaka, S., Passerini, T., Georgescu, B., Schwemmer, C., Schoebinger, M., et al. (2016). A Machine-Learning Approach for Computation of Fractional Flow reserve from Coronary Computed Tomography. *J. Appl. Physiol.* 121, 42–52. doi:10.1152/japplphysiol.00752.2015

Itu, L., Sharma, P., Mihalef, V., Kamen, A., Suciu, C., and Comaniciu, D. (2012). "A Patient-specific Reduced-Order Model for Coronary Circulation," in 2012 9th Ieee International Symposium on Biomedical Imaging (ISBI), Barcelona, Spain, 2-5 May 2012, 832–835.

Knuuti, J., Wijns, W., Saraste, A., Capodanno, D., Barbato, E., Funck-Brentano, C., et al. (2020). 2019 ESC Guidelines for the Diagnosis and Management of Chronic Coronary Syndromes. *Eur. Heart J.* 41, 407–477. doi:10.1093/eurheartj/ehz425

Kolh, P., Windecker, S., Alfonso, F., Collet, J.-P., Cremer, J., Falk, V., et al. (2014). 2014 ESC/EACTS Guidelines on Myocardial Revascularization. *Eur. J. Cardio-Thoracic Surg.* 46, 517–592. doi:10.1093/ejcts/ezu366

Li, B., Wang, H., Li, G., Liu, J., Zhang, Z., Gu, K., et al. (2020). A Patient-specific Modelling Method of Blood Circulatory System for the Numerical Simulation of Enhanced External Counterpulsation. *J. Biomech.* 111, 110002. doi:10.1016/j.jbiomech.2020.110002

Liu, J., Mao, B., Feng, Y., Li, B., Liu, J., and Liu, Y. (2021). Closed-loop Geometric Multi-Scale Heart-Coronary Artery Model for the Numerical Calculation of Fractional Flow reserve. *Comput. Methods Programs Biomed.* 208, 106266. doi:10.1016/j.cmpb.2021.106266

Mao, B., Feng, Y., Wang, W., Li, B., Zhao, Z., Zhang, X., et al. (2020). The Influence of Hemodynamics on Graft Patency Prediction Model Based on Support Vector Machine. *J. Biomech.* 98, 109426. doi:10.1016/j.jbiomech.2019.109426

Murray, C. D. (1926). The Physiological Principle of Minimum Work. *Proc. Natl. Acad. Sci. U.S.A.* 12, 207–214. doi:10.1073/pnas.12.3.207

Opie, L. H. (2003). *Heart Physiology: From Cell to Circulation*. Philadelphia, PA, USA: Lippincott Williams and Wilkins.

Pietrabissa, R., Mantero, S., Marotta, T., and Menicanti, L. (1996). A Lumped Parameter Model to Evaluate the Fluid Dynamics of Different Coronary Bypasses. *Med. Eng. Phys.* 18, 477–484. doi:10.1016/1350-4533(96)00002-1

Pijls, N. H. J., de Bruyne, B., Peels, K., van der Voort, P. H., Bonnier, H. J. R. M., Bartunek, J., et al. (1996). Measurement of Fractional Flow reserve to Assess the Functional Severity of Coronary-Artery Stenoses. *N. Engl. J. Med.* 334, 1703–1708. doi:10.1056/nejm199606273342604

Pijls, N. H. J. (2013). Fractional Flow Reserve to Guide Coronary Revascularization. *Circ. J.* 77, 561–569. doi:10.1253/circj.cj-13-0161

Raissi, M., Perdikaris, P., and Karniadakis, G. E. (2019). Physics-informed Neural Networks: A Deep Learning Framework for Solving Forward and Inverse Problems Involving Nonlinear Partial Differential Equations. *J. Comput. Phys.* 378, 686–707. doi:10.1016/j.jcp.2018.10.045

Sankaran, S., Kim, H. J., Choi, G., and Taylor, C. A. (2016). Uncertainty Quantification in Coronary Blood Flow Simulations: Impact of Geometry, Boundary Conditions and Blood Viscosity. *J. Biomech.* 49, 2540–2547. doi:10.1016/j.jbiomech.2016.01.002

Sdringola, S., Johnson, N. P., Kirkeeide, R. L., Cid, E., and Gould, K. L. (2011). Impact of Unexpected Factors on Quantitative Myocardial Perfusion and Coronary Flow Reserve in Young, Asymptomatic Volunteers. *JACC: Cardiovasc. Imaging* 4, 402–412. doi:10.1016/j.jcmg.2011.02.008

Sharma, P., Itu, L., Zheng, X., Kamen, A., Bernhardt, D., Suciu, C., et al. (2012). "A Framework for Personalization of Coronary Flow Computations during Rest and Hyperemia," in 2012 Annual International Conference of the IEEE Engineering-in-Medicine-and-Biology-Society, San Diego, CA, USA, 28 Aug.-1 Sept. 2012, 6665–6668.

Taylor, C. A., Fonte, T. A., and Min, J. K. (2013). Computational Fluid Dynamics Applied to Cardiac Computed Tomography for Noninvasive Quantification of Fractional Flow Reserve. *J. Am. Coll. Cardiol.* 61, 2233–2241. doi:10.1016/j.jacc.2012.11.083

Tosello, F., Guala, A., D'ascenzo, F., Bollati, M., Leone, D., Sabia, L., et al. (2021). Central Pulse Pressure Is Inversely Associated with Proximal Aortic Remodelling. *J. Hypertens.* 39, 919–925. doi:10.1097/hjh.0000000000002730

Wilson, K., Maccallum, H., Wilkinson, I. B., Hoskins, P. R., Lee, A. J., and Bradbury, A. W. (2001). Comparison of Brachial Artery Pressure and Derived central Pressure in the Measurement of Abdominal Aortic Aneurysm Distensibility. *Eur. J. Vasc. Endovascular Surg.* 22, 355–360. doi:10.1053/ejvs.2001.1465

Wilson, R. F., Wyche, K., Christensen, B. V., Zimmer, S., and Laxson, D. D. (1990). Effects of Adenosine on Human Coronary Arterial Circulation. *Circulation* 82, 1595–1606. doi:10.1161/01.cir.82.5.1595

Zarins, C. K., Taylor, C. A., and Min, J. K. (2013). Computed Fractional Flow Reserve (FFTCT) Derived from Coronary CT Angiography. *J. Cardiovasc. Trans. Res.* 6, 708–714. doi:10.1007/s12265-013-9498-4

Zhao, X., Liu, Y., Li, L., Wang, W., Xie, J., and Zhao, Z. (2016). Hemodynamics of the String Phenomenon in the Internal Thoracic Artery Grafted to the Left Anterior Descending Artery with Moderate Stenosis. *J. Biomech.* 49, 983–991. doi:10.1016/j.jbiomech.2015.11.044

Zreik, M., Lessmann, N., Van Hamersvelt, R. W., Wolterink, J. M., Voskuil, M., Viergever, M. A., et al. (2018). Deep Learning Analysis of the Myocardium in Coronary CT Angiography for Identification of Patients with Functionally Significant Coronary Artery Stenosis. *Med. Image Anal.* 44, 72–85. doi:10.1016/j.media.2017.11.008


**Conflict of Interest:** The authors declare that the research was conducted in the absence of any commercial or financial relationships that could be construed as a potential conflict of interest.

frontiers | Frontiers in Physiology

ORIGINAL RESEARCH
published: 12 April 2022
doi: 10.3389/fphys.2022.861446

# Accurate Calculation of FFR Based on a Physics-Driven Fluid-Structure Interaction Model

*Xiaolu Xi[1], Jincheng Liu[1], Hao Sun[1], Ke Xu[1], Xue Wang[1], Liyuan Zhang[1], Tianming Du[1], Jian Liu[2] and Bao Li[1]**

[1]Department of Biomedical Engineering, Faculty of Environment and Life, Beijing University of Technology, Beijing, China, [2]Cardiovascular Department, Peking University People's Hospital, Beijing, China

**Background**: The conventional FFRct numerical calculation method uses a model with a multi-scale geometry based upon CFD, and rigid walls. Therefore, important interactions between the elastic vessel wall and blood flow are not routinely considered. Changes in the resistance of coronary microcirculation during hyperaemia are likewise not typically incorporated using a fluid–structure interaction (FSI) algorithm. It is likely that both have resulted in FFRct calculation errors.

**Objective**: In this study we incorporated both the influence of vascular elasticity and coronary microcirculatory structure on FFR, to improve the accuracy of FFRct calculation. Thus, in this study, a physics-driven 3D–0D coupled model including fluid–structure interaction was established to calculate accurate FFRct values.

**Methods**: Based upon a novel geometric multi-scale modeling technology, a FSI simulation approach was used. A lumped parameter model (0D) was used as the outlet boundary condition for the 3D FSI coronary artery model to incorporate physiological microcirculation, with bidirectional coupling between the two models.

**Results**: The accuracy, sensitivity, specificity, and both positive and negative predictive values of $FFR_{DC}$ calculated based upon the coupled 3D–0D model were 86.7, 66.7, 84.6, 66.7, and 91.7%, respectively. Compared to the calculated value using the basic CFD model (MSE = 5.9%, accuracy rate = 80%), the $FFR_{CFD}$ calculated based on the coupled 3D–0D model has a smaller MSE of 1.9%.

**Conclusion**: The physics-driven coupled 3D–0D model that incorporates fluid–structure interactions not only consider the influence of the elastic vessel wall on blood flow, but also provides reliable microvascular resistance boundary conditions for the 3D FSI model. This allows for a calculation that is based upon conditions that are closer to the physiological environment, and thus improves the accuracy of FFRct calculation. It is likely that more accurate information will provide an enhanced recommendation regarding percutaneous coronary intervention (PCI) in the clinic.

**Keywords: coronary artery, fluid-structure interaction, 0D/3D geometric multi-scale model, fractional flow reserve, hemodynamic effects**

OPEN ACCESS

***Edited by:***
*Yunlong Huo,*
*Shanghai Jiao Tong University, China*

***Reviewed by:***
*Fan Tingting,*
*Capital Medical University, China*
*Weijuan Yao,*
*Peking University Health Science Centre, China*
*Junmei Zhang,*
*National Heart Centre Singapore, Singapore*

****Correspondence:***
*Bao Li*
*libao@bjut.edu.cn*

***Specialty section:***
*This article was submitted to Computational Physiology and Medicine, a section of the journal Frontiers in Physiology*

***Received:*** *24 January 2022*
***Accepted:*** *24 March 2022*
***Published:*** *12 April 2022*

***Citation:***
*Xi X, Liu J, Sun H, Xu K, Wang X, Zhang L, Du T, Liu J and Li B (2022) Accurate Calculation of FFR Based on a Physics-Driven Fluid-Structure Interaction Model. Front. Physiol. 13:861446. doi: 10.3389/fphys.2022.861446*

## INTRODUCTION

The hemodynamic environment inside coronary arteries significantly affects the abnormal growth of vascular endothelial cells and the deposition of cellular lipids, leading to the formation of vascular stenosis, which plays a key role in a heart attack (Bentzon et al., 2014). In the past few decades, hemodynamic studies on coronary artery stenosis have shown that arterial stenosis will severely disrupt normal blood flow, and that blood flow disorder can accelerate the growth of plaque to form a more stable stenosis. Fractional flow reserve (FFR), defined as the maximum myocardial ratio, i.e., the ratio of the blood flow of the stenotic branch of the coronary artery to the blood flow of the same coronary artery, is the current 'gold standard' for diagnosing functional myocardial ischemia (Pijls et al., 1996; Kakouros et al., 2013; Pijls et al., 2013; Van De Hoef et al., 2013). When small blood vessels in the coronary blood supply have a maximal dilation and the central venous pressure is assumed to be negligible, FFR can be approximated as:

$$\mathrm{FFR} = \frac{p_\mathrm{d}}{p_\mathrm{a}} \tag{1}$$

where $p_\mathrm{a}$ and $p_\mathrm{d}$ are respectively the average pressure of the aortic root and the distal portion of the stenotic coronary artery in the maximum hyperemia state.

Based upon computational fluid dynamics (CFD), FFRct (Fractional Flow Reserve derived from non-invasive coronary CT angiography) was first proposed by Taylor and co-workers (Taylor et al., 2013), who used a computerized numerical simulation to non-invasively calculate FFR. The study coupled lumped parameter models of the heart, systemic circulation, and coronary microcirculation to patient-specific models of the aortic root and epicardial coronary arteries reconstructed from data acquired from computed tomography angiography (CTA). Therefore, a geometric multi-scale model of the coronary artery was established to realize the non-invasive FFR calculation. The research team led by C. A. Taylor conducted the largest FFRct study in the world, representing the highest level of research on FFRct (Taylor et al., 2013; Zarins et al., 2013). After proposing the above-mentioned FFRct calculation method, they successively carried out three large-scale research projects: DISCOVER-FLOW, DeFACTO, and HeartFlowNXT. Clinical experiments proved that FFRct can accurately diagnose and rule out coronary stenosis causing myocardial functional ischemia. Recently the Heart Flow-funded PLATFORM study (Prospective Longitudinal Trial of FFRct: outcome and resource impacts) further demonstrated the effectiveness of FFRct in the clinical diagnosis of myocardial ischemia: compared with CTA, FFRct can significantly reduce the false positive rate in patients with coronary heart disease. (Grunau et al., 2013; Douglas et al., 2015). There are now studies pursuing fast numerical calculation of FFR. For instance, Zhang et al. (2016) used a simplified steady-state coronary flow model for non-invasive calculation of FFR. However, the studies ignored the elasticity of blood vessels based upon a single-coupled numerical calculation model. The model assumed that the vessel wall is rigid, resulting in inaccurate numerical simulation.

Human blood vessels are elastic, and pulsating blood flow presses upon the blood vessel wall in real time, causing the deformation of the blood vessel wall and a change in the flow field. Therefore, numerical simulation using a multi-scale CFD model with a fixed geometry will ignore the real-time influence of the blood vessel wall on blood flow. The hypothesis of a rigid wall cannot be used to reflect real hemodynamics within blood vessels, and this may bias FFRct calculation. The dilation of blood vessels and plaques in an elastic wall will cause a gap between true vascular resistance and that of the rigid wall, which leads to significant differences in calculated FFRct, and potentially a false-negative diagnosis (Kock et al., 2008; Tang et al., 2009; Teng et al., 2010).

In addition to the presence of vascular elasticity, the influence of microcirculation resistance on calculated FFRct should not be ignored. The fluid-structure interaction (FSI) analysis of blood flow and the blood vessel wall can consider the mechanical interaction between blood flow and the blood vessel wall (Perktold and Rappitsch, 1995; Tang et al., 2003), thereby reducing calculation errors. However, the traditional FSI model cannot fully consider the changes in microcirculation resistance of coronary arteries in a state of hyperemia. The total resistance of coronary arteries is related to coronary microcirculation, and myocardial blood flow is regulated by coronary microcirculation (Leung and Leung., 2011). Microcirculation is an important part of the circulatory system, which plays an irreplaceable role in promoting cardiovascular health. For a more accurate model incorporating microcirculation, a flow analysis of the circulatory system should be performed (He et al., 2021). To fully consider patient-specific microcirculation resistance, a geometric multi-scale model should be established to non-invasively calculate FFR (Lagana et al., 2005; Kim et al., 2010; Moghadam et al., 2013; Zhao et al., 2015).

Based on the rule of energy conservation, stenosis and microcirculation resistance should fit the following formula:

$$p_\mathrm{a} = \Delta p_\mathrm{stenosis} + \Delta p_\mathrm{micro-circulation} + p_\mathrm{v} \tag{2}$$

where $p_\mathrm{a}$ is the aortic pressure, $\Delta p_{stenosis}$ is the pressure drop of stenotic vessels, $\Delta p_{micro-circulation}$ is the microcirculation pressure drop, and $p_v$ is the right atrial pressure, which is generally small and can be ignored.

In order to consider the influence of both FSI and coronary microcirculation structure on FFR, this study proposes a dual-coupled 3D FSI–0D numerical model ($\mathrm{FFR_{DC}}$) for non-invasive calculation of FFR to improve the accuracy of FFRct calculation. In this study, 15 patient-specific CTA images were collected, as well as clinically measured FFR for comparison. $\mathrm{FFR_{DC}}$ was non-invasively calculated and compared with the clinically measured FFR to determine the reliability and accuracy of the method for diagnosing myocardial ischemia.

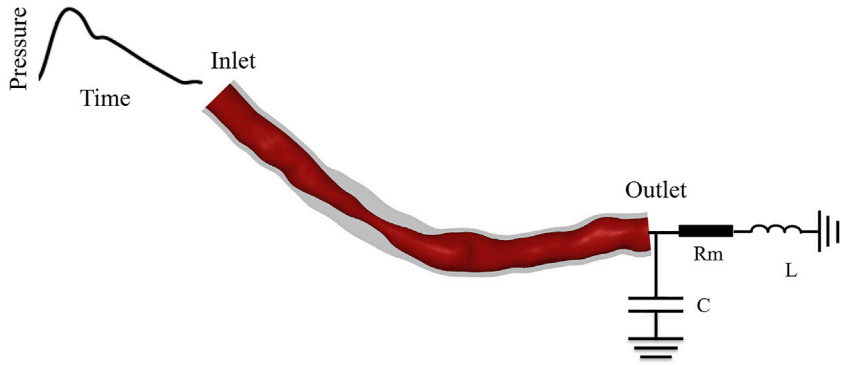


**FIGURE 1 |** Dual-coupled coronary model with 70% stenosis and 10 mm stenosis length.

# METHODS

## Establishment of Dual-Coupled Three-Dimensional Fluid–Structure Interaction–Zero-Dimensional Model

In this study, a coupled multi-scale 3D–0D model of the coronary artery incorporating FSI was established by coupling a zero-dimensional (0D) model with a three-dimensional (3D) model coronary using a blood flow domain and vascular structure domain, as shown in **Figure 1**. The complete model consisted of the coronary artery structure and microcirculation structure. The 3D FSI model described the coronary artery structure, and the 0D model was used to provide the boundary conditions for the coronary artery outlet.

The coronary artery structure described by the 3D model included structural domains and fluid domains. According to the patient's CTA image, the 3D reconstruction software Mimics was used to reconstruct the fluid domain of the patient-specific epicardial coronary artery, and then the fluid part was shelled to obtain coronary artery structural domains. The calculation of the geometric multi-scale model requires multiple iterative calculations in each time step. To simplify the calculation, the 3D model only included the stenotic segment for calculation, the specific length included followed the formula of Sankaran et al. (2016):

$$\mathrm{d}(z) = d_h(z)\left[1 - \frac{1}{2}\left[1 - \cos\left(\frac{z - z_c}{\Delta}\pi + \pi\right)\right]\alpha\right] z_t < z < z_u \quad (3)$$

where $d_h$ is the normal blood vessel diameter, $z_c$ is the position of the smallest diameter, $z_t$ and $z_u$ are respectively the start and end points of the stenosis, $\Delta$ is half of the length of the stenosis, and $\alpha$ is the modeled percentage stenosis.

The 0D model was established based upon similarity between the regulation of electronic circuits and blood flow. A 0D model containing electrical components was used to simulate the cardiovascular system, turning the complex 3D blood flow simulation into a simple circuit simulation (Wischgoll et al., 2008; Huo et al., 2012). Blood flow resistance was simulated by electrical resistance, while blood pressure and blood flow were equivalent to voltage and current. The equivalent relationship between hemodynamic parameters and electrical parameters is described in **Table 1**. The inductance parameter was set to the empirical value of 0.5, which has been described in detail in previous laboratory studies (Wang et al., 2018), so that the calculation results converged. Resistance values are determined based on physiological parameters such as blood pressure, cardiac output, and coronary branch flow.

## Dual Coupling Algorithm

Data transmission during 3D–0D coupling was performed by user-defined functions (UDF) in ANSYS-Fluent. The inlet boundary condition of the 3D model, $p_{3D,in}$, is the clinically measured aortic pressure waveform of the patient. The volumetric flow rate, $Q_{3D}$, is calculated according to the 0D model of microcirculation resistance, $R_m$, and the 3D FSI model in the hyperemic state determines the outlet pressure

$$p_{3D,out} = Q_{3D} \times R_m \times 0.24 \quad (4)$$

where $p_{3D,out}$ is the outlet pressure of the 3D model, $Q_{3D}$ is volumetric blood flow rate, and $R_m$ is the microcirculation resistance in the resting state.

The geometric multi-scale model is set up as a transient calculation driven by physics. We calculated FFRct by determining both stenosis resistance and microcirculation resistance. Based upon energy conservation, when **Eq 5** is satisfied in a time-step calculation, the 0D model and the 3D model have reached a pressure balance, and the calculation has reached convergence.

$$p_{3D,in} = \Delta p_{3D} + p_{3D,out} \quad (5)$$

where $\Delta p_{3D}$ is the pressure drop produced in this section of the blood vessel, and $p_{3D,in}$ is the inlet pressure of the 3D model.

FSI provides the calculation of the 3D model, including fluid domain and structure domain, using a two-way fluid–structure interaction method. Blood was set as an incompressible fluid in a

**TABLE 1 |** Hemodynamic parameters and equivalent electrical parameters.

| Hemodynamic parameter | Blood flow | Blood pressure | Microcirculation resistance | Vascular elasticity | Blood flow inertia |
|---|---|---|---|---|---|
| Equivalent electrical parameter | Current | Voltage | Electrical resistance | Capacitance | Inductance |

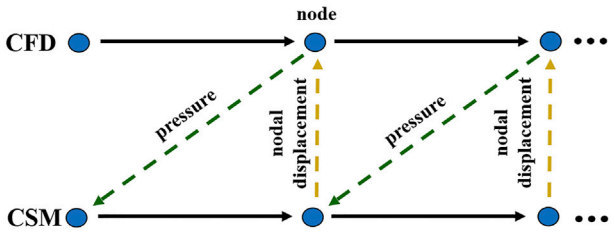


**FIGURE 2 |** Data transfer between fluid and solid domains. (CFD: computational fluid dynamics; CSM: computational structural mechanics).

3D, transient simulation. The fluid domain Navier–Stokes equation and momentum equation considering the dynamic mesh algorithm for the numerical calculation of FSI are:

$$\rho_{\mathrm{f}}\left[\frac{\partial v}{\partial t}+\left(\boldsymbol{v}-\boldsymbol{v}_{\mathrm{g}}\right)\cdot\nabla\boldsymbol{v}\right]=-\nabla p+\nabla\cdot\boldsymbol{T} \tag{6}$$

$$\nabla\cdot\boldsymbol{v}=0 \tag{7}$$

where $\nabla$ is the Hamiltonian, $\boldsymbol{v}$ is the fluid velocity vector, $v_g$ is the mesh shifting velocity, $\boldsymbol{T}$ is the stress tensor, $p$ is fluid pressure, and $\rho_f$ is fluid density (Bird et al., 1987; Fefferman, 2006; Alireza et al., 2014).

Without considering stress in the calculation, the governing equation of the movement of the vascular wall, namely the solid domain, is:

$$\nabla\cdot\boldsymbol{\sigma}_{\mathrm{s}}=\rho_{\mathrm{s}}\cdot\boldsymbol{a}_{\mathrm{s}} \tag{8}$$

In the formula, $\boldsymbol{\sigma}_s$ is the stress tensor of the vessel wall, $\rho_s$ is the density of the vessel wall, and $\boldsymbol{a}_s$ is the acceleration of the vessel wall (Fung and Cowin., 1993).

To follow the most basic principles of conservation, the surface that is subject to fluid–solid interaction should also satisfy conservation of stress, displacement, and flow rate of fluid and solid.

$$\boldsymbol{\sigma}_{\mathrm{s}}\cdot\hat{\boldsymbol{n}}_{s}=\sigma_{\mathrm{f}}\cdot\hat{\boldsymbol{n}}_{\mathrm{f}} \tag{9}$$

$$\boldsymbol{d}_{\mathrm{s}}=\boldsymbol{d}_{\mathrm{f}} \tag{10}$$

$$\boldsymbol{q}_{\mathrm{s}}=\boldsymbol{q}_{\mathrm{f}} \tag{11}$$

In the above formulæ $\boldsymbol{d}$ is the displacement vector, $\boldsymbol{q}$ is the flow rate, $\sigma$ is the stress tensor, $\hat{n}$ is the boundary normal, and the subscripts f and s represent the fluid and solid domains. The data transmission during the bidirectional fluid–solid coupling calculation is shown in **Figure 2**.

Based upon the physics-driven method, we implemented two-way coupling between the solid and fluid of the model while also realizing bidirectional coupling between the 0D and 3D models, thus completing the dual coupling model. At each time step of the algorithm, the calculation for the 0-dimensional model was used as the outlet boundary of the 3D model. The inlet pressure of the fluid domain of the 3D model, the displacement of the solid domain, the pressure of the fluid-solid interface, and the error in displacement data between the fluid and solid domains between different cardiac cycles were defined as the model residuals. When the model residuals were less than the pre-set value, the calculation result was deemed convergent, and then the next calculation proceeded until the end of the simulation. The specific calculation process is shown in **Figure 3**.

## Simulation of Hyperemia

The hyperemia model was obtained by reducing the coronary microcirculation resistance, and it was assumed that all of the patient's coronary vessels are without stenosis in the rest state. The myocardial mass was calculated by multiplying the reconstructed myocardial volume by the average myocardial density, and the total coronary artery flow was determined by the myocardial mass. According to an allometric scaling law, blood flow is proportional to vessel diameter raised to some power; that is, $Q\propto d^{k}$ (Murray, 1926). The total flow of the coronary vessels was used to calculate the flow of each coronary artery. The microcirculation resistance at the outlet of each branch was calculated according to the formula:

$$R_{\mathrm{m}}=\frac{p}{Q} \tag{12}$$

where $p$ is the coronary branch outlet pressure, and $Q$ is the allocated resting flow. Since the FFR was calculated in the hyperemic state, microcirculation resistance was 0.24 times that in the resting state (Wilson et al., 1990; Taylor et al., 2013), as shown in **Figure 4**.

## Calculation Settings

In this study, uniform material properties were used in the calculation of the vessel wall. It was assumed that the thickness of the blood vessel wall was 0.5 mm (Leach et al., 2010), the arterial wall was non-slip, linear elastic, isotropic and incompressible, the Young's modulus was 0.6 MPa, and the Poisson's ratio was 0.48 (Wang et al., 2020). Blood flow was assumed to correspond to incompressible laminar flow of a Newtonian fluid, and the viscosity and density of blood were 0.0035 Pa·s and 1050 kg/m$^3$, respectively (Ofili et al., 1995; Sun et al., 2010). The computation was performed on the ANSYS Workbench platform, solved using a workstation equipped with a 2.3 GHz Intel Xeon CPU and 64 GB of RAM. The systems coupling framework effected the complete coupling of transient fluid analysis (in Fluent CFD) and transient structure

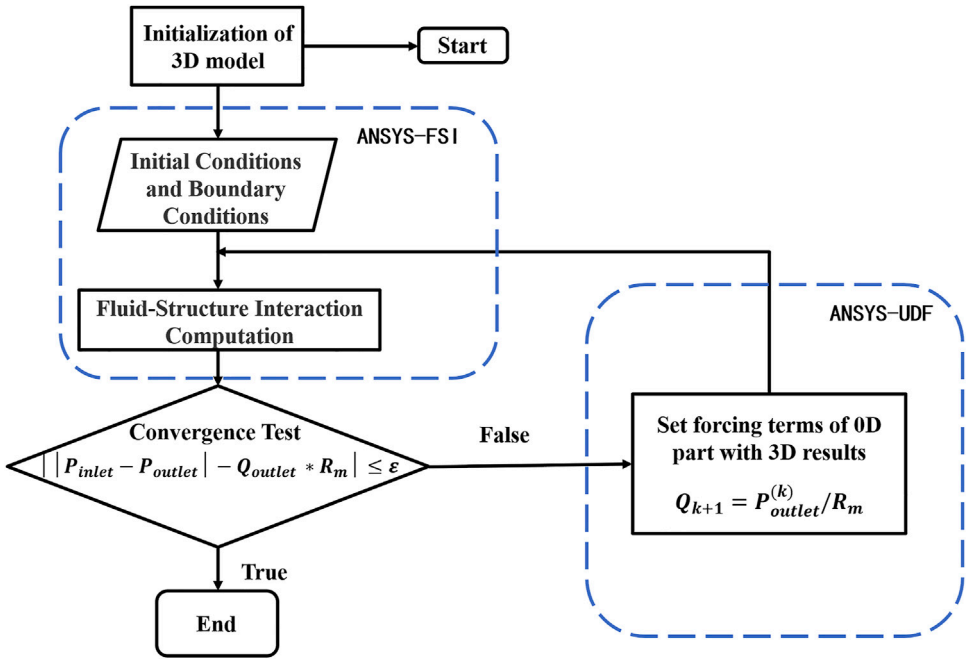


**FIGURE 3 |** Flow chart of dual-coupled model algorithm.

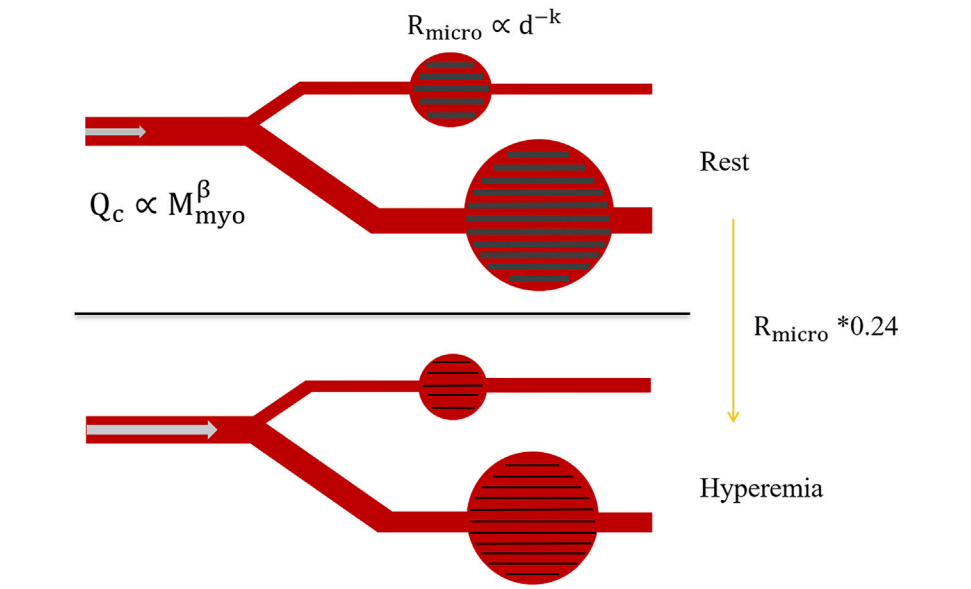


**FIGURE 4 |** Changes in microcirculation resistance due to hyperemia.

analysis. The side of the lumen was set as the interface between fluid and structure. The time steps of the fluid domain and structural domain models were both set to 0.01 s, and the simulation was run for three cardiac cycles. To improve the stability of the coupled simulation, the transmission data value linearly increased in the first five coupling iterations (minimum number of iterations) at each time step. To avoid unstable results of the initial time step, only the data from the second cardiac cycle was used for post-processing. In domains modelled by CFD, the fluid area was divided into tetrahedral elements with inflation layers, and the solid region was divided into a hexahedral grid (Wang et al., 2020).

**TABLE 2 |** Basic information describing the 15 enrolled patients. Values shown are either counts or mean values (with standard deviations in parentheses, where available).

| *Characteristic* | *Value* |
|---|---|
| Number of patients | 15 |
| Number of vessels | 15 |
| Ages | 64( ± 8.95) |
| Number of males | 10 |
| Number of females | 5 |
| Number of left artery descending (LAD) | 10 |
| Number of right coronary artery (RCA) | 5 |
| Systolic blood pressure/mmHg | 140( ± 17.99) |
| Diastolic blood pressure/mmHg | 79( ± 9.01) |
| Left ventricular systolic volume/$mm^3$ | 31.3( ± 4.3) |
| Left ventricular diastolic volume/$mm^3$ | 101.84( ± 7.2) |
| Heart rate/bpm | 60.42( ± 8.38) |
| Cardiac output/($L{\cdot}min^{-1}$) | 4.251( ± 2.18) |
| Myocardial mass/g | 141.7( ± 23.72) |

## Clinical Data Collection and Processing

The study was a prospective investigation. The coronary CTA images were obtained using a dual-layer detector CT system (IQon, Philips Healthcare) comprising 256-row CTA tomography, with a matrix size of 512 × 512 a slice thickness of 0.625 mm, and a pixel size within each slice was 0.5 mm × 0.5 mm. The coronary CTA used standard acquisition protocols in accordance with recommendations from professional societies. All data were collected at the Peking University People's Hospital, and FFR was measured clinically. The study was approved by the Internal Review Board and informed written consent was obtained from enrolled patients. The anonymous clinical data were independently reviewed and analysed by the Biomechanics Laboratory of Beijing University of Technology.

We set the specific criteria for enrollment, coronary angiography, and FFR catheter surgery. Exclusion criteria for this clinical trial included poor CTA image quality and coronary microcirculation disorders. Acute myocardial infarction (MI), small vascular lesions (defined as reference diameter < 2.5 mm), or N1 vascular lesions were excluded. Clinical data from 15 patients were collected in this study to confirm the accuracy of the dual-coupled model for FFRct calculation.

The dual-coupled calculation was performed for all 15 patients and results were analyzed for statistical significance. Sensitivity, specificity, positive predictive value (PPV), negative predictive value (NPV), and accuracy were expressed as percentages with 95% confidence intervals.

# RESULTS

## Patient Information

Basic information describing the 15 enrolled patients is presented in **Table 2**. Stenosis was moderate (40–80%), the mean age of patients was 64 years old, and most patients had stable angina and hypertension.

## FFRct Calculation Results

**Figure 5** shows the FFRct contours calculated using the dual-coupling model and the conventional geometric multi-scale model based upon CFD. **Table 3** shows the FFR calculation results for all of the 15 patients. **Figure 6** shows the comparison of FFRct calculation results for the 15 patients using the dual-coupling model and the geometric multi-scale model based on CFD: there is a gap between the respective mean FFRct values, demonstrating that the mean value based upon FSI is larger than that based upon CFD alone.

## Correlation Analysis for Fractional Flow Reserve

When the sample size is constant, the mean square error (MSE) can be used to evaluate the quality of a set of point estimates:

$$\mathrm{MSE}\left(\hat{\theta}\right) = \mathrm{E}\left(\hat{\theta} - \theta\right)^2 \tag{13}$$

The MSE of FFR calculated based on the dual-coupling model is 1.9%, whilst the MSE of FFR calculated based on the geometric multi-scale CFD model is 5.9%; in each case the reference data were the clinically measured FFR values.

The linear relationship between clinically measured FFR and calculated FFRct values is shown in **Figure 7** ($p < 0.01$). The Bland–Altman graph and ROC curve between FFR and FFRct are also provided. As shown in the figure, the calculated $FFR_{DC}$ values have a better correlation with the clinically measured values ($R = 0.87$), compared with the values calculated using the conventional CFD model ($R = 0.73$), indicating higher accuracy and diagnostic performance. The ROC curve is a comprehensive indicator reflecting the continuous variables of sensitivity and specificity. AUC (area under the ROC curve) refers to the area under the ROC curve. The closer the AUC is to 1, the higher the diagnostic value of the test. MedCalc 19.20 statistical software was used for ROC analysis. The ROC curves shown in **Figure 7E** indicate that the AUCs of $FFR_{DC,}$ and $FFR_{CFD}$ are 0.972 (95%CI 0.737–1), $p < 0.0001$ and 0.861 (95%CI 0.589–0.982), $p = 0.0007$. The $p$ value for the compare of ROC of $FFR_{DC,}$ and $FFR_{CFD}$ is 0.25. Using FFR ≤ 0.8 as the reference standard, the specificity of $FFR_{DC}$ and $FFR_{CFD}$ is 0.91 (95%CI 0.615–0.998) and 0.75 (95%CI 0.428–0.945) respectively and the sensitivity both are 1 (95%CI 0.292–1). Due to the limitation of quantity, the $p$ value of the comparison between the two ROC values indicates that the difference is not significant, but the comparison from AUC reflects the higher accuracy of $FFR_{DC}$. The diagnostic value of $FFR_{DC}$ is higher. The comprehensive results reflect the accuracy of the method for calculating FFRct using the double-coupling model introduced in the present study.

# DISCUSSION

## Influence of the Elastic Wall on FFRct

The FFR value calculated based on the dual-coupling model is 0.03 larger on average than the FFR value calculated by CFD alone. We hypothesize that the reason for that result is the dilation of blood

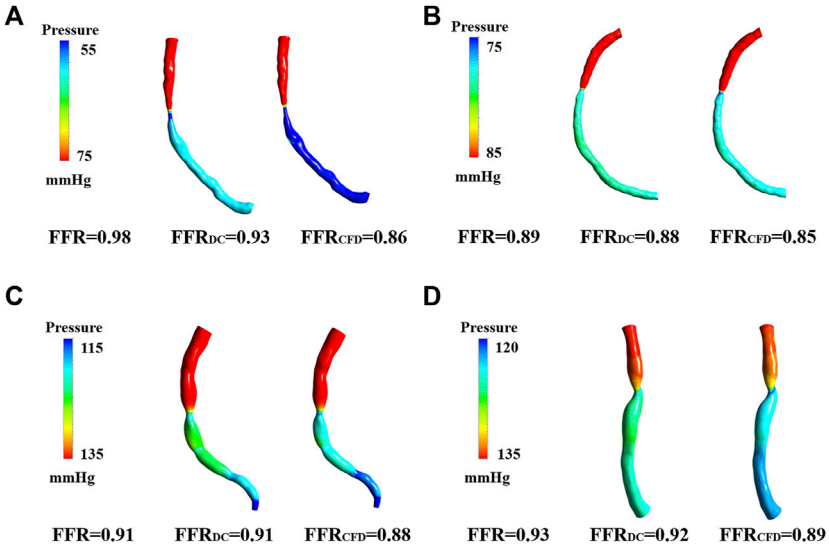


**FIGURE 5 |** FFRct Pressure cloud image calculated based on dual models. **(A)** Pressure cloud of patient 2 for both computational models. **(B)** Pressure cloud of patient 4 for both computational models. **(C)** Pressure cloud of patient 6 for both computational models. **(D)** Pressure cloud of patient 5 for both computational models.

**TABLE 3 |** The calculated and measured FFR results for all of the 15 patients.

| Patient | Clinically | $FFR_{DC}$ | $FFR_{CFD}$ | $R_m$ [mmHg s/ml] | Computation time (FFRDC/FFRCFD) [h] |
|---|---|---|---|---|---|
| 1 | 0.76 | 0.77 | 0.8 | 132.99 | 18/3 |
| 2 | 0.98 | 0.93 | 0.86 | 81.72 | 9/4.5 |
| 3 | 0.91 | 0.91 | 0.88 | 142.26 | 10.1/4 |
| 4 | 0.89 | 0.88 | 0.85 | 133.42 | 12.5/3 |
| 5 | 0.93 | 0.92 | 0.89 | 146.62 | 10.7/5 |
| 6 | 0.91 | 0.91 | 0.88 | 83.49 | 11.2/2 |
| 7 | 0.97 | 0.91 | 0.89 | 82.05 | 8.6/3.3 |
| 8 | 0.89 | 0.85 | 0.79 | 109.27 | 11.7/4 |
| 9 | 0.75 | 0.71 | 0.67 | 124.17 | 18.2/3.3 |
| 10 | 0.91 | 0.91 | 0.9 | 427.34 | 9.5/3 |
| 11 | 0.71 | 0.81 | 0.78 | 143.22 | 20.4/8 |
| 12 | 0.98 | 0.95 | 0.9 | 95.11 | 9.1/4 |
| 13 | 0.84 | 0.83 | 0.76 | 101.35 | 13.7/4 |
| 14 | 0.84 | 0.78 | 0.74 | 105.87 | 14.6/3.5 |
| 15 | 0.89 | 0.85 | 0.83 | 129.76 | 12.2/4.3 |

vessel walls, which reduced the resistance to blood flow (Wu et al., 2019). The conventional geometric multi-scale model based on CFD alone assumes that the vessel wall is rigid by default, and there is no change in displacement. Under the same pressure, the stenotic vessel was not deformed in the rigid-walled model, which tended to increase the flow resistance due to stenosis in the vessel. However, blood vessels are elastic during clinical FFR detection, and consequently the FFRct calculation using a rigid-wall model may lead to reduced estimates compared to clinical measurements.

## The Authenticity Based on Use of the Dual-Coupling Model

The FSI model can fully consider the elastic wall, and more closely parallel the physiological state of the human blood vessel. However, the FFRct calculation using conventional FSI cannot fully incorporate the changes in microcirculation resistance after hyperemia. Blood flow within the coronary microcirculation of patients cannot be continuously and non-invasively measured in real time. Therefore we developed and described the physics-driven 3D–0D coupling method. We described boundary conditions and loops at the interface of the modeling domain and specified the 0D model to simulate the resistance of microvessels on the exit boundary conditions of the 3D model to calculate FFRct.

## The Accuracy of the Dual Coupling Model to Calculate $FFR_{DC}$

The Discovery-flow study (Diagnosis of Smaller-Causing Stenoses *via* Noninvasive Fractional Flow Reserve) was an

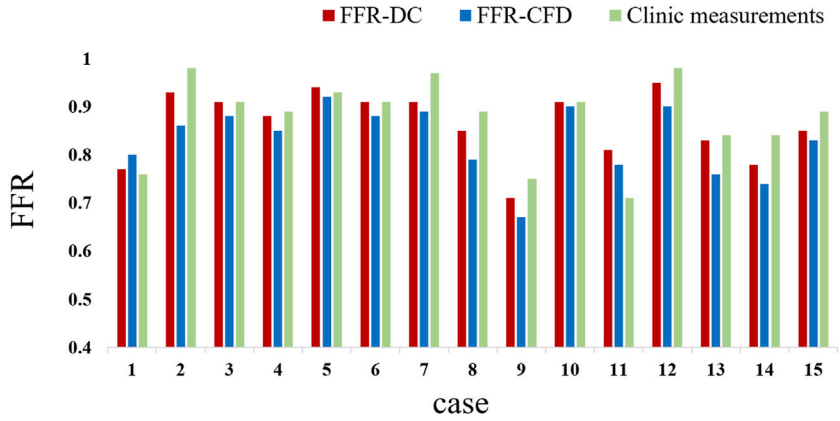


**FIGURE 6 |** Comparison between clinically measured FFR and FFRct calculated with different models.

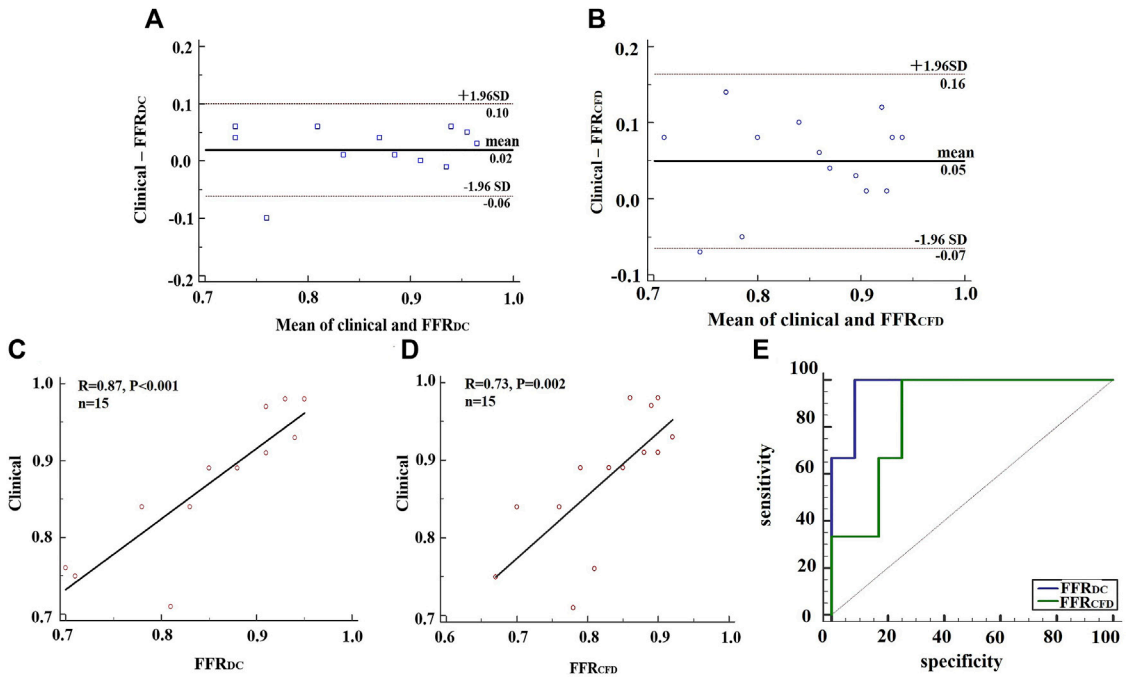


**FIGURE 7 |** Analysis of clinical FFR data, FFRDC and FFRCFD. **(A)** BlandAltman plots for the pairwise comparisons of clinical FFR data and FFRDC. **(B)** BlandAltman plots for the pairwise comparisons of clinical FFR data and FFRCFD. **(C)** A comparison of clinical FFR data and FFRDC. **(D)** A comparison of clinical FFR data and FFRCFD. **(E)** ROC analysis of FFRDC and FFRCFD, using clinical FFR data as a reference.

early multi-center, prospective evaluation of FFRct accuracy, which compared FFRct with invasive FFR, showing that FFRct had a diagnostic accuracy of 84.3% (Koo et al., 2011). In the present study, the accuracy of dual-coupling model for FFRct calculation was 86.7%, the sensitivity was 66.7%, the specificity was 84.6%, the positive predictive value was 66.7%, and the negative predictive value was 91.7%. This indicates that the capacity for diagnostic prediction of FFRct calculated by the dual-coupling model is not inferior to that of conventional FFRct. Therefore, there is higher accuracy using the dual coupling model. Because clinically measured FFR is measured under real physiological conditions, we introduced the elasticity of the blood vessel into the conventional geometric multi-scale model to take into account the interaction between blood and the artery walls. The individualization of the coronary artery model makes the parameters of the 0D model more reasonable. The sensitivity of $FFR_{DC}$ and $FFR_{CFD}$ in this study was 66.7%, which was lower than previous studies, because the sample size of this study was only 15, of which only three patients were FFR positive.

Patient-specific allocation methods for coronary artery flow enabled individualization of the coronary microcirculation resistance model, which matched the parameters of the 0D model to each patient. The dual coupling model appeared to have physiological significance since morphological distinctions between patients was considered. Methodologically, a physics-driven dual-coupling method as described herein can be used to simulate a more realistic coronary hemodynamic environment. In clinical application, this method can improve the accuracy of FFRct calculations and can potentially assist in guiding successful clinical percutaneous coronary intervention (PCI) surgery.

## LIMITATIONS AND FUTURE WORK

There are several limitations to the techniques and methodology used in the study. For instance, we assumed that the material properties of the three-layered structure of the blood vessel wall and the plaque were uniform, using a single elastic modulus. However, the blood vessel wall is divided into three layers, with plaques, and differs between patients. We propose to further develop the modeling system to personalize each patient's plaque type and parameters related to elasticity of the blood vessel wall.

In this study, we limited enrollment and collected clinical data for 15 patients, but this sample size is small. Additional enrollment will allow us to improve the accuracy of the dual-coupling model, and also improve the algorithm that we developed. We will continue to collect more patient cases and carry out prospective clinical trials on FFRct. Meanwhile we will conduct FFR-guided and PCI-guided double-blind trials. Prognostic analysis confirmed that dual-coupled FFRct could be applied clinically to guide the operation of PCI. In addition, all 15 patients in this study had a single stenosis, whereas this method is theoretically applicable to patients with multiple stenoses, which will be further verified at a later stage.

## CONCLUSION

In conclusion, a physics-driven dual-coupling model for numerical FFRct-DC calculation was established, and the results of such calculations were compared to those from a more conventional CFD-based geometric multi-scale method. This new model incorporates the influence of the elastic vessel wall on blood flow and provides reliable microvascular resistance boundary conditions for the 3D FSI model. Therefore, it more closely parallels physiological conditions, resulting in improved FFRct accuracy, and enhanced accuracy of myocardial ischemia prediction. The model may be used to non-invasively provide a more reliable recommendation for clinical PCI surgery.

## DATA AVAILABILITY STATEMENT

The original contributions presented in the study are included in the article/Supplementary Material, further inquiries can be directed to the corresponding author.

## ETHICS STATEMENT

The studies involving human participants were reviewed and approved by Medical Ethics Committee of Peking University People's Hospital. The patients/participants provided their written informed consent to participate in this study.

## AUTHOR CONTRIBUTIONS

XX was responsible for modeling, simulation, data analysis and paper preparation. JL (Beijing University of Technology) assisted in the hemodynamic simulation. HS assisted in 0D modeling. KX assisted in data analysis. XW assisted in the reconstruction of the 3D model. JL (Peking University Peoples Hospital) was responsible for providing experimental data. LZ and TD assisted in experimental design. BL was responsible for supervision.

## REFERENCES


Bentzon, J. F., Otsuka, F., Virmani, R., and Falk, E. (2014). Mechanisms of Plaque Formation and Rupture. *Circ. Res.* 114 (12), 1852–1866. doi:10.1161/circresaha.114.302721

Bird, R. B., Armstrong, R. C., and Hassager, O. (1987). *Dynamics of Polymeric Liquids. Fluid Mechanics*. Hoboken: Wiley.

Douglas, P. S., Pontone, G., Hlatky, M. A., Patel, M. R., Norgaard, B. L., Byrne, R. A., et al. (2015). Clinical Outcomes of Fractional Flow reserve by Computed Tomographic Angiography-Guided Diagnostic Strategies vs. Usual Care in Patients with Suspected Coronary Artery Disease: the Prospective Longitudinal Trial of FFRCT: Outcome and Resource Impacts Study. *Eur. Heart J.* 36 (47), 3359–3367. doi:10.1093/eurheartj/ehv444

Esmaily Moghadam, M., Vignon-Clementel, I. E., Figliola, R., and Marsden, A. L. (2013). Modeling of Congenital Hearts Alliance (MOCHA) InvestigatorsA Modular Numerical Method for Implicit 0D/3D Coupling in Cardiovascular Finite Element Simulations. *J. Comput. Phys.* 244, 63–79. doi:10.1016/j.jcp.2012.07.035

Fefferman, C. L. (2006). Existence and Smoothness of the Navier–Stokes Equation. *Millennium Prize Probl.* 57 (67), 22.

Fung, Y. C., and Cowin, S. C. (1993). Biomechanics: Motion, Flow, Stress, and Growth. *J. Appl. Mech.* 60 (2), 567. doi:10.1115/1.2900838

Grunau, G. L., Min, J. K., and Leipsic, J. (2013). Modeling of Fractional Flow reserve Based on Coronary CT Angiography. *Curr. Cardiol. Rep.* 15 (1), 336. doi:10.1007/s11886-012-0336-0

He, F., Hua, L., and Guo, T. (2021). Fluid–structure Interaction Analysis of Hemodynamics in Different Degrees of Stenoses Considering Microcirculation Function. *Adv. Mech. Eng.* 13 (1), 1687814021989012. doi:10.1177/1687814021989012

Huo, Y., Svendsen, M., Choy, J. S., Zhang, Z.-D., and Kassab, G. S. (2012). A Validated Predictive Model of Coronary Fractional Flow reserve. *J. R. Soc. Interf.* 9 (71), 1325–1338. doi:10.1098/rsif.2011.0605

Kakouros, N., Rybicki, F. J., Mitsouras, D., and Miller, J. M. (2013). Coronary Pressure-Derived Fractional Flow reserve in the Assessment of Coronary Artery Stenoses. *Eur. Radiol.* 23 (4), 958–967. doi:10.1007/s00330-012-2670-4

Karimi, A., Navidbakhsh, M., Razaghi, R., and Haghpanahi, M. (2014). A Computational Fluid-Structure Interaction Model for Plaque Vulnerability

Assessment in Atherosclerotic Human Coronary Arteries. *J. Appl. Phys.* 115, 144702. doi:10.1063/1.4870945

Kim, H. J., Vignon-Clementel, I. E., Coogan, J. S., Figueroa, C. A., Jansen, K. E., and Taylor, C. A. (2010). Patient-specific Modeling of Blood Flow and Pressure in Human Coronary Arteries. *Ann. Biomed. Eng.* 38 (10), 3195–3209. doi:10.1007/s10439-010-0083-6

Kock, S. A., Nygaard, J. V., Eldrup, N., Fründ, E.-T., Klærke, A., Paaske, W. P., et al. (2008). Mechanical Stresses in Carotid Plaques Using MRI-Based Fluid-Structure Interaction Models. *J. Biomech.* 41 (8), 1651–1658. doi:10.1016/j.jbiomech.2008.03.019

Koo, B.-K., Erglis, A., Doh, J.-H., Daniels, D. V., Jegere, S., Kim, H.-S., et al. (2011). Diagnosis of Ischemia-Causing Coronary Stenoses by Noninvasive Fractional Flow reserve Computed from Coronary Computed Tomographic Angiograms. *J. Am. Coll. Cardiol.* 58 (19), 1989–1997. doi:10.1016/j.jacc.2011.06.066

Laganà, K., Balossino, R., Migliavacca, F., Pennati, G., Bove, E. L., de Leval, M. R., et al. (2005). Multiscale Modeling of the Cardiovascular System: Application to the Study of Pulmonary and Coronary Perfusions in the Univentricular Circulation. *J. Biomech.* 38 (5), 1129–1141. doi:10.1016/j.jbiomech.2004.05.027

Leach, J. R., Rayz, V. L., Soares, B., Wintermark, M., Mofrad, M. R. K., and Saloner, D. (2010). Carotid Atheroma Rupture Observed *In Vivo* and FSI-Predicted Stress Distribution Based on Pre-rupture Imaging. *Ann. Biomed. Eng.* 38 (8), 2748–2765. doi:10.1007/s10439-010-0004-8

Leung, D. Y., and Leung, M. (2011). Significance and Assessment of Coronary Microvascular Dysfunction. *Heart* 97 (7), 587–595. doi:10.1136/hrt.2009.183327

Murray, C. D. (1926). The Physiological Principle of Minimum Work. *Proc. Natl. Acad. Sci. U.S.A.* 12 (3), 207–214. doi:10.1073/pnas.12.3.207

Ofili, E. O., Kern, M. J., St. Vrain, J. A., Donohue, T. J., Bach, R., Al-Joundi, B., et al. (1995). Differential Characterization of Blood Flow, Velocity, and Vascular Resistance between Proximal and Distal normal Epicardial Human Coronary Arteries: Analysis by Intracoronary Doppler Spectral Flow Velocity. *Am. Heart J.* 130 (1), 37–46. doi:10.1016/0002-8703(95)90233-3

Perktold, K., and Rappitsch, G. (1995). Computer Simulation of Local Blood Flow and Vessel Mechanics in a Compliant Carotid Artery Bifurcation Model. *J. Biomech.* 28 (7), 845–856. doi:10.1016/0021-9290(95)95273-8

Pijls, N. H. J., de Bruyne, B., Peels, K., van der Voort, P. H., Bonnier, H. J. R. M., Bartunek, J., et al. (1996). Measurement of Fractional Flow reserve to Assess the Functional Severity of Coronary-Artery Stenoses. *N. Engl. J. Med.* 334 (26), 1703–1708. doi:10.1056/nejm199606273342604

Pijls, N. H. J., Tanaka, N., and Fearon, W. F. (2013). Functional Assessment of Coronary Stenoses: Can We Live without it? *Eur. Heart J.* 34 (18), 1335–1344. doi:10.1093/eurheartj/ehs436

Sankaran, S., Kim, H. J., Choi, G., and Taylor, C. A. (2016). Uncertainty Quantification in Coronary Blood Flow Simulations: Impact of Geometry, Boundary Conditions and Blood Viscosity. *J. Biomech.* 49 (12), 2540–2547. doi:10.1016/j.jbiomech.2016.01.002

Sun, A., Fan, Y., and Deng, X. (2010). "Numerical Study of Hemodynamics at Coronary Bifurcation with and without Swirling Flow," in 6th World Congress of Biomechanics (WCB 2010). *1–6 August 2010, Singapore* (Berlin/Heidelberg: Springer), 1428–1430. doi:10.1007/978-3-642-14515-5_364

Tang, D., Yang, C., Kobayashi, S., Zheng, J., and Vito, R. P. (2003). Effect of Stenosis Asymmetry on Blood Flow and Artery Compression: a Three-Dimensional Fluid-Structure Interaction Model. *Ann. Biomed. Eng.* 31 (10), 1182–1193. doi:10.1114/1.1615577

Tang, D., Yang, C., Kobayashi, S., Zheng, J., Woodard, P. K., Teng, Z., et al. (2009). 3D MRI-Based Anisotropic FSI Models with Cyclic Bending for Human Coronary Atherosclerotic Plaque Mechanical Analysis. *J. Biomechanical Eng.* 131 (6). doi:10.1115/1.3127253

Taylor, C. A., Fonte, T. A., and Min, J. K. (2013). Computational Fluid Dynamics Applied to Cardiac Computed Tomography for Noninvasive Quantification of Fractional Flow Reserve. *J. Am. Coll. Cardiol.* 61 (22), 2233–2241. doi:10.1016/j.jacc.2012.11.083

Teng, Z., Canton, G., Yuan, C., Ferguson, M., Yang, C., Huang, X., et al. (2010). 3D Critical Plaque wall Stress Is a Better Predictor of Carotid Plaque Rupture Sites Than Flow Shear Stress: an *In Vivo* MRI-Based 3D FSI Study. *J. Biomechanical Eng.* 132 (3). doi:10.1115/1.4001028

van de Hoef, T. P., Meuwissen, M., Escaned, J., Davies, J. E., Siebes, M., Spaan, J. A. E., et al. (2013). Fractional Flow reserve as a Surrogate for Inducible Myocardial Ischaemia. *Nat. Rev. Cardiol.* 10 (8), 439–452. doi:10.1038/nrcardio.2013.86

Wang, J., Paritala, P. K., Mendieta, J. B., Komori, Y., Raffel, O. C., Gu, Y., et al. (2020). Optical Coherence Tomography-Based Patient-specific Coronary Artery Reconstruction and Fluid-Structure Interaction Simulation. *Biomech. Model. Mechanobiol* 19 (1), 7–20. doi:10.1007/s10237-019-01191-9

Wang, W., Tang, D., Mao, B., Li, B., Zhao, X., Liu, J., et al. (2018). A Fast-Fractional Flow reserve Simulation Method in a Patient with Coronary Stenosis Based on Resistance Boundary Conditions. *Cmes* 116 (2), 163–173. doi:10.31614/cmes.2018.04219

Wilson, R. F., Wyche, K., Christensen, B. V., Zimmer, S., and Laxson, D. D. (1990). Effects of Adenosine on Human Coronary Arterial Circulation. *Circulation* 82 (5), 1595–1606. doi:10.1161/01.cir.82.5.1595

Wischgoll, T., Choy, J. S., Ritman, E. L., and Kassab, G. S. (2008). Validation of Image-Based Method for Extraction of Coronary Morphometry. *Ann. Biomed. Eng.* 36 (3), 356–368. doi:10.1007/s10439-008-9443-x

Wu, X., von Birgelen, C., Zhang, S., Ding, D., Huang, J., and Tu, S. (2019). Simultaneous Evaluation of Plaque Stability and Ischemic Potential of Coronary Lesions in a Fluid-Structure Interaction Analysis. *Int. J. Cardiovasc. Imaging* 35 (9), 1563–1572. doi:10.1007/s10554-019-01611-y

Zarins, C. K., Taylor, C. A., and Min, J. K. (2013). Computed Fractional Flow Reserve (FFTCT) Derived from Coronary CT Angiography. *J. Cardiovasc. Trans. Res.* 6 (5), 708–714. doi:10.1007/s12265-013-9498-4

Zhang, J.-M., Zhong, L., Luo, T., Lomarda, A. M., Huo, Y., Yap, J., et al. (2016). Simplified Models of Non-invasive Fractional Flow reserve Based on CT Images. *PLoS One* 11 (5), e0153070. doi:10.1371/journal.pone.0153070

Zhao, X., Liu, Y., Ding, J., Ren, X., Bai, F., Zhang, M., et al. (2015). Hemodynamic Effects of the Anastomoses in the Modified Blalock-Taussig Shunt: a Numerical Study Using a 0D/3D Coupling Method. *J. Mech. Med. Biol.* 15 (01), 1550017. doi:10.1142/s0219519415500177

**Conflict of Interest:** The authors declare that the research was conducted in the absence of any commercial or financial relationships that could be construed as a potential conflict of interest.

frontiers | Frontiers in Physiology

ORIGINAL RESEARCH
published: 10 May 2022
doi: 10.3389/fphys.2022.912447

# Predicting Coronary Stenosis Progression Using Plaque Fatigue From IVUS-Based Thin-Slice Models: A Machine Learning Random Forest Approach

*Xiaoya Guo[1]*, Akiko Maehara[2], Mingming Yang[3], Liang Wang[4], Jie Zheng[5], Habib Samady[6], Gary S. Mintz[2], Don P. Giddens[6,7] and Dalin Tang[4,8]**

[1]School of Science, Nanjing University of Posts and Telecommunications, Nanjing, China, [2]The Cardiovascular Research Foundation, Columbia University, New York, NY, United States, [3]Department of Cardiology, Zhongda Hospital, Southeast University, Nanjing, China, [4]School of Biological Science and Medical Engineering, Southeast University, Nanjing, China, [5]Mallinckrodt Institute of Radiology, Washington University, St. Louis, MO, United States, [6]Department of Medicine, Emory University School of Medicine, Atlanta, GA, United States, [7]The Wallace H. Coulter Department of Biomedical Engineering, Georgia Institute of Technology, Atlanta, GA, United States, [8]Mathematical Sciences Department, Worcester Polytechnic Institute, Worcester, MA, United States

OPEN ACCESS

**Edited by:**
Yunlong Huo,
Shanghai Jiao Tong University, China

**Reviewed by:**
Peng Wu,
Soochow University, China
Lingfeng Chen,
Taiyuan University of Technology, China

***Correspondence:**
Xiaoya Guo
guoxiaoya1990@163.com
Dalin Tang
dtang@wpi.edu

**Specialty section:**
This article was submitted to Computational Physiology and Medicine, a section of the journal Frontiers in Physiology

**Received:** 04 April 2022
**Accepted:** 22 April 2022
**Published:** 10 May 2022

**Citation:**
Guo X, Maehara A, Yang M, Wang L, Zheng J, Samady H, Mintz GS, Giddens DP and Tang D (2022) Predicting Coronary Stenosis Progression Using Plaque Fatigue From IVUS-Based Thin-Slice Models: A Machine Learning Random Forest Approach. Front. Physiol. 13:912447. doi: 10.3389/fphys.2022.912447

**Introduction:** Coronary stenosis due to atherosclerosis restricts blood flow. Stenosis progression would lead to increased clinical risk such as heart attack. Although many risk factors were found to contribute to atherosclerosis progression, factors associated with fatigue is underemphasized. Our goal is to investigate the relationship between fatigue and stenosis progression based on *in vivo* intravascular ultrasound (IVUS) images and finite element models.

**Methods:** Baseline and follow-up *in vivo* IVUS and angiography data were acquired from seven patients using Institutional Review Board approved protocols with informed consent obtained. Three hundred and five paired slices at baseline and follow-up were matched and used for plaque modeling and analysis. IVUS-based thin-slice models were constructed to obtain the coronary biomechanics and stress/strain amplitudes (stress/strain variations in one cardiac cycle) were used as the measurement of fatigue. The change of lumen area (DLA) from baseline to follow-up were calculated to measure stenosis progression. Nineteen morphological and biomechanical factors were extracted from 305 slices at baseline. Correlation analyses of these factors with DLA were performed. Random forest (RF) method was used to fit morphological and biomechanical factors at baseline to predict stenosis progression during follow-up.

**Results:** Significant correlations were found between stenosis progression and maximum stress amplitude, average stress amplitude and average strain amplitude ($p < 0.05$). After factors selection implemented by random forest (RF) method, eight morphological and biomechanical factors were selected for classification prediction of stenosis progression. Using eight factors including fatigue, the overall classification accuracy, sensitivity and

specificity of stenosis progression prediction with RF method were 83.61%, 86.25% and 80.69%, respectively.

**Conclusion:** Fatigue correlated positively with stenosis progression. Factors associated with fatigue could contribute to better prediction for atherosclerosis progression.

**Keywords: coronary atherosclerosis, stenosis prediction, IVUS, fatigue, random forest, patient-specific models**

## INTRODUCTION

Atherosclerotic plaque rupture is regarded as the clinical end-point event in the process of atherosclerosis progression. Stenosis is a common abnormal condition in arteries mainly due to atherosclerosis. Coronary gradual narrowing restricts blood flow, which causes ischemia and may induce heart attack. From a biomechanical perspective, vessel tissue fatigue is a chronic failure process induced by repetitive loading and could impact plaque development under the periodical arterial pressure (Bank et al., 2000; Ku & McCord, 1993; Stehbens, 1997; 2002). Plaque rupture can be considered as the result of accumulated fatigue damage (Versluis et al., 2006). Li et al. (2007) and his coworkers studied the fatigue crack with constructed two-dimensional model using *in vivo* magnetic resonance imaging (MRI) data (Pei et al., 2014). Huang et al. (2013) employed *in vivo* MRI-based 2D carotid model to study the development of crack and fatigue life. Their results showed that plaque without fibrous cap (FC) rupture or ulceration had a longer fatigue life compared with those with FC rupture or ulceration ($p = 0.03$).

Paritala et al. (2020) characterized the fatigue behavior of carotid arteries using uniaxial tensile test and provided an understanding of stress-relaxation and cyclic behavior. Bank et al. (2000) showed that fatigue is caused from cyclic stress by *ex-vivo* experiments, and found that fatigue is proportional to stress amplitude and mean stress. Gao et al. (2009) also pointed out that relative stress variation during a cycle in the fibrous cap is a potential indicator for plaque fatigue process by fluid-structure interaction (FSI) models of carotid arteries. The mainstream opinion is that stresses derived from periodical pressure is alternating stress, which is the main cause of fatigue.

Many researchers tried to find risk factors related to plaque progression. Using serial coronary computed tomography angiography, Won et al. used change of coronary plaque volume to measure plaque progression and explored the effects of the triglyceride glucose (TyG) index and body mass index (BMI) on plaque progression, respectively (Won et al., 2019; Won et al., 2020). Their studies have shown that BMI were not associated with plaque progression and TyG index had a positive and significant association with plaque progression (odd ratio = 1.409, confidence interval = [1.062–1.869], $p = 0.017$). Morphological factors, such as plaque composition and size, lumen size, fibrous cap thickness and others, may play significant roles in atherosclerosis progression. Ever since computational fluid dynamic (CFD) models have been used as a common tool to explore the mechanism of atherosclerosis progression and rupture, endothelial shear stress was found to be an important biomechanical factor for atherosclerosis progression (Vergallo et al., 2014). Corban et al. (2014) indicated that combining plaque burden, wall shear stress (WSS) and plaque phenotype was helpful to improve prediction accuracy of plaque progression. However, a study based on carotid atherosclerotic mouse model showed that WSS decreased strikingly during atherosclerotic progression, but the correlation between WSS and plaque area was weak and no statistical significance was found ($p > 0.05$) (Xing et al., 2018).

Besides, plaque fatigue would be a noteworthy factor in plaque progression. Stehbens (1997) hypothesized that atherosclerosis was the response to hemodynamically induced repetitive stresses due to the pulse pressure. Thondapu et al. (2017) pointed out that axial stress arises from longitudinal stretching of vessels exposed to cyclical blood flow and cardiac motion, and circumferential stress arises from hydrostatic pressure exerting outward radial force on vessels. The periodic pressure caused from pulsatile blood flow generates mechanical stresses. These mechanical factors contribute to plaque fatigue in an integrated manner and play a vital role in plaque progression (Wang L. et al, 2019; Guo et al., 2021).

In this paper, *in vivo* Virtual Histology intravascular ultrasound (VH-IVUS) data at baseline and follow-up were acquired from seven patients and used to construct thin-slice models for stress/strain calculations. Plaque fatigue was measured by stress/strain amplitudes in one cardiac cycle at baseline. The change of lumen area between baseline and follow-up was used as the measurement for atherosclerosis stenosis progression. Analyses for correlations between plaque fatigue and morphological characters and correlations predictors (morphological and biomechanical factors) and stenosis progression were performed. Machine learning approaches including random forest was employed to determine the prediction accuracy of plaque fatigue for predicting stenosis progression.

## METHODS

### Virtual Histology-Intravascular Ultrasound Data Acquisition and Processing

Baseline and follow-up *in vivo* intravascular ultrasound (IVUS) and angiography data were acquired from seven participants (gender: 5M and 2F, average age: 59.2) at Cardiovascular Research Foundation (CRF) using protocol approved by the Institutional Review Board and informed consents were obtained from these patients. Patients were selected from a CRF data set where patients were with stable angina pectoris undergoing percutaneous coronary intervention (PCI). Patients with acute coronary syndrome, severe

calcified lesion, chronic total occlusion or chronic kidney disease (Cr > 1.5 mg/dl) were excluded. Baseline data is the data set acquired at the first screening, which included IVUS, OCT, angiography, blood pressure, and general patient demographic information. These spans of the follow-up time for seven participants were 6–12 months (median 9 months). When electrocardiogram (ECG) signal was connected, VH-IVUS images were acquired automatically using Volcano S5 Imaging System (Volcano Crop., Rancho Cordova, CA, United States). Four tissue types were marked in color on VH-IVUS image: lipid-rich necrotic core in red, calcium in white, fibrous tissue in dark green and fibro-fatty tissue in light green. Segmentation of VH-IVUS images was performed by an in-house software package programmed in MATLAB (The MathWorks, Inc., Natick, MA, United States). The target vessel segment was selected based on angiography data. The registration of VH-IVUS images at baseline and follow-up from same vessel segment was executed using vessel branches which is the main landmark for location of vessel segment. These 305 paired VH-IVUS slices were matched and used for plaque modeling. Images generated at vessel bifurcations were excluded from this study.

## The Thin-Slice Model With Mooney-Rivlin Material Model

A 3D thin-slice modeling approach was adopted in this paper to obtain plaque stress/strain values. Thin slice models were selected since the model construction requires much less time (a few minutes per model) and is more suitable for potential clinical implementations (Wang L. et al, 2019). For each slice, the 3D thin-slice model was constructed by adding a thin slice thickness (0.5 mm, which is the spatial distance between two adjacent images generated during catheter pullback) to the 2D slice. For plaque models based on *in vivo* data, axial stretch is a non-negligible factor when calculating the stress/strain distribution in coronary (Thondapu et al., 2017). Axial shrinkage was set to be 5% in our models because atherosclerotic vessels were stiffer than healthy vessels. *In-vivo* VH-IVUS image was reconstructed with radiofrequency data captured at the peak of R-wave in ECG signal (Garcìa-Garcìa et al., 2011). The peak of the R-wave is commonly used to represent the end-diastole phase, so the acquired VH-IVUS data can be regarded as being generated at minimum arterial pressure. Hence circumferential shrinkage was applied in our models in order to make model shape under minimum pressure consistent with VH-IVUS. Pulsating arm pressure conditions were prescribed at lumen surface in thin-slice models. The construction of thin-slice models can be found in our previous publication (Guo et al., 2017). Lipid/calcification and other tissues were assumed to be isotropic and anisotropic, respectively. The strain energy density function of modified Mooney-Rivlin model for isotropic and anisotropic were **Eqs 1**, **2**, respectively (Holzapfel et al., 2000):

$$W_{iso} = c_1(I_1 - 3) + c_2(I_2 - 3) + D_1\{\exp[D_2(I_1 - 3)] - 1\} \quad (1)$$

$$W_{aniso} = W_{iso} + \frac{K_1}{K_2}\{\exp[K_2(I_4 - 1)^2 - 1]\} \quad (2)$$

Where $I_1 = \sum C_{ij}$, $I_2 = \frac{1}{2}(I_1^2 - C_{ij}C_{ij})$, $I_1$ and $I_2$ are the first and second invariants of right Cauchy-Green deformation tensor $\boldsymbol{C} = [C_{ij}] = \mathbf{X}^T\mathbf{X}$, $\mathbf{X} = [X_{ij}] = [\partial x_i/\partial a_j]$, $(x_i)$ is current position, $(a_i)$ is original position, $I_4 = C_{ij}(\boldsymbol{n}_c)_i(\boldsymbol{n}_c)_j$, $\boldsymbol{n}_c$ is the unit vector in the circumferential direction of the vessel, $c_1, c_2, D_1, D_2$, $K_1$ and $K_2$ are material parameters.

The material parameters of lipid, calcification and other vessel tissues from existing literature were used (Guo et al., 2017): Lipid: $c_1 = 0.5$ kPa, $c_2 = 0$ kPa, $D_1 = 0.5$ kPa, $D_2 = 1.5$. Calcification: $c_1 = 92$ kPa, $c_2 = 0$ kPa, $D_1 = 36$ kPa and $D_2 = 2$. Other vessel tissues: $c_1 = -278.7$ kPa, $c_2 = 24.35$ kPa, $D_1 = 133.7$ kPa, $D_2 = 2$, $K_1 = 7.19$ kPa, $K_2 = 23.5$.

All models were solved by a finite element software ADINA (Adina R & D, Watertown, MA, United States) following our established procedures (Guo et al., 2017). **Figure 1** shows distributions of stress and strain under maximum and minimum pressure conditions at baseline and follow-up. More details can be found from Guo et al. (2017).

## Measurements of Plaque Fatigue

The stress and strain of each slice were extracted from the solution of the thin-slice model. The stress and strain mentioned below refer to maximum principal stress and maximum principal strain. The values of stress and strain during cardiac cycle were extracted for each slice ($2 \times 305 = 610$ slices in total).

Since plaque rupture usually occurs on luminal wall, the stress and strain at the location of superficial vascular wall was used in the following analysis. The stress amplitude and strain amplitude were defined as the stress variation and strain variation during one cardiac cycle, respectively. The stress and strain amplitudes were regarded as measurements for plaque fatigue in our study. The amplitude of average stress/strain on luminal wall and amplitude of maximum stress/strain on luminal wall during one cardiac cycle were all calculated to access plaque fatigue. These formulas are as follows:

$$\text{Maximum stress amplitude} = \text{maximum stress}_{\text{at max pressure}} - \text{maximum stress}_{\text{at min pressure}} \quad (3)$$

$$\text{Maximum strain amplitude} = \text{maximum strain}_{\text{at max pressure}} - \text{maximum strain}_{\text{at min pressure}} \quad (4)$$

$$\text{Average stress amplitude} = \text{average stress}_{\text{at max pressure}} - \text{average stress}_{\text{at min pressure}} \quad (5)$$

$$\text{Average strain amplitude} = \text{average strain}_{\text{at max pressure}} - \text{average strain}_{\text{at min pressure}} \quad (6)$$

## Measurements of Stenosis Progression

The cross-section area of lumen is an important index of vessels stenosis. The change of lumen area from baseline to follow-up was used as the measurement for stenosis progression (reduction in lumen area), which definition is as follows:

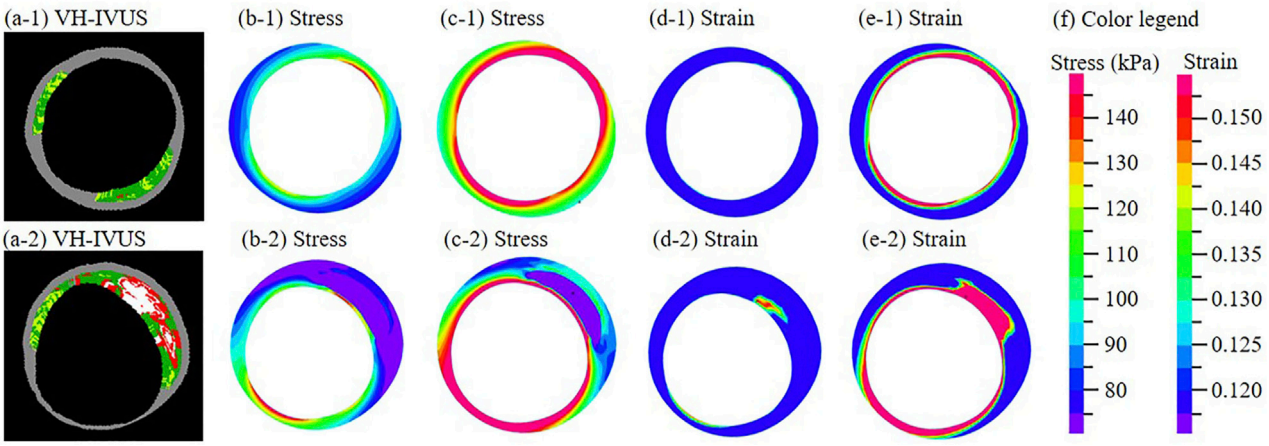


**FIGURE 1 | (a-1)–(a-2)** One paired VH-IVUS images from the same location at baseline **(a-1)** and follow-up **(a-2)**. **(b-1)–(b-2)** Stress distribution of the thin-slice model at minimum pressure. **(c-1)–(c-2)** Stress distribution at maximum pressure. **(d-1)–(d-2)** Strain distribution at minimum pressure. **(e-1)–(e-2)** Strain distribution at maximum pressure. **(f)** Color legend. For sub-figures **(a-□)–(e-□)**, □ = 1 is for the baseline slice; □ = 2 is for the follow-up slice.

$$\text{Delta lumen area (DLA)} = \text{Lumen area at baseline} - \text{lumen area at follow} - \text{up} \quad (7)$$

Positive DLA value means luminal narrowing from baseline to follow-up. All 305 slices at baseline were divided in two classes (label 0 and label 1) according to the non-positive or positive sign of DLA value. Label 0 class represents the set of slices with non-progressive luminal stenosis while label 1 class represents the set of slices with progressive luminal stenosis. Classification prediction of stenosis progression was performed by machine learning methods.

## Morphological and Biomechanical Factors Used as Predictors

Values of twelve biomechanical factors were extracted at baseline from thin-slice models. Those factors included maximum and average stress/strain amplitudes, maximum and average stress/strain at minimum and maximum pressure etc. and were prepared to be used as candidate predictors for stenosis progression. Seven morphological factors including plaque burden (PB) at minimum pressure, lumen/wall area at minimum and maximum pressure, and changes of lumen and wall from minimum pressure to maximum pressure [called lumen area amplitude (9) and wall area amplitude (10) for briefly] were also used as candidate factors.

$$\text{PB} = (\text{plaque area}/\text{cross} - \text{sectional area of external elastic membrane})^{*}100\% \quad (8)$$

$$\text{lumen area amplitude} = \text{lumen area}_{\text{at max pressure}} - \text{lumen area}_{\text{at min pressure}} \quad (9)$$

$$\text{wall area amplitude} = \text{wall area}_{\text{at max pressure}} - \text{wall area}_{\text{at min pressure}} \quad (10)$$

## Correlation Analysis

Linear Mixed-Effects (LME) model was used to study the correlation between morphological factors, biomechanical factors and DLA. The correlation analysis of DLA and maximum stress amplitude was taken as an example to explain how the LME model was used in this study below.

The LME model was defined as

$$y_{ij} = \beta_0 + \beta_1 x_{ij} + b_j + \varepsilon_{ij} \quad (11)$$

where $y_{ij}$ is the DLA value on the $i$ th slice of $j$ th patient, $x_{ij}$ is the corresponding value of maximum stress amplitude. $\beta_0$ and $\beta_1$ are the fixed effects of DLA and maximum stress amplitude at baseline, respectively. $\varepsilon_{ij}$ is the random error terms which is assumed to follow a joint Gaussian distribution with mean 0.

The dependence-adjusted correlation coefficient r is given by

$$r = \hat{\beta}_1 \sqrt{\frac{\widehat{var}(x)}{\widehat{var}(y)}} \quad (12)$$

where $\hat{\beta}_1$ is the estimated slope coefficient by fitting maximum stress amplitude to DLA with the LME model, $\widehat{var}(x)$ and $\widehat{var}(y)$ are the sample variances.

The correlation analyses between plaque fatigue and morphological characters, predictors and stenosis progression were performed by R software (R 3.1.3, The R Foundation for Statistical Computing). The dependence-adjusted correlation coefficient was adopted to measure the dependence of variables and statistical significant was assumed if $p < 0.05$.

## Predictor Selection and Classification Prediction Using Random Forest

After 100 times testing using our data, our results indicated that the performance of random forest (RF) was better than that from

the other machine learning methods (least square support vector machine (SVM), discriminant analysis and generalized linear mixed model). Therefore, RF was used as our prediction method in this study. The RF method uses multiple trees to train and predict the samples and uses the voting mechanism of multiple decision trees to resist the overfitting of decision trees. Training data consists of resampling n times with replacement from dataset (size equal to n). Some samples would not appear in training data because of sampling with replacement, which is called out-of-bag (OOB) data. OOB data is used as test set in our RF method.

Nineteen factors extracted from 305 slices (their values stored in a 305 × 19 matrix) were used as the input dataset for RF. The number of factors tried for splitting (Mtry) and the number of trees grown (Ntree) in the RF were two input parameters. Two parameters (Ntree and Mtry) of RF were optimized to guarantee high accuracy of classification prediction. The number of variables to be selected and tested for the best split when growing the trees (Mtry) was obtained by iteration based on OOB error. After Mtry value obtained, the number of decision trees to be generated (Ntree) would be set to minimum value that satisfies the error in RF model minimum and stable.

Dimensionality reduction of candidate factors were performed using "varSelRF" package. The mean decrease Gini index of factors were also calculated to ensure availability of factors selection. Gini index was defined as

$$\text{Gini}(t) = 1 - \sum_{i=0}^{1} P(i)^2 \quad (13)$$

where $P(i)$ is the proportion of "lable $i$" class in the dataset at the current node t. Gini impurity at node t was denoted as $I(t)$, then Mean Decrease Gini index was defined as

$$\text{Mean Decrease Gini index} = \sum_{Ntree} \sum_{t} (I(t) - \text{Gini}(t)) \quad (14)$$

The classification prediction was implemented with "randomForest" package in R. The output from RF was a 305-dimensional binary vector. Cross validation or a separate accuracy assessment dataset is not necessary for RF algorithm, because the OOB error provides an unbiased estimate of error (Liaw & Wiener, 2002; Lawrence et al., 2006; Prinzie & Van den Poel, 2008). Therefore, the OOB error was adopted to estimate the misclassification error. Then confusion matrix was constructed to compare the true class with the class predicted by RF classifier and to calculate the overall accuracy. Sensitivity, specificity, positive and negative prediction values were also calculated as following.

$$\text{Overall accuracy} = (TP + TN)/(TP + FN + FP + TN) \quad (15)$$

$$\text{Sensitivity} = TP/(TP + FN) \quad (16)$$

$$\text{Specificity} = TN/(FP + TN) \quad (17)$$

$$\text{Positive prediction value} = TP/(TP + FP) \quad (18)$$

$$\text{Negative prediction value} = TN/(FN + TN) \quad (19)$$

where TP is the number of true positive, FN is the number of false negative, FP is the number of false positive and TN is the number of true negative.

# RESULTS

## Fatigue Correlated Positively With Lumen Area Amplitude and Negatively With Plaque Burden

The maximum and average stress/strain amplitude were regarded as the measurement of fatigue. In one cardiac cycle, there were a strong positive correlation between lumen area amplitude and fatigue and a negative correlation between PB and fatigue (**Table 1**). Especially, the correlation between average strain amplitude and lumen area amplitude was 0.3247 ($p < 0.0001$), and the correlation between average stress amplitude was −0.2808 ($p < 0.0001$).

## Fatigue Correlated Positively With Stenosis Progression

Factors that had a significant correlation with DLA were shown in **Table 2**. There were significant correlations between stenosis progression and maximum stress amplitude ($r = 0.1313$, $p < 0.05$), average stress amplitude ($r = 0.3357$, $p < 0.05$) and average strain amplitude ($r = 0.5376$, $p < 0.05$). In addition, the correlation between PB and DLA was best ($r = -0.5729$, $p < 0.05$).

## RF Method Input Parameters

Before performing factors selection, it was essential to evaluate the effect of the two RF parameters (Mtry and Ntree) on the misclassification error. **Figure 2** shows that Mtry = 4 was proved to be the best choice in terms of the OOB error rate (17.8%). When examining the Ntree parameter, results showed that OOB error rates were stabilized after 3,000 trees (**Figure 3**). Therefore, two parameters were set as Mtry = 4 and Ntree = 3,000 for all further analyses.

## Factors Selection

Predictor values obtained from all 305 slices were used as input variables into the RF algorithm using two determined parameters--Mtry and Ntree. Eight factors were selected by "varSelRF" package including average stress amplitude, wall area at minimum pressure and maximum pressure, lumen area at minimum pressure and maximum pressure, wall area amplitude, lumen area amplitude and PB. The mean decrease in Gini index as calculated by 19 factors was then used to rank the factors and check factors selection. Eight Factors selected from "varSelRF" package and ranking of mean decrease in Gini index are consistent. **Tables 3**, **4** shows mean decrease in Gini index of eight factors as calculated by RF. Results showed that the baseline PB had the highest mean decrease in Gini index. In addition, average stress amplitude was the only one mechanical factors in top eight factors.

**TABLE 1 |** The correlation of morphological and biomechanical factors at baseline.

| Morphological factors | Biomechanical factors | Correlation coefficient | *p* value |
|---|---|---|---|
| Lumen area amplitude | Maximum stress amplitude | 0.0708 | $9.7 \times 10^{-6}$ |
| | Average stress amplitude | 0.2103 | $2.3 \times 10^{-26}$ |
| | Maximum strain amplitude | 0.1409 | $9.6 \times 10^{-61}$ |
| | Average strain amplitude | 0.3247 | $1.3 \times 10^{-66}$ |
| PB | Maximum stress amplitude | −0.0992 | $3.6 \times 10^{-4}$ |
| | Average stress amplitude | −0.2808 | $2.0 \times 10^{-24}$ |
| | Maximum strain amplitude | −0.0888 | 0.007 |
| | Average strain amplitude | −0.1786 | $9.7 \times 10^{-12}$ |

**TABLE 2 |** The correlation of baseline factors and stenosis progression.

| Stenosis progression | Factors | Correlation coefficient | *p* value |
|---|---|---|---|
| DLA | Maximum stress amplitude | 0.1313 | 0.0499 |
| | Average stress amplitude | 0.3357 | 0.0019 |
| | Average strain amplitude | 0.5376 | 0.0235 |
| | Average stress at maximum pressure | 0.3813 | 0.0199 |
| | Average strain at maximum pressure | 0.5613 | 0.0208 |
| | PB | −0.5729 | $4.6 \times 10^{-6}$ |

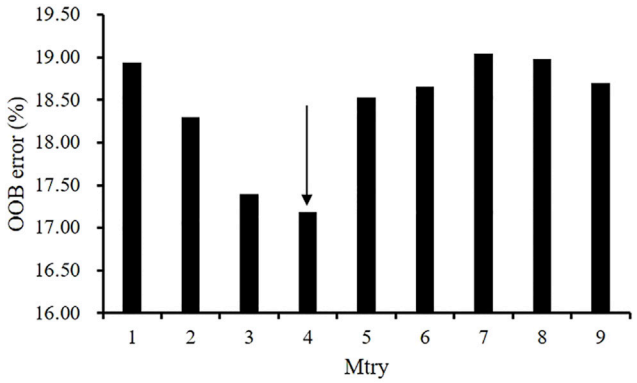


**FIGURE 2 |** The effect of the number of variables tried at each split (Mtry) on the performance of RF using the OOB estimate of error (%).

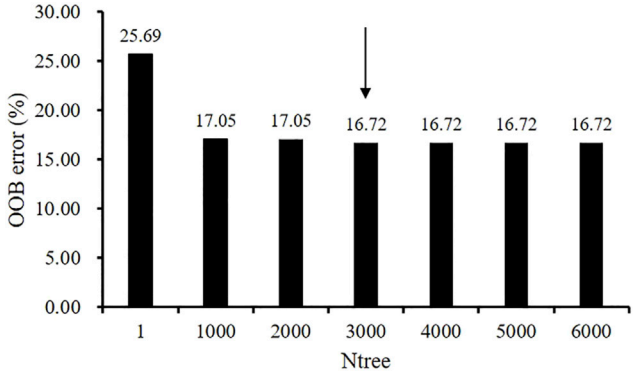


**FIGURE 3 |** The effect of the number of trees (Ntree) parameter on the performance of random forest RF using the OOB estimate of error (%).

**TABLE 3 |** The value of mean decrease in Gini index for top eight factors.

| Factors | Mean decrease in gini index |
|---|---|
| PB | 15.03 |
| Lumen area amplitude | 13.38 |
| Lumen area at maximum pressure | 12.07 |
| Lumen area at minimum pressure | 11.88 |
| Wall area at minimum pressure | 11.67 |
| Wall area at maximum pressure | 11.43 |
| Wall area amplitude | 10.45 |
| Average stress amplitude | 8.81 |

**TABLE 4 |** The confusion matrix showing the overall classification accuracy for two classes.

| | | Prediction | |
|---|---|---|---|
| | | Non- narrowing | Narrowing |
| Ground truth | Non- narrowing | 138 | 22 |
| | Narrowing | 28 | 117 |
| Overall classification accuracy = 83.61% | | | |

## Classification and Accuracy Assessment

The best predictor was the combination of PB, lumen area amplitude, lumen areas at maximum and minimum pressure, wall areas at maximum and minimum pressure, wall area amplitude and average stress amplitude. Using the combination of eight factors as the predictor and RF as the prediction method, the overall classification accuracy is 83.61%. The sensitivity (i.e., recall) is 86.25%, and specificity is 80.69%. Precision (i.e., positive prediction value) and negative prediction value is 83.13% and 84.17%, respectively. The overall

OOB error rate for all the classes was 16.39% using the best predictor. For discriminating two classifications (progressive and non-progressive luminal stenosis), the confusion matrix shows that the label 0 class (non-progressive) has the lower error rate (13.75%), while the label 1 class (progressive) has the higher error rate (19.31%).

# DISCUSSION

## Plaque Fatigue Factors Related to Plaque Progression

Even though there have been a number of publications using morphological, biomechanical and biochemical factors for atherosclerosis progression prediction in existing research, seeking key factors contributing to atherosclerosis progression is still a challenging problem (Saam et al., 2007; Wang et al., 2019; Won et al., 2019; Won et al., 2020). Wang et al. (2015) conducted IVUS-based fluid-structure interaction (FSI) modeling analysis to study the correlation between the biomechanical factors and morphological factors. Their results indicated that critical plaque wall stress (CPWS) correlated with minimum cap thickness and lipid percentage with $r = -0.6414$ and $r = 0.2445$ respectively ($p < 0.0001$). Although the correlation of CPWS and minimum cap thickness was strong, it remains to be confirmed by more studies based on high-resolution images since low resolution of IVUS image (~150 μm) cannot capture the thin fibrous cap (<65 μm).

The studies mentioned above concentrated on plaque morphology and biomechanical factors extracted from one static moment, whereas amplitudes of morphology and biomechanics during one dynamic cardiac has gone unheeded. Vascular tissue fatigue occurs under cyclic stress and is related to atherosclerosis progression closely. The study of Bank et al. (2000) showed that fatigue is proportional to stress amplitude and mean stress by *ex-vivo* experiments. Our results indicated that average strain amplitude had a significant positive correlation with lumen area amplitude ($r = 0.3247$, $p < 0.05$) and average stress amplitude had a significant negative correlation with PB ($r = -0.2808$, $p < 0.05$). Our study also showed that fatigue has a positive correlation to stenosis progression according **Table 2**. **Tables 2**, **3** also show that the amplitudes of lumen area, wall area and average stress are significant factors for atherosclerosis progression, which improved our understanding for the relationship between plaque fatigue and stenosis progression.

## Plaque Progression Prediction Using Plaque Fatigue

Atherosclerosis progression could be measured by different plaque morphological parameters such as lumen area change, plaque burden change, plaque area change, plaque volume change, lipid percentage change, etc. (Guo et al., 2021; Saam et al., 2007; Wang Q. et al, 2019; Won et al., 2020; Won et al., 2019). Wang et al. used IVUS-based FSI models and found that the combination of plaque wall stress and wall shear stress is the optimal predictor for changes of plaque burden from baseline to follow-up with a prediction accuracy of 68.1% (Wang L. et al, 2019). Corban et al. (2014) found that combination of plaque burden, wall shear stress, and plaque phenotype has incremental value for prediction of coronary atherosclerotic plaque progression. Bourantas et al. (2020) defined atherosclerotic progression as a significant reduction in lumen (>7.5%) and increase in plaque burden (>8.8%) at follow-up, and gave the atherosclerotic progression prediction using multivariate linear regression models. Their study showed that area under the curve (AUC) using IVUS-based morphological predictors is 0.824 and the AUC is raised to 0.847 after adding WSS into predictor. A research group from Turkey employed different artificial neural network models to predict coronary stenosis, and their results were more than 71% for sensitivity, 76% for specificity and 81% for accuracy (Çolak et al., 2008). A large number of traditional statistical methods and machine learning methods have been used in atherosclerosis progression with different measurements, for instance, generalized linear mixed model, RF, SVM, neural network, etc. In fact, no matter which method we choose, we are faced with the problem of predictor selection, parameter tuning, and so on. In this study, we used RF algorithm with optimal performance on our dataset as the prediction method, employed change of lumen area as the measurement of stenosis progression, added plaque fatigue as a class of predictor, the evaluation of the effect of RF parameters is shown in **Figures 2**, **3**. Overall classification accuracy was 83.61% in this study. Our previous study showed that AUC is 0.963 for the prediction of lipid percentage progression using multi-factors (plaque fatigue was not included) and SVM, but the specificity was 0.777 (sensitivity = 0.974) (Guo et al., 2021). In this study, the values of sensitivity (86.25%) and specificity (80.69%) are both above 80% and the difference between sensitivity and specificity is only 5.56%.

## Measurements of Plaque Fatigue From Medical Images and Models

Although plaque fatigue has been mentioned as one of the mechanism that might play an important role in plaque progression, the plaque fatigue information, such as ultimate tensile stress amplitude, critical mechanical condition and plaque fatigue life, have never been measured *in vivo* from existing technology with the real time information (Huang et al., 2013; Riou et al., 2014). Fatigue life is often divided into three periods: crack nucleation, crack propagation and final rupture, but the first two periods are silent in clinical symptoms and cannot be detected by medical image, and only rupture could be captured by medical imaging. Most researchers studied the plaque fatigue (especially dynamics of rupture) using crack propagation models (Versluis et al., 2006; Li et al., 2007; Huang et al., 2013; Pei et al., 2014). Our study used stress/strain amplitudes as the measurements of plaque fatigue in IVUS images without rupture. Compared with IVUS, intravascular optical coherence tomography (OCT) with high resolution (~10 μm) is sufficient to obtain more accurate measurement of morphology of superficial coronary, but OCT has only 1–2 mm penetration depth not enough to detecting whole vessel wall (Jang et al., 2002). However, wall area calculated by the contour of outer vessel wall was an important morphological factor for prediction of stenosis progression in this

study (**Table 3**). In the future, medical imaging technology with high resolution and strong penetration may detect morphological features accurately and then acquire accurate fatigue information from models that are important to predict stenosis progression.

### Limitations

Our study has the following major limitations: 1) Sample size. Only 305 slices from seven patients were used in our studies since it is challenging to obtain a large number of follow-up data with high quality IVUS and angiography images. Large-scale patient studies are needed to further validate our findings. 2) Each thin-slice model is essentially only one slice and could not include vessel curvature. This is a model limitation. 3) Modeling limitation. Thin-slice models used in this study only provided structure stress and strain. They could not provide hemodynamic information (such as flow shear stress) which is a limitation. Thin-slice models need much less man power to construct and could be more practical for potential clinical implementations. While stress/strain values from thin-slice models have modest errors (5–12% depending on the samples) compared to the full 3D FSI models, Wang et al. showed that correlation relationship from thin-slice models had an impressive 90.5% agreement rate compared to the results from 3D FSI models (Wang Q. et al, 2019). Clearly, it remains to be true that full 3D FSI models could be a better choice for more accurate stress/strain and wall shear stress calculations if model construction could be automated to reduce labor cost.

## CONCLUSION

Our preliminary results indicated that fatigue has a positive correlation with stenosis progression. Using eight morphological and biomechanical factors including fatigue, the overall classification accuracy, sensitivity and specificity of stenosis progression prediction with RF method were 83.61%, 86.25% and 80.69%, respectively. Factors associated with fatigue could contribute to better prediction for atherosclerosis progression.

## DATA AVAILABILITY STATEMENT

The original contributions presented in the study are included in the article/Supplementary Material, further inquiries can be directed to the corresponding authors.

## ETHICS STATEMENT

Written informed consent was obtained from the individual(s) for the publication of any potentially identifiable images or data included in this article.

## AUTHOR CONTRIBUTIONS

XG wrote the manuscript, performed data processing, simulation, prediction and analysis; DG and DT designed this study; GM and AM collected data; MY and JZ offered guidance in image processing; HS, LW and DT provided critical review.

## FUNDING

This research was supported in part by National Sciences Foundation of China grants 11972117 and 11672001, the Foundation of Jiangsu Provincial Double-Innovation Doctor Program grant CZ007SC20006 and NUPTSF grant NY219163.

## REFERENCES

Bank, A. J., Versluis, A., Dodge, S. M., and Douglas, W. H. (2000). Atherosclerotic Plaque Rupture: a Fatigue Process? *Med. Hypotheses* 55 (6), 480–484. doi:10.1054/mehy.2000.1096

Bourantas, C. V., Räber, L., Sakellarios, A., Ueki, Y., Zanchin, T., Koskinas, K. C., et al. (2020). Utility of Multimodality Intravascular Imaging and the Local Hemodynamic Forces to Predict Atherosclerotic Disease Progression. *JACC Cardiovasc. Imaging* 13 (4), 1021–1032. doi:10.1016/j.jcmg.2019.02.026

Çolak, M. C., Çolak, C., Koçatürk, H., Sağıroğlu, Ş., and Barutçu, İ. (2008). Predicting Coronary Artery Disease Using Different Artificial Neural Network Models. *Anatolian Journal of Cardiology* 8 (4), 249–254.

Corban, M. T., Eshtehardi, P., Suo, J., McDaniel, M. C., Timmins, L. H., Rassoul-Arzrumly, E., et al. (2014). Combination of Plaque Burden, Wall Shear Stress, and Plaque Phenotype Has Incremental Value for Prediction of Coronary Atherosclerotic Plaque Progression and Vulnerability. *Atherosclerosis* 232 (2), 271–276. doi:10.1016/j.atherosclerosis.2013.11.049

Gao, H., Long, Q., Graves, M., Gillard, J. H., and Li, Z.-Y. (2009). Carotid Arterial Plaque Stress Analysis Using Fluid-Structure Interactive Simulation Based on Iin-Vvivo Magnetic Resonance Images of Four Patients. *J. Biomechanics* 42 (10), 1416–1423. doi:10.1016/j.jbiomech.2009.04.010

Garcìa-Garcìa, H. M., Gogas, B. D., Serruys, P. W., and Bruining, N. (2011). IVUS-based Imaging Modalities for Tissue Characterization: Similarities and Differences. *Int. J. Cardiovasc Imaging* 27 (2), 215–224. doi:10.1007/s10554-010-9789-7

Guo, X., Maehara, A., Matsumura, M., Wang, L., Zheng, J., Samady, H., et al. (2021). Predicting Plaque Vulnerability Change Using Intravascular Ultrasound Plus Optical Coherence Tomography Image-Based Fluid-Structure Interaction Models and Machine Learning Methods with Patient Follow-Up Data: a Feasibility Study. *Biomed. Eng. Online* 20 (1), 6. doi:10.1186/s12938-021-00868-6

Guo, X., Zhu, J., Maehara, A., Monoly, D., Samady, H., Wang, L., et al. (2017). Quantify Patient-specific Coronary Material Property and its Impact on Stress/strain Calculations Using *In Vivo* IVUS Data and 3D FSI Models: a Pilot Study. *Biomech. Model Mechanobiol.* 16 (1), 333–344. doi:10.1007/s10237-016-0820-3

Holzapfel, G. A., Gasser, T. C., and Ogden, R. W. (2000). A New Constitutive Framework for Arterial Wall Mechanics and a Comparative Study of Material Models. *J. Elast. Phys. Sci. solids* 61 (1), 1–48. doi:10.1023/a:1010835316564

Huang, Y., Teng, Z., Sadat, U., He, J., Graves, M. J., and Gillard, J. H. (2013). *In Vivo* MRI-based Simulation of Fatigue Process: a Possible Trigger for Human Carotid Atherosclerotic Plaque Rupture. *Biomed. Eng. Online* 12, 36. doi:10.1186/1475-925X-12-36

Jang, I.-K., Bouma, B. E., Kang, D.-H., Park, S.-J., Park, S.-W., Seung, K.-B., et al. (2002). Visualization of Coronary Atherosclerotic Plaques in Patients Using Optical Coherence Tomography: Comparison with Intravascular Ultrasound. *J. Am. Coll. Cardiol.* 39 (4), 604–609. doi:10.1016/s0735-1097(01)01799-5

Ku, D. N., and McCord, B. N. (1993). Cyclic Stress Causes Rupture of the Atherosclerotic Plaque Cap. *Circulation* 88 (4), 254.

Lawrence, R. L., Wood, S. D., and Sheley, R. L. (2006). Mapping Invasive Plants Using Hyperspectral Imagery and Breiman Cutler Classifications (RandomForest). *Remote Sens. Environ.* 100 (3), 356–362. doi:10.1016/j.rse.2005.10.014

Li, Z.-Y., Howarth, S. P. S., Tang, T., Graves, M. J., U-King-Im, J., Trivedi, R. A., et al. (2007). Structural Analysis and Magnetic Resonance Imaging Predict Plaque Vulnerability: a Study Comparing Symptomatic and Asymptomatic Individuals. *J. Vasc. Surg.* 45 (4), 768–775. doi:10.1016/j.jvs.2006.12.065

Liaw, A., and Wiener, M. (2002). Classification and Regression by randomForest. *R. news* 2 (3), 18–22.

Paritala, P. K., Yarlagadda, P. K. D. V., Kansky, R., Wang, J., Mendieta, J. B., Gu, Y., et al. (2020). Stress-Relaxation and Cyclic Behavior of Human Carotid Plaque Tissue. *Front. Bioeng. Biotechnol.* 8, 60. doi:10.3389/fbioe.2020.00060

Pei, X., Wu, B., Tang, T. Y., Gillard, J. H., and Li, Z.-Y. (2014). Fatigue Crack Growth under Pulsatile Pressure and Plaque Rupture. *JACC Cardiovasc. Imaging* 7 (7), 738–740. doi:10.1016/j.jcmg.2014.01.019

Prinzie, A., and Van den Poel, D. (2008). Random Forests for Multiclass Classification: Random Multinomial Logit. *Expert Syst. Appl.* 34 (3), 1721–1732. doi:10.1016/j.eswa.2007.01.029

Riou, L. M., Broisat, A., Ghezzi, C., Finet, G., Rioufol, G., Gharib, A. M., et al. (2014). Effects of Mechanical Properties and Atherosclerotic Artery Size on Biomechanical Plaque Disruption - Mouse vs. Human. *J. Biomechanics* 47 (4), 765–772. doi:10.1016/j.jbiomech.2014.01.020

Saam, T., Yuan, C., Chu, B., Takaya, N., Underhill, H., Cai, J., et al. (2007). Predictors of Carotid Atherosclerotic Plaque Progression as Measured by Noninvasive Magnetic Resonance Imaging. *Atherosclerosis* 194 (2), e34–e42. doi:10.1016/j.atherosclerosis.2006.08.016

Stehbens, W. E. (2002). The Fatigue Hypothesis of Plaque Rupture and Atherosclerosis. *Med. Hypotheses* 58 (4), 359–360. doi:10.1054/mehy.2001.1540

Stehbens, W. E. (1997). The Pathogenesis of Atherosclerosis: A Critical Evaluation of the Evidence. *Cardiovasc. Pathol.* 6 (3), 123–153. doi:10.1016/s1054-8807(96)00090-7

Thondapu, V., Bourantas, C. V., Foin, N., Jang, I. K., Serruys, P. W., and Barlis, P. (2017). Biomechanical Stress in Coronary Atherosclerosis: Emerging Insights from Computational Modelling. *Eur. Heart J.* 38 (2), 81–92. doi:10.1093/eurheartj/ehv689

Vergallo, R., Papafaklis, M. I., Yonetsu, T., Bourantas, C. V., Andreou, I., Wang, Z., et al. (2014). Endothelial Shear Stress and Coronary Plaque Characteristics in Humans. *Circ. Cardiovasc. Imaging* 7 (6), 905–911. doi:10.1161/circimaging.114.001932

Versluis, A., Bank, A. J., and Douglas, W. H. (2006). Fatigue and Plaque Rupture in Myocardial Infarction. *J. Biomechanics* 39 (2), 339–347. doi:10.1016/j.jbiomech.2004.10.041

Wang, L., Zheng, J., Maehara, A., Yang, C., Billiar, K. L., Wu, Z., et al. (2015). Morphological and Stress Vulnerability Indices for Human Coronary Plaques and Their Correlations with Cap Thickness and Lipid Percent: An IVUS-Based Fluid-Structure Interaction Multi-Patient Study. *PLoS Comput. Biol.* 11 (12), e1004652. doi:10.1371/journal.pcbi.1004652

Wang, L., Tang, D., Maehara, A., Molony, D., Zheng, J., Samady, H., et al. (2019a). Multi-factor Decision-Making Strategy for Better Coronary Plaque Burden Increase Prediction: a Patient-specific 3D FSI Study Using IVUS Follow-Up Data. *Biomech. Model Mechanobiol.* 18 (5), 1269–1280. doi:10.1007/s10237-019-01143-3

Wang, Q., Tang, D., Wang, L., Canton, G., Wu, Z., Hatsukami, T. S., et al. (2019b). Combining Morphological and Biomechanical Factors for Optimal Carotid Plaque Progression Prediction: An MRI-Based Follow-Up Study Using 3D Thin-Layer Models. *Int. J. Cardiol.* 293, 266–271. doi:10.1016/j.ijcard.2019.07.005

Won, K.-B., Lee, S.-E., Lee, B. K., Park, H.-B., Heo, R., Rizvi, A., et al. (2019). Longitudinal Quantitative Assessment of Coronary Plaque Progression Related to Body Mass Index Using Serial Coronary Computed Tomography Angiography. *Eur. Heart Journal-Cardiovascular Imaging* 20 (5), 591–599. doi:10.1093/ehjci/jey192

Won, K. B., Lee, B. K., Park, H. B., Heo, R., Lee, S. E., Rizvi, A., et al. (2020). Quantitative Assessment of Coronary Plaque Volume Change Related to Triglyceride Glucose Index: The Progression of AtheRosclerotic PlAque DetermIned by Computed TomoGraphic Angiography IMaging (PARADIGM) Registry. *Cardiovasc Diabetol.* 19 (1), 113–210. doi:10.1186/s12933-020-01081-w

Xing, R., Moerman, A. M., Ridwan, Y., Daemen, M. J., van der Steen, A. F. W., Gijsen, F. J. H., et al. (2018). Temporal and Spatial Changes in Wall Shear Stress during Atherosclerotic Plaque Progression in Mice. *R. Soc. open Sci.* 5 (3), 171447. doi:10.1098/rsos.171447

**Conflict of Interest:** The authors declare that the research was conducted in the absence of any commercial or financial relationships that could be construed as a potential conflict of interest.

**Publisher's Note:** All claims expressed in this article are solely those of the authors and do not necessarily represent those of their affiliated organizations, or those of the publisher, the editors and the reviewers. Any product that may be evaluated in this article, or claim that may be made by its manufacturer, is not guaranteed or endorsed by the publisher.

frontiers | Frontiers in Physiology

ORIGINAL RESEARCH
published: 13 May 2022
doi: 10.3389/fphys.2022.904453

# Fluid-Structure Interaction Analysis on the Influence of the Aortic Valve Stent Leaflet Structure in Hemodynamics

*Xiangkun Liu, Wen Zhang, Ping Ye, Qiyi Luo and Zhaohua Chang**

*School of Health Science and Engineering, University of Shanghai for Science and Technology, Shanghai, China*

Transcatheter aortic valve replacement (TAVR) is a minimally invasive surgical treatment for heart valve disease. At present, personalized TAVR valves are not available for some patients. This study adopts the fluid-structure interaction (FSI) model of the research object that has a three-disc leaflet form and structural design in the valve leaflet area. The valve opening shape, orifice area, stress-strain, and distribution of hemodynamic flow and pressure were compared under the condition of equal contact area between valve and blood. The FSI method was used to simulate the complex three dimensional characteristics of the flow field more accurately around the valve after TAVR stent implantation. Three personalized stent systems were established to study the performance of the leaflet design based on computational fluid dynamics. By comparing the different leaflet geometries, the maximum stress on leaflets and stents of model B was relatively reduced, which effectively improved the reliability of the stent design. Such valve design also causes the opening area of the valve leaflet to increase and the low-velocity area of the flow field to decrease during the working process of the valve, thus reducing the possibility of thrombosis. These findings can underpin breakthroughs in product design, and provide important theoretical support and technical guidance for clinical research.

**Keywords: aortic valve stent, leaflet structure, fluid-structure interaction, computational fluid dynamics, operator-split lagrangian eulerian, hemodynamic effect**

OPEN ACCESS

***Edited by:***
*Yunlong Huo,*
*Shanghai Jiao Tong University, China*

***Reviewed by:***
*Bao Li,*
*Beijing University of Technology, China*
*Peng Wu,*
*Soochow University, China*
*Shengzhang Wang,*
*Fudan University, China*

****Correspondence:***
*Zhaohua Chang*
*m8090313@126.com*

***Specialty section:***
*This article was submitted to Computational Physiology and Medicine, a section of the journal Frontiers in Physiology*

***Received:*** *25 March 2022*
***Accepted:*** *21 April 2022*
***Published:*** *13 May 2022*

***Citation:***
*Liu X, Zhang W, Ye P, Luo Q and Chang Z (2022) Fluid-Structure Interaction Analysis on the Influence of the Aortic Valve Stent Leaflet Structure in Hemodynamics. Front. Physiol. 13:904453. doi: 10.3389/fphys.2022.904453*

## INTRODUCTION

Among cardiovascular diseases, aortic valve disease has the second highest morbidity and mortality in the world (Go et al., 2013). Nearly 30,000 patients worldwide undergo aortic valve-replacement surgery every year (Dasi et al., 2009). Transcatheter aortic valves (TAVs) were initially used as a minimally invasive alternative to thoracotomy in order to replace the aortic valve (Guidoin et al., 2010), and mainly used in patients that had high surgical risk. In recent years, due to the advancement of related technologies and the development of clinical treatments, the use of TAVs has gradually expanded to reach low- and moderate-risk patients. Numerical simulation can provide detailed information that is difficult to obtain from experiments, and can help to evaluate the impact of blood flow on valve biomechanics. Such findings, in turn, can be used to guide clinical interventions for the treatment of aortic valve disease. Due to the strong interaction between the aortic valve and the surrounding blood, fluid-structure interaction (FSI) analysis is widely used and is considered the best method of numerical simulation for accurate simulation of the valve load and the surrounding flow field (Luraghi et al., 2021).

Transcatheter aortic valve (TAV) devices consist of three biological valve leaflets, self-expanding or mechanically expandable metal stents, and inner or outer skirts (Wei et al., 2018). This arrangement differs from traditional thoracotomy replacement valves and brings new challenges to FSI simulation. Wu et al. (2016) used the immersed boundary (IB) method to conduct an FSI simulation of a self-expanding TAV for the first time (Rotman et al., 2018). Subsequently, quite a few researchers have been focused on developing the accuracy and validity of the FSI method for transcatheter aortic valve replacement (TAVR) simulation. Both moving-mesh methods such as the arbitrary Lagrangian-Eulerian method (Ghosh et al., 2018) and fixed-mesh methods such as the immersed boundary method, and even combined fixed-moving grid methods such as the "operator-split" Lagrangian-Eulerian method (Luraghi et al., 2019) and mesh-free method such as the smoothed particle hemodynamic method (Pasta et al., 2020), have been applied. On the other hand, although TAVR complications have been decreasing since its introduction, some adverse outcomes are still present including leaflet durability, paravalvular leaks, and thrombosis (Luraghi et al., 2021), which makes the mechanical and hemodynamic performance of the TAV device of great concern. With a patient-specific model or an ideal model, FSI simulations have been performed to evaluate the leaflet opening area (Wu et al., 2016), mechanical stress (Ghosh et al., 2020), wall shear stress (Kandail et al., 2018), PVL severity (Luraghi et al., 2019), and the influence of calcification (Luraghi et al., 2020) or calcification of the bicuspid native aortic valve (Pasta et al., 2020), and so on.

However, most studies only involve one or two particular TAV devices. When it comes to the problem of understanding how the design parameters of a TAV device affect its performance, the relevant literature, to the best of our knowledge, is limited. Van Aswegen et al. (2012) modified a prosthetic aortic valve and created two configurations of the attachment to the surrounding stent. Through FSI simulation, the von Mises stress distribution was shown to be different between two configurations. However, the aortic root model used was highly simplified. Travaglino et al. (2020) parametrized a generic TAV model and developed a Bayesian optimization approach that succeeded in reducing the peak stress under a blood pressure of 120 mmHg. In their study, however, only leaflets were considered and finite element analysis was applied instead of FSI simulation. Carbonaro et al. (2021) utilized a mesh-morphing procedure to parametrize the TAV frame, and finite element analyses of TAV implantation were performed in idealized aortic root models with and without calcification. A multi-objective design optimization was conducted by coupling the design of the experiment with surrogate modeling to optimize the magnitude of the pullout force, peak maximum principal stress within the aortic wall, and contact pressure in the left ventricular outflow tract. Again, finite element analysis was applied instead of FSI simulation, and leaflet geometry was neglected. Thus, the influence of different design parameters needs to be further studied with a more complete TAV geometry model, and with consideration of the interaction between the device and blood.

In terms of the research literature concerning valve support, some researchers typically use numerical methods to evaluate the accuracy and validity of the heart valve unit (De Hart et al., 2003; Ghosh et al., 2018; Wu et al., 2019; Luraghi et al., 2021), while others study the performance of heart valve devices already on the market (Luraghi et al., 2019; Pasta et al., 2020; Pasta and Gandolfo, 2021). Most of these studies do not involve basic design methods, especially the relationship between structural design and flow fields, as well as related parametric studies. The main purpose of the current paper is to study how different flap designs affect the mechanical properties and flow field of TAV using the FSI method based on computational fluid dynamics, which would be instructive to TAV designing and clinical practice in terms of improving product performance. With the TAV device deployed in an ideal aortic root model, three parametrically modified leaflet designs with the same contact area with blood were investigated. Through computational fluid dynamics, intravascular hemodynamic characteristic, including the blood flow velocity and pressure distribution were assessed after the implantation of each valve stent. Using numerical calculations and comparisons, it was found that different valve shapes have a great impact on the valve opening area, stent force, and intravascular flow field.

# METHODS

## Aortic Valve Stents Geometry

Aortic valve stents typically consist of three leaflets, self- or mechanically expandable stents, and inner/outer skirts (Wei et al., 2018). The stent is divided into two parts: the inflow tract and the outflow tract. The three leaflets and the skirt are sutured in the inflow tract area of the stent. In the present study, three valve leaflet geometries were designed for the same stent, and three personalized heart valve stent devices were established. Twelve basic units were arranged in the circumferential direction of the stent and 2.5 basic units were arranged in the axial direction of the stent. According to the specific aortic root structure of the patient, the axial length of the stent was controlled at about 30 mm, the initial stent radius diameter was $R$ = 3.5 mm, the number of basic circumferential units was $n_c$ = 12, the number of axial basic units was $n_a$ = 2.5, the wall thickness was $t$ = 0.42 mm, the trunk width was $t_b$ = 0.614 mm, the branch trunk width was $t_a$ = 0.3 mm, the inner arc radius was $r_a$ = 0.07 mm, and $r_b$ = 1 mm. The single cell width was calculated as:

$$w = 2\pi R/n_c \tag{1}$$

The original tube diameter of the stent was 7.0 mm, the wall thickness was 0.4 mm, and the expanded diameter of the stent was 27 mm. **Figure 1** shows the geometric structure of the aortic valve stent and the three-dimensional model used in this study. A complete parametric CAD model of the stent was established using SolidWorks (Dassault Systèmes SolidWorks Corp., Waltham, MA, United States). For the mesh generation of the stent, the unit size of the stent model was controlled at 0.1 mm, the number of self-expanding stent units was 17,280, and the number of nodes was 37,440. Abaqus (SIMULIA, Johnston, RI, United States) was used to complete the processing of the stent

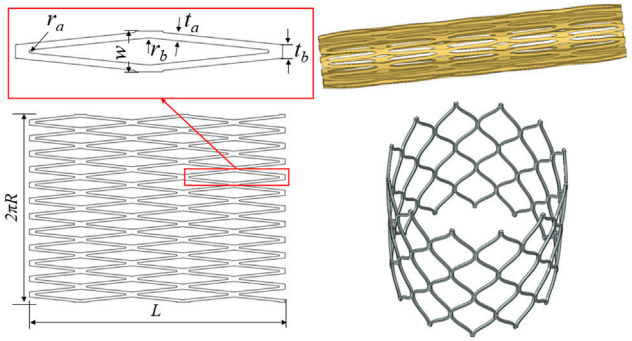


**FIGURE 1 |** Diagram of the geometric structure of the aortic valve stent and three-dimensional model.

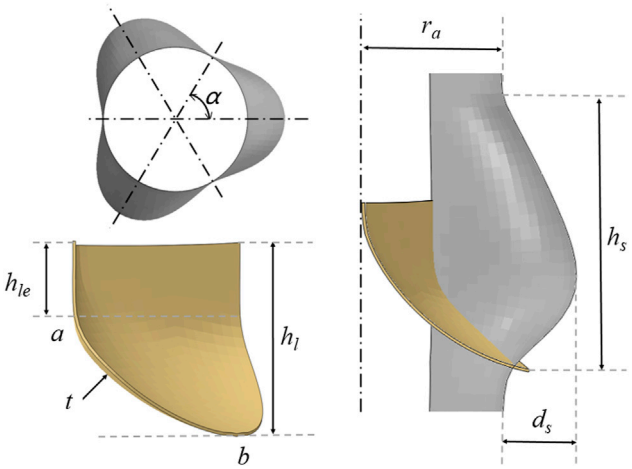


**FIGURE 2 |** Schematic diagram of the geometry of the aorta and valve leaflets and definition of relevant dimensions of the aorta and valve leaflets.

model. First, according to the design parameters of the stent, a two-dimensional plane model of the stent was established, and the mesh division was completed. Second, the mesh model was wrapped so as to form a tubular shape to establish a laser cutting stent model, the diameter of the stent being 7.0 mm. Third, the laser cutting stent model was expanded and finalized. In other words, the process was divided into three steps: the diameter of the stent was expanded from 7 to 12 mm, then to 19 mm, and then to 27 mm, which completed the expansion of the stent.

With reference to the waveform structure of the stent, three structural forms of the valve were established to compare mechanical properties. The geometric design of the valve refers to the aortic structure proposed by De Hart et al. (2003) and was drawn on the connecting line with the stent commissure using reference points. The physiological structure of the aortic geometry shows three main components: the root, the base, and the tubular ascending aorta. The bases of the three aortic valve leaflets followed a hyperbola from one connection point to another at the aortic root. The aortic root began to form the

**TABLE 1 |** Aortic model structure size parameters (mm).

| | $r_a$ | $d_s$ | $h_s$ | $\alpha$ |
|---|---|---|---|---|
| Aortic model | 11.40 | 5.68 | 21.00 | 60° |

**TABLE 2 |** Valve leaflets model structure size parameters (mm).

| | $h_1$ | $h_{1e}$ | *Line* |
|---|---|---|---|
| Model A | 13.0 | 4.2 | $-4.243ln(x) + 8.1557$ |
| Model B | 14.0 | 3.5 | $-4.727ln(x) + 10.867$ |
| Model C | 16.0 | 3.2 | $-5.492ln(x) + 13.229$ |

sinus cavity, which was the origin of the ascending aorta. The three sinus cavities consisted of three circular arcs forming a clover-shaped section with α angles of 60°. Both the bottom part and the ascending part of the aorta were composed of cylinders.

**Figure 2** shows the relevant dimensions of the aortic root geometry and valve leaflet geometry, as well as the established aortic wall model and the valve leaflet model based on the dimensions of the physiological structure shown in **Tables 1**, **2**. In this study, $r_a$ is the aortic valve radius, $d_s$ is the sinus depth, $h_s$ is the sinus height, $h_1$ is the total leaflet height thickness, $h_{1e}$ is the vertical leaflet height thickness, $t$ is the leaflet thickness, and *Line* is the spatial location of the leaflet curve from point $a$ to point $b$. Afterwards, the spatial position of the *Line* was determined, which can generate the valve. During modeling of the valve, the position of point $a$ is defined at the coordinate origin. The CAD models of the leaflets and skirt were established using SolidWorks. For the mesh generation of valve leaflet and skirt, the number of three leaflet elements was 16,080 and the number of nodes was 24,885; the number of skirt elements was 25,176 and the number of nodes was 40,358. Size parameters for the aortic model structure and valve leaflets model are shown in **Tables 1**, **2**.

The valve leaflet model based on the size of the physiological structure had an area of about 350 $mm^2$. When establishing the other two valve models, the valve and blood contact area of the three models was the same. These valve models ware established with reference to the stent design, and the valve area was equal in the three structures. The leaflet thickness was $t = 0.2$ mm. Model A was based on the size of the physiological structure. The upper half of the valve leaflet fell along the axis of the stent rod unit, and the lower half related to the shape of the bottom of the aortic sinus cavity. The bottom line of the leaflet of model B was basically perpendicular to the axis of the stent rod or intersected it at a certain angle. The bottom line of the leaflet of model C was along the axis of the stent rod, which was basically consistent with the axis. A complete stent model with three leaflet shapes was established (**Figure 3**). Because the skirt structure played a role in preventing peripheral leakage and was close to the aortic wall after implantation, it had little effect on the central flow field. The structure was simplified and was equal to the thickness of the stent, and the inner skirt coincided with the bottom edge of the valve leaflet. After the position of *Line* was determined, the valve leaflet, skirt, and stent were integrated to

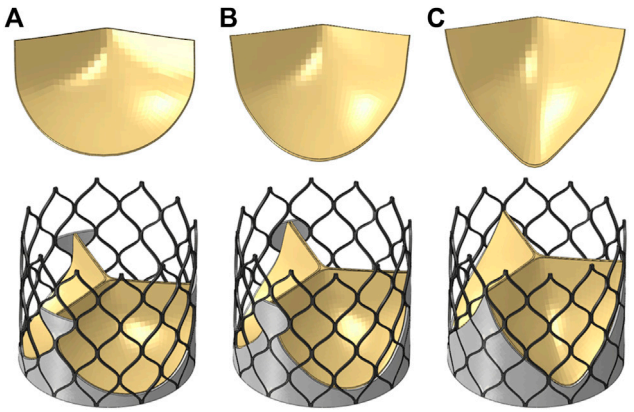


**FIGURE 3 |** Three valve leaflet models and three valve stent models, **(A)** model A, **(B)** model B, **(C)** model C.

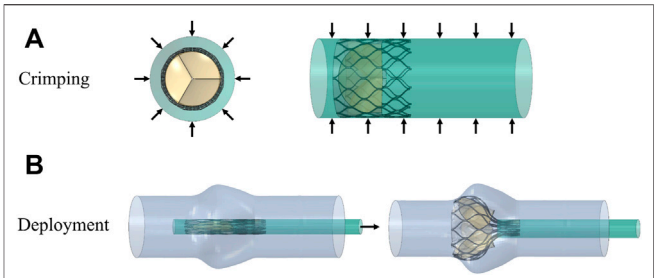


**FIGURE 4 |** Schematic diagram of the valve stent intervention process, **(A)** stent crimping by applying a radial displacement on an outer cylindrical surface and **(B)** progressive deployment of the crimped stent.

generate the aortic valve device. The integration of valve leaflet, skirt, and stent was completed through the fusion and sharing of near nodes. Sewing sutures among the stent, leaflets, and skirt was neglected.

## Valve Stent Implantation

The valve stent was delivered to the aortic root region by a delivery system and self-expanding to a predetermined position to play a supporting role. Combining stent production and processing technology, a three-dimensional model of the valve stent was developed using finite element simulation, and hemodynamic fluid-structure coupling analysis of the valve stent was carried out. Abaqus was used to simulate valve stent implantation, which included the crimp and self-expanding release of TAV device. In the first step, TAV device crimp analysis was performed, using a crimping tool to crimp the valve stent from a diameter of 27 to 10 mm. The crimping tool was used instead of a rigid cylinder surface. In the cylindrical coordinate system, radial displacement boundary conditions were applied to the rigid cylinder surface to gradually shrink it radially so as to crimp the stent, as shown in **Figure 4**. The contact between the inner surface of the rigid cylinder and the outer surface of the stent was defined as face-to-face, where the inner surface of the rigid cylinder surface was the main surface and the friction coefficient was defined as 0.1.

The material of the stent was a nickel-titanium alloy, a hyperelastic material with coupled temperature parameters and mechanical parameters. This material model divided strain into three components: elastic strain, phase transformation strain, and plastic strain. When the material was completely transformed into martensite, the strain became plastic strain. The material data required for the simulation analysis were obtained with uniaxial tensile tests from loading and unloading, and reverse loading and unloading. Uniaxial tensile tests were conducted with an Instron 5,565 tensile tester (Instron Corporation, Norwood, MA, United States) at 37 ± 0.2°C to obtain stress-strain data. In the first group, the nickel-titanium wires were stretched to a strain of 6% then released; the other group of nickel-titanium wires were stretched to a strain of about 13.5%, and all the test data were recorded. The experimental data were fitted to a stress-strain curve, and the curve was used for simulation analysis as shown in **Figure 5**. The material property parameters were: $E_A$ = 59,000 MPa, martensitic elastic modulus $E_M$ = 26,100 MPa, Poisson's ratio = 0.33, and the tensile limit of the material = 13.5%.

In the second step, TAV device was released and bounced back. In the cylindrical coordinate system, TAV device was released after being crimped and held by the crimping tool at the aortic valve site, and release analysis of TAV device in the aortic valve was conducted. During the entire analysis, the penalty function of self-contact was defined in the analysis. The face-to-face contact between TAV device and the aortic valve was defined as a penalty function contact, and the friction coefficient was set as 0.2.

The leaflets and skirts were modeled as linear elastic materials with a Young's modulus of 1 Mpa, a Poisson's ratio of 0.45, and a density of 1,100 kg/m$^3$ (Luraghi et al., 2019). The penalty function of self-contact was defined in the analysis. The suture between the skirt and the stent, and the suture between the leaflet and the skirt were approximated as a bound contact; that is, the edge of the skirt was bound to the inflow end of the stent, and the edge of the three leaflets was bound to the skirt. A simplified model of the aorta with three stents that was solved by Abaqus is shown in **Figure 6**. The upper and lower ends of the stent had a slight tendency to buckle inward, and the circumferential shape changed with the structure of the aortic sinus cavity. Because the areas of the three valve leaflet models were the same, the valve leaflet height gradually approached the sinus height.

In this study, Abaqus was applied to complete the modeling and finalization of the stent. The stent was implanted into the ideal heart model to obtain a simulation model of the stent when implanted. The simulation model completed in Abaqus was substituted into LS-DYNA (ANSYS, Canonsburg, PA, United States), and fluid-structure coupling related simulation analysis was carried out in LS-DYNA. In general, the molding and implantation of the stent were preliminarily completed in Abaqus software, and the fluid-structure coupling study was carried out and post-processed in LS-DYNA.

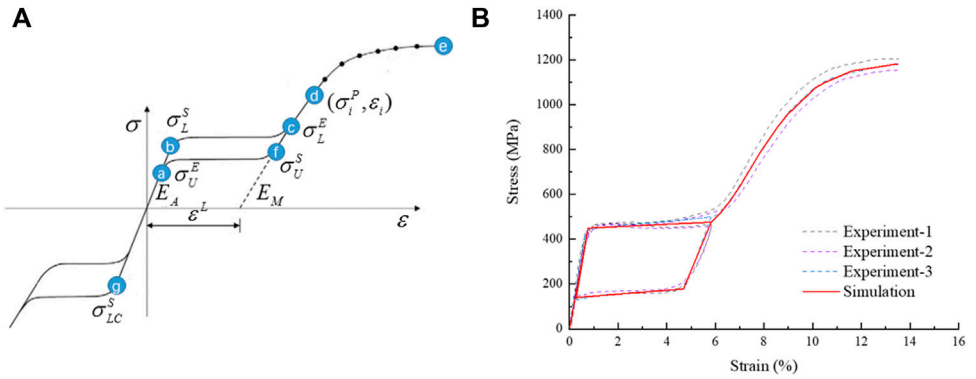


**FIGURE 5 |** Schematic diagram of NiTi material properties, **(A)** the tensile strain-stress curve of the material and **(B)** the stress-strain curve fitted by simulation analysis.

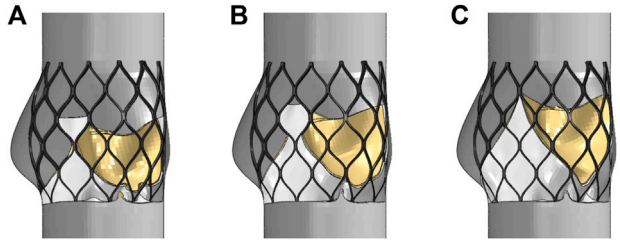


**FIGURE 6 |** Structural model after valve stent intervention, **(A)** valve stent intervention of model A, **(B)** valve stent intervention of model B, **(C)** valve stent intervention of model C.

## Fluid-Structure Interaction Analysis

In a CFD only analysis, the moving reference frame was fixed in space, and a full Eulerian formulation was achieved in the LS-DYNA software. However, in cases of problems regarding fluid-structure interaction (FSI), the boundaries between the solid and fluid are Lagrangian and deform with the structure. An arbitrary Lagrangian-Eulerian (ALE) formulation was therefore retrieved. This approach allowed a strong and exact imposition of the solid boundary conditions on the fluid. The solid and fluid geometry must match at the interface but not necessarily the meshes. For FSI simulations, the solver used an ALE approach for mesh movement, which means that large deformations of the fluid mesh could occur. By default, the solver only rebuilt the mesh if elements got inverted. An "operator-split" Lagrangian-Eulerian method (Marom, 2015) was adopted using the finite element software LS-DYNA. The structure was handled in a Lagrangian manner, while the calculation of the Eulerian fluid conservation equations was split into two steps. In the first Lagrangian step, the mesh moved with fluid particles and the following mass conservation equation (Marom, 2015) and the Navier-Stokes equation (Luraghi et al., 2019) were solved:

$$\rho \boldsymbol{J} = \rho_{\boldsymbol{0}} \tag{2}$$

$$\rho \frac{\partial \boldsymbol{v_i}}{\partial \boldsymbol{t}} + \rho \boldsymbol{v_i} \frac{\partial \boldsymbol{v_j}}{\partial \boldsymbol{x_j}} = \frac{\partial \sigma_{ij}}{\partial \boldsymbol{x_j}} + \rho \boldsymbol{f_i} \tag{3}$$

Where $\rho$ is the density of the fluid, $J$ the volumetric strain given by the Jacobian matrix of the deformation gradient, $\rho_0$ the initial density, $v_i$ the velocity of the fluid particles at position $x_i$, $\sigma_{ij}$ the Cauchy stress tensor, and $f_i$ the fluid forces per unit volume.

In the second Eulerian step, also called advection step, the mesh was remapped to its initial Eulerian position and an advection algorithm was used to calculate the conservation variables. The following transport equations were solved with initial conditions from the solution of the Lagrangian step at the same time (Marom, 2015):

$$\frac{\partial \phi}{\partial \boldsymbol{t}} + (\boldsymbol{v} - \boldsymbol{v_m}) \cdot \nabla \phi = \boldsymbol{0} \tag{4}$$

Where $\phi$ is the conservation variable. The coupling of structure and fluid was realized by means of a penalty-based approach, where the problem was regarded as a spring system. The spring was connected to a structure node and a fluid particle, and thus penalty forces proportional to the penetration depth and stiffness coefficient were applied. The coupling force of the fluid particle was then distributed to surrounding fluid nodes using shape functions (Nobari, 2012). The FSI analysis was performed with a time step of 0.01 s and 20 iterations per step. Related equations are as follow:

$$\boldsymbol{F} = \boldsymbol{k} \cdot \boldsymbol{d} \tag{5}$$

$$\boldsymbol{F_s} = -\boldsymbol{F} \tag{6}$$

$$\boldsymbol{F_f^i} = \boldsymbol{N_i} \cdot \boldsymbol{F} \tag{7}$$

Where $F$ is the coupling force, $k$ the stiffness coefficient, $d$ the penetration depth, $F_s$ the force at the corresponding structure node, $F_f^i$ the force at the surrounding fluid node $i$, $N_i$ the shape function at node $i$.

The FSI analysis of this study includes the valve opening and closing due to hemodynamics under pulsatile load after three personalized heart valve stent devices were implanted into the aortic valve. The inner wall of the aorta is simplified and is shown as the wall of the fluid domain in the computational model of fluid mechanics. The calculation cost and structural size were measured, the mesh division process was repeatedly adjusted, and the division size was controlled within 0.6 mm.

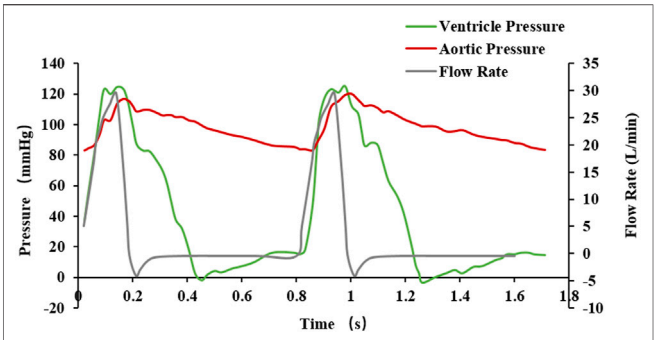


**FIGURE 7 |** Fluctuating load boundary curve.

For the boundary conditions of the fluid analysis, which relate to the data of a previous study (Sodhani et al., 2018), pressure inlet and pressure outlet conditions under the pulsation cycle load were selected. The boundary condition data are shown in **Figure 7**, and two pulsation cycles were calculated. In the analysis, blood was considered an incompressible fluid with a density of 1,060 kg/m$^3$ and a viscosity of 0.004 Pa s. The turbulence was neglected and the flow was assumed to be laminar. Because the diameter of the blood vessel was larger than 1 mm, the blood was considered to be a Newtonian fluid (Aenis et al., 1997) and the pulsatile loading of the blood was assessed for transient flow analysis. For the mesh generation of the discrete model of the fluid domain calculation, the number of fluid domain elements was 253,748, and the number of nodes was 371,526.

# RESULT

## Aortic Valve Dynamics

Under the same boundary conditions, the motion states of the leaflets of the three valve stents were analyzed and compared. **Figure 8** shows the opening and closing states of the leaflets and

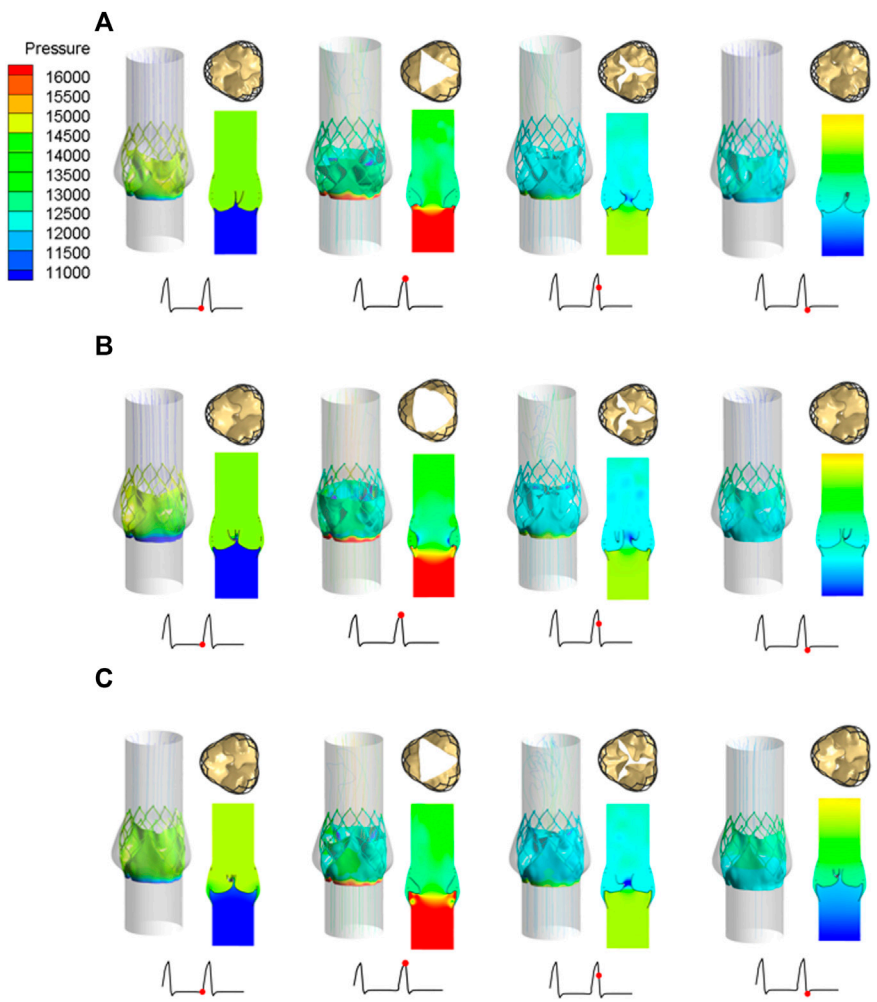


**FIGURE 8 |** Leaflet opening and closing states and pressure distribution diagrams at four different flow stages, **(A)** valve stent model A, **(B)** valve stent model B, **(C)** valve stent model C.

the pressure distributions at four different flow stages. The four flow phases were late diastole (0.8 s) of the first pulsatile cycle, peak systolic phase (0.93 s) of the second pulsatile cycle, maximum deceleration (0.96 s), and early diastole (1.01 s). The flow field pressure assessed the motion state of the valve leaflets. After the three valve stents were implanted, the pressure distributions in the flow field were similar. In the late diastole, the outlet pressure was much greater than the inlet pressure, and the three valve leaflets were in a closed state. At 0.93 s, the inlet pressure was greater than the outlet pressure by about 20 mmHg, and the three leaflets were in a fully open state and near to the maximum opening state. After about 0.03 s, the valve leaflets entered a closed state and remained in a closed state throughout the diastolic period.

During peak systole, the cross-sections of the leaflet openings also showed very different leaflet motion profiles. The opening area of the valve stent was directly calculated according to the shape of the deformed valve leaflet (**Figure 8**). The edges of leaflet models A and C should fit along the metal frame structure of the stent to the greatest extent possible. In the vicinity of the implanted sinus, due to the dual effects of sinus shape extrusion and blood flow impact, these two leaflet structures appeared as obvious triangular openings. Between the two, the morphological structure with greater curvature at the bottom of the leaflet, that is, the opening area of model C (175.779 $mm^2$), was larger than that of model A (134.768 $mm^2$), which is consistent with the results of Ghosh et al. (2018). Among the three models, leaflet model B had the largest opening area, of 243.668 $mm^2$, and its area was about 1.8 times that of model A, and about 1.4 times that of model C.

The structural dynamics of the valve leaflets were compared according to the maximum principal stress and strain values. **Figures 9–11** shows the valve stent structure and the maximum principal stress distribution of the valve leaflets. The distribution of the maximum principal stress and strain of the valve leaflets under different loads showed a relationship with the flow pulsation cycle stage and mechanical properties. Due to the extrusion of the stent and valve leaflets by the sinus structure during implantation, the three valve leaflets were not completely consistent in structure. Under the influence of blood flow, the force shape differed slightly, but the stress-strain distribution trend of the three leaflets in the same structure was basically the same. **Table 3** shows the maximum principal stress of the valve leaflet and valve stent, and the logarithmic strain (LE) of the valve leaflet. In the middle and late diastole and peak systolic period, both the valve leaflets and the stent had higher stress and strain values, and the stress on the valve stent structure of model A was much greater than that in the other two models (**Table 3**). The stress and strain were relatively similar between models. The stress on the valve of model A was relatively large, which almost always occurred at the junction of the valve with the stent and skirt, and was close to the outlet end. The maximum stress on the leaflets of models B and C was inside the leaflets, and this large stress was affected by the curvature of the structure when the leaflets were opened and closed.

## Hemodynamic Effects of the Three Valve Stents

After implantation of the three valve stents, the flow fields had similar pressure distributions and blood flow characteristics, but the peak velocities were different. The valve leaflet models A and C had a narrower central jet at peak contraction. The section perpendicular to the axial direction at the maximum convex point of the sinus surface was taken, and the flow rate of the three models at this section was calculated. The maximum flow rate of model A was 337.68 ml/s, that of model B was 536.31 ml/s, and that of model C was 439.02 ml/s; the ejection flow of model B was about 1.6 times that of model A, and about 1.2 times that of model C. The effects of leaflet opening and closing on the flow field were compared during the peak contraction period (0.93 s) and to the maximum deceleration period (0.96 s) of the three models (**Figure 12**). The velocity streamline diagram in **Figure 12** shows the state of the vortex in the flow field when the valve leaflets opened and closed. Model B only had relatively regular counter-rotating vortices in the sinus cavity, while the other two models were close to the outlet of the blood vessel during the peak systolic period. Except model A, the other two models produced multiple vortices, which also affected the opening and closing state of the valve leaflets.

# DISCUSSION

Millions of patients are diagnosed with aortic valve disease every year. The incidence of aortic valve disease caused by degenerative aortic valve changes is up to 10% in the elderly. With many country's demographics aging, the proportion of populations with aortic valve disease is increasing. Aortic valve diseases are mainly divided into two types: aortic stenosis and aortic insufficiency (Marom, 2015). With the rapid development of modern medicine, most patients' quality of life can be improved through surgical procedures and minimally invasive interventions. TAVR is a minimally invasive treatment for patients with high-risk aortic diseases. With the development in recent years of interventional therapy technologies, TAVR is used more and more in clinics, but many important factors still need to be studied, especially in the context of blood hydrodynamics. TAVR is mainly used to improve the blood flow through the aortic valve, which involves the FSI at the aortic valve, valve stents and blood flow (Travaglino et al., 2020). A powerful tool to study this problem is numerical analysis. Through numerical analysis, we can realize hemodynamic characteristics that cannot be explored through experiments, simulate the situation after valve stent implantation, and preliminarily complete preoperative evaluation so as to find the best clinical treatment scheme.

Multiple approaches have been applied to the research of FSI analysis technology, including ALE (Nguyen et al., 2011; Cao, 2016; Borowski et al., 2018), "operator split" Lagrangian-Euler method (Luraghi et al., 2019; Pasta et al., 2020), the immersed boundary method (IBM) (Lemmon and Yoganathan, 2000; Jendoubi et al., 2014; Kallemov et al.,

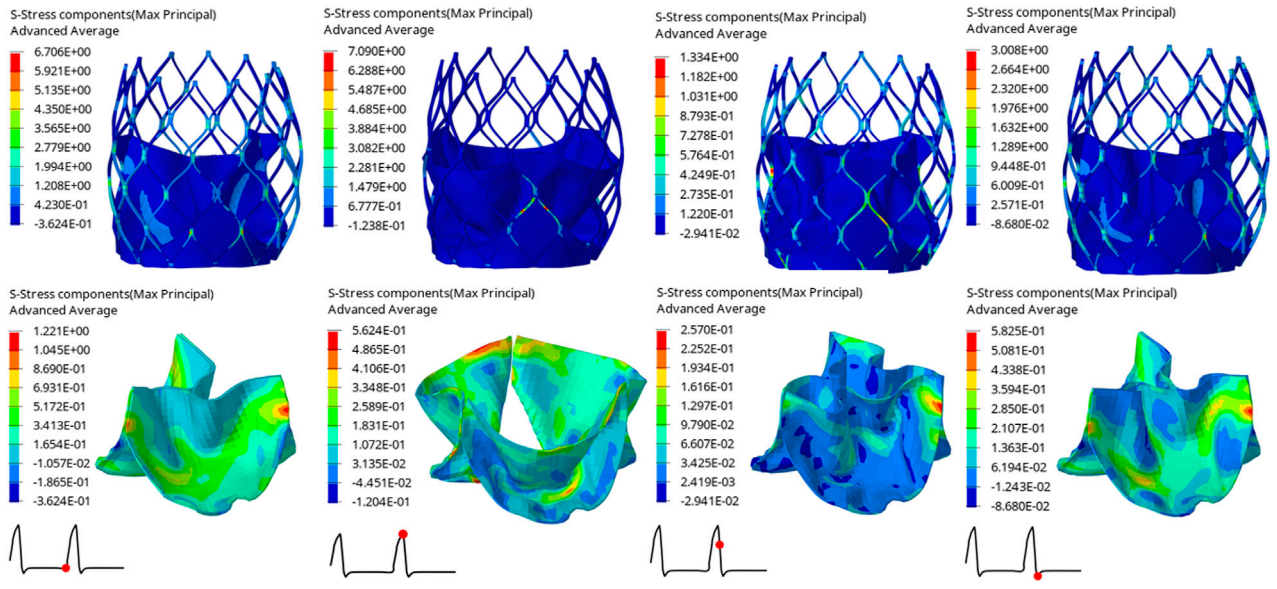


**FIGURE 9 |** Maximum principal stress distribution of valve stent and valve leaflet of model A.

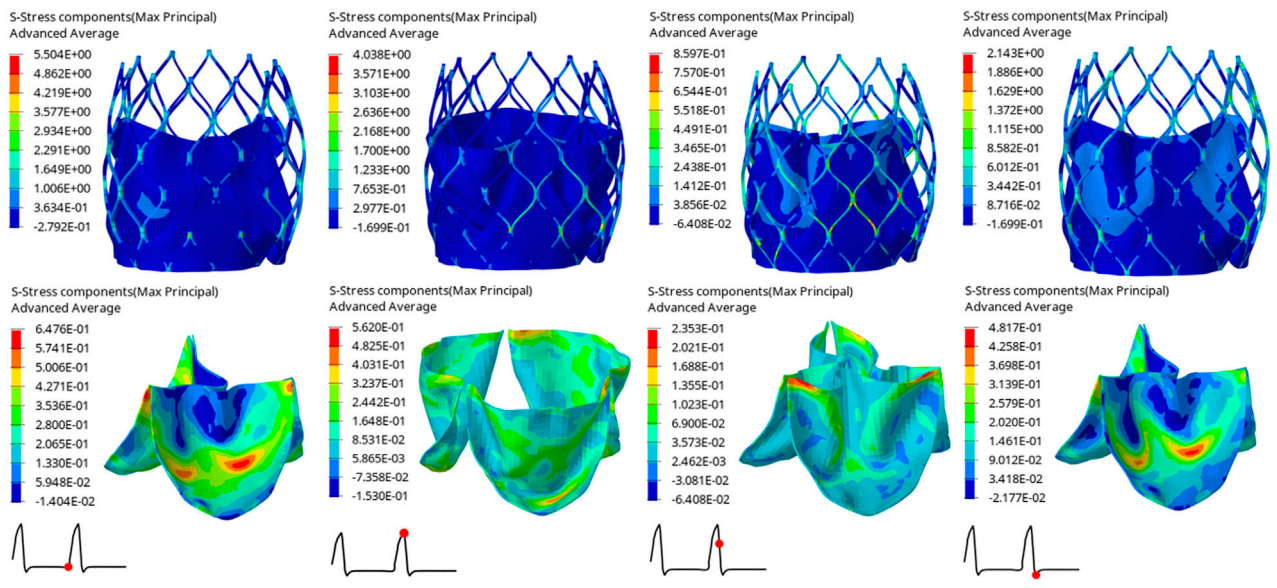


**FIGURE 10 |** Maximum principal stress distribution of valve stent and valve leaflet of model B.

2016), and the curvilinear immersed boundary (CURVIB) method (Ge and Sotiropoulos, 2007; Borazjani et al., 2008). Each of these technical methods have their own specific characteristics. When considered in combination with the results of previous studies, insightful research results have been achieved using these methods, which supports the development of the FSI method to study aortic valve disease and its treatment devices. In the present study, the "operator split" Lagrangian-Euler method was chosen to study the relationship between valve stent structure design and flow field. This method solves the conservation equation in two steps: the Lagrangian equation and the Eulerian equation. In the "operator split" Lagrangian-Euler method, the influence of the moving structure is transmitted to the fluid through structural forces, and the advection algorithm is used to couple the structural and fluid domains. The main objective of this study was to use the FSI method, which is based on computational fluid dynamics, to study the mechanical and fluid properties of different valve stent structural designs after aortic valve implantation. Through such basic research, the

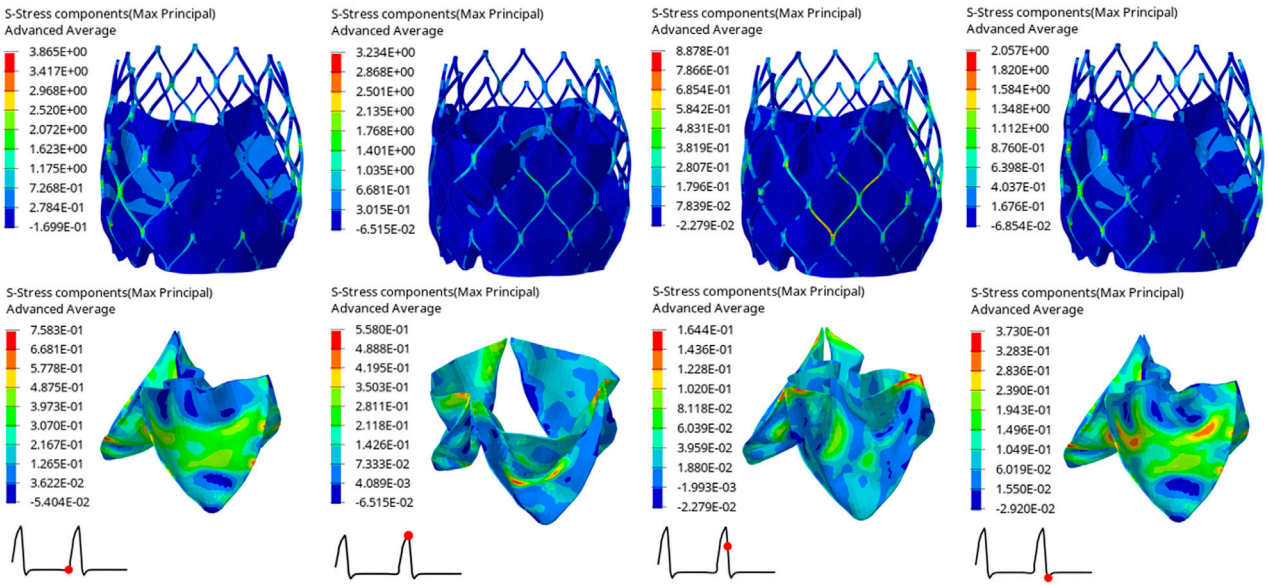


**FIGURE 11 |** Maximum principal stress distribution of valve stent and valve leaflet of model C.

**TABLE 3 |** The maximum principal stress of the valve leaflet and valve stent, the LE of valve leaflet.

| | Time(s) | Model A | Model B | Model C |
|---|---|---|---|---|
| Max. principal stress of valve leaflet (MPa) | 0.80 | 1.2210 | 0.6476 | 0.7583 |
| | 0.93 | 0.5624 | 0.5620 | 0.5580 |
| | 0.96 | 0.2570 | 0.2353 | 0.1644 |
| | 1.01 | 0.5825 | 0.4817 | 0.3730 |
| Max. principal stress of valve stent (MPa) | 0.80 | 6.7060 | 5.5040 | 3.8650 |
| | 0.93 | 7.0900 | 4.0380 | 3.2340 |
| | 0.96 | 1.3340 | 0.8597 | 0.8878 |
| | 1.01 | 3.0080 | 2.1430 | 2.0570 |
| The LE of valve leaflet | 0.80 | 0.1167 | 0.0754 | 0.0776 |
| | 0.93 | 0.1733 | 0.1101 | 0.1081 |
| | 0.96 | 0.0239 | 0.0273 | 0.0164 |
| | 1.01 | 0.0559 | 0.0511 | 0.0469 |

relationship between structural design and blood can be understood.

The stent material used in this study was nickel titanium alloy, which is a shape memory alloy. When the valve stent is transported to the lesion position, it will self-expanding after release. Using the memory characteristics of the nickel titanium alloy material, after stent implantation, its shape can change adaptively with the change of aortic valve structure, which can enhance the fit between stent and aortic valve, prevent valve stent displacement, and reduce the probability of leakage. Although the self-expanding valve stents have been significantly improved, for some patients with valve diseases the application of TAVR may not achieve good therapeutic effects, and the stability of TAVR and the scope of surgical indications still need to be improved. Valve stent dislocation is a rare but serious complication after TAVR. If it is not treated in time, it seriously affects prognosis. For such patients, it is necessary to improve the stability of self-expanding valve stents through design improvements, in turn to improve the success rate of TAVR implantation. In this paper, simulations of the valve stent implantation process are realized, which is of great significance for the study of the mechanical characteristics between the valve stent and aortic valve tissue, and can be used to evaluate the fit level between them.

With the progress of technology, indications of TAVR have increased. In addition, the age of the target group has decreased. Complications after TAVR have been attended to, especially perivalvular leakage, which directly affects the medium- and long-term life quality of patients after TAVR (Mylotte et al., 2015; Ando et al., 2016; Siemieniuk et al., 2016). In the current study, three personalized stent systems were established to evaluate the kinematic characteristics of the three stent-valve leaflets and their effects on the flow field. The complex three-dimensional flow field characteristics in the valve region were simulated by a fluid-structure interaction (FSI) method. In this

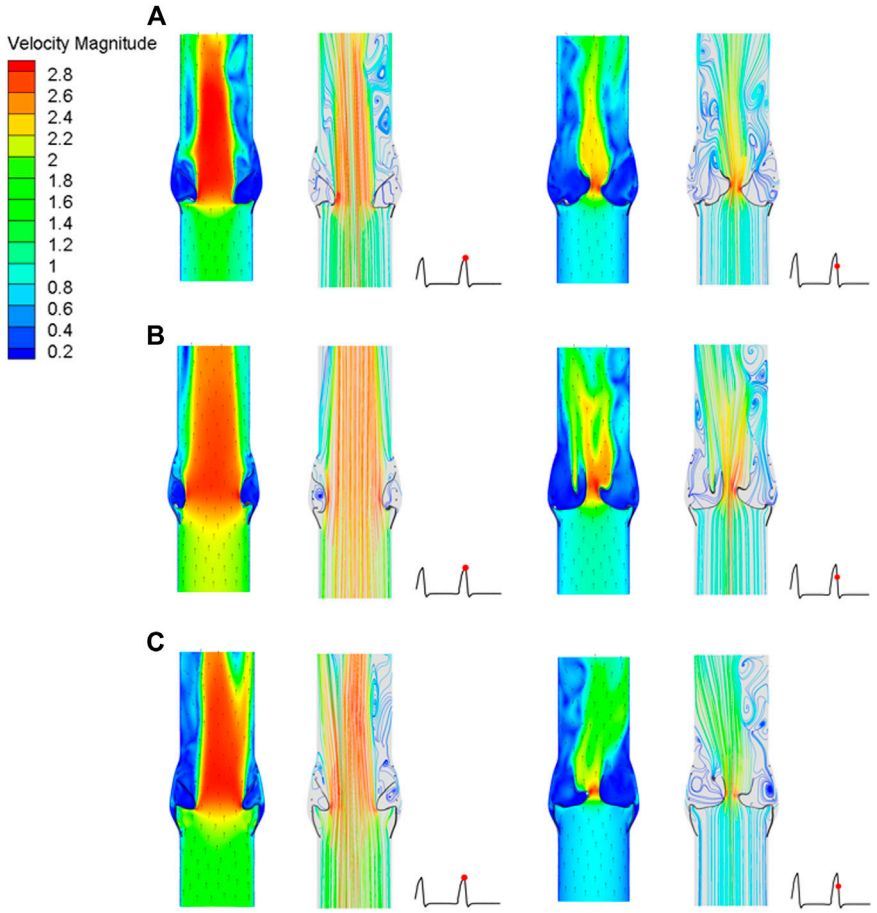


**FIGURE 12 |** Cross-sectional flow velocity distribution in two flow stages, **(A)** valve stent model A, **(B)** valve stent model B, **(C)** valve stent model C.

study, the valve opening morphology, opening area, stress and strain, hemodynamic flow field distribution, and pressure distribution of three heart valve devices with the same valve and blood contact area were compared. It can be seen from the analysis results that the leaflet shape had a significant impact on the overall performance of the stent, which means that better hemodynamic performance of TAVR will improve that performance. The simulation of three models verified the repeatability and effectiveness of the FSI method, which can be applied to the design of aortic valve stent devices. FSI was used to analyze the TAVR of the whole heart pulsation cycle and to evaluate the stent performance and hemodynamics completely, aiding in the design of better aortic valve stent devices.

This study has the following limitations: 1) The ideal aortic valve model was used in this paper, and the pathological valve model was not applied to FSI; 2) In the simulation analysis, the aortic valve was not fully considered in the process of valve stent implantation and FSI analysis; 3) Only one stent structure was designed, and the influence of different stent structures on mechanical properties was not fully investigated. 4) Turbulence models were not included in the analysis of the current study. The blood fluid model used in this study is considered to be an incompressible Newtonian fluid, and laminar flow model and actual *in vivo* blood flow pulsation patterns are used for transient flow analysis. In subsequent research, the study should be combined with the patient's pathological aortic model, and various clinical factors should be gradually added into the study. The turbulence model should be considered in order to achieve a better technology progress. In addition, this calculation model and analysis method requires a large amount of computation, so it is necessary to try different CFD models and FSI models to achieve higher computational efficiency. Greater investment in computing power is also required to achieve higher computational capacity. The results of this study can underpin key breakthroughs in product design, and provide important theoretical support and technical guidance for clinical research.

## CONCLUSION

The FSI analysis results of three personalized stent systems was compared in the current study. The main difference in the leaflet kinematics was that, during systole, the leaflets were pushed outward by a strong jet stream, with models A and C both forming triangular-like openings while model B leaflets formed

nearly circular openings. The different opening shapes made the opening area and instantaneous flow rate of model B larger than those of the other two models. The magnitudes of structural stress and strain provided insight into potential areas where leaflets and stents may fail. The stress concentration of the leaflet of model A mainly occurred near the attachment point of the stent, and the outlet end received the highest stress and strain values, with the maximum value beings greater than that of the other two models, which may cause damage to the leaflet at the connection with the stent and the skirt. Where the stress and strain of models B and C were the largest, this was mostly caused by a change in valve shape and a large change in the curvature of the curved structure. Comparing the effects of model B and the two models, all had a more ideal vortex shape on the flow field in the systolic period. In the existing valve stent design, greater attention was paid to the mechanical properties and reliability of the stent structure, but the influence of valve shape was ignored. In this study, three valve leaflet shapes were designed for the same stent frame structure. The fluid-structure coupling calculation showed that the impact of the valve leaflet shape on the overall performance of the stent was important, and superior hemodynamic effects could also improve the stent performance.

## DATA AVAILABILITY STATEMENT

The original contributions presented in the study are included in the article/Supplementary Material, further inquiries can be directed to the corresponding author.

## AUTHOR CONTRIBUTIONS

PY, QL, and ZC contributed to conception and design of the study. XL and WZ were done computational modelling and results analysis. XL, WZ, and PY wrote the manuscript. All authors contributed to manuscript revision, read, and approved the submitted version.

## REFERENCES


Aenis, M., Stancampiano, A. P., Wakhloo, A. K., and Lieber, B. B. (1997). Modeling of Flow in a Straight Stented and Nonstented Side Wall Aneurysm Model. *J. biomechanical Eng.* 119 (2), 206–212. doi:10.1115/1.2796081

Ando, T., Takagi, H., and Grp, A. (2016). Percutaneous Closure of Paravalvular Regurgitation after Transcatheter Aortic Valve Implantation: A Systematic Review. *Clin. Cardiol.* 39 (10), 608–614. doi:10.1002/clc.22569

Borazjani, I., Ge, L., and Sotiropoulos, F. (2008). Curvilinear Immersed Boundary Method for Simulating Fluid Structure Interaction with Complex 3D Rigid Bodies. *J. Comput. Phys.* 227 (16), 7587–7620. doi:10.1016/j.jcp.2008.04.028

Borowski, F., Sämann, M., Pfensig, S., Wüstenhagen, C., Ott, R., Kaule, S., et al. (2018). Fluid-structure Interaction of Heart Valve Dynamics in Comparison to Finite-Element Analysis. *Curr. Dir. Biomed. Eng.* 4 (1), 259–262. doi:10.1515/cdbme-2018-0063

Cao, K. (2016). "Fluid-structure Interaction Modeling of Valvular Hemodynamics and Secondary Aortopathy," (Notre Dame, United States: University of Notre Dame). Doctoral Dissertation, Doctor of Philosophy.

Carbonaro, D., Gallo, D., Morbiducci, U., Audenino, A., and Chiastra, C. (2021). In Silico biomechanical Design of the Metal Frame of Transcatheter Aortic Valves: Multi-Objective Shape and Cross-Sectional Size Optimization. *Struct. Multidisc Optim.* 64 (4), 1825–1842. doi:10.1007/s00158-021-02944-w

Dasi, L. P., Simon, H. A., Sucosky, P., and Yoganathan, A. P. (2009). Fluid Mechanics of Artificial Heart Valves. *Clin. Exp. Pharmacol. Physiology* 36 (2), 225–237. doi:10.1111/j.1440-1681.2008.05099.x

De Hart, J., Baaijens, F. P. T., Peters, G. W. M., and Schreurs, P. J. G. (2003). A Computational Fluid-Structure Interaction Analysis of a Fiber-Reinforced Stentless Aortic Valve. *J. Biomechanics* 36 (5), 699–712. doi:10.1016/s0021-9290(02)00448-7

Ge, L., and Sotiropoulos, F. (2007). A Numerical Method for Solving the 3D Unsteady Incompressible Navier-Stokes Equations in Curvilinear Domains with Complex Immersed Boundaries. *J. Comput. Phys.* 225 (2), 1782–1809. doi:10.1016/j.jcp.2007.02.017

Ghosh, R. P., Marom, G., Bianchi, M., D'souza, K., Zietak, W., and Bluestein, D. (2020). Numerical Evaluation of Transcatheter Aortic Valve Performance during Heart Beating and its Post-deployment Fluid-Structure Interaction Analysis. *Biomech. Model. Mechanobiol.* 19 (5), 1725–1740. doi:10.1007/s10237-020-01304-9

Ghosh, R. P., Marom, G., Rotman, O. M., Slepian, M. J., Prabhakar, S., Horner, M., et al. (2018). Comparative Fluid-Structure Interaction Analysis of Polymeric Transcatheter and Surgical Aortic Valves' Hemodynamics and Structural Mechanics. *J. Biomechanical Engineering-Transactions Asme* 140 (12), 121002. doi:10.1115/1.4040600

Go, A. S., Mozaffarian, D., Roger, V. L., Benjamin, E. J., Berry, J. D., Borden, W. B., et al. (2013). Heart Disease and Stroke Statistics-2013 Update. *Circulation* 127 (1), E6–E245. doi:10.1161/CIR.0b013e31828124ad

Guidoin, R., Douville, Y., Clavel, M.-A., Zhang, Z., Nutley, M., Pîbarot, P., et al. (2010). "The Marvel of Percutaneous Cardiovascular Devices in the Elderly," in *Aging, Cancer, and Age-Related Diseases: Common Mechanism?* Editor R. M. Tanguay, 188–199.

Jendoubi, A., Yakoubi, D., Fortin, A., and Tibirna, C. (2014). An Immersed Boundary Method for Fluid Flows Around Rigid Objects. *Int. J. Numer. Meth. Fluids* 75 (1), 63–80. doi:10.1002/fld.3884

Kallemov, B., Bhalla, A., Griffith, B., and Donev, A. (2016). An Immersed Boundary Method for Rigid Bodies. *Commun. Appl. Math. Comput. Sci.* 11 (1), 79–141. doi:10.2140/camcos.2016.11.79

Kandail, H. S., Trivedi, S. D., Shaikh, A. C., Bajwa, T. K., O'Hair, D. P., Jahangir, A., et al. (2018). Impact of Annular and Supra-annular CoreValve Deployment Locations on Aortic and Coronary Artery Hemodynamics. *J. Mech. Behav. Biomed. Mater.* 86, 131–142. doi:10.1016/j.jmbbm.2018.06.032

Lemmon, J. D., and Yoganathan, A. P. (2000). Three-dimensional Computational Model of Left Heart Diastolic Function with Fluid-Structure Interaction. *J. Biomechanical Engineering-Transactions Asme* 122 (2), 109–117. doi:10.1115/1.429648

Luraghi, G., Matas, J. F. R., Beretta, M., Chiozzi, N., Iannetti, L., and Migliavacca, F. (2020). The Impact of Calcification Patterns in Transcatheter Aortic Valve Performance: A Fluid-Structure Interaction Analysis. *Comput. Methods Biomechanics Biomed. Eng.* 24 (4), 375–383. doi:10.1080/10255842.2020.1817409

Luraghi, G., Migliavacca, F., García-González, A., Chiastra, C., Rossi, A., Cao, D., et al. (2019). On the Modeling of Patient-specific Transcatheter Aortic Valve Replacement: A Fluid-Structure Interaction Approach. *Cardiovasc Eng. Tech.* 10 (3), 437–455. doi:10.1007/s13239-019-00427-0

Luraghi, G., Rodriguez Matas, J. F., and Migliavacca, F. (2021). In Silico approaches for Transcatheter Aortic Valve Replacement Inspection. *Expert Rev. Cardiovasc. Ther.* 19 (1), 61–70. doi:10.1080/14779072.2021.1850265

Marom, G. (2015). Numerical Methods for Fluid-Structure Interaction Models of Aortic Valves. *Arch. Comput. Methods Eng.* 22 (4), 595–620. doi:10.1007/s11831-014-9133-9

Mylotte, D., Andalib, A., Theriault-Lauzier, P., Dorfmeister, M., Girgis, M., Alharbi, W., et al. (2015). Transcatheter Heart Valve Failure: A Systematic Review. *Eur. Heart J.* 36 (21), 1306–1327. doi:10.1093/eurheartj/ehu388

Nguyen, V.-T., Kuan, Y. H., Chen, P.-Y., Ge, L., Sotiropoulos, F., Yoganathan, A. P., et al. (2011). Experimentally Validated Hemodynamics Simulations of

Mechanical Heart Valves in Three Dimensions. *Cardiovasc Eng. Tech.* 3 (1), 88–100. doi:10.1007/s13239-011-0077-z

Nobari, S. (2012). "Fluid Structure Interaction and Hemodynamic Analysis of the Aortic Valve," (Canada: McGill University). Doctoral Dissertation.

Pasta, S., Cannata, S., Gentile, G., Di Giuseppe, M., Cosentino, F., Pasta, F., et al. (2020). Simulation Study of Transcatheter Heart Valve Implantation in Patients with Stenotic Bicuspid Aortic Valve. *Med. Biol. Eng. Comput.* 58 (4), 815–829. doi:10.1007/s11517-020-02138-4

Pasta, S., and Gandolfo, C. (2021). Computational Analysis of Self-Expanding and Balloon-Expandable Transcatheter Heart Valves. *Biomechanics* 1 (1), 43–52. doi:10.3390/biomechanics1010004

Rotman, O. M., Bianchi, M., Ghosh, R. P., Kovarovic, B., and Bluestein, D. (2018). Principles of TAVR Valve Design, Modelling, and Testing. *Expert Rev. Med. Devices* 15 (11), 771–791. doi:10.1080/17434440.2018.1536427

Siemieniuk, R. A., Agoritsas, T., Manja, V., Devji, T., Chang, Y., Bala, M. M., et al. (2016). Transcatheter versus Surgical Aortic Valve Replacement in Patients with Severe Aortic Stenosis at Low and Intermediate Risk: Systematic Review and Meta-Analysis. *Bmj* 354, i5130. doi:10.1136/bmj.i5130

Sodhani, D., Reese, S., Aksenov, A., Soğanci, S., Jockenhövel, S., Mela, P., et al. (2018). Fluid-structure Interaction Simulation of Artificial Textile Reinforced Aortic Heart Valve: Validation with an *In-Vitro* Test. *J. Biomechanics* 78, 52–69. doi:10.1016/j.jbiomech.2018.07.018

Travaglino, S., Murdock, K., Tran, A., Martin, C., Liang, L., Wang, Y., et al. (2020). Computational Optimization Study of Transcatheter Aortic Valve Leaflet Design Using Porcine and Bovine Leaflets. *J. Biomechanical Engineering-Transactions Asme* 142 (1), 011007. doi:10.1115/1.4044244

Van Aswegen, K. H. J., Smuts, A. N., Scheffer, C., Weich, H. S. V., and Doubell, A. F. (2012). Investigation of Leaflet Geometry in a Percutaneous Aortic Valve with the Use of Fluid-Structure Interaction Simulation. *J. Mech. Med. Biol.* 12 (1), 1250003. doi:10.1142/s0219519411004538

Wei, Z. A., Sonntag, S. J., Toma, M., Singh-Gryzbon, S., and Sun, W. (2018). Computational Fluid Dynamics Assessment Associated with Transcatheter Heart Valve Prostheses: A Position Paper of the ISO Working Group. *Cardiovasc Eng. Tech.* 9 (3), 289–299. doi:10.1007/s13239-018-0349-y

Wu, M. C. H., Muchowski, H. M., Johnson, E. L., Rajanna, M. R., and Hsu, M.-C. (2019). Immersogeometric Fluid-Structure Interaction Modeling and Simulation of Transcatheter Aortic Valve Replacement. *Comput. Methods Appl. Mech. Eng.* 357, 112556. doi:10.1016/j.cma.2019.07.025

Wu, W., Pott, D., Mazza, B., Sironi, T., Dordoni, E., Chiastra, C., et al. (2016). Fluid-Structure Interaction Model of a Percutaneous Aortic Valve: Comparison with an *In Vitro* Test and Feasibility Study in a Patient-specific Case. *Ann. Biomed. Eng.* 44 (2), 590–603. doi:10.1007/s10439-015-1429-x

**Conflict of Interest:** The authors declare that the research was conducted in the absence of any commercial or financial relationships that could be construed as a potential conflict of interest.

**Publisher's Note:** All claims expressed in this article are solely those of the authors and do not necessarily represent those of their affiliated organizations, or those of the publisher, the editors and the reviewers. Any product that may be evaluated in this article, or claim that may be made by its manufacturer, is not guaranteed or endorsed by the publisher.

frontiers | Frontiers in Physiology

ORIGINAL RESEARCH
published: 23 May 2022
doi: 10.3389/fphys.2022.906502

# A Hemodynamic Analysis of the Thrombosis Within Occluded Coronary Arterial Fistulas With Terminal Aneurysms Using a Blood Stasis Model

*Xudong Jiang*[1,2†], *Haoyao Cao*[3,4†], *Zijian Zhang*[1], *Tinghui Zheng*[3,4], *Xiaoqiang Li*[2] *and Peng Wu*[1*]

[1]Artificial Organ Technology Laboratory, School of Mechanical and Electric Engineering, Soochow University, Suzhou, China, [2]Department of Vascular Surgery, Nanjing Drum Tower Hospital Clinical College of Traditional Chinese and Western Medicine, Nanjing University of Chinese Medicine, Nanjing, China, [3]College of Architecture and Environmental Engineering, Sichuan University, Chengdu, China, [4]Sichuan University Yibin Park/Yibin Institute of Industrial Technology, Yibin, China

OPEN ACCESS

**Edited by:**
Yunlong Huo,
Shanghai Jiao Tong University, China

**Reviewed by:**
Xiao Liu,
Beihang University, China
Liyuan Zhang,
Beihang University, China

***Correspondence:**
Peng Wu
pwu@suda.edu.cn

[†]These authors have contributed equally to this work

**Specialty section:**
This article was submitted to Computational Physiology and Medicine, a section of the journal Frontiers in Physiology

**Received:** 28 March 2022
**Accepted:** 04 May 2022
**Published:** 23 May 2022

**Citation:**
Jiang X, Cao H, Zhang Z, Zheng T, Li X and Wu P (2022) A Hemodynamic Analysis of the Thrombosis Within Occluded Coronary Arterial Fistulas With Terminal Aneurysms Using a Blood Stasis Model. Front. Physiol. 13:906502. doi: 10.3389/fphys.2022.906502

**Objective:** The aim of this study is to numerically evaluate thrombosis risk within occluded coronary arterial fistulas (CAF) with terminal aneurysms, and provide guidance in choosing occlusion positions, with clinical observations as reference.

**Method:** Four patients with CAF were studied, with different occlusion positions in actual treatments. Hemodynamics simulations were conducted, with blood residue predicted using the blood stasis model. Three types of models (untreated model, aneurysm-reserved model and aneurysm-removed model) were studeid for each patient. Four metrics, i.e., proportion of high oscillatory shear index (OSI), area of high OSI, old blood volume fraction (OBVF)) and old blood volume (OBV) was obtained to distinguish the thrombosis risk of different treatments (proximal or distal occlusion), comparing with the follow-up CTA.

**Results:** For all the postopertive models, the high OBVF, high OSI(>0.3) and low time-averaged wall shear stress (TAWSS) regions were mainly at the distal fistula, indicating these regions were prone to thrombosis. The regions where blood residue remains are roughly regions of high OSI, corresponding well with clinical observations. In contrast, TAWSS failed to distinguish the difference in thrombosis risk. Absolute values (area of high OSI, OBV) can better reflect the degree of thrombosis risk between treatment types compared with percentage values (proportion of high OSI, OBVF). By comparing with the actual clinical treatments and observations, the OBV is superior to the area of high OSI in determining treatment type.

**Conclusion:** The OBV, a volumetric parameter for blood stasis, can better account for the CAF thrombosis and reflect the degree of blood stasis compared with OSI or TAWSS, is a more appropriate metric for thrombosis in the fistula. Together with morphological parameters, the OBV could guide clinicians to formulate more appropriate surgical

plans, which is of great significance for the preoperative evaluation and treatment prognosis of CAF patients.

**Keywords: coronary arterial fistulas, thrombosis, blood stasis, occlusion position, CFD**

## INTRODUCTION

Coronary arterial fistula (CAF) is defined as an abnormal connection between one of the coronary arteries and a heart chamber or another blood vessel, such as the coronary vein, pulmonary artery, superior vena cava, or bronchial artery etc. (Qureshi, 2006; Iskandrian et al., 1978; Verdini et al., 2016; Amin et al., 2001). CAF is relatively rare, with a prevalence of 0.002% in the general population. Even among patients undergoing coronary angiography or coronary computed tomography angiography, the prevalence of CAFs is only approximately 0.05–0.9% (Karazisi et al., 2017). Most patients have no symptoms when they are young. However, with age, clinical symptoms gradually occur, such as exertional dyspnea, chest pain, infective arteritis, etc. (Firouzi et al., 2021). If combined with coronary arteries dilation or aneurysms, it may cause serious complications such as acute myocardial infarction, cardiac failure, rupture, arrhythmias, etc (Qureshi, 2006). Therefore, immediate clinical intervention is necessary.

The treatments of CAF mainly include surgical ligation, transcatheter closure (TCC) and drug therapy (Kilic et al., 2008; Akcay et al., 2009; Jama et al., 2011; Centella et al., 2016; Haweleh et al., 2018; Firouzi et al., 2021). A recent study proposed that in patients with medium- to large-sized fistulas, irrespective of symptoms, closure (either surgical ligation or TCC) is recommended (Firouzi et al., 2021). The common method is to occlude the terminal of the fistula, while retaining small branches to maintain the blood supply of the myocardium (Kilic et al., 2008; Jama et al., 2011) and improve the phenomenon of stealing blood. However, postoperative patients, especially those with coronary arteries dilation and aneurysms, are prone to thrombus formation in the occluded fistula, which may induce serious consequences such as angina, myocardial infarction, etc. (Saboo et al., 2014). Therefore, for CAF patients undergoing intervention, warfarin is recommended postoperatively. Furthermore, if thrombosis is observed in the occluded fistula, long-term anticoagulation with warfarin is necessary (Karazisi et al., 2017). Unfortunately, long-term anticoagulation therapy is often accompanied by the risk of bleeding. If the patient is young, it will directly affect the patient's life safety and long-term quality of life (Pu et al., 2016). Therefore, surgical procedures need to be optimized to reduce the risk of thrombosis. Some clinicians have suggested that in CAF patients with aneurysms, the use of proximal aneurysm closure is effective in reducing the incidence of postoperative fistula thrombosis (Reul et al., 2002; Gowda et al., 2011). However, these are only clinical retrospective studies, more systematic quantitative studies will be needed.

Hemodynamics play an important role in the initiation, formation, and aggregation of thrombosis (Jama et al., 2011; Skorczewski et al., 2013; Liang et al., 2015). In recent years, computational fluid dynamics (CFD) studies have been employed to study hemodynamics (Wu et al., 2020, 2021, 2022; Huo et al., 2021) and evaluate risk of thrombosis in abdominal aortic aneurysm, atrial appendages, aortic dissection, etc. (Georgakarakos et al., 2009; Menichini et al., 2017; Bosi et al., 2018; García-Isla., 2018). In our previous studies, four patient-specific CAF models were studied using CFD (Cao et al., 2019,2020), with conventional hemodynamics parameters such as time-averaged wall shear stress (TAWSS) and oscillatory shear index (OSI) to evaluate the thrombosis risk. The results showed that a proximal occlusion to remove the terminal aneurysm may potentially reduce the post-operative thrombotic risk (Cao et al., 2019), while a terminal occlusion of CAF fistula may increase the risk of thrombosis.

In this study, a two-fluid blood stasis model (Jiang et al., 2021a; Jiang et al., 2021b; Dai et al., 2021), which can locate the regions of blood stasis both in space and time was used together with conventional hemodynamic parameters such as OSI and TAWSS as well as morphological parameters, to access the influence of occlusion positions to the risk of thrombosis in the fistula of CAF patients. The approach employed in this study can better assist clinicians choosing the correct surgical plan, so that myocardial blood supply can be improved while minimizing the risk of thrombosis in the fistula.

## MATERIALS AND METHODS

### Subject Data

This study used the same patient-specific models as our previous research (Cao et al., 2020). Four patient-specific models were reconstructed based on computed tomography angiography (CTA) images, as shown in **Figure 1**. These four patients were treated between May 2015 and March 2018, with three right coronary fistulas and one left coronary fistula. The parameters of the models are shown in **Table 1**. Patient approval and informed consent were waived off since it is an observational and retrospective study with anonymized data.

In the actual treatment, Patient one and Patient two had distal occlusions, while Patient three and Patient four had proximal occlusions. In this study, each patient underwent virtual occlusion of the distal and proximal aneurysm. Therefore, three types of models, i.e., untreated model, aneurysm-reserved model and aneurysm-removed model (as shown in **Figure 1**) were studied for each patient, to simulate three treatments, namely, no treatment, proximal and distal occlusions.

### Mesh

The computational domains of all the four models were divided into two separate parts: the fistula regions and the rest, to facilitate the quantitative analysis of blood stasis in the fistula. Structured grids of 1–1.5 million elements were generated by using

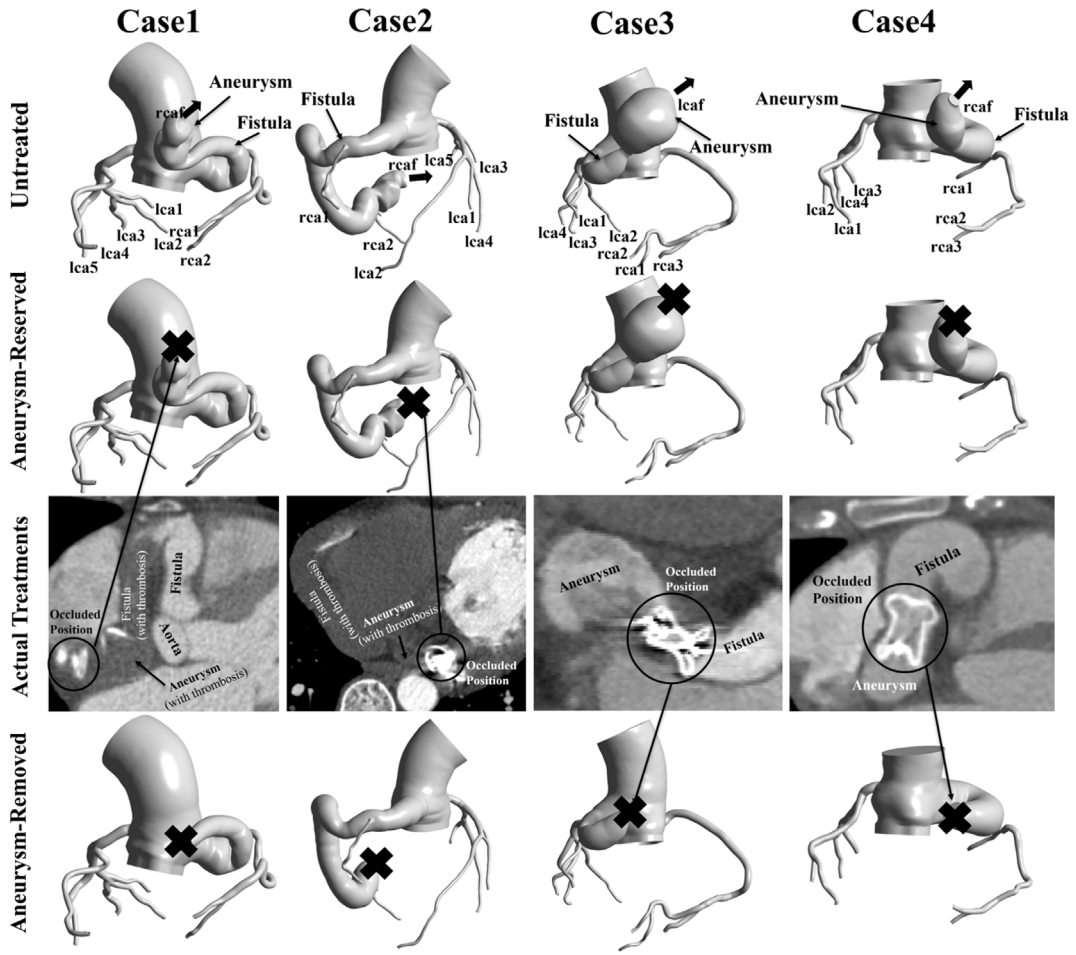


**FIGURE 1 |** Patient-specific models reconstructed from CTA data. "Aneurysm-reserved model" and "Aneurysm-removed model" referred to the proximal or distal occlusions. In actual treatments, case1 and case2 had distal occlusions, while case3 and case4 had proximal occlusions. "X" indicates the occluded position of the model.

**TABLE 1 |** Patient specifics.

| | Gender | Age | Origin and Drainage | $D_E$ | $L_F$ | $D_{MA}$ | $L_A$ | $V_F$ | $V_A$ |
|---|---|---|---|---|---|---|---|---|---|
| Case 1 | Female | 70 | RCA - RA | 16.3 | 130.2 | 40.8 | 39 | 20,262 | 7,055 |
| Case 2 | Male | 25 | RCA - LV | 17.6 | 227.6 | 20.5 | 31.1 | 33,230 | 923 |
| Case 3 | Female | 46 | LCA - RA | 14.2 | 105.5 | 45.7 | 42.2 | 41,788 | 35,367 |
| Case 4 | Female | 27 | RCA - RA | 21.5 | 99.8 | 23.5 | 31.2 | 32,343 | 9,810 |

*RCA, right coronary artery; LCA, left coronary artery; RA, right atrium; LV, left ventricle. $D_E$, average diameter of fistula entrance (mm); $L_F$, length of fistula (mm); $D_{MA}$, max diameter of aneurysm (mm); $L_A$, length of aneurysm (mm); $V_F$, volume of fistula ($mm^3$); $V_A$, volume of aneurysm ($mm^3$).*

commercial software Ansys Meshing (Ansys, Inc., Canonsburg, PA, United States). Five grid layers were added to all the arterial walls to properly resolve the boundary layer, as shown in **Figure 2**.

## Boundary Conditions

As shown in **Figure 3A**, a time-varying volumetric flow rate extracted from the literature was applied at the inlet of each model with a period of 1s (Cheng et al., 2014). Windkessel RCR boundary conditions (**Figure 3B**) and lumped parameter network (LPN) coronary model (**Figure 3C**) were applied at the aortic outlet and the coronary outlets, respectively (Reul et al., 2002; Cheng et al., 2014; Cao et al., 2020). The total resistance ($R_{total}$) of each case were shown in **Table 2**, and in the Windkessel model, the distal resistance was set to $0.91R_{total}$, the proximal resistance was set to 0.09 $R_{total}$, and

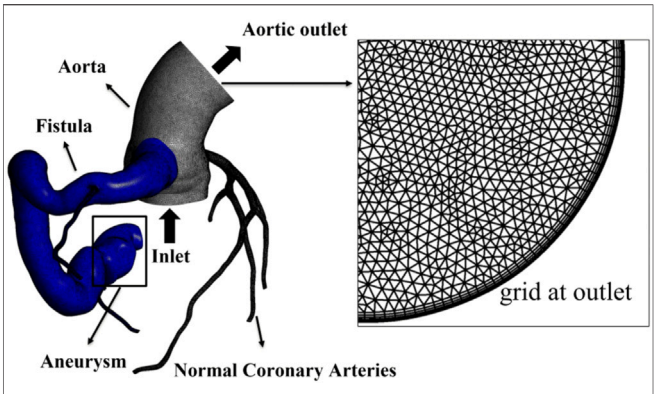


**FIGURE 2 |** Computational domain and mesh of case 2, with local grid at the aortic outlet showing five boundary layers. The fistula region is indicated by blue part.

the capacitance was set to 0.001 $cm^5$/dyne. The outlet of the fistula was set to "wall" to represent the occlusion. All the walls were assumed to be rigid with no slip conditions.

## Numerical Simulations

In this study, all the simulations were transient and conducted using the commercial software Ansys Fluent (Ansys, Inc, Canonsburg, PA, United States). Blood was regarded as incompressible Newtonian fluids, with density of 1055 $kg/m^3$, and dynamic viscosity of $3.5 \times 10^{-3}$ Pa s. Since the flow in aorta might lie in turbulence flow regime (Bigras 2020; Mandell et al., 2021; Manchester et al., 2022), the RNG k-ε model was employed to solve for turbulence. The near-wall treatment was set as standard wall function. A second-order implicit backward Euler scheme was chosen for temporal discretization, with a fixed time-step of 10 ms so that per cardiac cycle was resolved using 100 time steps. Maximum 50 sub-iterations were used for each physical time step, and the maximum RMS residual was set to $10^{-5}$ as a convergence criterion. First, unsteady single-fluid simulations were carried out for about 10 cardiac cycles to get statistically converged flow field.

Then, a two-fluid model for blood stasis was employed to simulate the process of blood washout and stasis (Jiang et al., 2021a; Jiang et al., 2021b; Dai et al., 2021). Simulation of blood stasis continued from the converged single-fluid flow field. A new fluid was defined with the same material properties as the existing

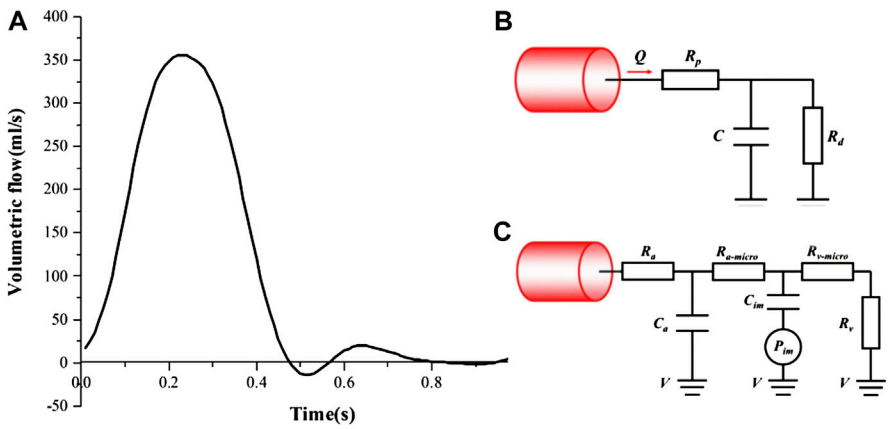


**FIGURE 3 |** Boundary conditions: **(A)** The inlet velocity profile; **(B)** Windkessel RCR boundary conditions; **(C)** Lumped parameter boundary conditions.

**TABLE 2 |** Total resistance.

| Outlets/Total Resistance (Pa*S/m³) | Case 1 | Case 2 | Case 3 | Case 4 |
|---|---|---|---|---|
| aorta | $2.3171*10^8$ | $2.7095*10^8$ | $1.9165*10^8$ | $2.8273*10^8$ |
| rcaf | $6.8721*10^8$ | $3.7588*10^8$ | — | $3.9499*10^8$ |
| rca1 | $6.2281*10^9$ | $2.7159*10^{10}$ | $4.3397*10^{10}$ | $1.2955*10^{10}$ |
| rca2 | $1.2908*10^{10}$ | $2.7642*10^{10}$ | $2.4138*10^{10}$ | $9.8035*10^9$ |
| rca3 | — | $2.4753*10^{10}$ | $1.1231*10^{10}$ | $1.2419*10^{10}$ |
| lcaf | — | — | $3.7154*10^8$ | — |
| lca1 | $7.7446*10^9$ | $2.6813*10^{10}$ | $3.2448*10^{10}$ | $9.3985*10^9$ |
| lca2 | $7.3605*10^9$ | $1.9396*10^{10}$ | $2.2431*10^{10}$ | $1.5694*10^{10}$ |
| lca3 | $3.9235*10^9$ | $1.8043*10^{10}$ | $1.9728*10^{10}$ | $1.7522*10^{10}$ |
| lca4 | $1.4137*10^{10}$ | $1.9588*10^{10}$ | $2.7451*10^{10}$ | $6.9969*10^9$ |
| lca5 | $1.0121*10^{10}$ | $2.6045*10^{10}$ | — | — |

**TABLE 3 |** Percentage (%) of blood flow rate at the aortic outlets.

| Case/Model | Untreated | Aneurysm-Reserved | Aneurysm-Removed |
|---|---|---|---|
| Case 1 | 69.52 | 72.72 | 87.93 |
| Case 2 | 60.83 | 91.90 | 97.22 |
| Case 3 | 77.82 | 90.36 | 95.54 |
| Case 4 | 57.64 | 89.16 | 97.28 |

blood in the computational domain. Then, the new fluid and the existing blood were defined as two fluids: the "new" and "old" blood. All the computational setup was the same as the single-fluid runs, except that the VOF method was employed to solve for the two-fluid flow field. The volume fraction of the new blood was set as one at the inlet, while that of the old blood was 0 at the inlet. The surface tension was set to be 0. As time evolves, the new blood will gradually replace the old blood. The location of and volume fraction of old blood can be tracked and monitored over time. Convergence criteria was set that the old blood volume fractions (OBVFs, defined as the ratio of residual blood volume to fistula volume) dropped within 1% in the past 10 cardiac cycles for all cases. Due to the disparity in fistula volume and treatment for different cases, 10–60 s (cardiac cycles) were needed to reach convergence. All computations were carried out on a 192-core cluster equipped with 16 Intel Xeon E5-2680 v3 CPUs. The single-fluid simulations normally converged within 1 h, while the blood stasis simulations took less than 1 day.

# RESULTS

## Flow Pattern

The ratio of flow rate at the aortic outlet to the inlet flow rate is shown in **Table 3**, which shows that proximal occlusion of aneurysm indeed effectively improved the phenomenon of blood stealing. The flow streamlines of case 1 at systolic peak were shown in **Figure 4**, after the proximal occlusion, the blood flow in the fistula was significantly less than that of the untreated models.

## Results of TAWSS and OSI

TAWSS and OSI are hemodynamic parameters which are commonly used as metrics to evaluate thrombosis in arterial system. It is generally believed that high OSI (>0.3) and low TAWSS (<10 dyne/cm$^2$) are associated with thrombosis (Nerem et al., 1998; Ward et al., 2001; Himburg et al., 2004; Katritsis et al., 2012). **Figure 5A** shows that TAWSS was generally low in the distal fistula of all the post-treated models, so the results of TAWSS proved that the occlusion treatment will be more prone to thrombosis. However, it can be observed that there was almost no difference in the level of TAWSS in the fistula between different patients and treatments. Thus, TAWSS is not a proper metric for the risk of thrombosis in this scenario. **Figure 5B** shows the OSI contours. In contrast to TAWSS, the OSI was high in the distal fistula of the post-treated models, and low near the junction with aorta. It is also worth noting that the area of high OSI varies greatly among cases, and regions of high OSI can always be observed near the occlusion positions.

## Results of Blood Stasis

The OBVFs of all models is shown in **Figure 6**, where the red color represents the blood residue (old blood), and the transparent color indicates where the old blood had been replaced by new blood. In all models, the old blood in the aorta was eventually replaced by new blood. Comparing the distribution of blood residue, there was almost no blood residue in the fistula of the untreated model, while for the post-treated model, the blood residue at the distal fistula was significantly higher than other regions, indicating that this region was prone to blood stasis. This phenomenon was more obvious in the aneurysm-reserved models and it can be observed that the distal occlusion was associated with the most serious blood stasis, among the three ways fistulas were treated. The distributions of blood residue in the aneurysm-removed and aneurysm-reserved models were generally consistent, except for the aneurysm. As shown in **Figure 6**, for case3 and case4, the high OBVF regions (red part) in proximal occluded models were significantly smaller than that in distal occluded models. However, for case1 and case2,

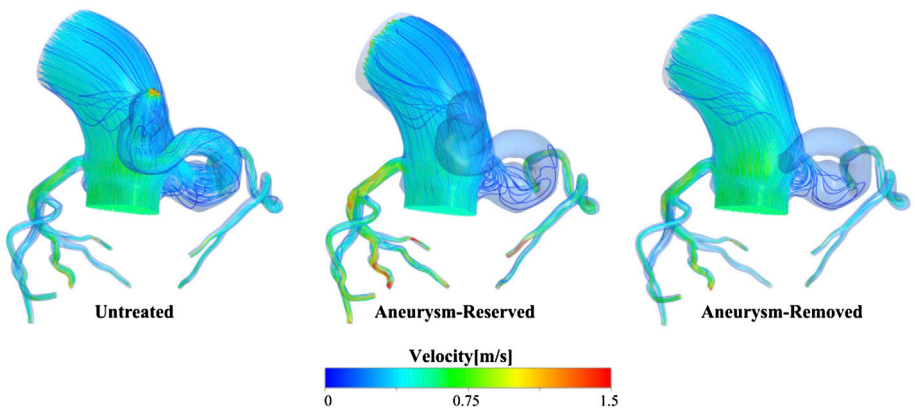


**FIGURE 4 |** Streamlines of case 1 at systolic peak.

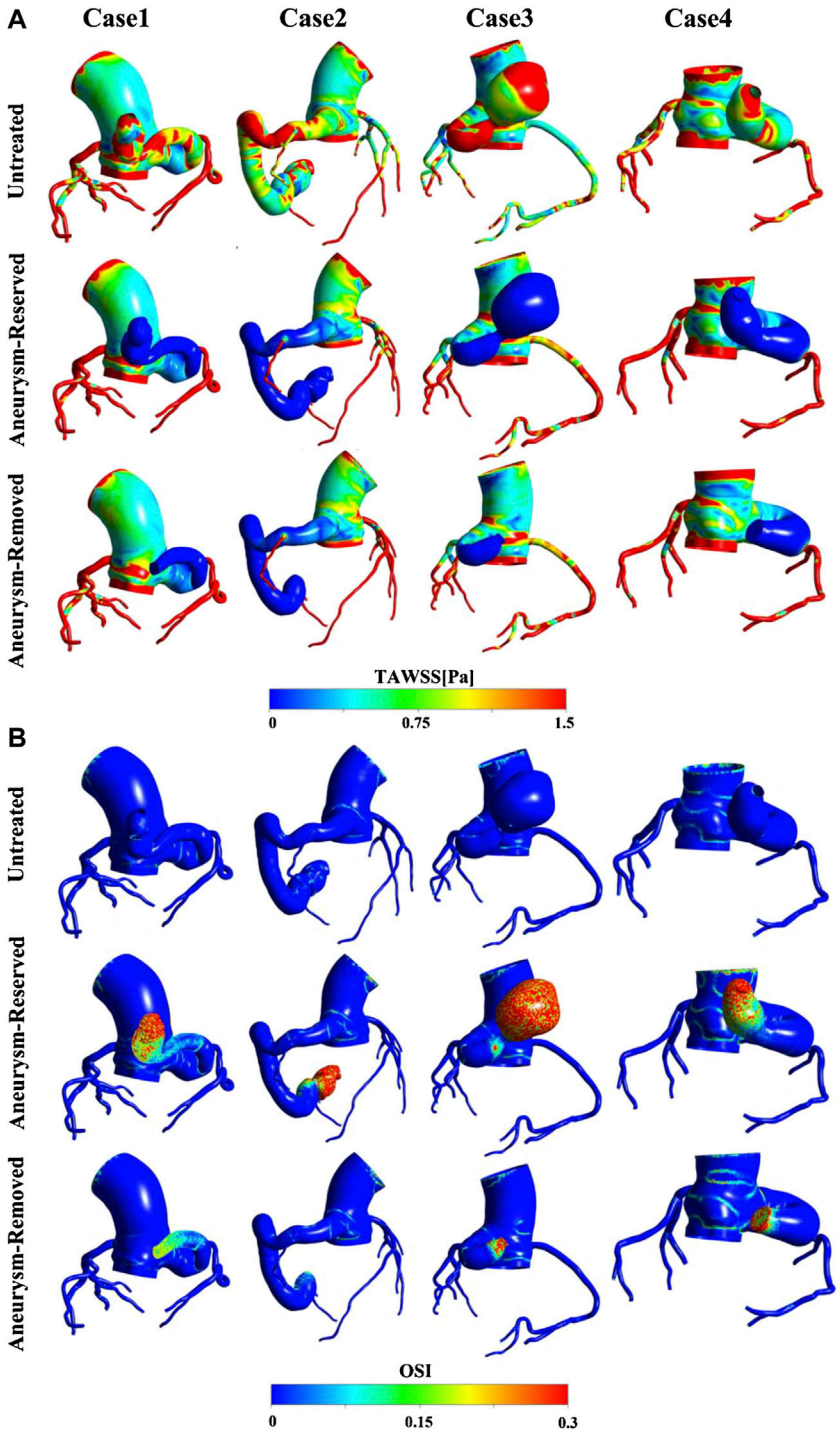


**FIGURE 5 | (A)** TAWSS contours; **(B)** OSI contours.

the differences between two occluded positions were not obvious.

## Comparison With Clinical Follow-Ups

**Figure 7** shows the clinical follow-ups after a short period of time, together with the predicted old blood residue, OSI and TAWSS contours of the actual treatment models. It can be observed that severe thrombosis occurred in the fistulas of case1 (1 week) and case2 (9 months) after the distal aneurysm occlusions, while no thrombosis was found in the fistulas of case3 (3 weeks) and case4 (1 month) after the proximal aneurysm occlusions. It can be observed that the location of thrombosis was consistent with the predicted old

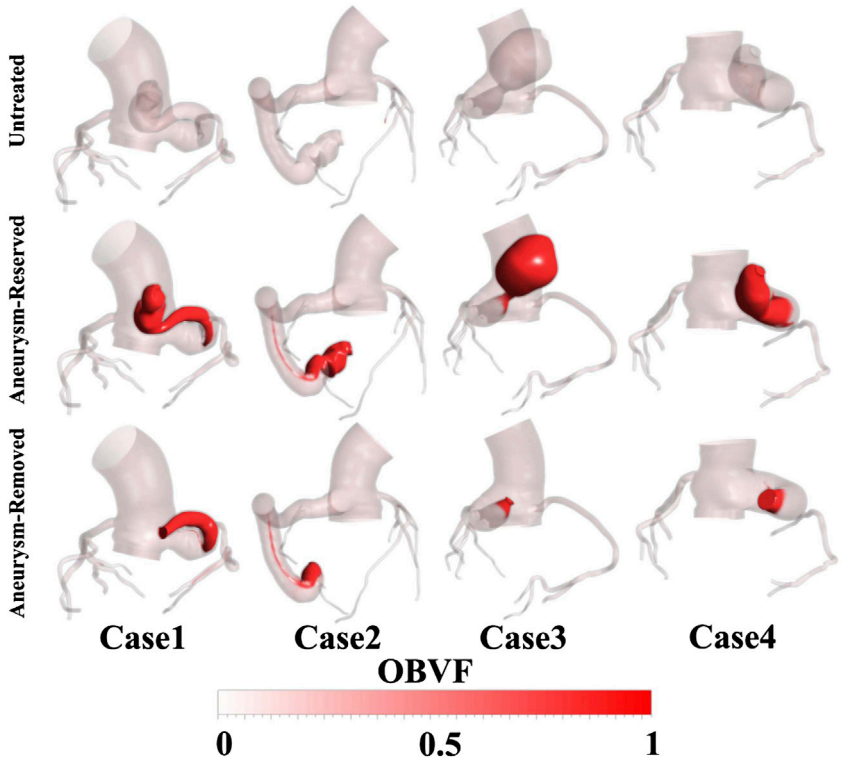


**FIGURE 6 |** The OBVFs of all models, with the red color representing the blood residue.

blood residue. Moreover, the regions where blood residue remained were also roughly regions of high OSI (>0.3). In contrast, the TAWSS contours failed to reflect the actual thrombus in the fistula.

## Quantitative Comparison Between Patients and Treatments

As shown in **Figure 8**, all the four metrics (proportion of area of high OSI, area of high OSI, OBVF and OBV) distinguished the thrombosis risk of distal and proximal aneurysm occlusions well. All the four metrics decreased for aneurysm-removed models compared to aneurysm-reserved models. Thus, all of them could distinguish the thrombosis risk of distal and proximal aneurysm occlusions for each individual patient.

However, as aforementioned, severe thrombosis occurred in the fistula of case2 after the distal aneurysm occlusions and no thrombosis was found in the fistulas of case4 after the proximal aneurysm occlusions, while the proportions of area of high OSI were roughly the same (cf. **Figure 8A**). On the contrary, as shown in **Figure 8B**, the area of high OSI could distinguish the degree of thrombosis between these two scenarios, so could the metrics of blood stasis (OBVF&OBV).

The degree of difference in the thrombosis risk for the aneurysm-reserved and aneurysm-removed models also determines the type of treatment (proximal occlusion or distal occlusion) to be chosen. **Figures 8C, D** show that, case3 and case4 are more suitable for proximal aneurysm occlusion compared with case1 and case2, for which the OBVF and OBV between the two treatments is not much different. For case1, the OBV (3322 $mm^3$) is the highest among all aneurysm-removed models, which means even under proximal occlusion, the thrombosis risk would still be high, and postoperative long-term anticoagulation is inevitable. Moreover, case1 has the second largest aneurysm size, proximal occlusion will greatly reduce the blood supply of the myocardium. Therefore, case1 is more suitable for distal aneurysm occlusion. For case2, the difference in OBV between the distal and proximal occlusions is less than 50%. Due to the largest fistula size and the smallest aneurysm size, removal of the aneurysm will not have a big impact on the blood supply. Therefore, either treatment can be applied to case2, subject to patient conditions and intraoperative conditions. These conclusions are also in line with the actual clinical treatments and observations. On the other hand, the OSI metrics (cf. **Figure 8B**) suggest a proximal occlusion for case 2, and a distal occlusion for case4, which are contradictory to the metrics of blood stasis as well as clinical observations.

# DISCUSSION

Improving blood-stealing phenomena is the primary goal of CAF treatment, and it is effective in maintaining long-term outcomes by reducing the risk of post-treated fistula

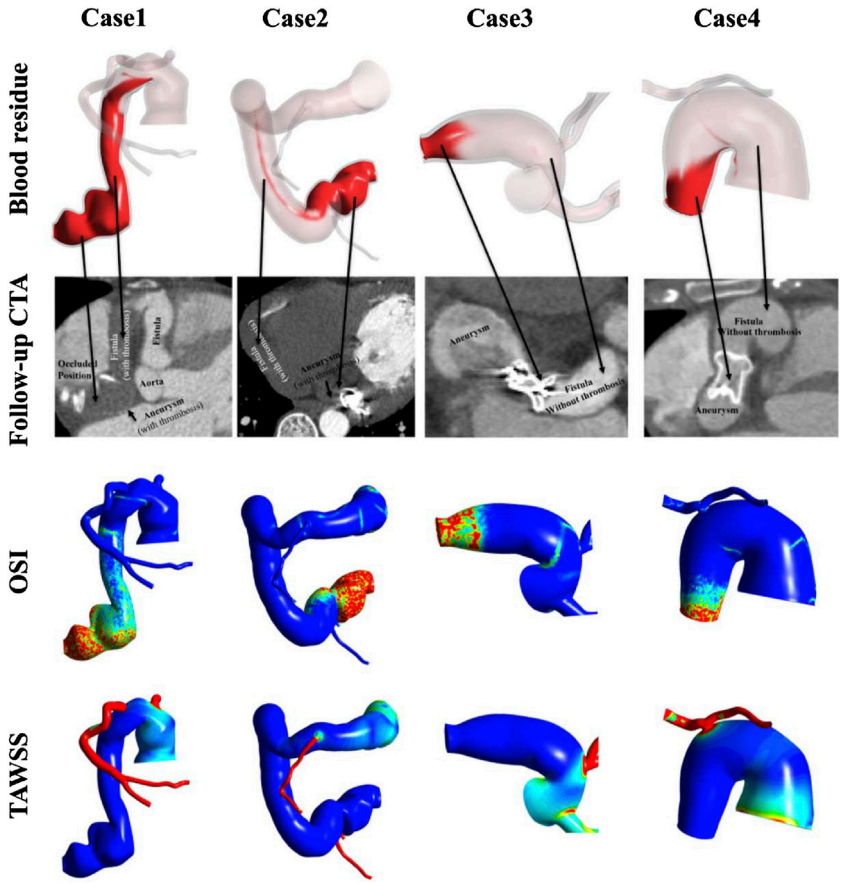


**FIGURE 7 |** Comparison of blood residue, the follow-up CT after the occlusion operation, and contours of OSI and TAWSS (in order from top to bottom) of the models under actual treatments.

thrombosis. This study shows both distal and proximal aneurysm occlusions can reduce the blood flow of fistula, and the percentage of ascending aorta blood flow all increased to close normal value (96%), which corresponds well with our prior study (Cao et al., 2020). On the other hand, the indication of anticoagulation is the most critical issue for occluded CAF patients. According to the American Heart Association (AHA) guidelines, postoperative anticoagulation is required if the maximum diameter of the fistula is greater than 8 mm (Sengupta et al., 2012). As shown in **Table 1**, the average fistula diameters of four patients were all above this value, requiring a long-term anticoagulation for all patients. However, the fistula is a complex structure, the maximum diameter is not sufficient to determine the risk of thrombosis, and there are currently no suitable criteria for the selection of the occluded position (proximal or distal to the aneurysm). Therefore, it is crucial to find a method to evaluate the degree of thrombosis in the fistula. In our previous study (Cao et al., 2020), the proportion of high OSI areas (>0.3) were used as a metric for risk of thrombosis. Nonetheless, this study shows that area of high OSI other than percentage is a more proper metric for thrombosis, and more accurate for inter-patient comparison.

This study also employed two metrics of blood stasis, i.e. OBVF and OBV, to evaluate thrombosis potential in the fistula. The predicted location of blood residue was roughly consistent with clinical follow-ups for post-treated patients, and also with the high OSI regions. Moreover, the differences in the absolute values (area of high OSI, OBV) between the aneurysm-reserved and aneurysm-removed models were more pronounced than the percentage values (proportion of areas of high OSI, OBVF). The reason for this is that the percentage values are normalized using the surface area or volume of fistula, which also decreased if the aneurysms are removed. Therefore, the absolute values may reflect the degree of thrombosis risk more accurately than the percentage values.

The treatments type decided upon the OBVs is roughly in line with the actual clinical treatment. Nonetheless, this study also shows that OBV is superior to the area of high OSI in determining treatment type (proximal or distal occlusion). This problem can be understood from the nature of the OSI, which is an indicator of oscillatory flows, and believed to play roles in the vessel remodeling and plaque development in arteries (Katritsis et al., 2012). On the other hand, the primary cause of CAF thrombosis is blood stagnation and stasis in the regions proximal to dead ends, which is a "volumetric" process. Therefore, OSI as a metric defined at the wall to account for plaque growth, might not be

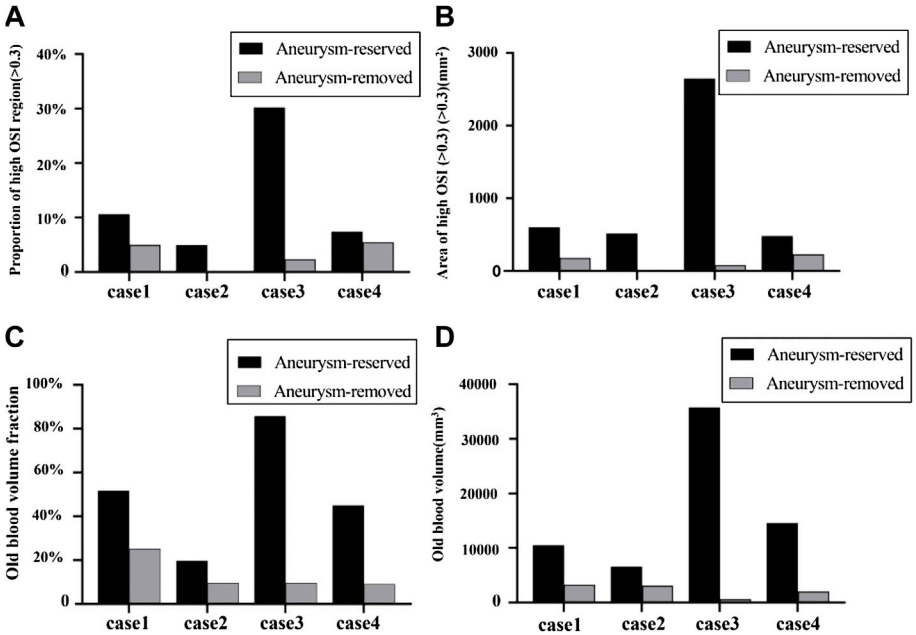


**FIGURE 8 |** Quantitative comparison between patients and treatments in terms of OSI and blood stasis: **(A)** proportion of high OSI (>0.3) regions; **(B)** area of high OSI (>0.3) for aneurysm-reserved and aneurysm-removed models; **(C)** OBVF (old blood volume fraction, defined as the ratio of volume of blood residue and volume of the fistula); **(D)** OBVs (old blood volume).

appropriate to reflect the "volumetric" thrombosis in the fistula, and may misjudge the risk of thrombosis. In contrast, the OBV, a volumetric parameter reflecting the degree of blood stasis, is a more appropriate metric for thrombosis in the fistula. In the future, clinicians may choose an appropriate occluded position according to the predicted fistula OBVs of different treatments. If the OBVs between the two surgical treatments is significantly different, proximal occlusion should be directly selected. If not, morphological parameters need to be involved to opt for the most appropriate treatment based on the relative size of the aneurysm.

## Limitation

This study also has some limitations. First, thrombosis is a very complex process, this study only considered one element in Virchow's triad, i.e. blood stasis. Since the flow is largely in a stagnant state, endothelial injury due to high WSS is unlikely to happen here. The last factor, i.e. hypercoagulability might influence the thrombosis, and should be considered in the future. Second, this study did not consider the non-Newtonian properties of blood, because it has been reported to hardly affect the hemodynamic parameters of the coronary arteries (Kabinejadian and Ghista, 2012; Vimmr et al., 2013; Frolov et al., 2016). Third, there are two types of multiphase flows, namely, disperse flows and separated flows (Brennen, 2005). The formation of thrombosis is more of disperse flows, while the interaction of the new and old blood over time is more of separated flows. The model of blood stasis employed in study do not model the formation of thrombosis directly, but model the blood stasis which we believe is the primary cause of the thrombosis in the occluded coronary arterial fistulas. Nonetheless, the VOF method used in this study to model blood stasis can handle both separate and dispersed flows. Fourth, since this study is purely retrospective, the four patients investigated in this study only had CTA images shortly after operations. Clinical follow-ups at more time points can better follow the process of thrombosis, which will provide better reference for thrombosis prediction. Moreover, as a retrospective study, patient-specific waveforms were not available. In the future, patient-specific flow rates should be measured and a sensitivity analysis for boundary conditions should be conducted in the follow-up study. Finally, the number of patients investigated in this study is limited, more patients will be needed in future research to make the results statistically significant. In the future, more patients and more CTA images at various time points will be collected to provide better reference for thrombosis prediction. *In vitro* experiments such as microfluidics and animal experiments are also planned to improve our findings.

## CONCLUSION

In conclusion, the blood stasis model is more intuitive and accurate to simulate the thrombosis risk of postoperative fistulas than the OSI and TAWSS. Together with morphological parameters, the OBV could guide clinicians to formulate more appropriate surgical plans, and provide an efficient non-invasive method for evaluating the risk of thrombosis in the post-treated fistula, which is of great significance for the preoperative evaluation and treatment prognosis of CAF patients.

## DATA AVAILABILITY STATEMENT

The raw data supporting the conclusion of this article will be made available by the authors, without undue reservation.

## ETHICS STATEMENT

The studies involving human participants were reviewed and approved by The Medical Ethic Committee of Nanjing Drum Tower Hospital. Written informed consent for participation was not required for this study in accordance with the national legislation and the institutional requirements. Written informed consent was not obtained from the individual(s) for the publication of any potentially identifiable images or data included in this article.

## AUTHOR CONTRIBUTIONS

TZ, XL, and HC: data collection. XJ and ZZ: computational modelling and results analysis. XJ: drafting of the manuscript. PW: study concept and design, critical revision of the manuscript. All authors contributed to manuscript revision, read, and approved the submitted version.

## FUNDING

This study was primarily supported by Natural Science Foundation of China (NSFC, Grant No. 12072216), the Mobility Programme of the Sino-German Center (Grant No. M-0231), and by the NSFC (Grant Nos. 12072214, 81770483, 82070496, 11802253).

## REFERENCES

Akcay, A., Yasim, A., and Koroglu, S. (2009). Successful Surgical Treatment of Giant Main Coronary Artery Fistula Connecting to Right Atrium. *Thorac. Cardiovasc Surg.* 57 (8), 493–495. doi:10.1055/s-0029-1185572

Amin, H., Solankhi, N., and Uzun, O. (2001). Coronary Arterial-Left Ventricular Fistulae. *Heart* 85 (6), 648. doi:10.1136/heart.85.6.648

Bigras, J.-L. (2020). Cardiovascular Risk Factors in Patients with Congenital Heart Disease. *Can. J. Cardiol.* 36, 1458–1466. doi:10.1016/j.cjca.2020.06.013

Bosi, G. M., Cook, A., Rai, R., Menezes, L. J., Schievano, S., Torii, R., et al. (2018). Computational Fluid Dynamic Analysis of the Left Atrial Appendage to Predict Thrombosis Risk. *Front. Cardiovasc. Med.* 5, 34. doi:10.3389/fcvm.2018.00034

Brennen, C. E. (2005). *Fundamentals of Multiphase Flow*. Cambridge University Press.

Cao, H., Qiu, Y., Yuan, D., Yu, J., Li, D., Jiang, Y., et al. (2019). A Computational Fluid Dynamics Study Pre- and Post-fistula Closure in a Coronary Artery Fistula. *Comput. Methods Biomech. Biomed. Engin* 23 (6), 33–42. doi:10.1080/10255842.2019.1699540

Cao, H., Li, D., Li, Y., Qiu, Y., Liu, J., Pu, H., et al. (2020). Role of Occlusion Position in Coronary Artery Fistulas with Terminal Aneurysms: A Hemodynamic Perspective. *Cardiovasc Eng. Tech.* 11 (4), 394–404. doi:10.1007/s13239-020-00468-w

Centella, T., Coca, A., and Collado, R. (2016). Combined Percutaneous and Surgical Treatment of a Large Coronary Artery Fistula Connecting the Left Anterior Descending Artery to the Right Ventricle in an 8-Year-Old Child. *Ann. Pediatr. Card.* 9 (2), 197–198. doi:10.4103/0974-2069.181498

Cheng, Z., Juli, C., Wood, N. B., Gibbs, R. G. J., and Xu, X. Y. (2014). Predicting Flow in Aortic Dissection: Comparison of Computational Model with PC-MRI Velocity Measurements. *Med. Eng. Phys.* 36 (9), 1176–1184. doi:10.1016/j.medengphy.2014.07.006

Dai, W.-F., Wu, P., and Liu, G.-M. (2021). A Two-phase Flow Approach for Modeling Blood Stasis and Estimating the Thrombosis Potential of a Ventricular Assist Device. *Int. J. Artif. Organs* 44 (7), 471–480. doi:10.1177/0391398820975405

Firouzi, A., Alemzadeh-Ansari, M. J., Mohebbi, B., Khajali, Z., Khalilipur, E., Baay, M., et al. (2021). Diverse Transcatheter Closure Strategies in Coronary Artery Fistulas A State-Of-The-Art Approach. *Curr. Problems Cardiol.* 29, 101010. doi:10.1016/j.cpcardiol.2021.101010

Frolov, S. V., Sindeev, S. V., Liepsch, D., and Balasso, A. (2016). Experimental and CFD Flow Studies in an Intracranial Aneurysm Model with Newtonian and Non-newtonian Fluids. *Technol. Health Care* 24 (3), 317–333. doi:10.3233/THC-161132

García-Isla, G., Olivares, A. L., Silva, E., Nuñez-Garcia, M., Butakoff, C., Sanchez-Quintana, D., et al. (2018). Sensitivity Analysis of Geometrical Parameters to Study Haemodynamics and Thrombus Formation in the Left Atrial Appendage. *Int. J. Numer. Meth Biomed. Engng* 34, e3100. doi:10.1002/cnm.3100

Georgakarakos, E., Ioannou, C. V., Volanis, S., Papaharilaou, Y., Ekaterinaris, J., and Katsamouris, A. N. (2009). The Influence of Intraluminal Thrombus on Abdominal Aortic Aneurysm Wall Stress. *Int. Angiol.* 28 (4), 325–333.

Gowda, S. T., Latson, L. A., Kutty, S., and Prieto, L. R. (2011). Intermediate to Long-Term Outcome Following Congenital Coronary Artery Fistulae Closure with Focus on Thrombus Formation. *Am. J. Cardiol.* 107 (2), 302–308. doi:10.1016/j.amjcard.2010.09.018

Haweleh, A. A., Baangood, L., and DeGiovanni, J. V. (2018). Transcatheter Closure of Right Coronary Artery Fistula to the Right Ventricle. *J. Saudi Heart Assoc.* 30 (1), 47–51. doi:10.1016/j.jsha.2017.01.005

Himburg, H. A., Grzybowski, D. M., Hazel, A. L., LaMack, J. A., Li, X.-M., and Friedman, M. H. (2004). Spatial Comparison between Wall Shear Stress Measures and Porcine Arterial Endothelial Permeability. *Am. J. Physiology-Heart Circulatory Physiology* 286 (5), H1916–H1922. doi:10.1152/ajpheart.00897.2003

Huo, J.-D., Wu, P., Zhang, L., and Wu, W.-T. (2021). Large Eddy Simulation as a Fast and Accurate Engineering Approach for the Simulation of Rotary Blood Pumps. *Int. J. Artif. Organs* 44 (11), 887–899. doi:10.1177/03913988211041636

Iskandrian, A. S., Kimbiris, D., Bemis, C. E., and Segal, B. L. (1978). Coronary Artery to Pulmonary Artery Fistulas. *Am. Heart J.* 96 (5), 605–609. doi:10.1016/0002-8703(78)90196-5

Jama, A., Barsoum, M., BjarnasonHolmes, H., Jr, Holmes, D. R., and Rihal, C. S. (2011). Percutaneous Closure of Congenital Coronary Artery Fistulae. *JACC Cardiovasc. Interv.* 4 (7), 814–821. doi:10.1016/j.jcin.2011.03.014

Jiang, X. D., Da, L., Wu, P., Li, X. Q., and Zheng, T. H. (2021b). A Two-Fluid Blood Stasis Model for False Lumen Thrombosis after Type B Dissection Repair. *Comput. Methods Biomech. Biomed. Engin*. doi:10.1080/10255842.2021.2018421

Jiang, X. D., Gu, X. P., Xu, T. Z., Li, X. Q., Wu, P., and Sun, L. L. (2021a). Patient-specific Hemodynamic Analysis of IVCS-Induced DVT. *Comput. Methods Biomech. Biomed. Engin*. doi:10.1080/10255842.2021.2003791

Kabinejadian, F., and Ghista, D. N. (2012). Compliant Model of a Coupled Sequential Coronary Arterial Bypass Graft: Effects of Vessel Wall Elasticity and Non-newtonian Rheology on Blood Flow Regime and Hemodynamic Parameters Distribution. *Med. Eng. Phys.* 34 (7), 860–872. doi:10.1016/j.medengphy.2011.10.001

Karazisi, C., Eriksson, P., and Dellborg, M. (2017). Coronary Artery Fistulas: Case Series and Literature Review. *Cardiology* 136 (2), 93–101. doi:10.1159/000447445

Katritsis, D. G., Theodorakakos, A., Pantos, I., Gavaises, M., Karcanias, N., and Efstathopoulos, E. P. (2012). Flow Patterns at Stented Coronary Bifurcations. *Circ. Cardiovasc. Interv.* 5 (4), 530–539. doi:10.1161/circinterventions.112.968347

Kilic, H., Akdemir, R., Bicer, A., and Dogan, M. (2008). Transcatheter Closure of Congenital Coronary Arterial Fistulas in Adults. *Coron. Artery Dis.* 19 (1), 43–45. doi:10.1097/mca.0b013e3282f19ad8

Liang, M. L., Da, X. W., He, A. D., Yao, G. Q., Xie, W., Liu, G., et al. (2015). Pentamethylquercetin (PMQ) Reduces Thrombus Formation by Inhibiting Platelet Function. *Sci. Rep.* 5, 11142. doi:10.1038/srep11142

Manchester, E. L., Pirola, S., Salmasi, M. Y., O'Regan, D. P., Athanasiou, T., and Xu, X. Y. (2022). Evaluation of Computational Methodologies for Accurate Prediction of Wall Shear Stress and Turbulence Parameters in a Patient-specific Aorta. *Front. Bioeng. Biotechnol.* 10, 836611. doi:10.3389/fbioe.2022.836611

Mandell, J. G., Loke, Y.-H., Mass, P. N., Cleveland, V., Delaney, M., Opfermann, J., et al. (2021). Altered Hemodynamics by 4D Flow Cardiovascular Magnetic Resonance Predict Exercise Intolerance in Repaired Coarctation of the Aorta: an *In Vitro* Study. *J. Cardiovasc Magn. Reson* 23 (1), 99. doi:10.1186/s12968-021-00796-3

Menichini, C., Cheng, Z., Gibbs, R. G. J., and Xu, X. Y. (2017). A Computational Model for False Lumen Thrombosis in Type B Aortic Dissection Following Thoracic Endovascular Repair. *J. Biomech.* 66, 36–43. doi:10.1016/j.jbiomech.2017.10.029

Nerem, R. M., Alexander, R. W., Chappell, D. C., Medford, R. M., Varner, S. E., and Taylor, W. R. (1998). The Study of the Influence of Flow on Vascular Endothelial Biology. *Am. J. Med. Sci.* 316, 169–175. doi:10.1097/00000441-199809000-00004

Pu, J., Huang, L., Li, T., Huang, X., Guo, X., and Liu, G. (2016). Trans-catheter Closure of Coronary Artery Fistula in Retrograde Approach. *J. Cardiovasc Pulm. Dis.* 35 (8), 591–594.

Qureshi, S. A. (2006). Coronary Arterial Fistulas. *Orphanet J. Rare Dis.* 1, 51. doi:10.1186/1750-1172-1-51

Reul, R. M., Cooley, D. A., Hallman, G. L., and Reul, G. J. (2002). Surgical Treatment of Coronary Artery Anomalies: Report of a 37 1/2-year Experience at the Texas Heart Institute. *Tex Heart Inst. J.* 29, 299–307.

Saboo, S. S., Juan, Y. H., Khandelwal, A., George, E., Steigner, M. L., Landzberg, M., et al. (2014). Mdct of Congenital Coronary Artery Fistulas. *AJR Am. J. Roentgenol.* 203 (3), W244–W252. doi:10.2214/AJR.13.12026

Sengupta, D., Kahn, A. M., Burns, J. C., Sankaran, S., Shadden, S. C., and Marsden, A. L. (2012). Image-based Modeling of Hemodynamics in Coronary Artery Aneurysms Caused by Kawasaki Disease. *Biomech. Model Mechanobiol.* 11 (6), 915–932. doi:10.1007/s10237-011-0361-8

Skorczewski, T., Erickson, L. C., and Fogelson, A. L. (2013). Platelet Motion Near a Vessel Wall or Thrombus Surface in Two-Dimensional Whole Blood Simulations. *Biophysical J.* 104 (8), 1764–1772. doi:10.1016/j.bpj.2013.01.061

Verdini, D., Vargas, D., Kuo, A., Ghoshhajra, B., Kim, P., Murillo, H., et al. (2016). Coronary-Pulmonary Artery Fistulas. *J. Thorac. Imaging* 31 (6), 380–390. doi:10.1097/rti.0000000000000232

Vimmr, J., Jonášová, A., and Bublík, O. (2013). Numerical Analysis of Non-newtonian Blood Flow and Wall Shear Stress in Realistic Single, Double and Triple Aorto-Coronary Bypasses. *Int. J. Numer. Meth. Biomed. Engng.* 29 (10), 1057–1081. doi:10.1002/cnm.2560

Ward, M. R., Tsao, P. S., Agrotis, A., Dilley, R. J., Jennings, G. L., and Bobik, A. (2001). Low Blood Flow after Angioplasty Augments Mechanisms of Restenosis. *Atvb* 21, 208–213. doi:10.1161/01.atv.21.2.208

Wu, P., Gross-Hardt, S., Boehning, F., and Hsu, P.-L. (2020). An Energy-Dissipation-Based Power-Law Formulation for Estimating Hemolysis. *Biomech. Model Mechanobiol.* 19 (2), 591–602. doi:10.1007/s10237-019-01232-3

Wu, P., Huo, J., Dai, W., Wu, W.-T., Yin, C., and Li, S. (2021). On the Optimization of a Centrifugal Maglev Blood Pump through Design Variations. *Front. Physiol.* 12, 699891. doi:10.3389/fphys.2021.699891

Wu, P., Huo, J. D., Zhang, Z. J., and Wang, C. J. (2022). The Influence of Non-conformal Grid Interfaces on the Results of Large Eddy Simulation of Centrifugal Blood Pumps. *Artif. Organs* 00, 1–13. doi:10.1111/aor.14263

**Conflict of Interest:** The authors declare that the research was conducted in the absence of any commercial or financial relationships that could be construed as a potential conflict of interest.

**Publisher's Note:** All claims expressed in this article are solely those of the authors and do not necessarily represent those of their affiliated organizations, or those of the publisher, the editors and the reviewers. Any product that may be evaluated in this article, or claim that may be made by its manufacturer, is not guaranteed or endorsed by the publisher.

frontiers | Frontiers in Physiology

ORIGINAL RESEARCH
published: 24 May 2022
doi: 10.3389/fphys.2022.898659

# Computational Pressure-Fluid Dynamics Applied to Index of Microcirculatory Resistance, Predicting the Prognosis of Drug-Coated Balloons Compared With Drug-Eluting Stents in STEMI Patients

*Yang Duan†, Yiwen Wang†, Min Zhang, Zhi Li, Lei Chen, Hao Miao, Siyu Pei, Yuan Lu* and Zhirong Wang**

*Department of Cardiology, The Affiliated Hospital of Xuzhou Medical University, Xuzhou, China*

OPEN ACCESS

**Edited by:**
*Shengzhang Wang,*
*Fudan University, China*

**Reviewed by:**
*Yue Han,*
*Shanghai Jiao Tong University, China*
*Anqiang Sun,*
*Beihang University, China*

***Correspondence:**
*Yuan Lu*
*luyuan329@163.com*
*Zhirong Wang*
*xzzrw@163.com*

*†These authors have contributed equally to this work*

**Specialty section:**
*This article was submitted to Computational Physiology and Medicine, a section of the journal Frontiers in Physiology*

**Received:** *17 March 2022*
**Accepted:** *21 April 2022*
**Published:** *24 May 2022*

**Citation:**
*Duan Y, Wang Y, Zhang M, Li Z, Chen L, Miao H, Pei S, Lu Y and Wang Z (2022) Computational Pressure-Fluid Dynamics Applied to Index of Microcirculatory Resistance, Predicting the Prognosis of Drug-Coated Balloons Compared With Drug-Eluting Stents in STEMI Patients. Front. Physiol. 13:898659. doi: 10.3389/fphys.2022.898659*

**Background:** The impairment of microvascular injury on prognosis has increasingly drawn extensive awareness along with the high morbidity and mortality of ST-segment elevation myocardial infarction (STEMI) over recent years. The prognostic significance of computational pressure-fluid dynamics applied to index of microcirculatory resistance, derived from coronary angiography (CPFD-caIMR) in microvascular injury evaluation of STEMI patients remained inconclusive.

**Methods:** A total of 213 patients who met the inclusion criteria were selected retrospectively from 1003 STEMI patients from February 2018 to February 2020. Propensity score matching (PSM) was thereafter finished. CPFD-caIMR of all patients was obtained off-line using the software (FlashAngio, Rainmed Ltd., Suzhou, China) after PPCI. The primary endpoint was to compare the CPFD-caIMR and the incidence of major adverse cardiovascular events (MACEs) between drug-coated balloons (DCB) and drug-eluting stents (DES) groups. The correlation between CPFD-caIMR and MACEs was analyzed, and the prognosis of patients with STEMI was evaluated by CPFD-caIMR by multivariate regression analysis.

**Results:** Totally 213 STEMI patients with successful primary percutaneous coronary intervention (PPCI) were included, of whom 84 patients accepted DCB and 129 patients accepted DES respectively. Baseline characteristics and CPFD-caIMR were comparable between DCB and DES groups after PSM (62 patients in each group). CPFD-caIMR was not significantly different between two groups (DES vs. DCB: mean difference: 2.26, 95% CI -4.05 to 8.57, $p = 0.45$), and so was it when re-grouped by whether CPFD-caIMR > 40U or not (DES vs. DCB: 34.17% vs. 27.16%, $p = 0.29$). After a follow-up of 1 year, more MACEs occurred in DES group than DCB group (relative risk: 2.50, 95% CI 1.04 to 6.02, $p = 0.04$). The predictors of MACEs by multi-variate analysis found that, only time from symptom to balloon ($p = 0.03$) and time from door to balloon ($p < 0.01$) were independent predictors of MACEs, independent of treatment with DCB or DES intervention. Furthermore, CPFD-caIMR > 40U

became an independent predictor of the combined events including cardiovascular deaths or heart failure readmission irrespective of PSM (odds ratio: 4.07, 95% CI: 1.06 to 7.66, $p = 0.04$).

**Conclusion:** CPFD-caIMR was a promising method for prognosis, which can predict CV death or heart failure readmission in STEMI patients. DCB was a possible strategy in PPCI of STEMI patients, not inferior to DES based on microvascular injury evaluated by CPFD-caIMR.

**Keywords: computational pressure-fluid dynamics derived index of microcirculatory resistance, drug-coated balloon, ST-segment elevation myocardial infarction, primary percutaneous coronary intervention, retrospective study, major adverse cardiovascular event**

## INTRODUCTION

Microvascular injury is closely related to the prognosis of ST-segment elevation myocardial infarction (STEMI) (Alekseeva et al., 2021). Although the blood flow of criminal vessels is restored to Thrombolysis in myocardial infarction (TIMI) Level 3 after primary percutaneous coronary intervention (PPCI), the myocardium perfusion may not effectively resume with existence of coronary microvascular injury (Jaski et al., 2016). Index of microcirculatory resistance (IMR) was reported as a good index to reflect coronary microcirculation and predict the prognosis of STEMI (Cuculi et al., 2014; Carrick et al., 2016). But it was still perceived as a research tool and its application within clinical practice remains extremely limited due to a complex guide wire measurement, at the state of maximum hyperemia taking the risk of hypotension and arrhythmia (Geng et al., 2022). Computational pressure-fluid dynamics derived index of microcirculatory resistance, applied to coronary angiography (CAG, CPFD-caIMR), without extra steps, was proved to have high correlation and diagnostic accuracy with invasive IMR measured by traditional guidewire (Choi et al., 2021). A non-invasive method utilizing computational fluid dynamics to derive caIMR presented a high accuracy (Abuouf et al., 2021). Nowadays there has been rare studies elucidating the effectiveness of drug-coated balloon (DCB) treatment on the prognosis of STEMI patients with PPCI based on microvascular injury evaluation by CPFD-caIMR.

The occurrence of in-stent restenosis (ISR), late stent thrombosis and bleeding caused by long-term dual antiplatelet therapy (DAPT) gave rise to the new concept of "intervention without implantation" which was first emerging in Europe (De Luca et al., 2008; Neumann et al., 2019; Her et al., 2021). DCB can release effective therapeutic concentration of drugs at the lesion site for a short adherent time, thereby reducing restenosis without leaving foreign objects in the blood vessel (Aboyans et al., 2018). DCB was thereafter recommended as a strategy for coronary artery and peripheral vessels diseases. (Neumann et al., 2019; Her et al., 2021). However, DCB has not been recommended as an alternative of drug-eluting stent (DES) in the high-risk conditions like STEMI (De Luca et al., 2008), (Vos et al., 2014; Ho et al., 2015; Nijhoff et al., 2015; Gobić et al., 2017). From already published randomized controlled trials (RCTs) performed in STEMI patients, DCB presented no significant difference of major adverse cardiovascular events (MACEs) and late lumen loss versus DES with a follow-up of both 1 year and 2 years in the REVELATION trial (Vos et al., 2019; Niehe et al., 2022). Similar results were also manifested from another study with a follow-up of 6 mon (Gobić et al., 2017). The above-mentioned results suggested the potential effectiveness of DCB on the prognosis of STEMI patients, which was not inferior to DES in STEMI.

In this study, we intended to assess the effects of DCB on short and long-term prognosis in STEMI patients receiving PPCI by measuring CPFD-caIMR after PPCI, to assess the relationship between CPFD-caIMR and MACEs, and to determine the predictors of MACEs.

## MATERIALS AND METHODS

### Study Design

This study is a retrospective controlled cohort study. 1003 STEMI patients who underwent PPCI in the Affiliated Hospital of Xuzhou Medical University of China from February 2018 to February 2020 were selected. After strict screening, a total of 213 patients were finally included. Among them, 129 patients were treated by DES and 84 patients were treated by DCB. After 1:1 propensity score matching (PSM), 62 patients from each group who matched baseline characteristics were re-analyzed.

### Study Population and Eligibility

Patients were included if 1) STEMI was diagnosed according to current guidelines (Ibanez et al., 2018); 2) Spontaneous reperfusion of the infarct-related artery (IRA) confirmed by CAG or low-burden thrombus after percutaneous transluminal coronary angioplasty (PTCA) and patients accepted successful PPCI; 3) with complete and available follow-up more than a year; 4) the quality of angiography images met requirements of reconstruction.

Patients were excluded if they are combined with: 1) history of PCI or coronary artery bypass grafting; 2) severe liver and renal dysfunction; 3) occlusive lesions or severe distorted calcified lesions; 4) iodine contrast agent allergy or contraindication of adenosine drugs; 5) severe coagulation dysfunction or hemorrhagic diseases; 6) target lesions involving myocardial

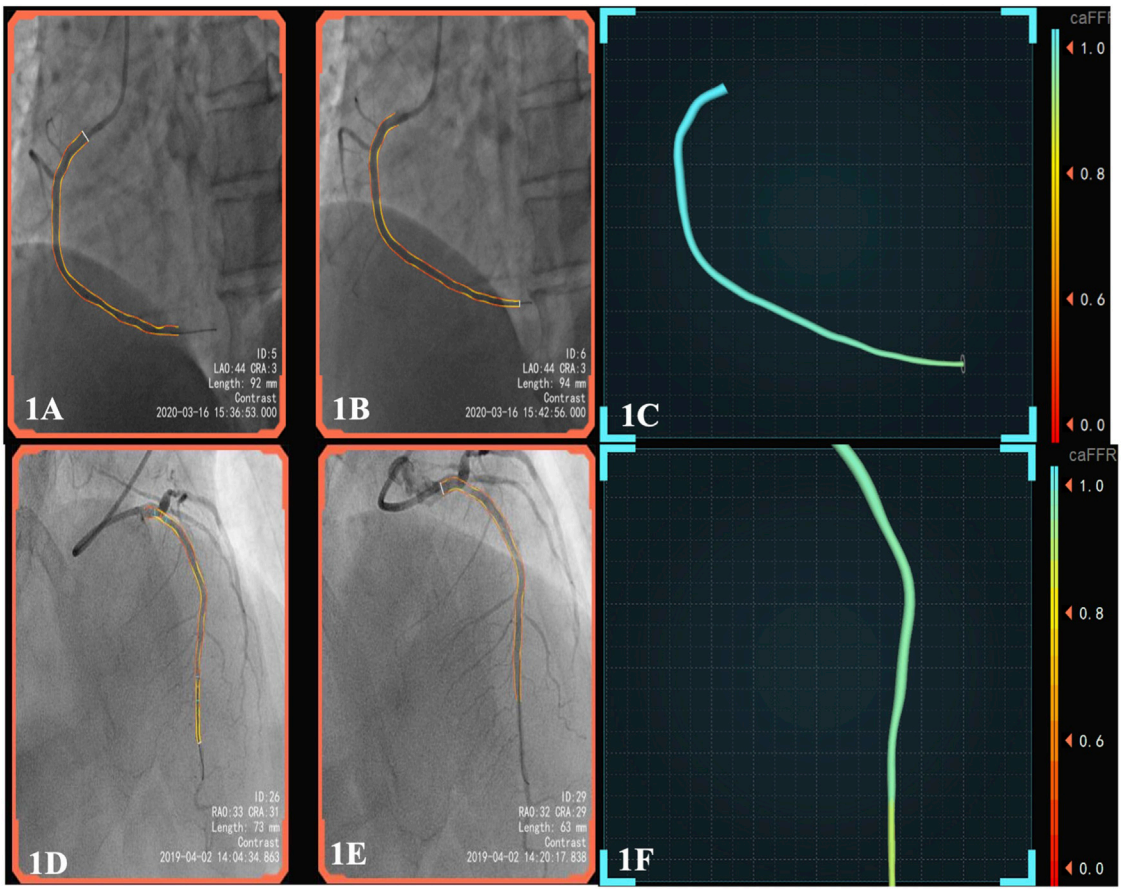


**FIGURE 1 | (A)**, pre-surgery angiography; **(B)**, post-surgery of DCB; **(C)**, the patient's post-operative caFFR was normal and calMR was high (caFFR = 0.92, calMR = 42.1). After 6 months of follow-up, the patient had myocardial infarction again.; **(D)**, pre-surgery angiography; **(E)**, post-surgery of DES; **(F)**, the patient's postoperative caFFR and calMR (caFFR = 0.91, calMR = 22.8) were normal and no MACEs events occurred in 1.5 years of follow-up. Abbreviations: caFFR, coronary angiography-derived fractional flow reserve; calMR, coronary-angiography-derived index of microcirculatory resistance; DES, drug-eluting stents; DCB, drug-coated balloons; MACE, major adverse cardiovascular events.

bridge; 7) lesions located within 3 mm (excluding 3 mm) at the ostial of the ascending aorta.

## Study Procedures

### PPCI Procedure

The medical treatments were performed by the same team, according to updated guidelines of STEMI (Ibanez et al., 2018). All patients administered the loading doses of DAPT before the surgery and received PPCI within 90 min after first medical contact (Neumann et al., 2019). Trans-radial or femoral artery was punctured and catheterized to conduct coronary angiography. During the procedure, IRA was merely intervened, using a 70–100 u/kg dosage of unfractionated heparin. GPIIB/IIIA receptor antagonists depended on the individual situation. Patients were selected if lesions had spontaneous reperfusion of the IRA or low-burden thrombus after PTCA confirmed by CAG. And all patients gave the written informed consent in the PPCI process.

The procedure of DCB group: After adequate pre-dilation, 200 ug nitroglycerin was injected to the IRA until the blood flow was restored to TIMI grade 3, with less than 20% residual stenosis and without dissection or dissection below type B. The size of DCB was determined by the diameter of the normal segment of IRA The ratio of the DCB diameter to the artery diameter was 1.0-1.1:1, and the length of DCB should be 3–5 mm beyond the target lesion, with dilation lasting from 40 to 60 s. Considering the comparability of follow-up, patients using Sequent Please DCBs were only selected in this study (B. Braun, Melsungen, Germany). Success criteria: the blood flow of IRA reached TIMI grade 3, residual stenosis less than 20%.

The procedure of DES group: After catheterization, the lesion was first treated by pre-dilated balloon with a low pressure (8–12 atm), using the double guide wire or cutting balloon for adequate dilation if necessary. Then 200 ug nitroglycerin was injected to the IRA and angiography was repeated. The size of DES accorded with the diameter of the IRA. The ratio of stent diameter to target artery diameter was 1.1-1.2:1.0. In case of stent malapposition observed from repeated angiography, the non-compliant balloon would be used for post-dilation. The second-generation DES was used

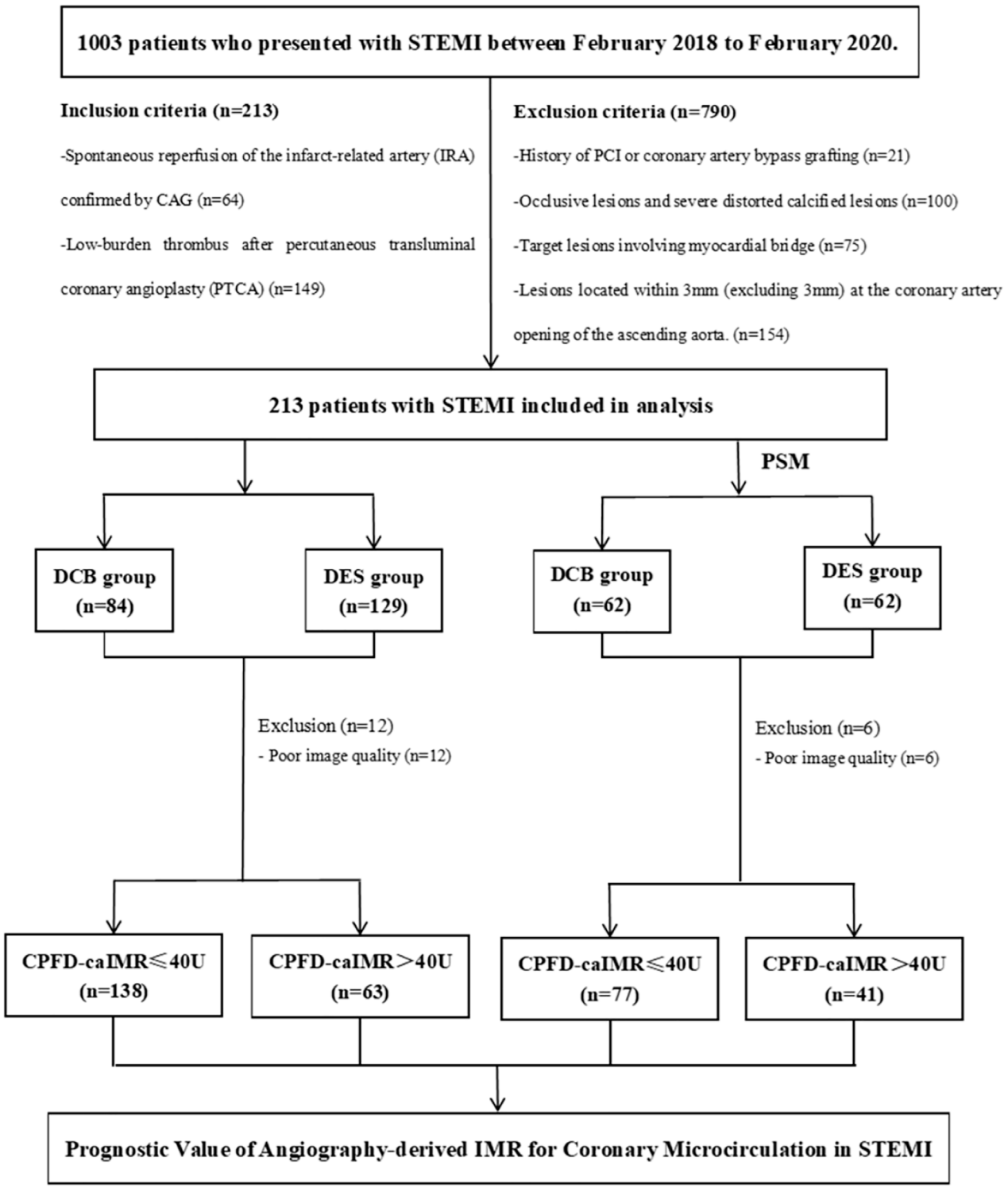


**FIGURE 2 |** The flow-chart of the study in detail. Abbreviations: STEMI, ST-segment elevation myocardial infarction; PCI, percutaneous coronary intervention; CPFD, computational pressure-fluid dynamics; caIMR, coronary-angiography-derived index of microcirculatory resistance; DES, drug-eluting stents; DCB, drug-coated balloons; MACE, major adverse cardiovascular events.

**TABLE 1 |** Baseline characteristics of the study population.

| Variable | Group DES | Group DCB | *p* value | Total |
|---|---|---|---|---|
| General characteristics | N = 129 | N = 84 | | N = 213 |
| Age, y, Mean (SD) | 56.91 (12.27) | 60.52 (14.11) | 0.05 | 58.34 (13.11) |
| Males, n (%) | 109 (84.50) | 70 (83.33) | 0.85 | 179 (84.04) |
| Systolic BP, mmHg, Mean (SD) | 123.15 (17.93) | 131.04 (18.32) | **<0.01** | 126.26 (18.45) |
| Heart rate, /min, Mean (SD) | 79.40 (15.92) | 75.57 (15.13) | 0.08 | 77.89 (15.69) |
| Body mass index, kg/m$^2$, Mean (SD) | 25.94 (4.74) | 25.06 (3.22) | 0.14 | 25.59 (4.22) |
| Hypertension, n (%) | 68 (52.71) | 37 (44.05) | 0.26 | 105 (49.30) |
| Diabetes, n (%) | 19 (14.73) | 19 (22.62) | 0.15 | 38 (17.84) |
| Smoking, n (%) | 68 (52.71) | 37 (44.05) | 0.26 | 105 (49.30) |
| Time from symptom to balloon, hours, Mean (SD) | 6.56 (3.44) | 7.30 (2.98) | 0.11 | 6.85 (3.28) |
| Killip level, n (%) | | | | |
| I | 116 (89.92) | 78 (92.86) | 0.33 | 194 (91.08) |
| II | 8 (6.20) | 4 (4.76) | | 12 (5.63) |
| III | 2 (1.55) | 2 (2.38) | | 4 (1.89) |
| IV | 3 (2.33) | 0 | | 3 (1.41) |
| Baseline LVEF and biomarkers | | | | |
| LVEF, %, Mean (SD) | 49.13 (9.88) | 56.54 (7.56) | **<0.01** | 52.05 (9.72) |
| Peak hsTnT, ng/L, Median (IQR) | 3543.00 (4483.00) | 1636.00 (4371.75) | **<0.01** | 2847.00 (4656.50) |
| Peak CK-MB, ng/L, Median (IQR) | 104.91 (163.25) | 71.85 (105.09) | 0.11 | 88.79 (144.67) |
| CRP, Mean (SD) | 12.49 (11.26) | 10.70 (9.08) | 0.22 | 11.78 (10.47) |
| Serum Creatinine, umol/L, Mean (SD) | 69.12 (13.36) | 66.93 (19.18) | 0.33 | 68.26 (15.91) |
| LDL-C, mmol/L, Mean (SD) | 2.72 (0.93) | 2.50 (0.81) | 0.08 | 2.63 (0.89) |
| Medication, n (%) | | | | |
| Asprin | 124 (100) | 89 (100) | NA | 213 (100) |
| P2Y12 inhibitors | 124 (100) | 89 (100) | NA | 213 (100) |
| Statins | 127 (98.45) | 81 (96.43) | 0.39 | 208 (97.65) |
| Beta-blocker | 117 (90.70) | 67 (79.76) | **0.03** | 184 (86.38) |
| RAASI | 97 (75.19) | 54 (64.29) | 0.09 | 151 (70.89) |
| IV diuretics | 61 (47.29) | 17 (20.24) | **<0.01** | 78 (36.62) |

*DES, drug-eluting stents; DCB, drug-coated balloons; SD, standard deviation; IQR, inter-quartile range; BP, blood pressure; PCI, percutaneous coronary intervention; AMI, acute myocardial infarction; LVEF, left ventricular ejection fraction; hsTnT, high sensitivity troponin T; CK-MB, MB isoenzyme of creatine kinase; CRP, C-reactive protein; LDL-C, low-density lipoprotein cholesterol; RAASI, renin-angiotensin-aldosterone system inhibitor; IV diuretics, Intravenous diuretics; NA, not available.*

**TABLE 2 |** Characteristics of PPCI process of the study population.

| Variable | Group DES | Group DCB | *p* value | Total |
|---|---|---|---|---|
| | N = 129 | N = 84 | | N = 213 |
| CPFD-calMR, Mean (SD)[a] | 36.49 (21.04) | 34.23 (23.91) | 0.48 | 35.58 (22.21) |
| CPFD-calMR>40, n (%)[a] | 41 (34.17) | 22 (27.16) | 0.29 | 63 (31.34) |
| Time from Door to balloon, minutes, Mean (SD) | 70.36 (14.16) | 62.18 (16.44) | <0.01 | 67.13 (15.59) |
| Criminal vessel, n (%) | | | | |
| Left anterior descending | 59 (45.70) | 31 (36.90) | 0.08 | 90 (42.30) |
| Left circumflex | 17 (13.18) | 21 (25.00) | | 38 (17.80) |
| Right coronary artery | 53 (41.10) | 32 (38.10) | | 85 (39.90) |
| Multi coronary artery lesions, n (%) | 81 (62.79) | 51 (60.71) | 0.77 | 132 (61.97) |
| IABP, n (%) | 3 (2.33) | 0 | 0.28 | 3 (1.41) |
| Pre-dilated balloon diameter, mm, Mean (SD) | 2.16 (0.28) | 2.64 (0.57) | <0.01 | 2.35 (0.48) |
| Pre-dilated balloon pressure, atm, Mean (SD) | 9.69 (2.04) | 9.69 (2.35) | 0.17 | 9.69 (2.17) |
| DES/DCB diameter, mm, Mean (SD) | 3.09 (0.44) | 2.74 (0.55) | 0.01 | 2.95 (0.51) |
| DES/DCB length, mm, Mean (SD) | 27.57 (6.61) | 24.63 (5.59) | 0.14 | 26.41 (6.38) |
| DES/DCB dilation released pressure, atm, Mean (SD) | 11.74 (2.35) | 9.56 (2.47) | 0.76 | 10.88 (2.62) |
| DES/DCB dilation duration, second, Mean (SD) | 11.01 (8.28) | 67.80 (17.82) | <0.01 | 33.40 (30.65) |

[a]*DES group included 121 patients; DCB groups included 80 patients.*

*PPCI, primary percutaneous coronary intervention; calMR, coronary-angiography-derived index of microcirculatory resistance; DES, drug-eluting stents; DCB, drug-coated balloons; SD, standard deviation; IABP, intra-aortic balloon pump; NA, not available.*

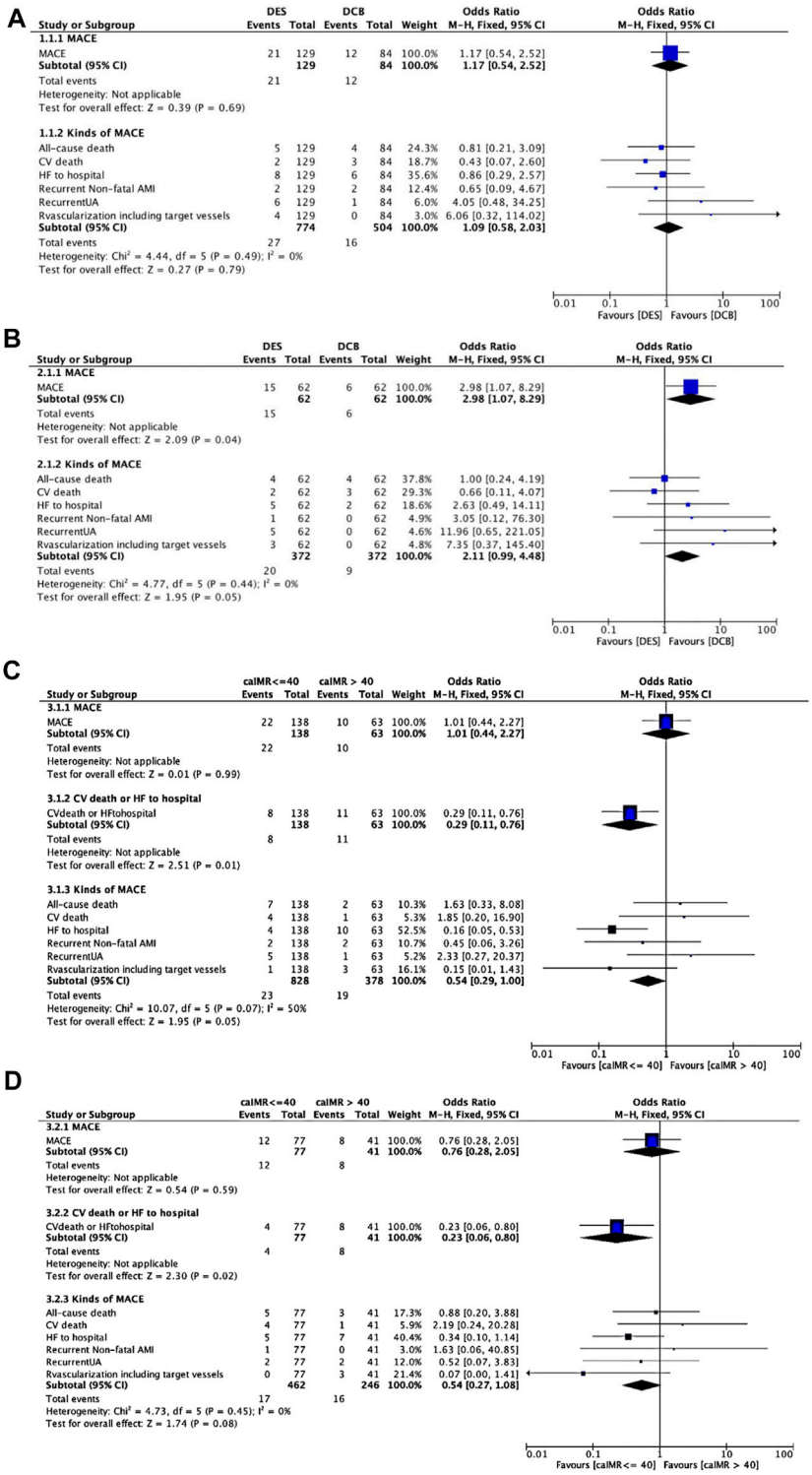


**FIGURE 3 |** MACEs comparing DES and DCB groups. **(A).** MACEs comparing DES and DCB groups before propensity score matching. **(B)**. MACEs comparing DES and DCB groups after propensity score matching. **(C)**. MACEs comparing calMR ≤ 40U and calMR >40U in group DES. **(D)**. MACEs comparing calMR ≤ 40U and calMR >40U in group DCB. Abbreviations: DES, drug-eluting stents; DCB, drug-coated balloons; calMR, coronary-angiography-derived index of microcirculatory resistance; MACE, major adverse cardiovascular events; CV, cardiovascular; HF, heart failure; AMI, acute myocardial infarction; UA, unstable angina; CI, confidence interval.

and no significant difference both in ischemia and bleeding risk was observed before between different kinds of DES (Schapiro-Dufour et al., 2019).

After successful surgery, patients were transferred to coronary care unit (CCU) after surgery for continuously intensive drug therapy.

## CPFD-CaIMR Examination Procedure

The CPFD-IMR measurement was conducted using the software (FlashAngio, Rainmed Ltd., Suzhou, China, **Figure 1**) as described before (Ai et al., 2020). In brief, a three-dimensional reconstruction of coronary arteries was firstly conducted for the target vessels, followed by the estimation of caIMR by CPFD with a validated method (Li et al., 2020).

After DCB or DES treatment, nitroglycerin was injected. After exposure for 1 s, the contrast agent was injected to IRA at a speed of 4 ml/s. The image recording rate was 15 frames/s, and the contrast agent was stably injected for ≥3 cardiac cycles. Angiographic images of two postures were selected through FlashAngio IMR system (the angle between the included two postures ≥30°), generating a three-dimensional model of the targeted coronary artery. Meanwhile, a 3-dimensional mesh reconstruction of the coronary artery was generated along the vessel path from the inlet to the distal segment of the target vessel. We computed the diastolic flow velocity (Vdiastole) by the TIMI Frame Count Method, i.e., diastolic flow velocity = (contrast passing length)/(diastolic time interval), where contrast passing length was the distance that contrast moves in 3D reconstructed coronary arteries during the period of diastole. The choose of diastolic phase was determined based on the motion of the guide catheter tip.

Using the fully automatic coronary angiography-based FlashAngio IMR system (including FlashAngio IMR console, FlashAngio IMR software, and FlashPressure IMR pressure transducer; Rainmed Ltd., Suzhou, China), a novel physiological parameter, caIMR (unit: mmHg·s/mm), is calculated as follows:

$$\mathrm{caIMR} = (P_a)_{hyp} \cdot \mathrm{caFFR} \cdot L/K \cdot \mathrm{Vdiastole} \quad (1)$$

$$\text{where: } \mathrm{caFFR} = (P_d)_{hyp} \big/ (P_a)_{hyp} \quad (2)$$

caFFR is the coronary angiography-derived fractional flow reserve (Ai et al., 2020; Li et al., 2020) that was verified to have a high accuracy compared with wire-based FFR in the previous study, from which we can get:

$$(P_d)_{hyp} = (P_a)_{hyp} \cdot \mathrm{caFFR} \quad (3)$$

**TABLE 3 |** Baseline characteristics of the study population grouped by MACEs.

| Variable | N-MACE | MACE | *p* value |
|---|---|---|---|
| General characteristics | N = 180 | N = 33 | |
| Age, y, Mean (SD) | 57.53 (12.92) | 62.76 (13.50) | **0.04** |
| Males, n (%) | 155 (86.11) | 24 (72.73) | 0.07 |
| Systolic BP, mmHg, Mean (SD) | 125.26 (17.71) | 131.73 (21.55) | 0.06 |
| Heart rate, /min, Mean (SD) | 78.47 (15.98) | 74.73 (13.78) | 0.21 |
| Body mass index, kg/m$^2$, Mean (SD) | 25.74 (4.33) | 24.80 (3.51) | 0.24 |
| Hypertension, n (%) | 85 (47.22) | 20 (60.61) | 0.19 |
| Diabetes, n (%) | 33 (18.33) | 5 (15.15) | 0.81 |
| Smoking, n (%) | 88 (48.89) | 17 (51.52) | 0.85 |
| Time from symptom to balloon, hours, Mean (SD) | 6.37 (3.18) | 9.47 (2.48) | <**0.01** |
| Killip level, n (%) | | | |
| I | 164 (91.11) | 30 (90.91) | 0.84 |
| II | 10 (5.56) | 2 (6.06) | |
| III | 3 (1.67) | 1 (3.03) | |
| IV | 3 (1.67) | 0 | |
| Baseline LVEF and biomarkers | | | |
| LVEF, %, Mean (SD) | 53.07 (9.44) | 46.52 (9.48) | <**0.01** |
| Peak hsTnT, ng/L, Median (IQR) | 2934.50 (4872.75) | 3011.44 (4493.50) | 0.32 |
| Peak CK-MB, ng/L, Median (IQR) | 67.96 (100.12) | 220.00 (153.85) | <**0.01** |
| CRP, Mean (SD) | 11.90 (10.67) | 11.15 (9.39) | 0.71 |
| Serum Creatinine, umol/L, Mean (SD) | 68.79 (15.90) | 65.33 (15.844) | 0.25 |
| LDL-C, mmol/L, Mean (SD) | 2.61 (0.90) | 2.74 (0.86) | 0.45 |
| Medication, n (%) | | | |
| Asprin | 180 (100) | 33 (100) | NA |
| P2Y12 inhibitors | 180 (100) | 33 (100) | NA |
| Statins | 175 (97.22) | 33 (100) | 0.99 |
| Beta-blocker | 154 (85.56) | 30 (90.91) | 0.58 |
| RAASI | 97 (53.88) | 54 (64.29) | 0.09 |
| IV diuretics | 62 (34.44) | 16 (48.48) | 0.17 |

*DES, drug-eluting stents; DCB, drug-coated balloons; SD, standard deviation; IQR, inter-quartile range; BP, blood pressure; PCI, percutaneous coronary intervention; AMI, acute myocardial infarction; LVEF, left ventricular ejection fraction; hsTnT, high sensitivity troponin T; CK-MB, MB isoenzyme of creatine kinase; CRP, C-reactive protein; LDL-C, low-density lipoprotein cholesterol; RAASI, renin-angiotensin-aldosterone system inhibitor; IV diuretics, Intravenous diuretics; NA, not available.*

$$\text{and}\,(\mathrm{P_d})_{\mathrm{hyp}} = (\mathrm{P_a})_{\mathrm{hyp}} - \Delta P \tag{4}$$

$(P_a)_{hyp}$ and $(P_d)_{hyp}$ is the mean pressure (unit: mmHg) at the aorta and the distal position at the maximal hyperemia respectively, the subscript "hyp" of $(P_d)_{hyp}$, $(P_a)_{hyp}$ refers to maximal hyperemia state, $\Delta P$ is the pressure drop along the coronary artery from the inlet to the most distal location; L is a constant that mimics the length from the inlet to the distal position, labeled with two pressure sensors on a pressure wire (L = 75 mm); $\mathrm{V_{diastole}}$ is the mean flow velocity (unit: mm/s) at diastole, and K, obtained from a previous literature, (Choi et al., 2021) is a constant (K = 1.1) proposed to mimics the flow velocity at the maximal hyperemia:

$$\mathrm{V_{hyp}} = \mathrm{K} \cdot \mathrm{V_{diastole}} \tag{5}$$

$V_{hyp}$ refers to the mean flow velocity (unit: mm/s) at the distal position at the maximal hyperemia.

According to formulations (**Eqs 1**, **3**, **4**), we can deduce:

$$\mathrm{caIMR} = \left((\mathrm{P_a})_{\mathrm{hyp}} - \Delta P\right) * \mathrm{L}/\mathrm{K} \cdot \mathrm{V_{diastole}} \tag{6}$$

$(P_a)_{hyp}$ is the maximal hyperemic mean aortic pressure; a pressure sensor was connected to the FlashAngio IMR system to record 3~8 circles of the pressures wave during the angiography, by averaging the pressure, we can get mean aortic pressure (MAP), based on which $(P_a)_{hyp}$, equals to MAP-MAP*0.2 when MAP ≥95 mmHg and MAP-MAP*0.15 when MAP <95 mmHg (Li et al., 2020).

To compute the pressure drop $\Delta P$, a specially-designed CPFD model was carried out to do the steady-state laminar flow simulation across the stenotic blood vessel, $\mathrm{V_{hyp}}$ calculated from formular (**Eq. 5**) was used as the inlet boundary condition to solve Navier-Stokes and continuity equations in the FlashAngio IMR system:

$$\nabla \cdot \hat{\mathrm{V}} = 0 \tag{7}$$

$$\rho \frac{\partial \hat{\mathrm{V}}}{\partial \mathrm{t}} + \rho \hat{\mathrm{V}} \cdot \nabla \hat{\mathrm{V}} = -\nabla \mathrm{P} + \nabla \cdot \mu \left( \nabla \hat{\mathrm{V}} + \left( \nabla \cdot \hat{\mathrm{V}} \right)^{\mathrm{T}} \right) \tag{8}$$

where $\hat{V}$, P, ρ, and μ represent the velocity, pressure, blood mass density, and viscosity, respectively. $\Delta P$ was obtained by integrating over each grid.

All the CPFD-caIMR metrics were analyzed offline in a core lab (Ai et al., 2020; Li et al., 2020; Choi et al., 2021). Normal reference range for STEMI patients was: CPFD-caIMR ≤ 40U.

## Study Outcomes

Patients were included with a follow-up of at least 12 months. Primary and secondary endpoints were recorded detailly.

The primary endpoint included: 1) difference of CPFD-caIMR between DES and DCB groups and 2) comparing MACEs incidence (cardiovascular or all-cause deaths, non-fatal MI, recurrent unstable angina pectoris (UA), revascularization including target vessel reconstruction, heart failure readmission) between DES and DCB group.

The secondary endpoints included: 1) CPFD-caIMR predicting effects on MACEs and 2) the determination of predictors for MACEs.

## Subgroup Analyses

According to MACEs results, patients were divided into non-MACEs or MACEs groups to find possible predictors including CPFD-caIMR. And according to the cutoff value

**TABLE 4 |** Characteristics of PPCI process of the study population grouped by MACEs.

| Variable | N-MACE | MACE | *p* value |
|---|---|---|---|
| | N = 180 | N = 33 | |
| DCB Intervention, n (%) | 72 (40.00) | 12 (36.36) | 0.85 |
| caIMR, Mean (SD)[a] | 35.70 (22.39) | 34.92 (21.55) | 0.85 |
| caIMR>40, n (%)[a] | 53 (31.36) | 10 (31.25) | 0.99 |
| Door to balloon, minutes, Mean (SD) | 63.42 (13.82) | 87.36 (6.42) | **<0.01** |
| Criminal vessel, n (%) | | | |
| Left anterior descending | 72 (40.00) | 18 (54.50) | 0.28 |
| Left circumflex | 34 (18.90) | 4 (12.12) | |
| Right coronary artery | 74 (41.10) | 11 (33.33) | |
| Multi coronary artery lesions, n (%) | 115 (63.89) | 17 (51.52) | 0.18 |
| IABP, n (%) | 2 (1.11) | 1 (3.03) | 0.39 |
| Pre-dilated balloon diameter, mm, Mean (SD) | 2.36 (0.49) | 2.28 (0.41) | 0.38 |
| Pre-dilated balloon pressure, atm, Mean (SD) | 9.76 (2.25) | 9.33 (1.63) | 0.21 |
| DES/DCB diameter, mm, Mean (SD) | 2.96 (0.51) | 2.88 (0.50) | 0.39 |
| DES/DCB length, mm, Mean (SD) | 26.15 (6.52) | 27.85 (5.38) | 0.16 |
| DES/DCB dilation released pressure, atm, Mean (SD) | 10.83 (2.65) | 11.12 (2.48) | 0.56 |
| DES/DCB dilation duration, second, Mean (SD) | 34.11 (31.28) | 29.55 (27.11) | 0.43 |

[a]*DES group included 121 patients; DCB groups included 80 patients.*

*PPCI, primary percutaneous coronary intervention; caIMR, coronary-angiography-derived index of microcirculatory resistance; DES, drug-eluting stents; DCB, drug-coated balloons; SD, standard deviation; IABP, intra-aortic balloon pump; NA, not available.*

of CPFD-caIMR of 40U, patients were re-grouped into caIMR ≤ 40U or caIMR >40U groups to determine its predicting value on MACEs. The flow-chart of the study was presented in **Figure 2**.

## Statistical Analysis

All analyses were conducted after matching baseline characteristics including age, sex, SBP, BMI using PSM. Continuous variables and categorical variables were expressed as mean (standard deviation), median (inter-quartile range) and proportions (%) depending on the circumstance. Student's or paired t test was used to analyze continuous variables and the chi-square or rank sum was used to analyze categorical variables. Univariate and multivariate logistic regression analysis were used to investigate the predictors of MACEs, reported as odds ratio (OR) and 95% confidence interval (CI). The Receiver Operating characteristic (ROC) curve and Area under curve (AUC) were utilized to evaluate the efficiency of predictors. A two-sided $p$ value of <0.05 was considered statistically significant. SPSS (version 23; IBM, Armonk, NY, USA) was used to analyze the relevant data of the study.

**A**

| Predictor | MACE N=33 n (%) or Mean (SD) or Median (IQR) | Non-MACE N=180 | Binary logistic regression Odds Ratio (95% CI) | P Value |
|---|---|---|---|---|
| Age, years | 62.76 (13.50) | 57.53 (12.92) | 1.00 (0.95-1.06) | 0.92 |
| PCI history | 9 (27.27) | 23 (12.78) | 1.69 (0.36-2.67) | 0.64 |
| DCB Intervention | 12 (36.36) | 72 (40.00) | 0.56 (0.36-4.35) | 0.59 |
| S to B, hours | 9.47 (2.48) | 6.37 (3.18) | 1.46 (1.11-1.92) | **0.01** |
| D to B, minutes | 87.36 (6.42) | 63.42 (13.82) | 1.22 (1.12-1.33) | **<0.01** |
| calMR* | 34.92 (21.55) | 35.70 (22.39) | 0.98 (0.95-1.02) | 0.36 |
| LVEF, % | 46.52 (9.48) | 53.07 (9.44) | 0.95 (0.88-1.02) | 0.15 |
| Peak CK-MB, ng/L | 220.00 (153.85) | 67.96 (100.12) | 1.01 (1.00-1.02) | **<0.01** |

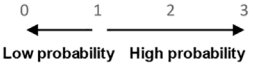


**B**

| Predictor | MACE N=21 n (%) or Mean (SD) or Median (IQR) | Non-MACE N=103 | Binary logistic regression Odds Ratio (95% CI) | P Value |
|---|---|---|---|---|
| Male | 13 (61.90) | 92 (89.32) | 0.41 (0.33-1.06) | 0.26 |
| DCB Intervention | 6 (28.57) | 56 (54.37) | 0.92 (0.80-2.73) | 0.09 |
| S to B, hours | 9.94 (2.26) | 6.67 (3.31) | 2.08 (1.06-4.06) | **0.03** |
| D to B, minutes | 88.95 (4.28) | 62.96 (14.43) | 1.36 (1.10-1.67) | **<0.01** |
| DCB/DES dilation, seconds | 25.48 (26.17) | 42.52 (32.61) | 0.98 (0.81-1.18) | 0.82 |
| Length of DCB/DES, mm | 28.90 (4.50) | 25.7 (6.31) | 1.24 (0.98-1.58) | 0.08 |
| calMR* | 39.81 (23.99) | 36.73 (23.80) | 0.94 (0.87-1.00) | 0.06 |
| LVEF, % | 46.19 (9.55) | 52.84 (10.02) | 0.91 (0.79-1.03) | 0.14 |
| Peak CK-MB, ng/L | 236.48 (130.30) | 69.27 (121.60) | 1.04 (0.99-1.10) | 0.13 |
| IV Diuretics | 11 (52.38) | 31 (30.10) | 1.04 (0.78-2.74) | 0.78 |

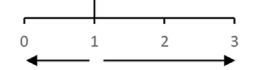


**FIGURE 4 |** Binary logistic regression analysis. Shown are odds ratios for MACEs among patients. **(A)** Binary logistic regression analysis before propensity score matching. Shown are odds ratios for MACEs among patients before propensity score matching. The size of the square corresponds to the number of patients in two groups. **(B)** Binary logistic regression analysis after propensity score matching. Shown are odds ratios for MACEs among patients after propensity score matching. The size of the square corresponds to the number of patients in two groups. Abbreviations: MACE, major adverse cardiovascular events; PCI, percutaneous coronary intervention; DCB, drug-coated balloons; DES, drug-eluting stents; S to B, time from symptom to balloon; D to B, time from door to balloon; calMR, coronary-angiography-derived index of microcirculatory resistance; LVEF, Left ventricular ejection fraction; CK-MB, MB isoenzyme of creatine kinase; IV diuretics, Intravenous diuretics; SD, standard deviation; IQR, inter-quartile range; CI, confidence interval.

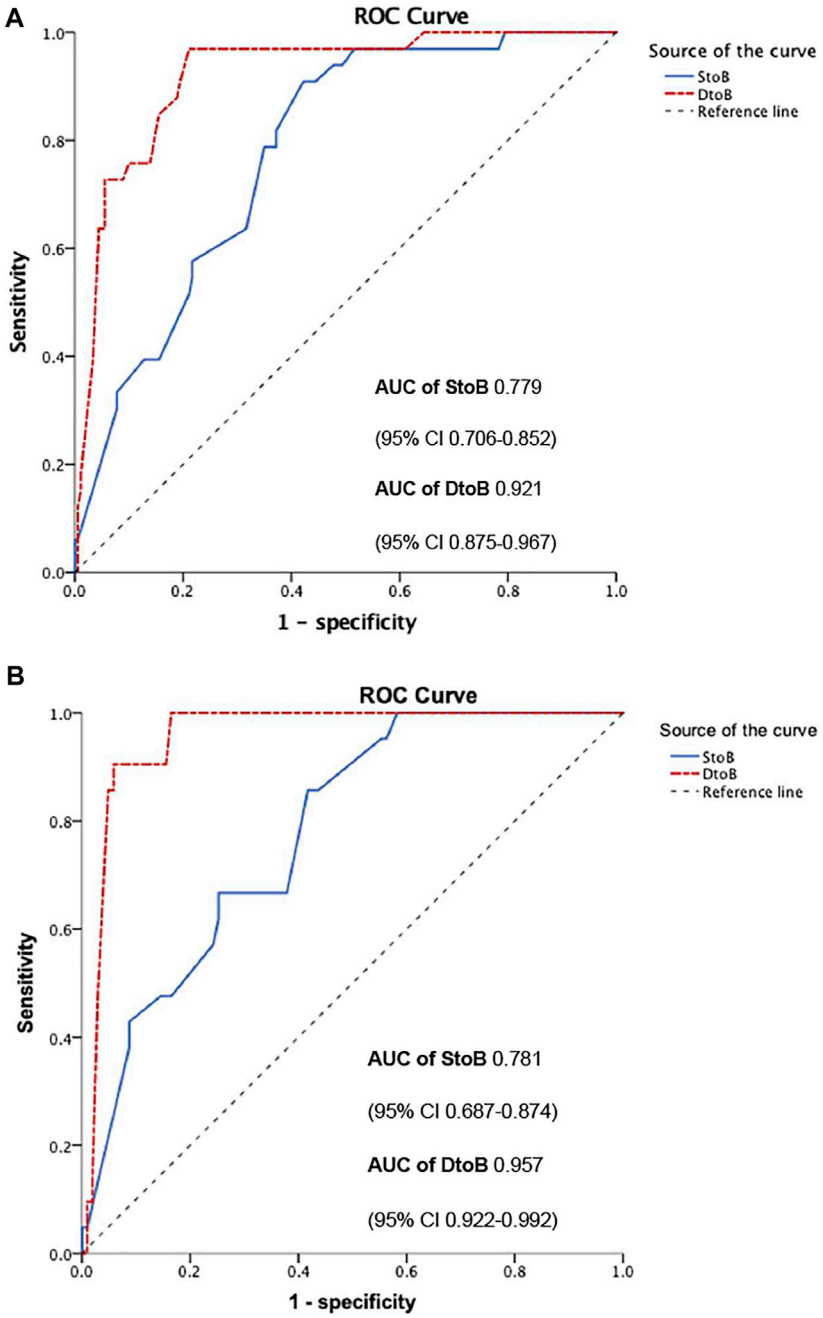


**FIGURE 5 |** ROC curve of STOB and DTOB predicting MACEs before **(A)** and after **(B)** propensity score matching. Abbreviations: S to B, time from symptom to balloon; D to B, time from door to balloon; ROC, Receiver Operating characteristic; AUC, Area under curve.

# RESULTS

## Study Patients

There were totally 213 patients involved in this retrospectively controlled study, including 84 patients adapting DCB and 129 DES with a follow-up of 1 year. After PSM, DCB and DES groups were comparable regarding characteristics of baseline and PPCI process (**Tables 1**, **2**; **Supplementary Tables S1, S2**). However, higher baseline left ventricular ejection fraction (LVEF, $p < 0.01$), lower peak high sensitivity troponin T (hsTnT, $p < 0.01$) and less diuretics use ($p < 0.01$) were observed in DCB group than those in DES group. With respect to PPCI process, DES/DCB diameter, pre-dilation released pressure and duration were significantly different in two groups ($p < 0.01$).

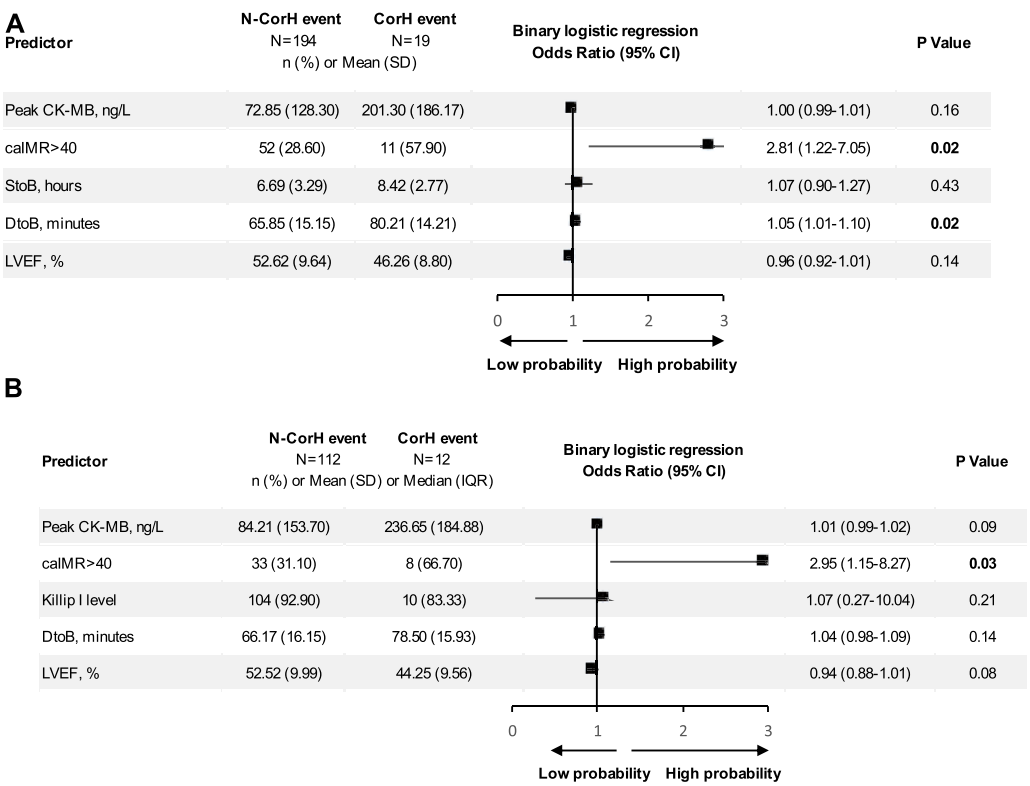


**FIGURE 6 |** Binary logistic regression analysis. Shown are odds ratios for CorH event among patients. **(A)** Binary logistic regression analysis of predicting the event group including CV deaths or heart failure readmission (CorH) before propensity score matching. Shown are odds ratios for CorH event among patients before propensity score matching. The size of the square corresponds to the number of patients in two groups. **(B)** Binary logistic regression analysis of predicting the event group including CV deaths or heart failure readmission (CorH) after propensity score matching. Shown are odds ratios for CorH event among patients after propensity score matching. The size of the square corresponds to the number of patients in two groups. Abbreviations: S to B, time from symptom to balloon; D to B, time from door to balloon; calMR, coronary-angiography-derived index of microcirculatory resistance; LVEF, Left ventricular ejection fraction; CK-MB, MB isoenzyme of creatine kinase; SD, standard deviation; IQR, inter-quartile range; CI, confidence interval.

## Primary Endpoints

After PPCI, CPFD-caIMR was calculated and found no significance between DCB and DES groups both before and after PSM (before PSM: DES 36.49 (21.04) vs. DCB 34.23 (23.91), $p = 0.48$; after PSM: DES 38.68 (22.66) vs. DCB 35.86 (24.89), $p = 0.52$, **Table 2**; **Supplementary Table S2**). The microvascular injury evaluation was still similar between two groups when re-grouped by whether CPFD-caIMR > 40U or not (DES vs. DCB: 34.17% vs. 27.16%, $p = 0.29$).

The statistics for MACEs were presented in **Figure 3**. MACEs occurred in 21 patients (16.28%) in the DES group and 12 patients (14.29%) in the DCB group (OR 1.17, 95% CI: 0.54 to 2.52, $p = 0.69$, **Figure 3A**). DCB was similar to DES as regards cardiovascular (CV) deaths ($p = 0.35$), non-CV deaths ($p = 0.56$), non-fatal MI ($p = 0.66$), revascularization ($p = 0.23$), heart failure readmission ($p = 0.79$) and recurrent UA ($p = 0.20$). After PSM (**Figure 3B**), MACEs were less in DCB than in DES group (DES vs. DCB: OR: 2.98, 95% CI: 1.07 to 8.29, $p = 0.04$) but the incidence of CV deaths (DES vs. DCB: OR: 0.66, 95% CI: 0.11 to 4.07, $p = 0.65$) were the same between the two groups.

## Secondary Endpoints and Subgroup Analysis

Patients were assigned into the MACEs (33 cases) and non-MACEs (180 cases) groups for logistic regression analysis. From ultivariate analysis (**Tables 3**, **4**; **Supplementary Tables S3, S4**), MACEs group consisted of patients with older age (62.76 (13.50) vs. 57.53 (12.92) years, $p = 0.04$), longer time from symptom to balloon (STOB) (9.47 (2.48) vs. 6.37 (3.18) hours, $p < 0.01$), longer time from door to balloon (DTOB) (87.36 (6.42) vs. 63.42 (13.82) minutes, $p < 0.01$), decreasing LVEF (46.52 (9.48) vs. 53.07 (9.44) %, $p < 0.01$) and higher peak MB isoenzyme of creatine kinase (CK-MB, 220.00 (153.85) vs. 67.96 (100.12) 218.62 ng/L, $p < 0.01$). After PSM, male ($p < 0.01$), LVEF ($p = 0.01$), peak CK-MB ($p < 0.01$), time from STOB ($p < 0.01$), time from DTOB ($p < 0.01$), DCB intervention ($p = 0.03$), pre-dilated balloon diameter ($p = 0.03$), duration of DCB/DES dilation ($p = 0.01$) and lengths of DCB/DES ($p = 0.01$) were associated with MACEs.

In multi-variate analysis (**Figure 4**), only time from STOB (after PSM: OR: 2.08, 95% CI: 1.06 to 4.06, $p = 0.03$) and time from DTOB (after PSM: OR: 1.36, 95% CI: 1.10 to 1.67, $p <$

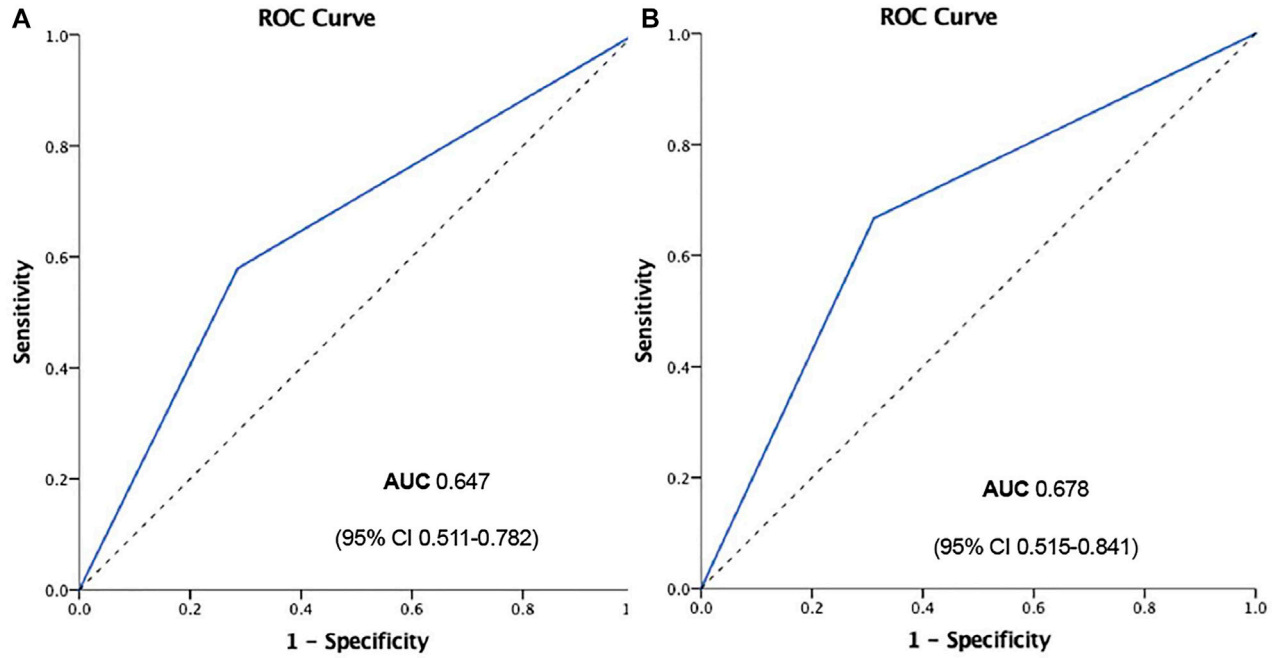


**FIGURE 7 |** ROC curve of CPFD-calMR predicting the event group including CV deaths or heart failure readmission (CorH) before **(A)** and after **(B)** propensity score matching. Abbreviations: CPFD, computational pressure-fluid dynamics; calMR, coronary-angiography-derived index of microcirculatory resistance; CV, cardiovascular; ROC, Receiver Operating characteristic; AUC, Area under curve.

0.01) were highly related to MACEs both before and after PSM. After PSM, the logistic model was statistically significant ($\chi 2$ = 87.91, $p$ = 0.000) and fitted well. Among 10 independent variables involved in the model, time from STOB and time from DTOB were statistically significant. The probability of MACEs of patients with a long time from STOB and DTOB was 2.08 times and 1.36 times that of patients with a short time from STOB and DTOB (**Figure 4**), respectively. The ROC curve of STOB and DTOB was presented in **Figure 5**. The sensitivity and specificity for predicting MACEs were 85.0% and 99.0%, respectively.

## The Relationship of CPFD-calMR and Prognosis

When we assigned patients into CPFD-calMR ≤ 40U and CPFD-calMR > 40U groups (Choi et al., 2021), characteristics were not significantly different between two groups, except the criminal vessels ($p$ < 0.05, **Supplementary Tables S5, S6**). Although the incidence of revascularization including target vessels was related to high CPFD-calMR (r = 0.22, $p$ = 0.02) when re-grouped by the cut-off value of CPFD-calMR of 40 after PSM, this effect was no longer significant from multivariate analysis.

However, when we separately analyzed every kind of event (**Figures 3C,D**), CPFD-calMR showed a significant relation with the event group including CV deaths or heart failure readmission (C or H, OR 2.81, 95% CI: 1.22 to 7.05, $p$ = 0.02). After PSM, the effects of CPFD-calMR > 40U predicting incidence of events of C or H remained significant (OR 2.95, 95% CI: 1.15 to 8.27, $p$ = 0.03, **Figures 6**, **7**).

## DISCUSSION

Restoring myocardial blood flow of IRA in STEMI patients is of importance in decreasing mortality, but it has been reported that recurrent angina after PCI happened to 20%–60% of patients (Alexander et al., 2016). Coronary microvascular injury as one of the main reasons may be a new therapeutic target (De Waha et al., 2017; Bil et al., 2018). Non-invasive imaging modalities such as cardiac magnetic resonance (MRI) was more recognized for microvascular injury evaluation, but not available at the cardiac catheterization laboratory during PPCI.

IMR has been widely studied as an invasive physiological index of microvascular injury after PPCI. Some studies have found that IMR is significantly correlated with prognosis (Cuculi et al., 2014; Fahrni et al., 2017; De Maria et al., 2019). The traditional IMR measurement is based on thermodilution-pressure wire. The risk for manipulation of guiding wire and hyperemic agent has limited its application in the clinical uses, added with the operation time over 40 min, it results in a research tool in the laboratory (Choi et al., 2021). Except for MRI and positron emission tomography, more noninvasive assessments for microvascular dysfunction have been brought to the public. A novel index of microcirculatory resistance that based on Digital Imaging and Communications in Medicine (DICOM) angiography images, computational fluid dynamics (CPFD) model and aortic pressure waves, calMR has been proved to have a high accuracy

compared with wire based IMR. By CPFD method, caIMR was calculated within 1min and the whole measuring process needs less than 5 min, which enables the diagnosis of microcirculatory dysfunction made synchronously with angiographic surgery (Collet et al., 2018). Noninvasive measurement has attracted more and more attention (Ai et al., 2020). Recent researches have confirmed that CPFD-caIMR is a promising alternative method of IMR to evaluate the prognosis of STEMI patients, since wired and hyperemic agent based IMR is not appropriate in the perioperative period for revascularization after STEMI (Abuouf et al., 2021). Our study took advantage of CPFD-caIMR as post-operative index and no significant difference of effects on microvascular injury comparing DCB with DES. Similarly, the cardiovascular outcomes of DCB group were also comparable to those of DES group no matter before or after PSM, suggesting possibly similar effects of DCB and DES.

PPCI remains the main means for rapid recovery of coronary blood flow, but its side-effect of bringing thrombosis is still worrying (Her et al., 2021). The advantage of DCB is to avoid the implantation of metal stents and minimize potential long-term safety problems. This single center, retrospectively controlled trial of DCB and DES in STEMI patients undergoing PPCI, whose lesions were spontaneous reperfusion of the IRA confirmed by CAG or low-burden thrombus after PTCA, showed that there was no significant difference of general characteristics between DCB and DES after PSM. And we found similar CPFD-caIMR between DCB and DES treatment but the incidence of MACEs was less in DCB group than that in DES group.

The using of DCB has been proved to be effective for ISR, and thus recommended by the European, German, and Asia Pacific consensus group (Aboyans et al., 2018; Her et al., 2021). In recent years, with the concept of "intervention without implantation" increasingly rooting and spreading, the application of DCB has gradually expanded to *de novo* lesions in RCTs even clinical practice (Steigen et al., 2006; Wöhrle and Werner, 2013; Her et al., 2016; Shin et al., 2016; Jeger et al., 2018). Hitherto, DCB alone has been proved similar effects with DES implantation in STEMI patients in terms of proximal and middle lesions in PAPPA research, with 5% occurrence of MACEs within 1 year. (Vos et al., 2014). The similar results manifested in Gobić et al. (2017) study and the late lumen loss of DCB at 6 months was better than that of DES . However, there was a positive result supporting DCB for reducing MACEs from our study after PSM eliminating the effects of confounders. There is no doubt that this positive finding benefits the application of DCB in clinical practice and provide some evidence of DCB use in PPCI of STEMI patients. Part of the reasons, there was a much higher drug concentration in the vascular wall after DCB use than after DES implantation (Vogt et al., 2004; Speck et al., 2012) resulting in cytostasis as well as mitotic and post-mitotic arrest (Axel et al., 1997). Kleber et al. (2015) showed that DCB had a positive remodeling effect, and more lumen was obtained in the late stage. This made up for the disadvantage of postoperative residual stenosis in DCB group, and explained another possible reason why prognosis in DCB group was better than DES group.

We also tried to determine predictors of MACEs including DCB intervention and CPFD-caIMR. In fact, high burden of thrombus and micro embolism were one of the main reasons affecting microvascular injury and CPFD-caIMR value (Gupta and Gupta, 2016), but patients in our study scarcely had the situations above mentioned. Lesions of patients all included spontaneous reperfusion of the IRA confirmed by CAG or low-burden thrombus after PTCA. The PPCI performance was well-prepared and the blood flow of criminal vessels resumed TIMI Level 3, so CPFD-caIMR value was not to such an extent as to be significantly different. However, CPFD-caIMR > 40U well predicted the combined events group including CV deaths or heart failure readmission. This point also corresponded to previous findings (Choi et al., 2021). Clinically, we need to pay more attention to CPFD-caIMR guided-treatment strategy and prognosis management to improve the quality of life of patients.

There are some limitations in this study. Firstly, this study was a retrospective controlled trial but not RCT with limited sample size. These contributed to differences of baseline characteristics, but PSM was conducted to deal with the study design of the observational study and to make the results more credible. Secondly, though we found DCB was not inferior to DES in MACEs in STEMI patients with PPCI, further large prospective RCTs were necessary to confirm this conclusion due to the unchangeable limitations of small sample size and short follow-up time. Our study data just provided some evidence about DCB clinical application.

## CONCLUSION

Microvascular injury evaluation based on CPFD-caIMR was similar between DES and DCB treatments. The DCB strategy during PPCI in STEMI patients may be a safe and feasible alternative strategy for DES treatment for less MACEs, in patients with spontaneous reperfusion of the IRA confirmed by CAG or low-burden thrombus after PTCA. CPFD-CaIMR is a promising alternative method of IMR, which can be used to evaluate the prognosis of STEMI patients with PPCI who will possibly experience CV deaths or heart failure readmission in future.

## DATA AVAILABILITY STATEMENT

The raw data supporting the conclusion of this article will be made available by the authors, without undue reservation.

## ETHICS STATEMENT

Written informed consent was obtained from the individual(s) for the publication of any potentially identifiable images or data included in this article.

## AUTHOR CONTRIBUTIONS

YD and YW contributed equally to the research design, data interpretation, manuscript writing, and modification. MZ, ZL, and LC were involved in data collection and analysis. HM and SP

performed the patient follow-up. YD and YL performed PPCI and post-processing analysis of IMR. ZW directed the entire research work and corrected the articles. All authors contributed to the article and approved the submitted version.

## FUNDING

This work was supported by the key research and development plan (social development) of the Science and Technology Project of Xuzhou City, Jiangsu Province (Grant No. KC20105).

## ACKNOWLEDGMENTS

We wish to thank the off-line software provided for us for analysis and the instructions from scientists.

## SUPPLEMENTARY MATERIAL

The Supplementary Material for this article can be found online at: https://www.frontiersin.org/articles/10.3389/fphys.2022.898659/full#supplementary-material

**Supplementary Table S1 |** Baseline characteristics of the study population after propensity score matching.

**Supplementary Table S2 |** Characteristics of PPCI process after propensity score matching.

**Supplementary Table S3 |** Baseline characteristics of the study population re-grouped by MACEs after propensity score matching.

**Supplementary Table S4 |** Characteristics of PPCI process re-grouped by MACEs after propensity score matching.

**Supplementary Table S5 |** Baseline characteristics of the study population grouped by calMR.

**Supplementary Table S6 |** Characteristics of PPCI process of the study population grouped by calMR.

## REFERENCES

Aboyans, V., Ricco, J. B., Bartelink, M. E. L., Björck, M., Brodmann, M., Cohnert, T., et al. (2018). 2017 ESC Guidelines on the Diagnosis and Treatment of Peripheral Arterial Diseases, in Collaboration with the European Society for Vascular Surgery (ESVS): Document Covering Atherosclerotic Disease of Extracranial Carotid and Vertebral, Mesenteric, Renal, Upper and Lower Extremity arteriesEndorsed by: the European Stroke Organization (ESO)The Task Force for the Diagnosis and Treatment of Peripheral Arterial Diseases of the European Society of Cardiology (ESC) and of the European Society for Vascular Surgery (ESVS). *Eur. Heart J.* 39, 763–816. doi:10.1093/eurheartj/ehx095

Abuouf, Y., AlBadawi, M., Ookawara, S., and Ahmed, M. (2021). Effect of Guidewire Insertion in Fractional Flow Reserve Procedure for Real Geometry Using Computational Fluid Dynamics. *Biomed. Eng. Online* 20, 95. doi:10.1186/s12938-021-00935-y

Ai, H., Feng, Y., Gong, Y., Zheng, B., Jin, Q., Zhang, H.-P., et al. (2020). Coronary Angiography-Derived Index of Microvascular Resistance. *Front. Physiol.* 11, 605356. doi:10.3389/fphys.2020.605356

Alekseeva, Y. V., Vyshlov, E. V., Pavlyukova, E. N., Ussov, V. Y., Markov, V. A., and Ryabov, V. V. (2021). Impact of Microvascular Injury Various Types on Function of Left Ventricular in Patients with Primary Myocardial Infarction with ST Segment Elevation. *Kardiologiia* 61, 23–31. doi:10.18087/cardio.2021.5.n1500

Alexander, K. P., Weisz, G., Prather, K., James, S., Mark, D. B., Anstrom, K. J., et al. (2016). Effects of Ranolazine on Angina and Quality of Life after Percutaneous Coronary Intervention with Incomplete Revascularization. *Circulation* 133, 39–47. doi:10.1161/CIRCULATIONAHA.115.019768

Axel, D. I., Kunert, W., Göggelmann, C., Oberhoff, M., Herdeg, C., Küttner, A., et al. (1997). Paclitaxel Inhibits Arterial Smooth Muscle Cell Proliferation and Migration *In Vitro* and *In Vivo* Using Local Drug Delivery. *Circulation* 96, 636–645. doi:10.1161/01.cir.96.2.636

Bil, J., Pietraszek, N., Pawlowski, T., and Gil, R. J. (2018). Advances in Mechanisms and Treatment Options of MINOCA Caused by Vasospasm or Microcirculation Dysfunction. *Cpd* 24, 517–531. doi:10.2174/1381612824666180108121253

Carrick, D., Haig, C., Ahmed, N., Carberry, J., Yue May, V. T., McEntegart, M., et al. (2016). Comparative Prognostic Utility of Indexes of Microvascular Function Alone or in Combination in Patients with an Acute ST-Segment-Elevation Myocardial Infarction. *Circulation* 134, 1833–1847. doi:10.1161/circulationaha.116.022603

Choi, K. H., Dai, N., Li, Y., Kim, J., Shin, D., Lee, S. H., et al. (2021). Functional Coronary Angiography-Derived Index of Microcirculatory Resistance in Patients with ST-Segment Elevation Myocardial Infarction. *JACC Cardiovasc. Interv.* 14, 1670–1684. doi:10.1016/j.jcin.2021.05.027

Collet, C., Onuma, Y., Sonck, J., Asano, T., Vandeloo, B., Kornowski, R., et al. (2018). Diagnostic Performance of Angiography-Derived Fractional Flow Reserve: a Systematic Review and Bayesian Meta-Analysis. *Eur. Heart J.* 39, 3314–3321. doi:10.1093/eurheartj/ehy445

Cuculi, F., De Maria, G. L., Meier, P., Dall'Armellina, E., de Caterina, A. R., Channon, K. M., et al. (2014). Impact of Microvascular Obstruction on the Assessment of Coronary Flow Reserve, Index of Microcirculatory Resistance, and Fractional Flow Reserve after ST-Segment Elevation Myocardial Infarction. *J. Am. Coll. Cardiol.* 64, 1894–1904. doi:10.1016/j.jacc.2014.07.987

De Luca, G., Suryapranata, H., Stone, G. W., Antoniucci, D., Biondi-Zoccai, G., Kastrati, A., et al. (2008). Coronary Stenting versus Balloon Angioplasty for Acute Myocardial Infarction: a Meta-Regression Analysis of Randomized Trials. *Int. J. Cardiol.* 126, 37–44. doi:10.1016/j.ijcard.2007.03.112

De Maria, G. L., Alkhalil, M., Wolfrum, M., Fahrni, G., Borlotti, A., Gaughran, L., et al. (2019). Index of Microcirculatory Resistance as a Tool to Characterize Microvascular Obstruction and to Predict Infarct Size Regression in Patients with STEMI Undergoing Primary PCI. *JACC Cardiovasc. Imaging* 12, 837–848. doi:10.1016/j.jcmg.2018.02.018

De Waha, S., Patel, M. R., Granger, C. B., Ohman, E. M., Maehara, A., Eitel, I., et al. (2017). Relationship between Microvascular Obstruction and Adverse Events Following Primary Percutaneous Coronary Intervention for ST-Segment Elevation Myocardial Infarction: an Individual Patient Data Pooled Analysis from Seven Randomized Trials. *Eur. Heart J.* 38, 3502–3510. doi:10.1093/eurheartj/ehx414

Fahrni, G., Wolfrum, M., De Maria, G. L., Cuculi, F., Dawkins, S., Alkhalil, M., et al. (2017). Index of Microcirculatory Resistance at the Time of Primary Percutaneous Coronary Intervention Predicts Early Cardiac Complications: Insights from the OxAMI (Oxford Study in Acute Myocardial Infarction) Cohort. *Jaha* 6, e005409. doi:10.1161/JAHA.116.005409

Geng, Y., Wu, X., Liu, H., Zheng, D., and Xia, L. (2022). Index of Microcirculatory Resistance: State-Of-The-Art and Potential Applications in Computational Simulation of Coronary Artery Disease. *J. Zhejiang Univ. Sci. B* 23, 123–140. doi:10.1631/jzus.B2100425

Gobić, D., Tomulić, V., Lulić, D., Židan, D., Brusich, S., Jakljević, T., et al. (2017). Drug-Coated Balloon versus Drug-Eluting Stent in Primary Percutaneous Coronary Intervention: A Feasibility Study. *Am. J. Med. Sci.* 354, 553–560. doi:10.1016/j.amjms.2017.07.005

Gupta, S., and Gupta, M. M. (2016). No Reflow Phenomenon in Percutaneous Coronary Interventions in ST-Segment Elevation Myocardial Infarction. *Indian Heart J.* 68, 539–551. doi:10.1016/j.ihj.2016.04.006

Her, A.-Y., Ann, S. H., Singh, G. B., Kim, Y. H., Okamura, T., Garg, S., et al. (2016). Serial Morphological Changes of Side-Branch Ostium after Paclitaxel-Coated

Balloon Treatment of De Novo Coronary Lesions of Main Vessels. *Yonsei Med. J.* 57, 606–613. doi:10.3349/ymj.2016.57.3.606

Her, A.-Y., Shin, E.-S., Bang, L. H., Nuruddin, A. A., Tang, Q., Hsieh, I.-C., et al. (2021). Drug-coated Balloon Treatment in Coronary Artery Disease: Recommendations from an Asia-Pacific Consensus Group. *Cardiol. J.* 28, 136–149. doi:10.5603/CJ.a2019.0093

Ho, H. H., Tan, J., Ooi, Y. W., Loh, K. K., Aung, T. H., Yin, N. T., et al. (2015). Preliminary Experience with Drug-Coated Balloon Angioplasty in Primary Percutaneous Coronary Intervention. *Wjc* 7, 311–314. doi:10.4330/wjc.v7.i6.311

Ibanez, B., James, S., Agewall, S., Antunes, M. J., Bucciarelli-Ducci, C., Bueno, H., et al. (2018). ESC Guidelines for the Management of Acute Myocardial Infarction in Patients Presenting with ST-Segment Elevation: The Task Force for the Management of Acute Myocardial Infarction in Patients Presenting with ST-Segment Elevation of the European Society of Cardiology (ESC). *Eur. Heart J.* 39, 119–177. doi:10.1093/eurheartj/ehx393

Jaski, B. E., Grigoriadis, C. E., Dai, X., Meredith, R. D., Ortiz, B. C., Stouffer, G. A., et al. (2016). Factors Associated with Ineligibility for PCI Differ between Inpatient and Outpatient ST-Elevation Myocardial Infarction. *J. Interv. Cardiol.* 29, 363–369. doi:10.1111/joic.12306

Jeger, R. V., Farah, A., Ohlow, M. A., Mangner, N., Möbius-Winkler, S., Leibundgut, G., et al. (2018). Drug-coated Balloons for Small Coronary Artery Disease (BASKET-SMALL 2): an Open-Label Randomised Non-inferiority Trial. *Lancet* 392, 849–856. doi:10.1016/S0140-6736(18)31719-7

Kleber, F. X., Schulz, A., Waliszewski, M., Hauschild, T., Böhm, M., Dietz, U., et al. (2015). Local Paclitaxel Induces Late Lumen Enlargement in Coronary Arteries after Balloon Angioplasty. *Clin. Res. Cardiol.* 104, 217–225. doi:10.1007/s00392-014-0775-2

Li, J., Gong, Y., Wang, W., Yang, Q., Liu, B., Lu, Y., et al. (2020). Accuracy of Computational Pressure-Fluid Dynamics Applied to Coronary Angiography to Derive Fractional Flow Reserve: FLASH FFR. *Cardiovasc Res.* 116, 1349–1356. doi:10.1093/cvr/cvz289

Neumann, F. J., Sousa-Uva, M., Ahlsson, A., Alfonso, F., Banning, A. P., Benedetto, U., et al. (2019). 2018 ESC/EACTS Guidelines on Myocardial Revascularization. *Eur. Heart J.* 40, 87–165. doi:10.1093/eurheartj/ehy394

Niehe, S. R., Vos, N. S., Van Der Schaaf, R. J., Amoroso, G., Herrman, J. R., Patterson, M. S., et al. (2022). Two-Year Clinical Outcomes of the REVELATION Study: Sustained Safety and Feasibility of Paclitaxel-Coated Balloon Angioplasty versus Drug-Eluting Stent in Acute Myocardial Infarction. *J. Invasive Cardiol.* 34, E39–E42.

Nijhoff, F., Agostoni, P., Belkacemi, A., Nathoe, H. M., Voskuil, M., Samim, M., et al. (2015). Primary Percutaneous Coronary Intervention by Drug-Eluting Balloon Angioplasty: the Nonrandomized Fourth Arm of the DEB-AMI (Drug-eluting Balloon in ST-Segment Elevation Myocardial Infarction) Trial. *Cathet. Cardiovasc. Interv.* 86, S34–S44. doi:10.1002/ccd.26060

Schapiro-Dufour, E., Tricotel, A., Slama, M. S., Ducimetière, P., Trinh-Duc, A., Sichel, C., et al. (2019). Major Ischaemic and Bleeding Risks Following Current Drug-Eluting Stent Implantation: Are There Differences across Current Drug-Eluting Stent Types in Real Life? *Archives Cardiovasc. Dis.* 112, 469–484. doi:10.1016/j.acvd.2019.04.007

Shin, E.-S., Ann, S. H., Balbir Singh, G., Lim, K. H., Kleber, F. X., and Koo, B.-K. (2016). Fractional Flow Reserve-Guided Paclitaxel-Coated Balloon Treatment for De Novo Coronary Lesions. *Cathet. Cardiovasc. Interv.* 88, 193–200. doi:10.1002/ccd.26257

Speck, U., Cremers, B., Kelsch, B., Biedermann, M., Clever, Y. P., Schaffner, S., et al. (2012). Do pharmacokinetics Explain Persistent Restenosis Inhibition by a Single Dose of Paclitaxel? *Circ. Cardiovasc. Interv.* 5, 392–400. doi:10.1161/circinterventions.111.967794

Steigen, T. K., Maeng, M., Wiseth, R., Erglis, A., Kumsars, I., Narbute, I., et al. (2006). Randomized Study on Simple versus Complex Stenting of Coronary Artery Bifurcation Lesions. *Circulation* 114, 1955–1961. doi:10.1161/CIRCULATIONAHA.106.664920

Vogt, F., Stein, A., Rettemeier, G., Krott, N., Hoffmann, R., vom Dahl, J., et al. (2004). Long-term Assessment of a Novel Biodegradable Paclitaxel-Eluting Coronary Polylactide Stent. *Eur. Heart J.* 25, 1330–1340. doi:10.1016/j.ehj.2004.06.010

Vos, N. S., Dirksen, M. T., Vink, M. A., van Nooijen, F. C., Amoroso, G., Herrman, J.-P. R., et al. (2014). Safety and Feasibility of a Paclitaxel-Eluting Balloon Angioplasty in Primary Percutaneous Coronary Intervention in Amsterdam (PAPPA): One-Year Clinical Outcome of a Pilot Study. *EuroIntervention* 10, 584–590. doi:10.4244/eijv10i5a101

Vos, N. S., Fagel, N. D., Amoroso, G., Herrman, J.-P. R., Patterson, M. S., Piers, L. H., et al. (2019). Paclitaxel-Coated Balloon Angioplasty versus Drug-Eluting Stent in Acute Myocardial Infarction. *JACC Cardiovasc. Interv.* 12, 1691–1699. doi:10.1016/j.jcin.2019.04.016

Wöhrle, J., and Werner, G. S. (2013). Paclitaxel-coated Balloon with Bare-Metal Stenting in Patients with Chronic Total Occlusions in Native Coronary Arteries. *Cathet. Cardiovasc. Interv.* 81, 793–799. doi:10.1002/ccd.24409

**Conflict of Interest:** The authors declare that the research was conducted in the absence of any commercial or financial relationships that could be construed as a potential conflict of interest.

**Publisher's Note:** All claims expressed in this article are solely those of the authors and do not necessarily represent those of their affiliated organizations, or those of the publisher, the editors and the reviewers. Any product that may be evaluated in this article, or claim that may be made by its manufacturer, is not guaranteed or endorsed by the publisher.

## GLOSSARY

**AUC** Area under curve

**caFFR** coronary angiography-derived fractional flow reserve

**CAG** coronary angiography

**CI** confidence interval

**CK-MB** MB isoenzyme of creatine kinase

**CCU** coronary care unit

**CPFD** computational pressure-fluid dynamics

**CPFD-caIMR** computational pressure-fluid dynamics derived index of microcirculatory resistance, applied to coronary angiography

**CV** cardiovascular

**DAPT** dual antiplatelet therapy

**DCB** Drug-coated balloon

**DES** Drug-eluting stent

**DTOB** door to balloon

**hsTnT** high sensitivity troponin T

**hyp** hyperemia flow velocity

**IMR** Index of microcirculatory resistance

**IRA** infarct-related artery

**ISR** in-stent restenosis

**LVEF** left ventricular ejection fraction

**MACEs** major adverse cardiovascular events

**MAP** Mean arterial pressure

**OR** odds ratio

**PPCI** primary percutaneous coronary intervention

**PSM** propensity score matching

**RCTs** randomized controlled trials

**ROC** Receiver Operating characteristic

**STEMI** ST-segment elevation myocardial infarction

**STOB** symptom to balloon

**TIMI** Thrombolysis in myocardial infarction

**UA** unstable angina pectoris

frontiers | Frontiers in Physiology

ORIGINAL RESEARCH
published: 02 June 2022
doi: 10.3389/fphys.2022.908552

# All Roads Lead to Rome: Diverse Etiologies of Tricuspid Regurgitation Create a Predictable Constellation of Right Ventricular Shape Changes

*Benjamin A. Orkild[1,2], Brian Zenger[1,2†], Krithika Iyer[1,3†], Lindsay C. Rupp[1,2], Majd M Ibrahim[5], Atefeh G. Khashani[1], Maura D. Perez[1], Markus D. Foote[1,2], Jake A. Bergquist[1,2], Alan K. Morris[1], Jiwon J. Kim[4], Benjamin A. Steinberg[5], Craig Selzman[6], Mark B. Ratcliffe[7], Rob S. MacLeod[1,2], Shireen Elhabian[1,3*‡] and Ashley E. Morgan[8*‡]*

[1]Scientific Computing and Imaging Institute, University of Utah, Salt Lake City, UT, United States, [2]Department of Biomedical Engineering, University of Utah, Salt Lake City, UT, United States, [3]School of Computing, University of Utah, Salt Lake City, UT, United States, [4]Weill-Cornell Medical College, Division of Cardiology, New York, NY, United States, [5]Division of Cardiovascular Medicine, University of Utah, Salt Lake City, UT, United States, [6]Division of Cardiothoracic Surgery, University of Utah, Salt Lake City, UT, United States, [7]Department of Surgery, The San Francisco VA Medical Center, University of California, San Francisco, San Francisco, CA, United States, [8]St. Luke's Medical Center Cardiothoracic and Vascular Surgery, Boise, ID, United States

**Introduction:** Myriad disorders cause right ventricular (RV) dilation and lead to tricuspid regurgitation (TR). Because the thin-walled, flexible RV is mechanically coupled to the pulmonary circulation and the left ventricular septum, it distorts with any disturbance in the cardiopulmonary system. TR, therefore, can result from pulmonary hypertension, left heart failure, or intrinsic RV dysfunction; but once it occurs, TR initiates a cycle of worsening RV volume overload, potentially progressing to right heart failure. Characteristic three-dimensional RV shape-changes from this process, and changes particular to individual TR causes, have not been defined in detail.

**Methods:** Cardiac MRI was obtained in 6 healthy volunteers, 41 patients with ≥ moderate TR, and 31 control patients with cardiac disease without TR. The mean shape of each group was constructed using a three-dimensional statistical shape model via the particle-based shape modeling approach. Changes in shape were examined across pulmonary hypertension and congestive heart failure subgroups using principal component analysis (PCA). A logistic regression approach based on these PCA modes identified patients with TR using RV shape alone.

**Results:** Mean RV shape in patients with TR exhibited free wall bulging, narrowing of the base, and blunting of the RV apex compared to controls ($p < 0.05$). Using four primary PCA modes, a logistic regression algorithm identified patients with TR correctly with 82% recall and 87% precision. In patients with pulmonary hypertension without TR, RV shape was narrower and more streamlined than in healthy volunteers. However, in RVs with TR and pulmonary hypertension, overall RV shape continued to demonstrate the free wall bulging characteristic of TR. In the subgroup of patients with congestive heart failure without TR, this intermediate state of RV muscular hypertrophy was not present.

OPEN ACCESS

**Edited by:**
Yunlong Huo,
Shanghai Jiao Tong University, China

**Reviewed by:**
Bao Li,
Beijing University of Technology, China
Shengzhang Wang,
Fudan University, China

***Correspondence:**
Ashley E. Morgan
asheleen@gmail.com
Shireen Elhabian
shireen@sci.utah.edu

[†]These authors have contributed equally to this work

[‡]These authors share senior authorship

**Specialty section:**
This article was submitted to Computational Physiology and Medicine, a section of the journal Frontiers in Physiology

**Received:** 30 March 2022
**Accepted:** 16 May 2022
**Published:** 02 June 2022

**Citation:**
Orkild BA, Zenger B, Iyer K, Rupp LC, Ibrahim MM, Khashani AG, Perez MD, Foote MD, Bergquist JA, Morris AK, Kim JJ, Steinberg BA, Selzman C, Ratcliffe MB, MacLeod RS, Elhabian S and Morgan AE (2022) All Roads Lead to Rome: Diverse Etiologies of Tricuspid Regurgitation Create a Predictable Constellation of Right Ventricular Shape Changes. Front. Physiol. 13:908552. doi: 10.3389/fphys.2022.908552

**Conclusion:** The multiple causes of TR examined in this study changed RV shape in similar ways. Logistic regression classification based on these shape changes reliably identified patients with TR regardless of etiology. Furthermore, pulmonary hypertension without TR had unique shape features, described here as the "well compensated" RV. These results suggest shape modeling as a promising tool for defining severity of RV disease and risk of decompensation, particularly in patients with pulmonary hypertension.

**Keywords: pulmonary hypertension, tricuspid regurgitation, statistical shape modeling, cardiac MRI, particle-based shape modeling, principal component analysis, congestive heart failure, valvular heart disease**

## 1 INTRODUCTION

The tricuspid valve sits between the right atrium and the right ventricle, anchored to the walls of the right heart. In the healthy heart, the tricuspid valve preserves one-way blood flow, preventing blood from returning to the right atrium during RV contraction. Many diseases disturb tricuspid valve function, including direct valve injury during pacemaker implantation, dilation of the RV as it faces high resistance to flow in pulmonary hypertension or left ventricular failure, and dilation of the right atrium in atrial fibrillation (Prins et al., 2019). Any disorder rendering the tricuspid valve leaflets unable to fully close allows retrograde flow of blood back into the right atrium, also known as tricuspid regurgitation (TR). As the right atrium dilates in response to the excess blood volume arising from TR, the supporting structures of the tricuspid valve also dilate, worsening the TR. If left untreated, the end result of this cycle is right heart failure and death (Cameli et al., 2013; Dawes et al., 2017; Subbotina et al., 2017; Prins et al., 2019).

An estimated 1.6 million Americans currently live with moderate or greater TR (Stuge and Liddicoat, 2006). The diagnosis of TR alone places them at a 2–3 fold increased risk of death and a 3–4 fold increased risk of congestive heart failure, compared to age-matched individuals without TR (Topilsky et al., 2019; Singh et al., 1999). TR can be treatable with surgical valve repair or replacement, and with therapy targeted at the culprit cardiac disease, but morbidity and mortality of treatment rise with increasing RV dysfunction (Subbotina et al., 2017; Topilsky et al., 2019; LaPar et al., 2018). As the RV deteriorates in response to TR, it changes shape. The shape of the healthy RV is complex, and cannot be modeled as a simple shape such as a sphere, ovoid or cone. (**Figure 1**). Changes in RV geometry with disease have therefore been historically difficult to quantify. Previous studies relied on descriptions such as increasing resemblance to a sphere, or used global shape descriptors such as wall curvature (Morgan et al., 2020a; Addetia et al., 2018). With advances in cardiac imaging and statistical shape modeling, high resolution detailed RV shape analysis has become a promising avenue for identifying the fine details of RV shape change specific to particular pathologies (**Figure 1**).. (Marcu et al., 2006; Kochav et al., 2015; Farrar et al., 2016; Dawes et al., 2017; Mauger et al., 2019)

In this study, we sought to:

1) Develop a population-level anatomical description of RV shape, directly from detailed three-dimensional (3D) models of RVs generated from cardiac MRI.
2) Discover statistically significant group differences.
3) Classify the RV shape changes characteristic of TR.

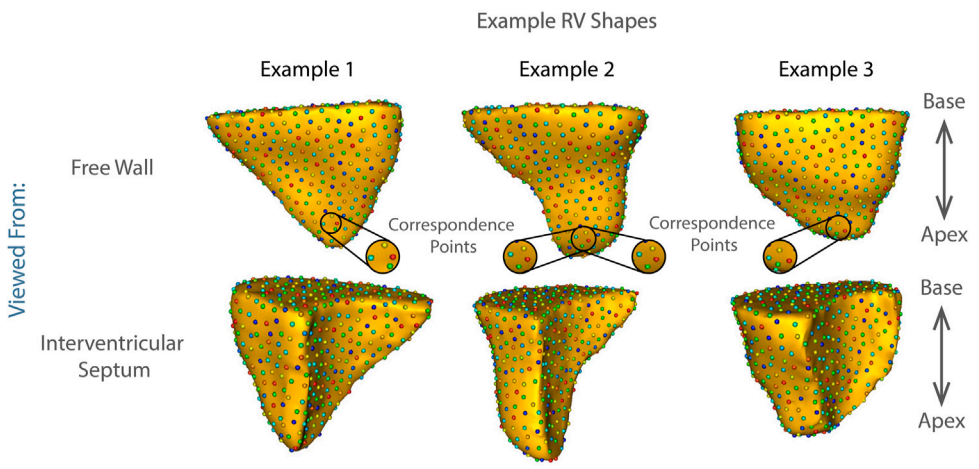


**FIGURE 1 |** Examples of shape correspondence models of right ventricular shape obtained using ShapeWorks. The colored spheres on the surface of each RV are the optimized correspondence points/corresponding landmarks that fully parameterize the right ventricular shape based on the population data (see Methods: Statistical Shape Model Construction). The three examples showcase the complexity of the RV shapes in the cohort.

4) Examine whether those changes are similar in various TR etiologies.

To accomplish these aims we obtained cardiac MRI in three groups: healthy volunteers; patients with diverse cardiac diseases resulting in moderate or greater TR; and a matched cohort of patients with cardiac disease without TR. We then employed a particle-based shape modeling tool, the open-source software package, ShapeWorks, which provides a computational approach to automatically parse shape into population-level numerical representations (Cates et al., 2017). Using this approach, we identified primary modes of shape variation between patients with and without TR, which were then applied using a logistic regression algorithm with automated feature selection to a testing subset to identify patients with TR based on RV shape alone.

In our recent publication, we used this technique to compare the RV shape of patients with TR to those of healthy volunteers (Morgan et al., 2020b). The current study expands significantly on that technique, as follows.

1) Here we included a matched cohort of patients with cardiac disease without TR, allowing analysis of progression of RV shape along a spectrum from complete health to significant impairment.
2) Beyond identifying changes in TR compared to healthy patients, here we also highlighted unique changes occurring in the specific disease states of pulmonary hypertension and congestive heart failure (CHF).
3) We increased the number of cases and improved the statistical power of our study. To mitigate the bias of the classification model due to the imbalanced dataset, we performed minority upsampling and increased the predictive performance of the model.
4) To gain insight into the geometric differences that are most statistically significant between subgroups, we performed linear discrimination of variation using the mean shape of the groups and mapping the high dimensional differences to a single scalar value.

We propose that these techniques will form the foundation of future predictive tools, with the potential to identify patients at risk for RV dysfunction in TR before their disease progresses.

# 2 MATERIALS AND METHODS

## 2.1 Patient Selection

This study included three groups of patients:

1) Patients with moderate or greater TR
2) Comorbidity-matched controls with cardiac disease but without TR
3) Healthy volunteers without cardiac disease or risk factors

Groups 1 & 2 were identified retrospectively using the University of Utah medical data warehouse and a combination of procedure (cardiac MRI) and diagnosis (TR) codes. Each patient chart was manually reviewed to verify TR and sort patients by TR grade. This study was declared to be of minimal risk and granted exemption by the University of Utah IRB. Healthy volunteer images were obtained during a previous study at Weill-Cornell Medical College, after IRB approval (Morgan et al., 2018).

All MRI images were reviewed for quality, as well as for grade of TR and to classify ventricular volumes, by a board-certified cardiologist with additional certification in cardiac MRI (M Ibrahim). Images without clearly defined RV endocardial borders, or which did not include the entirety of the RV from tricuspid valve to apex, were excluded from analysis. TR grade was classified based on MRI regurgitant volume, or echocardiographic criteria if an echo had been obtained within 30 days of the MRI (Zhan et al., 2020).

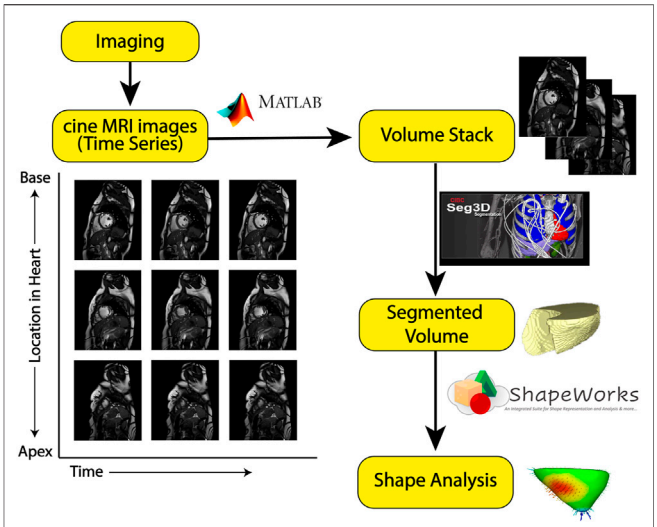


**FIGURE 2 |** Image processing pipeline: The yellow boxes represent each step in the processing pipeline. The symbols along the arrows show the software tool used to go from one step to another. From cine-MRI images, volume stacks were created and segmented using Seg3D, then uploaded to ShapeWorks for particle-based shape modeling.

## 2.2 Image Processing Pipeline

The overall method of image processing is depicted in **Figure 2**.

### 2.2.1 MRI Imaging

MRI was performed on a 3T Prisma scanner (Siemens Healthineers, Erlangen Germany) using body and spine array coils. Cine MRI images were acquired as a stack of 12–16 short axis slices covering the RV from above the tricuspid valve to beyond the cardiac apex. Typical scan parameters for Cine MRI were true-FISP pulse sequence with TE/TR = 1.5/3.3 ms, flip angle (FA) = 50°, 6 mm slice thickness, spatial resolution of 1.25 × 1.56 mm, and temporal resolution of 23.4 ms.

### 2.2.2 CINE MRI to Volume Stack

To create three-dimensional models of the RV at end-diastole, a volume stack was created from a series of CINE MRI scans. CINE MRI time stacks capture one short axis slice of the heart through

time (multiple heart beats). From each CINE short axis time stack, an image of the heart at end diastole was extracted to create a volume image stack. End-diastole was manually identified as the time point immediately after tricuspid valve closure. Image extraction was performed using a custom-built MATLAB image processing tool, available at https://github.com/borkild/CINEtoVolume/releases/tag/1.0.

#### 2.2.3 Segmentation Creation and Processing

From the volume stacks, RV segmentations were created using the open-source Seg3D software (SCI Institute, University of Utah, SLC UT). RV endocardial segmentations were semi-automatically created using the "implicit model" tool. Implicit model seed points were placed along the endocardial border at each slice of the volume stack. Prior to running the implicit model tool, the image was upsampled in the $z$-direction using a box interpolation. This upsampled segmentation was then manually edited to remove artifacts or errors. The final segmentation was exported as a binary mask volume for further analysis.

Prior to shape analysis, segmentations were pre-processed using ShapeWorks tools, wherein the segmentations were isotropically resampled and rigidly aligned to have identical dimensions and centroids. Segmentations were then converted to distance transforms for shape analysis.

### 2.3 Shape Modeling Workflow

Statistical shape modeling (SSM) is a valuable and powerful tool to generate a detailed representation of complex anatomy that enables quantitative analysis and the comparison of shapes and their variations. The steps involved in shape modeling were:

1) Statistical shape-model construction with ShapeWorks
2) Modeling shape variation with the method of Principal Component Analysis (PCA)

To study the differences between controls and pathology subjects, we have designed downstream classification tasks that help us verify if the shape model obtained contains clinically relevant morphological features that capture the population level variability. Workflows for downstream classification tasks included:

1) Train-test split and upsampling of training data
2) Feature selection using lasso regression and classification

Analyzing specific pathology characteristics involved:

1) Linear discriminant analysis
2) Determining statistical significance of shape differences

Each of the workflow steps is explained in detail in the following section.

#### 2.3.1 Statistical Shape Model Construction

Shape modeling was performed using the open-source ShapeWorks (http://sciinstitute.github.io/ShapeWorks/) software. The methodology of ShapeWorks has been described previously (Cates et al., 2017). Briefly, the particle-based shape model of a shape sample represents its segmentation using a densely ordered set of computationally derived landmarks automatically placed on consistent 3D locations across the entire shape cohort. Therefore, such landmarks provide 3D correspondence points across the population, allowing for comparison between individual and group shapes and computation of statistical differences. In this application, 512 particles were distributed across the processed RV endocardial shapes using a gradient-descent optimization strategy. Particle placement was further optimized by minimizing the cost function associated with individual shapes compared to the overall shape population. This pipeline created a uniform distribution of particles that adequately represented each shape across each RV surface. From these particles, mean shapes and differences were computed.

#### 2.3.2 Modeling Shape Variation With Principal Component Analysis

Principal component analysis (PCA) was used to reduce the correspondence data to a smaller set of linearly uncorrelated components, determining the number of modes explaining significant shape variation. We mapped each RV shape to its respective PCA loading vector.

#### 2.3.3 Training and Testing

PCA loadings of RV shapes were divided into training and testing sets, using train_test_split in sklearn (scikit-learn.org) (Pedregosa et al., 2011). The training set comprised 80% of the population and the testing set 20%. We then upsampled the training data to increase the statistical power, minimizing the difference between group sizes to construct balanced cohorts. For this, we employed a version of the Synthetic Minority Oversampling Technique (SMOTE), known as Borderline-SMOTE (Han et al., 2005). This technique generates additional synthetic samples from the easily misclassified borderline region—the shapes between shapes definitely belonging to the patient set and those definitely belonging to the control set. In our dataset, the two minority groups were 1) patients with TR and 2) healthy controls; compared to a majority group of controls with comorbid conditions. Using Borderline-SMOTE, representative RV shapes of the minority groups were selected, and the shapes of their nearest neighbors identified. If those shapes belonged entirely to the same set as the selected shape, they were not selected for upsampling. However, if the shapes of its nearest neighbors belonged to the opposite group (e.g., patient, if the original is a healthy volunteer), it is considered to exist on the borderline, and it is upsampled by generating synthetic samples along the line of transformation from the original to the nearest neighbor shape. This process was repeated until the minority classes had the same proportion as the majority class.

#### 2.3.4 Feature Selection

We determined the number of PCA components required to explain 99% of the data variation, as follows: Assume $s_i$ is the PCA loading vector for shape $i$ and $y_i$ is its corresponding label. We set $y_i$ equal to 1 for patients and 0 for control subjects. Our objective

was to identify the principal components (*i.e.,* shape-based parameters) that were most predictive of the patient group. In this regard, we solved the lasso regression for 1000 random subsets of data, and accordingly found a weight vector, $w$, such that:

$$y_i = w^T s_i + \lambda \|w\| \quad (1)$$

where $\lambda$ is the regularization parameter. A non-zero entry in $w$ shows the relevance of its respective PCA component to predicting patients. Then, we found the dominance probability of each PCA component, defined as the number of times it appeared as a non-zero entry in $w$ divided by the 1000 times the regression was run. We used sklearn.linear_model.LassoCV (Pedregosa et al., 2011) to fit the model. This function uses kfold cross-validation within the training set to find the best model parameters and the regularization strength. The parameters used for LassoCV were: optimization tolerance of $10^{-4}$, 3 fold CV, without fitting the intercept of the model, 100,000 maximum iterations, 100 number of lambdas along the regularization path, and the other parameters set to default. Subsequently, we selected the top four components with the highest probabilities, and used those components to train a logistic regression classifier for predicting patients, and to determine the precision and accuracy of classification using these four modes of variation. We used sklearn.linear_model.LogisticRegressionCV (Pedregosa et al., 2011) to fit the classification model. This function also uses k_fold cross validation to find the best model. The parameters used for the function were: lbfgs solver, 100,000 maximum iterations, ROC AUC metric used for selecting the best model, 3 fold CV, and the other parameters set to default values.

### 2.3.5 Linear Discrimination of Variation

To analyze shape variation between the subgroups of patients with CHF and with pulmonary hypertension, and the distribution of individual shapes among these groups, a linear discrimination of variation was created, as follows: In the group of patients with CHF, the mean shape (*i.e.,* average correspondence particle locations) of the group of patients with CHF but without TR, was compared to the mean shape of the group with CHF and TR. The linear discrimination between the two groups was defined as the difference vector between the two mean shape vectors. The shape of each subject was then mapped/projected onto this vector by taking the dot product between the subject-specific shape representation (the particle correspondences) and this difference vector. This mapping results in a single scalar value (or a "shape-based score") that places a subject-specific anatomy on a group-based shape difference that is statistically derived from the shape population. For the purpose of interpretability, the mappings of the group mean shapes were normalized to −1 (patients with CHF and TR) and 1 (CHF without TR). The mappings of all the other subjects were then similarly normalized relative to these values, giving a shape distribution of individual members of the population relative to the mean shapes of their respective groups. A univariate Gaussian distribution was then fit to the normalized mapping of each group, to define the probability density function of the shape scores for each group. The same process was repeated for the group of patients with pulmonary hypertension.

**TABLE 1 |** Patient Characteristics. RV = Right ventricle. EF = ejection fraction. EDV = End-Diastolic Volume, EDVI = End-Diastolic Volume Indexed to body surface area, ESV = End-Systolic Volume, ESVI = End-Systolic Volume Indexed to body surface area.

| | Disease-Matched Controls | Patients with TR | p |
|---|---|---|---|
| Age | 64 ± 10 | 59 ± 18 | |
| RVEF | 49.9 ± 11.2% | 42.6 ± 12.8 | 0.03 |
| RV EDV | 150.9 ± 43.5 ml | 184.6 ± 65 | 0.03 |
| RV EDVI | 76.4 ± 22.5 | 105.2 ± 36 | 0.02 |
| RV ESV | 76.6 ± 29.5 | 106 ± 44.5 | 0.007 |
| RV ESVI | 40.7 ± 15 | 62.4 ± 28.6 | 0.002 |

### 2.3.6 Statistical Significance of Shape Differences

To determine which RV correspondence points represented areas of statistically significant differences in shape, a Hotelling t-squared statistic was calculated for each point, and corrected for the false discovery rate; $p < 0.05$ was considered significant (Cates, 2010).

## 3 RESULTS

Of 78 total MRIs meeting criteria for inclusion (see Methods: patient selection), 24 were excluded due to inadequate image quality. The remaining 54 MRIs comprised: 21 patients with TR; 27 comorbidity-matched controls; and 6 healthy volunteers. **Table 1** contains patient-level characteristics. Unsurprisingly, end-diastolic and end-systolic RV volumes were significantly higher in patients with TR compared to matched controls, and RV ejection fraction was significantly lower. Ejection fraction could not be calculated for the 7 patients in atrial fibrillation at the time of MRI.

In the patient group, TR was secondary to pulmonary hypertension in three patients (as documented in the medical record by their treating cardiologist); congestive heart failure (CHF) in 9 patients; and other causes (atrial fibrillation, pacemaker lead injury, congenital heart disease) in 9 patients. In the control group, four patients had a diagnosis of pulmonary hypertension, 12 had CHF, and 11 had other cardiac diagnoses (atrial fibrillation, pacemaker implantation, congenital heart disease). The healthy volunteers had no diagnosis of cardiac disease and no cardiovascular risk factors.

The technique of particle-based shape modeling was then applied to identify differences in group-level RV shape. **Figure 3** depicts the mean end-diastolic RV shape of each group, with the regions of between-group difference color-coded on the RV shapes. There is a distinct shape change between the group of healthy volunteers compared to the shape of the comorbidity-matched controls, particularly with inward displacement of the mid-RV free wall. This change reverses as TR develops, with outward protrusion of the RV free wall, widening of the RV base and blunting of the apex. This change is statistically significant, with $p$ values approaching zero for the protrusion of the RV free wall,

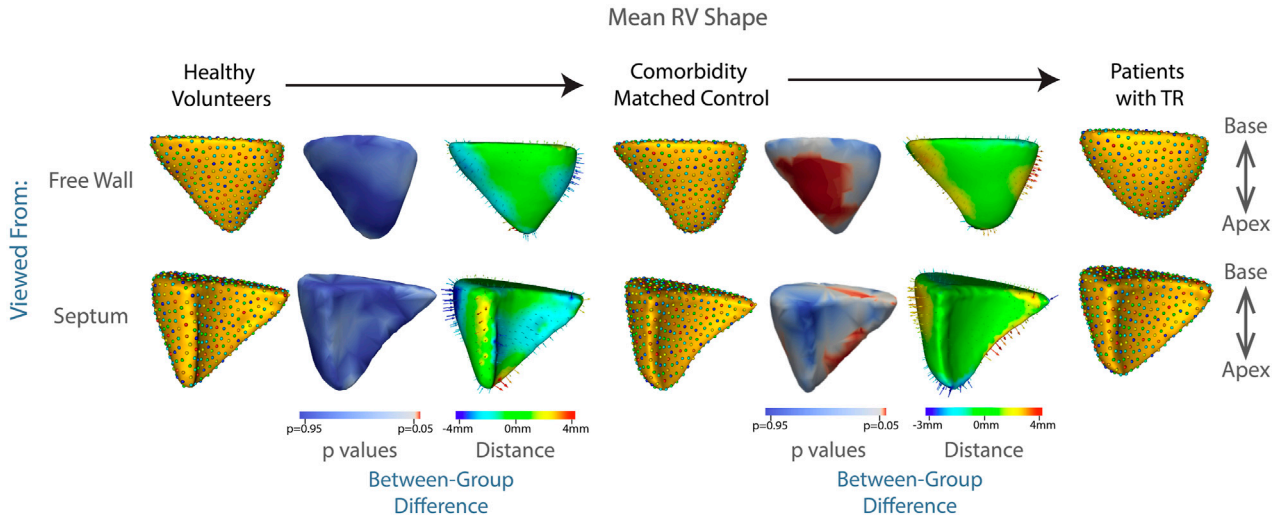


**FIGURE 3 |** Summary of mean shapes. Columns, 1, 4, and 7 contain the mean shape of the right ventricle in healthy volunteers, patients with cardiac comorbidities, and patients with moderate or greater TR, respectively. Columns 3 and 6 show the difference between the group-mean shapes. The arrows indicate the direction of group differences, and the color represents the magnitude of the group difference. Columns 2 and 5 show the *p*-values of the group differences. The regions with red color showcase statistically significant group differences.

and <0.05 for large regions of the RV (250 of 512 total correspondence points, or 48.8% of the RV surface), as shown in **Figure 3**.

To identify granular features of RV shape specific to patients with TR, we divided the overall group of controls (comorbidity-matched and healthy volunteers) and patients with TR into training and testing sets and performed a principal component analysis (PCA). Thirty-one distinct modes of shape variation accounted for 99% of the shape variability between the group with TR and the control group. We identified the four most dominant modes shown in **Figure 4**.

Applying this analysis to the testing set, these four modes of variation correctly distinguished between RV shapes with TR compared to matched controls with 82% recall, 87% precision, and 82% accuracy. The F1 score for this model was 82%.

We used sklearn.metric (Pedregosa et al., 2011) to calculate all the metrics of classification model. Based on the confusion matrix of **Table 2**, the formulas for the metrics are:

$$Accuracy = \frac{TN + TP}{TN + TP + FN + FP}, Precision = \frac{TP}{TP + FP},$$
$$Recall = \frac{TP}{TP + FN}, F1 = 2\frac{Recall^{*}Precision}{Recall + Precision}$$

**Figure 5** contains the ROC curve (receiver operating characteristic) for the model plotted using sklearn.metrics.roc_curve and sklearn.metrics.auc (Pedregosa et al., 2011).

## 3.1 TR Secondary to Pulmonary Hypertension

Of all etiologies of TR, one of the most difficult to treat is pulmonary hypertension. In this disease, RV dilation and resulting TR occur due to narrowing or obstruction of the pulmonary arteries. These arterial changes result in increased resistance to blood flow, as the RV attempts to eject the same amount of blood through a smaller outlet. In the early stages of disease, the RV compensates *via* hypertrophy of muscle fibers and increased expression of cytoskeletal contractile proteins, allowing for increased force generation (Ryan, 2014; Onno, 2015; Thenappan et al., 2016; Prins et al., 2019). However, as the disease progresses, the compensatory mechanisms of the RV ultimately fail. At this point, the RV progressively dilates and the tricuspid leaflets are unable to close, leading to TR. With RV failure and TR comes decreased cardiac output and eventually death. Our results make this trajectory visible—from the shape of the RV in healthy volunteers, to the more streamlined, muscular shape of the RV in patients with pulmonary hypertension but without TR, in whom the RV is well compensated. Following development of TR, the RV balloons outward, indicating progression towards RV failure, shown in **Figure 6**. These results did not reach statistical significance, likely due to the small sample size, with the lowest $p$ value associated with protrusion of the RV free wall at $p = 0.13$.

## 3.2 TR Secondary to Congestive Heart Failure

Failure of the heart to supply adequate blood to the body is known as congestive heart failure (CHF). While many of the diseases leading to CHF may affect primarily or initially the left ventricle, there is a more global distribution of disease than in pulmonary hypertension. RV dysfunction can occur due to direct involvement in the underlying disease process, such as ischemia or genetic cardiomyopathy, or as a

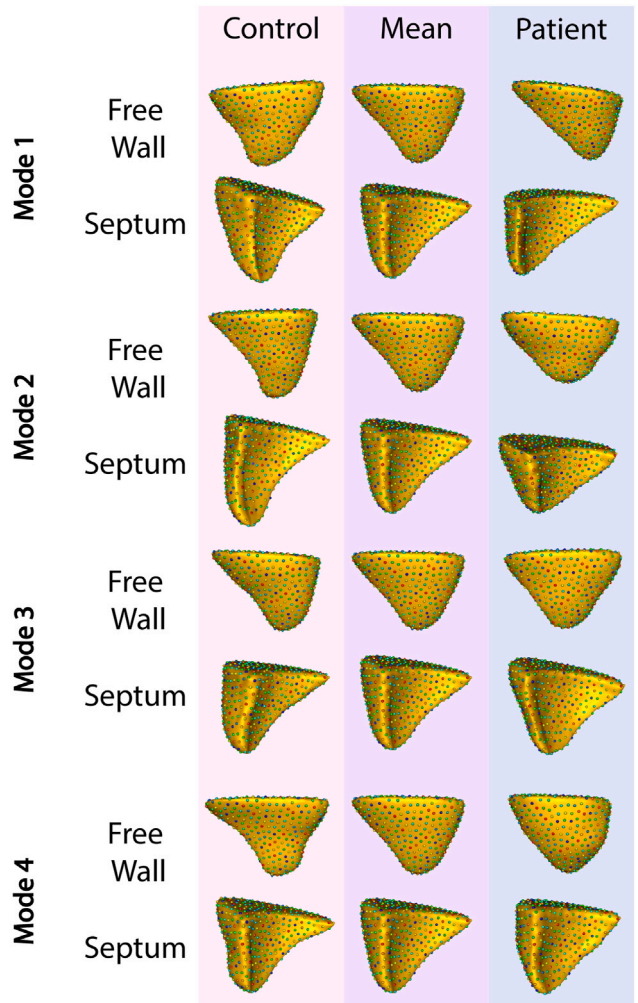


**FIGURE 4 |** The four primary modes of shape variation between patients with TR and controls. The control group is shown in the leftmost column, patient group in the rightmost, and the overall mean in the center.

secondary response to volume overload as the left ventricle fails. As the RV becomes affected by volume overload, it may initially compensate in a way similar to that seen in pulmonary hypertension (if the RV itself is uninjured by the pathologic process causing the CHF) (Voelkel Norbert et al., 2006). However, as compensatory mechanisms fail, the RV becomes increasingly dilated, leading to failure of leaflet coaptation, and resulting in TR. In our patient population, this process is evident in **Figure 7**. These results did not reach statistical significance, with the lowest $p$ value again associated with protrusion of the RV free wall, at $p = 0.1$.

## 3.3 Linear Discrimination of Variation by TR Etiology

While common modes of shape variation characterized the RV changes seen in TR regardless of etiology, the model had different abilities to discriminate between patient and control RVs due to the distinct changes seen in pulmonary hypertension compared to CHF. **Figure 8** depicts the mapping of each RV shape within these subgroups to a linear discrimination of variation based on population mean shapes (see Methods: Linear Discrimination of Variation). In the group of patients with CHF, 75% of RV shapes fell into an overlapping region of shape described by characteristics of both those with TR and controls. However, in the group of patients with pulmonary hypertension, 57% of RV shapes were clustered in distinct regions on either the TR or control side, with a minority demonstrating shapes that could be characteristic of either the TR or control state.

# 4 DISCUSSION

In this study, we aimed to:

1) Develop a population-level anatomical description of RV shape, directly from detailed 3D models of RVs generated from cardiac MRI
2) Discover statistically significant group differences
3) Classify the RV shape changes characteristic of TR
4) Examine whether those changes are similar in various TR etiologies

## 4.1 Population-Level 3D RV Shape

Constructing 3-dimensional models of 54 RVs, we quantified mean RV shape in healthy controls, patients with cardiac disease, and patients with TR. Highlighting the complexity of RV shape in general, our principal component analysis identified 31 individual modes of shape variation required to explain 99% of the variation between the mean RV shape of patients with TR compared to controls.

## 4.2 RV Shape Differences Between Groups

We demonstrated that the fine details of RV shape in patients with TR are significantly different over large regions (250 out of 512 correspondence points) of the RV when compared to comorbidity-matched controls. This heterogeneity was particularly noted with bulging of the free wall, blunting of the apex, and widening of the RV base ($p < 0.05$ for large regions of the RV, $p$ approaching 0 for the protruding RV free wall, see **Figure 3**). Highlighting the potential for shape modeling as a diagnostic tool in cardiac disease, we trained a linear regression algorithm to identify the RV shapes of those patients with TR versus matched controls, with >80% recall, sensitivity, and specificity.

**TABLE 2 |** Confusion matrix for Binary classification. TN = True negatives, TP = True Positives, FN = False Negatives, FP = False positives.

| | | Predicted | |
|---|---|---|---|
| Actual | | Negative | Positive |
| | Negative | TN | FP |
| | Positive | FN | TP |

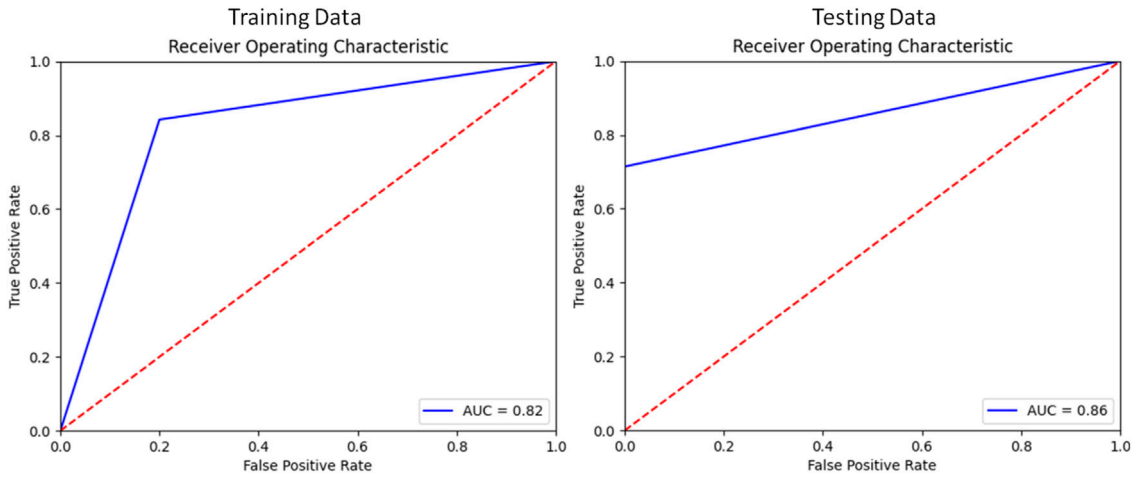


**FIGURE 5 |** Receiver Operator Characteristic of the Classification model for Training and Testing splits.

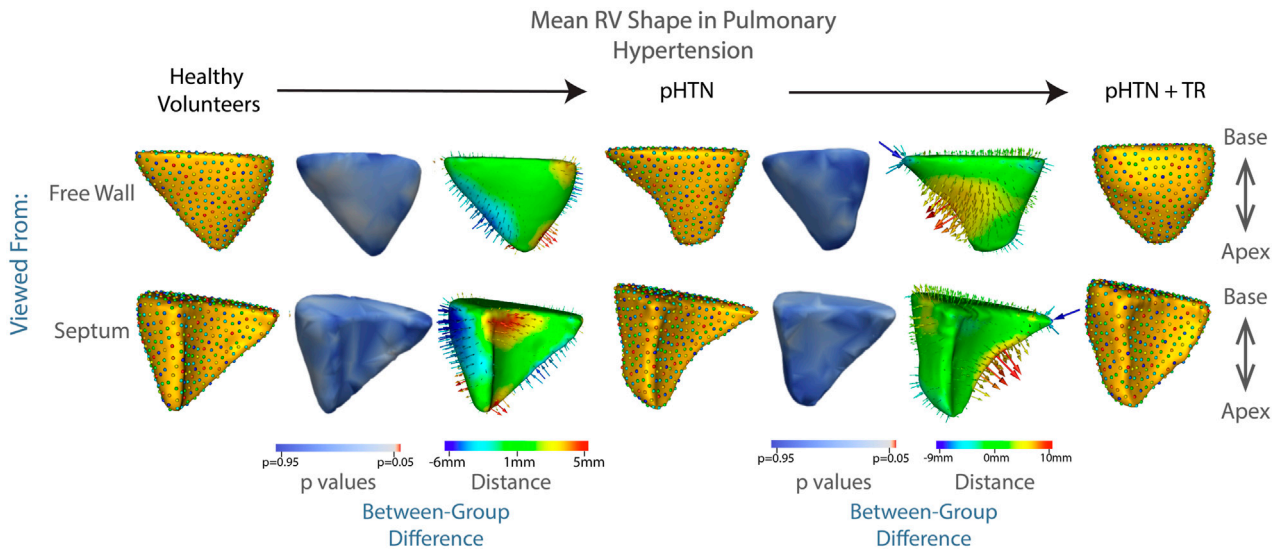


**FIGURE 6 |** The mean shape of the right ventricle in healthy volunteers, patients with pulmonary hypertension, and patients with pulmonary hypertension plus moderate or greater TR are shown in columns 1,4,7. Columns 3 and 6 show the difference between the group mean shapes. The arrows indicate the direction of group differences, and the color represents the magnitude of the group difference. Columns 2 and 5 show the *p*-values of the group differences. The regions with red color showcase statistically significant group differences.

## 4.3 Characteristic RV Shape Changes

Patients with TR showed a consistent bulging along the free wall of the RV regardless of etiology (**Figures 3**, **6**, **7**), consistent with the known underlying RV volume overload occurring in TR (Vargas Abello et al., 2013). Also noted were blunting of the RV apex, and narrowing of the base. These features correspond in granular detail to the known overall transition from a more triangular towards a more spherical shape, as documented in prior echocardiographic studies, as will be discussed below.

## 4.4 Changes Unique to Pulmonary Hypertension and CHF

While our overall subgroup analysis of mean RV shape in patients with CHF and pulmonary hypertension did not reach statistical

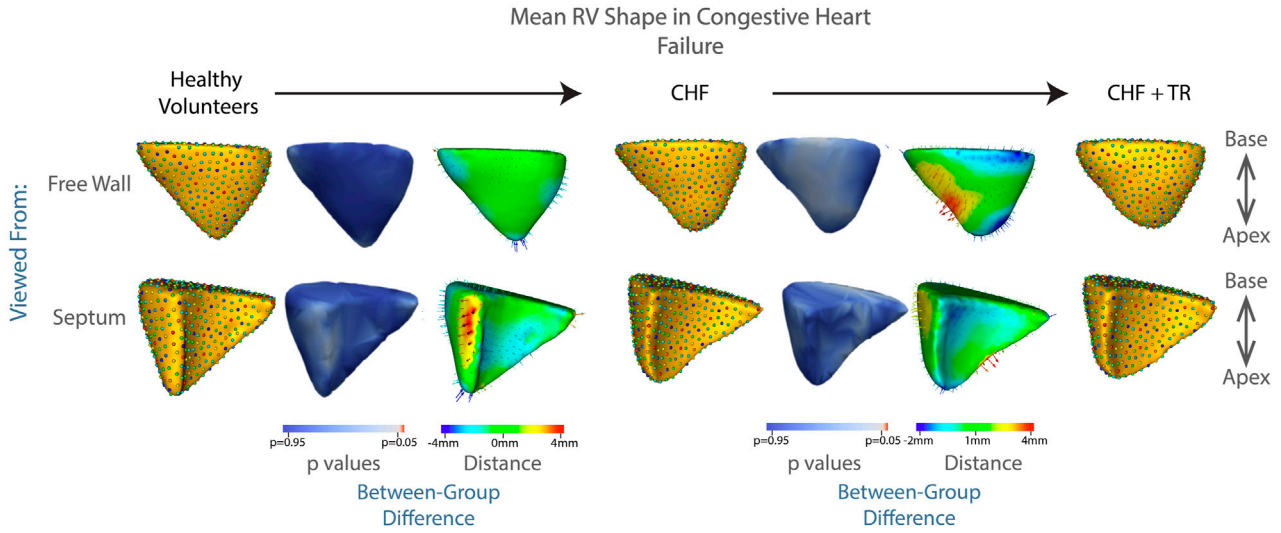


**FIGURE 7 |** Progression of RV shape change in congestive heart failure (CHF). The mean shape of the right ventricle in healthy volunteers, patients with CHF without TR, and patients with CHF and TR are shown in columns 1, 4, 7. Columns 3 and 6 show the difference between the group mean shapes. The arrows indicate the direction of group differences, and the color represents the magnitude of the group difference. Columns 2 and 5 show the *p*-values of the group differences. The regions with red color showcase statistically significant group differences.

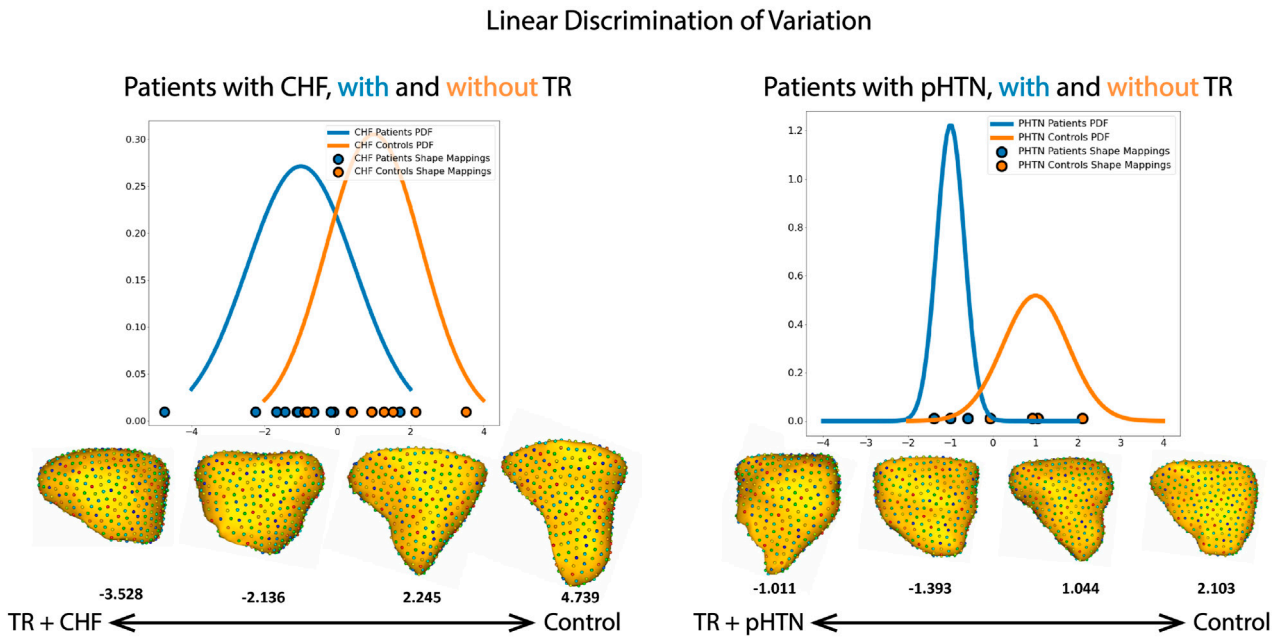


**FIGURE 8 |** Shape mapping to linear discrimination of variation between population means, for the subgroups of patients with CHF and pulmonary hypertension (pHTN). The group mean for patients with TR is set as −1, and for patients without TR is set as 1. PDF = probability density function. Selected RV shapes correspond to individual points on the graph, and are shown as seen from the free wall. The number below each shape denote the single scalar value (or a "shape-based-score") that places a subject-specific anatomy on a group-based shape difference that is statistically derived from the shape population.

significance, likely due to the small number of patients in each group, there were striking qualitative differences which correlate well to the known pathophysiologies of each condition, and with distinct relevance to our understanding of RV/pulmonary arterial coupling. First, as seen in **Figure 6**, for patients with pulmonary hypertension we noted a shape change from healthy volunteer RV shape to the 'well compensated' pulmonary hypertension RV shape. These RVs exhibited narrowing of the mid RV and a streamlining of

shape, which corresponds well to the known muscular hypertrophy which occurs in these patients as the RV adapts to pump against a higher pressure pulmonary circulation (Prins et al., 2019; Thenappan et al., 2016; Ryan, 2014; Onno, 2015). As coupling ultimately fails, and RV filling becomes volume dependent, we see a decompensated RV shape consistent with the rest of the TR group *i.e.,* with outward bulging of the RV free wall. This shape change is characteristic and was detectable in a computational algorithm; for example, analyzing each 3D RV shape individually using a linear discrimination of variation, the majority of RV shapes in our pulmonary hypertension groups clustered into regions marked by either the TR or control shapes, (**Figure 8**). Comparatively, the group of patients with CHF showed a 75% overlap in RV shape between the CHF controls and patients with CHF and TR, as shown in **Figure 8**. This finding is consistent with the differing pathophysiologies of these two disease processes, described above; whereas CHF may affect the right ventricle and tricuspid valve with varying severity and at different time points of disease, in pulmonary hypertension the development of TR is typically a marker of severe disease with associated RV failure (Chen et al., 2018). As such, we posit that it presents with a distinct shape change upon the transition from well-to poorly-compensated.

### 4.5 Conclusion

To date, cardiac shape analysis has focused primarily on the left heart. It has, for example, been used to predict stroke risk based on the shape of the left atrial appendage (Di Biase et al., 2012; Bhalodia et al., 2019). When applied to the more complex RV, shape analysis using echocardiography at end-diastole has demonstrated alterations in gross global parameters including increased bulging of the lateral RV wall from the base to the apex in patients with pulmonary hypertension (Leary et al., 2012). MRI-based shape analysis of cardiac motion, comparing the end-systolic to end-diastolic RV shape, has been shown to correlate with risk of death in patients with pulmonary hypertension (Dawes et al., 2017). To our knowledge there has been no prior analysis of the complex RV shape changes associated with TR.

In our study, across all groups, we observed a progression of RV shape from healthy, to compensating for pulmonary hypertension and CHF, to poorly compensated with TR. The fact that this progression occurs on a spectrum, both in the overall cohort and in the subgroups of patients with the particularly vexing problems of pulmonary hypertension and CHF, favors the idea that the RV shape for a particular patient can be scored along this spectrum, from health to decompensated disease. As such, we posit that this shape analysis pipeline will become the backbone of future diagnostic and prognostic tools. Such a toolkit will aid in identifying those at highest risk of RV dysfunction, guiding therapy and prompting intervention before time is up.

### 4.6 Limitations

This study was obtained using retrospective data. The size of our dataset was limited due to the historically small numbers of patients undergoing cardiac MRI for TR—although this number will continue to increase in the future, as MRI is now part of the standard armamentarium for TR evaluation (Hahn et al., 2019). Consequently, statistical methods were used, as described above, to enhance the size of the dataset and render group sizes approximately equal. Further, invasive hemodynamic measurements (right heart catheterization) were available for very few of the patients included in the study, limiting our ability to compare patient volume status and grade the severity of right heart failure and pulmonary hypertension.

## DATA AVAILABILITY STATEMENT

The raw data supporting the conclusion of this article will be made available by the authors, without undue reservation.

## ETHICS STATEMENT

The studies involving human participants were reviewed and approved by University of Utah IRB. Written informed consent for participation was not required for this study in accordance with the national legislation and the institutional requirements.

## AUTHOR CONTRIBUTIONS

BO headed the image processing, smoothing and alignment, MATLAB tool development, and ShapeWorks analysis of mean shapes. BZ headed assembly and supervision of image processing pipeline team, creation of figures. KI ran the statistical analysis, including principal component and linear discrimination analysis, along with the testing and verification of statistical methods. LR carried out the MRI contouring and supervision of image processing. MI completed MRI analysis, graded of TR severity, and determined RV volumes and ejection fraction. AK completed initial statistical analysis and development of first generation principal component analysis code. MP and MF assisted with image processing. JB assisted with setting up ShapeWorks and preparing the manuscript. AM developed and maintained ShapeWorks studio. JK acquired the MRIs of healthy volunteers. BS provided clinical input on the manuscript and data collection for clinical variables associated with patients enrolled in this study. CS and MR assisted with manuscript editing. RM provided access and project oversight within the SCI institute. SE developed and maintained ShapeWorks studio, supervised statistical analysis, and is co-senior author with AM. AM headed project origination and oversight, acquisition of clinical data, manuscript writing, is the corresponding author, and co-senior author with SE.

## ACKNOWLEDGMENTS

The National Institutes of Health supported this work under grant numbers NIBIB-U24EB029011, NIAMS-R01AR076120, NHLBI-R01HL135568, NIBIB-R01EB016701 (Elhabian), NIGMS-P41GM103545, NIGMS-R24GM136986 (MacLeod),

and NHLBI-1F30HL149327 (Zenger). Steinberg was supported by the National Heart, Lung, and Blood Institute of the National Institutes of Health under Award Number K23HL143156. The content is solely the responsibility of the authors and does not necessarily represent the official views of the National Institutes of Health.

## REFERENCES

Addetia, K., Maffessanti, F., Muraru, D., Singh, A., Surkova, E., Mor-Avi, V., et al. (2018). Morphologic Analysis of the Normal Right Ventricle Using Three-Dimensional Echocardiography-Derived Curvature Indices. *J. Am. Soc. Echocardiogr.* 31 (5), 614–623. doi:10.1016/j.echo.2017.12.009

Bhalodia, R., Subramanian, A., Morris, A., Cates, J., Whitaker, R., Kholmovski, E., et al. (2019). Does Alignment in Statistical Shape Modeling of Left Atrium Appendage Impact Stroke Prediction? *Comput. Cardiol.* 46. doi:10.22489/cinc.2019.200

Cameli, M., Righini, F. M., Lisi, M., Bennati, E., Navarri, R., Lunghetti, S., et al. (2013). Comparison of Right versus Left Ventricular Strain Analysis as a Predictor of Outcome in Patients with Systolic Heart Failure Referred for Heart Transplantation. *Am. J. Cardiol.* 112 (11), 1778–1784. doi:10.1016/j.amjcard.2013.07.046

Cates, J. (2010). *Shape Modeling and Analysis with Entropy-Based Particle Systems*. Salt Lake City, UT: The University of Utah. Ph.d. thesis.

Cates, J., Elhabian, S., and Whitaker, R. (2017). Shapeworks: Particle-Based Shape Correspondence and Visualization Software. *Stat. Shape Deformation Analysis*, 257–298. doi:10.1016/b978-0-12-810493-4.00012-2

Chen, L., Carolyn, M., Larsen, R. J., Pislaru, S. V., Murphy, J. G., McGoon, M. D., et al. (2018). The Prognostic Significance of Tricuspid Valve Regurgitation in Pulmonary Arterial Hypertension. *Clin. Respir. J.* 12, 1572–1580. doi:10.1111/crj.12713

Dawes, T. J. W., de Marvao, A., Shi, W., Fletcher, T., Watson, G. M. J., Wharton, J., et al. (2017). Machine Learning of Three-Dimensional Right Ventricular Motion Enables Outcome Prediction in Pulmonary Hypertension: A Cardiac MR Imaging Study. *Radiology* 283 (2), 381–390. doi:10.1148/radiol.2016161315

Di Biase, L., Santangeli, P., Anselmino, M., Mohanty, P., Salvetti, I., Gili, S., et al. (2012). Does the Left Atrial Appendage Morphology Correlate with the Risk of Stroke in Patients with Atrial Fibrillation? Results from a Multicenter Study. *J. Am. Coll. Cardiol.* 60 (6), 531–538. doi:10.1016/j.jacc.2012.04.032

Farrar, G., Suinesiaputra, A., Gilbert, K., Perry, J. C., Hegde, S., Marsden, A., et al. (2016). Atlas-based Ventricular Shape Analysis for Understanding Congenital Heart Disease. *Prog. Pediatr. Cardiol.* 43, 61–69. doi:10.1016/j.ppedcard.2016.07.010

Hahn, R. T., Thomas, J. D., Khalique, O. K., Cavalcante, J. L., Praz, F., and Zoghbi, W. A. (2019). Imaging Assessment of Tricuspid Regurgitation Severity. *JACC Cardiovasc. Imaging* 12 (3), 469–490. doi:10.1016/j.jcmg.2018.07.033

Han, H., Wang, W.-Y., and Mao, B-H. (2005). Borderline-SMOTE: a New Over-sampling Method in Imbalanced Data Sets Learning. International conference on intelligent computing. Springer, 878–887. doi:10.1007/11538059_91

Kochav, J., Simprini, L., and Weinsaft, J. W. (2015). Imaging of the Right Heart-CT and CMR. *Echocardiography* 32, S53–S68. doi:10.1111/echo.12212

LaPar, D. J., Likosky, D. S., Zhang, M., Theurer, P., Fonner, C. E., Kern, J. A., et al. (2018). Development of a Risk Prediction Model and Clinical Risk Score for Isolated Tricuspid Valve Surgery. *Ann. Thorac. Surg.* 106 (1), 129–136. doi:10.1016/j.athoracsur.2017.11.077

Leary, P. J., Kurtz, C. E., Hough, C. L., Waiss, M-P., Ralph, D. D., and Sheehan, F. H. (2012). Three-dimensional Analysis of Right Ventricular Shape and Function in Pulmonary Hypertension. *Pulm. Circ.* 2 (1), 34–40. doi:10.4103/2045-8932.94828

Marcu, C. B., Beek, A. M., and Van Rossum, A. C. (2006). Cardiovascular Magnetic Resonance Imaging for the Assessment of Right Heart Involvement in Cardiac and Pulmonary Disease. *Heart, Lung Circulation* 15 (6), 362–370. doi:10.1016/j.hlc.2006.08.003

Mauger, C., Gilbert, K., Lee, A. M., Sanghvi, M. M., Aung, N., Fung, K., et al. (2019). Right Ventricular Shape and Function: Cardiovascular Magnetic Resonance Reference Morphology and Biventricular Risk Factor Morphometrics in UK Biobank. *J. Cardiovasc Magn. Reson* 21 (1), 41. doi:10.1186/s12968-019-0551-6

Morgan, A. E., Howell, K., Chen, S., Serrone, R. O., Zheng, Y., Wang, V. Y., et al. (2020). Imaging and Computational Modeling of Tricuspid Regurgitation and Repair. *Vessel Plus* 4 (6).

Morgan, A. E., Kashani, A., Zenger, B., Rupp, L. C., Perez, M. D., Foote, M. D., et al. (2020). Right Ventricular Shape Distortion in Tricuspid Regurgitation. *Comput. Cardiol. (2010)* 47, 2020. doi:10.22489/cinc.2020.346

Morgan, A. E., Zhang, Y., Tartibi, M., Goldburg, S., Kim, J. J., Nguyen, T. D., et al. (2018). Ischemic Mitral Regurgitation: Abnormal Strain Overestimates Nonviable Myocardium. *Ann. Thorac. Surg.* 105 (6), 1754–1761. doi:10.1016/j.athoracsur.2018.01.005

Onno, A. (2015). Spruijt, Frances S. de Man, Herman Groepenhoff, Frank Oosterveer, Nico Westerhof, Anton Vonk-Noordegraaf, and Harm-Jan Bogaard. The effects of exercise on right ventricular contractility and right ventricular–arterial coupling in pulmonary hypertension. *Am. J. Respir. Crit. Care Med.* 191 (9), 1050–1057.

Pedregosa, F., Varoquaux, G., Gramfort, A., Michel, V., Bertrand, T., Grisel, O., et al. (2011). Scikit-learn: Machine Learning in python. *J. Mach. Learn. Res.* 12 (null), 2825–2830.

Prins, K. W., Rose, L., Archer, S. L., Pritzker, M., Weir, E. K., Olson, M. D., et al. (2019). Clinical Determinants and Prognostic Implications of Right Ventricular Dysfunction in Pulmonary Hypertension Caused by Chronic Lung Disease. *J. Am. Heart Assoc.* 8 (2), e011464. doi:10.1161/JAHA.118.011464

Ryan, J. (2014). Tedford. Determinants of Right Ventricular Afterload (2013 Grover Conference Series). *Pulm. Circ.* 4 (2), 211–219. doi:10.1086/676020

Singh, J. P., Evans, J. C., Levy, D., Larson, M. G., Freed, L. A., Fuller, D. L., et al. (1999). Prevalence and Clinical Determinants of Mitral, Tricuspid, and Aortic Regurgitation (The Framingham Heart Study). *Am. J. Cardiol.* 83 (6), 897–902. doi:10.1016/s0002-9149(98)01064-9

Stuge, O., and Liddicoat, J. (2006). Emerging Opportunities for Cardiac Surgeons within Structural Heart Disease. *J. Thorac. Cardiovasc. Surg.* 132 (6), 1258–1261. doi:10.1016/j.jtcvs.2006.08.049

Subbotina, I., Girdauskas, E., Bernhardt, A. M., Sinning, C., Reichenspurner, H., and Sill, B. (2017). Comparison of Outcomes of Tricuspid Valve Surgery in Patients with Reduced and Normal Right Ventricular Function. *Thorac. Cardiovasc Surg.* 65 (8), 617–625. doi:10.1055/s-0037-1604450

Thenappan, T., Prins, K. W., Pritzker, M. R., Scandurra, J., Volmers, K., and Kenneth Weir, E. (2016). The Critical Role of Pulmonary Arterial Compliance in Pulmonary Hypertension. *Ann. Am. Thorac. Soc.* 13 (2), 276–284. doi:10.1513/AnnalsATS.201509-599FR

Topilsky, Y., Maltais, S., Medina Inojosa, J., Oguz, D., Michelena, H., Maalouf, J., et al. (2019). Burden of Tricuspid Regurgitation in Patients Diagnosed in the Community Setting. *JACC Cardiovasc. Imaging* 12 (3), 433–442. doi:10.1016/j.jcmg.2018.06.014

Vargas Abello, L. M., Klein, A. L., Marwick, T. H., Nowicki, E. R., Rajeswaran, J., Puwanant, S., et al. (2013). Understanding Right Ventricular Dysfunction and Functional Tricuspid Regurgitation Accompanying Mitral Valve Disease. *J. Thorac. Cardiovasc Surg.* 145 (5), 1234–1241. doi:10.1016/j.jtcvs.2012.01.088

Voelkel Norbert, F., Quaife Robert, A., Leinwand Leslie, A., Barst Robyn, J., McGoon Michael, D., Meldrum Daniel, R., et al. (2006). Right Ventricular Function and Failure. *Circulation* 114 (17), 1883–1891. doi:10.1161/circulationaha.106.632208

Zhan, Y., Senapati, A., Vejpongsa, P., Xu, J., Shah, D. J., and Nagueh, S. F. (2020). Comparison of Echocardiographic Assessment of Tricuspid Regurgitation

against Cardiovascular Magnetic Resonance. *JACC Cardiovasc. Imaging* 13 (7), 1461–1471. doi:10.1016/j.jcmg.2020.01.008

**Conflict of Interest:** BS reports research support from AltaThera, Cardiva, Abbott, Sanofi, and Janssen; and consulting to AltaThera.

The remaining authors declare that the research was conducted in the absence of any commercial or financial relationships that could be construed as a potential conflict of interest.

**Publisher's Note:** All claims expressed in this article are solely those of the authors and do not necessarily represent those of their affiliated organizations, or those of the publisher, the editors and the reviewers. Any product that may be evaluated in this article, or claim that may be made by its manufacturer, is not guaranteed or endorsed by the publisher.

frontiers | Frontiers in Physiology

ORIGINAL RESEARCH
published: 30 June 2022
doi: 10.3389/fphys.2022.901280

# A Novel Method to Determine the Cause of Left Internal Mammary Artery Instant Non-Patency Based on Transit Time Flow Measurement

*Boyan Mao[1], Yue Feng[2,3], Mengyao Duan[1], Yihang Dong[1], Gaoyang Li[4], Bao Li[2], Jincheng Liu[2], Yuting Guo[4], Minghui Wei[1], Zhou Zhao[5] and Youjun Liu[2]**

[1]School of Life Sciences, Beijing University of Chinese Medicine, Beijing, China, [2]Department of Biomedical Engineering, Faculty of Environment and Life, Beijing University of Technology, Beijing, China, [3]Medical Equipment Department, Peking University First Hospital, Beijing, China, [4]Institute of Fluid Science, Tohoku University, Sendai, Japan, [5]Cardiac Surgery Department, Peking University People's Hospital, Beijing, China

**Objective:** After coronary artery bypass grafting (CABG) surgery, the main causes of poor instant patency of left internal mammary arteries (LIMAs) are competitive flow and anastomotic stenosis, but how to determine the cause of LIMA non-patency without interfering with the native coronary artery is still a difficult problem to be solved urgently.

**Methods:** In this study, a 0D-3D coupled multiscaled CABG model of anastomotic stenosis and competitive flow was constructed. After calculation, the flow waveform of the LIMA was extracted, and the waveform shape, common clinical parameters (average flow, PI, and DF), and graft flow FFT ratio results (F0/H1 and F0/H2) were analyzed.

**Results:** For LIMA, these three common clinical parameters did not differ significantly between the anastomotic stenosis group and competitive flow group. However, the waveform shape and FFT ratio (especially F0/H2) of the competitive flow group were significantly different from those of the anastomotic stenosis group. When the cause was competitive flow, there was systolic backflow, and F0/H2 was too high (>14.89). When the cause was anastomotic stenosis, the waveform maintained a bimodal state and F0/H2 was in a normal state (about 1.17).

**Conclusion:** When poor instant patency of the LIMA is found after CABG, the causes can be determined by graft flow waveform shape and F0/H2.

**Keywords: computational fluid dynamics, multiscaled model, coronary artery bypass grafting, graft patency, lumped parameter model**

OPEN ACCESS

***Edited by:***
*Yunlong Huo,*
*Shanghai Jiao Tong University, China*

***Reviewed by:***
*Mingzi Zhang,*
*Macquarie University, Australia*
*Yonggang Lv,*
*Wuhan Textile University, China*

****Correspondence:***
*Youjun Liu*
*lyjlma@bjut.edu.cn*

***Specialty section:***
*This article was submitted to Computational Physiology and Medicine, a section of the journal Frontiers in Physiology*

***Received:*** *21 March 2022*
***Accepted:*** *16 May 2022*
***Published:*** *30 June 2022*

***Citation:***
*Mao B, Feng Y, Duan M, Dong Y, Li G, Li B, Liu J, Guo Y, Wei M, Zhao Z and Liu Y (2022) A Novel Method to Determine the Cause of Left Internal Mammary Artery Instant Non-Patency Based on Transit Time Flow Measurement. Front. Physiol. 13:901280. doi: 10.3389/fphys.2022.901280*

## 1 INTRODUCTION

Coronary artery bypass grafting surgery (CABG) is a common method to cure myocardial ischemia. The graft bypasses the stenosis and maintains blood supply to the distal end of the coronary artery, significantly reducing the risk of myocardial ischemia (Beck, 1935; Vineberg and Jewett, 1947; Favaloro et al., 1971). In CABG, left internal mammary arteries (LIMAs) have become the most commonly used graft material due to their excellent long-term patency. The most common anastomosis way is the LIMA to the left anterior descending (LAD) branch.

However, LIMA grafts sometimes have poor instant patency due to their own properties and hemodynamics.

When all grafts are anastomosed, the graft patency is called instant patency. When the instant patency is poor, it will affect the blood supply and even cause the graft occlusion in a very short term after the operation. There are two main causes for poor graft instant patency: one is due to anastomotic stenosis and the other is due to competitive flow (Iii and Blackstone, 2008; Nikolaos et al., 2011). Anastomotic stenosis is mainly caused by errors during the operation, and its patency can be improved after the graft is removed and re-anastomosed. However, when the native coronary artery's stenosis is not serious, some blood can still flow through it, and this blood flow through the native coronary artery is called competitive flow. For LIMA grafts, competitive flow reduces the blood flow within the graft and, in severe cases, leads to the string phenomenon (Seki et al., 1992; Villareal and Mathur, 2000; Beijk and Harskamp, 2013; Halfwerk et al., 2021). At present, the method to determine the occurrence of competitive flow is to clamp the native coronary artery and measure graft flow again. If there is a significant increase in the graft flow, it indicates that competitive flow is significant. However, clamping the native coronary artery can be harmful to the patient, causing plaque to detach and block the distal coronary artery. Therefore, the clinical application of this method is greatly limited.

When the graft is considered to be of poor instant patency, it needs to be repaired. Usually, the surgeon removes the graft and performs the surgery again, which can improve the blood flow in some of the grafts (caused by anastomotic stenosis) but not in the others (caused by competitive flow). Re-performing this surgery arbitrarily not only does not help improve the graft flow but also increases the surgery risk. Therefore, it is an urgent problem to determine the cause of graft instant non-patency.

In clinical practice, transit time flow measurement (TTFM) technology is usually used to obtain the graft flow waveform and determine the graft's instant patency (P Malagón et al., 2020; Quin et al., 2020; Stastny et al., 2021). TTFM is based on the theory of ultrasonic velocity measurement, and its probe mainly includes an ultrasonic transmitter, reflection plate, and ultrasonic receiving device. It calculates the flow in the graft by measuring the time between the ultrasonic transmitting device and the ultrasonic receiving device. After CABG and before chest closure, surgeons will use a TTFM probe to measure the flow waveform of each graft, determine the graft patency according to the waveform, and decide whether to repair it. In general, three parameters in the waveform are often used to help surgeons assess graft patency: Average flow, pulsatility index (PI), and diastolic velocity–time integral fraction (DF). Low average flow, high PI, and low DF mean a higher risk of instant graft patency. However, no scholar has studied how to classify the specific causes of the poor graft instant patency. Therefore, in order to study this problem, this study chose the modeling and simulation method of CABG to simulate the graft waveform under different instant patency conditions and find the characteristics of the graft waveform that can determine competitive flow or anastomotic stenosis.

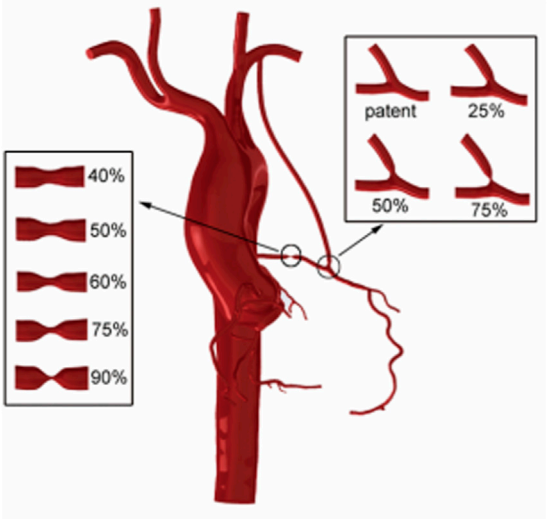


**FIGURE 1 |** CABG models using the LIMA graft which contain models with different LAD stenosis and different anastomotic stenosis.

# 2 METHODS

## 2.1 The CABG Multiscale Model

### 2.1.1 Reconstruction of the 3D CABG Model

This study reconstructed a 3D operation model of the coronary artery system and aortic arch from a patient's CT image data. The data were obtained from a male 55-year-old patient, and it contained 460 layers in total, each layer had 512*512 pixels, and the space between layers was 1 mm. The patient's cardiac output was 4.6 L/min, measured by Doppler ultrasound. Also, his diastolic and systolic blood pressures were 103 and 147 mmHg, respectively. A software named "Mimics" was used to conduct reconstruction of CT image data and used threshold segmentation to distinguish the aortic and coronary artery sections. "Freeform" was used to smooth models and complete LIMA-LAD bypass surgery. The LIMA diameter was set as 3 mm. Based on the LIMA-LAD bypass method, the stenosis rates in LAD were set as 90, 75, 60, 50, and 40% to simulate different degrees of competitive flow. In this competitive flow group, the degree of competitive flow increases with the decrease of the LAD stenosis (Li et al., 2017). Also, stenosis in anastomosis was set as 25, 50, and 75% based on a 90% stenosis in LAD (competitive flow is non-significant in this stenosis rate) for the anastomotic stenosis group. Finally, there are eight reconstructed 3D models which are shown in **Figure 1**. **Figure 1** shows the LIMA-LAD models.

"ANSYS-ICEM" was used in meshing these CABG models. All models adopted the tetrahedral meshing method and passed the grid sensitivity analysis. The vessel was assumed to be rigid walled, and the blood flow was a Newtonian fluid, with a dynamic viscosity of 0.0035 Pa s and a density of 1050 kg/m$^3$.

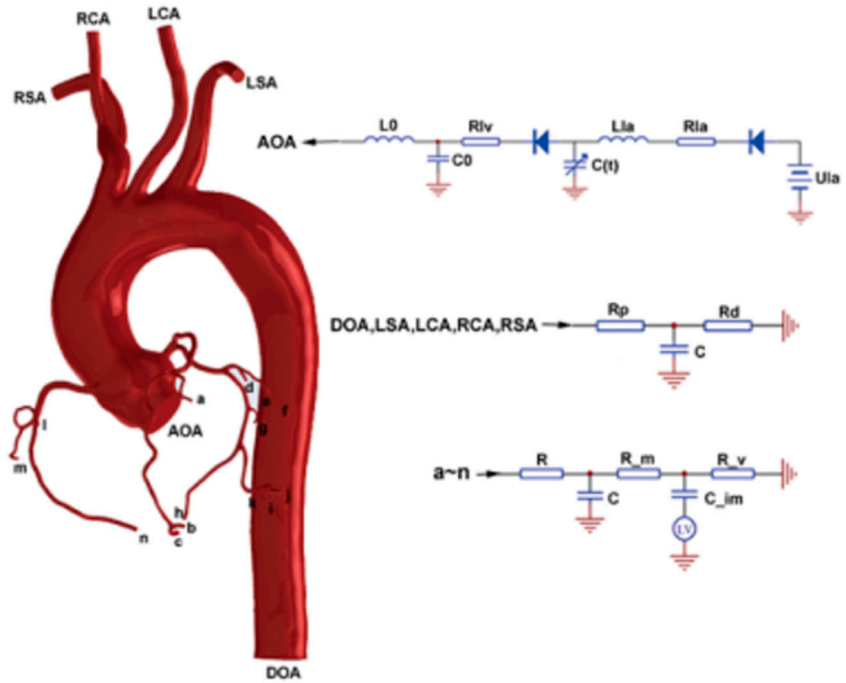


**FIGURE 2 |** 0D/3D coupled multiscaled model.

### 2.1.2 Lumped Parameter Model Construction

The lumped parameter model (0D model) used in this work was proposed by Taylor et al. (Taylor et al., 2013), and has been proved to be effective by our previous work (Zhao et al., 2016; Li et al., 2021). The lumped parameter model used a circuit network to simulate the vascular system, and blood flow problem was simplified to a circuit solution problem.

In this work, the lumped parameter model consisted of the following three modules: the heart module, the aorta module, and the coronary module, as seen on the right side of **Figure 2**.

For the heart module, a constant voltage power supply Ula was used to represent the pressure of the left atrium, and two diodes were used to simulate the mitral valve and aortic valve in turn. Rla and Lla were used to simulate the blood flow resistance and blood flow inertia flowing through the mitral valve in turn. Time-varying capacitance C (t) was used to represent the relaxation and contraction of the left ventricle. The formula is as follows:

$$C(t) = \frac{1}{E(t)}, \tag{1}$$

where E (t) is a time-varying elasticity (mmHg/ml), which could be approximated as follows:

$$E(t) = E_n(t_n) \cdot (E_{max} - E_{min}) + E_{min}. \tag{2}$$

$E_n(t_n)$ is the time-varying elasticity after normalization (Stergiopulos et al., 1996).

$$E_n(t_n) = 1.55 \cdot \left[\frac{1}{1 + \left(\frac{t_n}{1.17}\right)^{21.9}}\right] \cdot \left[\frac{\left(\frac{t_n}{0.7}\right)^{1.9}}{1 + \left(\frac{t_n}{0.7}\right)^{1.9}}\right], \tag{3}$$

where $t_n = \frac{t}{0.2+0.15t_c}$ and $t_c$ is the time of one cardiac cycle. For this research, the settings are as follows: $t_c$ = 0.8s, $E_{max}$ = 2.0, and $E_{min}$ = 0.002458.

For the aortic module, Rp represented arterial flow resistance; Rd represented the sum of the arterial terminal, microcirculation, and venous resistance; and C represented arterial vascular elasticity.

For the coronary module, R represented the coronary artery blood flow resistance, Rm represented the coronary microcirculation resistance, and Rv represented the coronary vein resistance. C represented coronary artery elasticity, and Cim represented coronary microcirculation elasticity. A voltage source was connected to Cim, and its value followed left ventricular pressure.

After determining the structure of the lumped parameter model, the next task is to select the appropriate parameters for each component of the model. In this article, a genetic algorithm was used to optimize the parameters (Li et al., 2018), and the problem of matching component parameters with physiological data was solved by taking the patient's personalized physiological characteristic data as the target.

First, the data of systolic blood pressure, diastolic blood pressure, heart rate, and cardiac output of normal people were used to fit the waveform of aortic pressure and cardiac output of normal people as two optimization target waveforms. Based on the research of Kim et al. (Kim et al., 2010), manual adjustment was adopted to adjust the parameter values to the degree that the output waveform matched the target waveform, and the parameters at this time were used as the reference values of subsequent personalized parameters. In this process, two

important points should be noted: 1) total coronary flow accounted for 4% of cardiac output and left coronary flow and right coronary flow accounted for 60 and 40% of total coronary flow, respectively; 2) the blood flow of coronary artery branches is proportional to 2.7 power of coronary artery diameter.

Second, the clinical measurements of aortic pressure and cardiac output were taken as the optimization objectives, and sensitivity analysis of the parameters of the lumped parameter model was conducted to find the parameters which had a great influence on the optimization objectives. It is found that the sensitive parameters include left atrial pressure and parameters of $E_{max}$ and $E_{min}$, which determine time-varying capacitance and microcirculation resistance.

Finally, the measured systolic blood pressure, diastolic blood pressure, and heart rate were used to adjust the standard aortic pressure waveform, and then the patient's personalized aortic pressure waveform was obtained. The pressure waveform was compared with the pressure waveform calculated by the lumped parameter model, and the root mean square error between the two waveforms was obtained. The root mean square error between the aortic pressure waveform and the simulated waveform and the mean cardiac output were used as the objective function to optimize the sensitive parameters in the model.

### 2.1.3 0D/3D Coupled Multiscaled Modeling Method

A 3D model was coupled with a lumped parameter model using a coupling algorithm and an interface condition. ANSYS-CFX commercial software was used for the 0D-3D coupling calculation. In this study, the lumped parameter model was used to provide boundary conditions for the 3D model, instead of directly calling the existing functions in the software as the boundary conditions, so the secondary development of CFX was needed. The secondary development of CFX is a user-defined subroutine based on the FORTRAN language. This study used FORTRAN language to write a subroutine based on CFX specification to calculate the lumped parameter model. The subroutine can assign an initial value to the model, calculate the lumped parameter model, transfer data between the 3D model and the lumped parameter model, coordinate multiprocess calculation, and calculate the hemodynamic parameters not included in CFX. All subroutines can be used in CFX calculation in the form of User CEL Function and User Junction Box Routine.

The lumped parameter model provided a flow boundary condition at the aortic inlet and pressure boundary conditions at the artery outlets of the 3D model. After fluid calculation, a pressure value was returned at the aortic inlet, and flow values were returned at artery outlets so as to facilitate the calculation of the lumped parameter model. ANSYS-CFX was used in 3D model calculation, and FORTRAN subroutines were used in lumped parameter model calculation.

The construction of a CABG multiscaled model was then completed, as shown in **Figure 2**. The blood flow waveform of the mid-side of the graft calculated by each model was extracted for subsequent analysis.

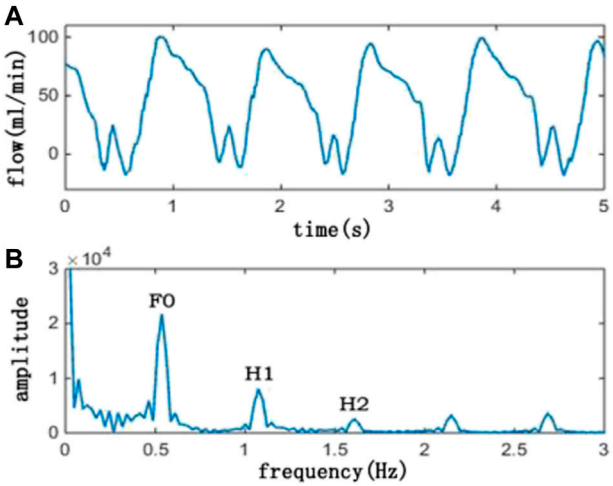


**FIGURE 3 |** Picture above **(A)** is a TTFM waveform, and the picture below **(B)** is its corresponding spectrum. In the spectrum picture, F0 is the amplitude of the fundamental frequency, H1 is the amplitude of the first harmonic, and H2 is the amplitude of the second harmonic. Also, F0/H1 is the ratio of F0 and H1, and F0/H2 is the ratio of F0 and H2

## 2.2 The Data From Flow Waveform

The data extracted from the flow waveforms for this research included the average flow, diastolic velocity–time integral fraction (DF), pulsatility index (PI), and a frequency index called the fast Fourier transformation (FFT) ratio. The FFT method is a classical signal processing method, which has been used to analyze the graft flow waveform. Takami et al. creatively proposed that FFT results of TTFM can be used as an indicator to determine the graft's patency. Researchers performed FFT transformation on the TTFM waveform, calculated the ratio of the fundamental wave to the first harmonic wave, took whether the ratio was higher than 1 as the distinguishing value to determine whether the graft was patent, and proposed that the FFT ratio had more accurate distinguishing ability than traditional parameters such as average flow, PI, and backflow rate (Takami and Ina, 2001). Later, Une et al. studied whether the FFT ratio of TTFM waveform would be different among different grafts of target coronary arteries. Also, whether the FFT ratio is more accurate than TTFM waveform parameters alone is analyzed to determine the graft patency. After research, both questions have been answered in the affirmative (Une et al., 2011). All these indicate that the FFT ratio has a very good performance in determining whether the graft is patent. Therefore, in this study, we also tried to use the FFT ratio to determine the cause of graft non-patency and observe whether it can play a significant role.

The average flow was defined as follows: Total flow/time; DF was defined as follows: diastolic flow/total flow; and PI was defined as follows: (maximum flow—minimum flow)/average flow. The FFT method is a classic signal processing method. The TTFM flow measured in the clinic and its spectrum are shown in **Figure 3**.

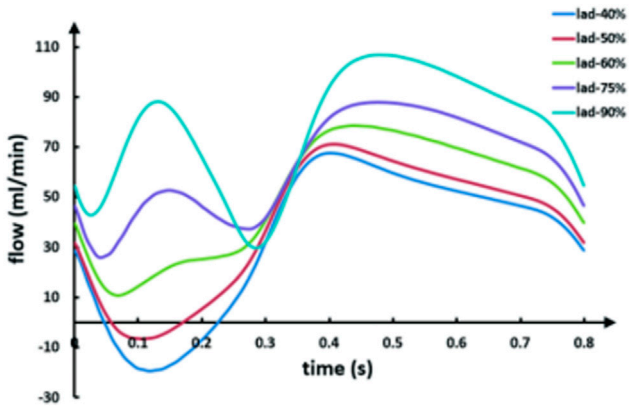


**FIGURE 4 |** LIMA flow waveforms in models with different degrees of the competitive flow.

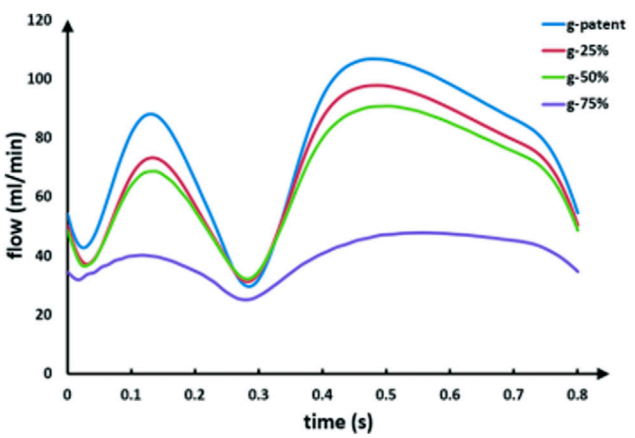


**FIGURE 5 |** LIMA flow waveforms in models with different anastomotic stenosis based on a 90% LAD stenosis. The g-patent and lad-90% flow waveforms are coming from the same model.

In this study, F0/H1 and F0/H2 were selected for research objectives. In order to avoid spectrum leak, cycle extension has been adopted and the flow wave was extended to 10 periods. The sampling frequency was set as 50 Hz, and the sampling point was set as 2048.

# 3 RESULTS

## 3.1 The Comparison of LIMA Graft Flow Waveforms

The flow waveforms have been extracted from the mid-side of the grafts and are shown as the following figures.

**Figure 4** shows graft flow waveforms under different LAD stenosis rates. The competitive flow is negatively correlated with the LAD stenosis rate, that is, the lower the LAD stenosis rate, the higher the competitive flow. Therefore, the waveforms shown in the figure are graft flow waveforms under different degrees of competitive flow. It can be seen from the figure that under ideal conditions (i.e., lad-90%, at which the effect of competitive flow can be considered to be very weak), the flow waveform in the graft is a bimodal waveform in systolic and diastolic stages, and the peak value in the systolic stage is slightly lower than that in the diastolic stage. With the increase of competitive flow, the systolic peak flow and diastolic peak flow decrease, but the systolic peak flow decreases more obviously, and the waveform gradually shows a single peak shape. When the LAD stenosis rate is lower than 50%, the peak systolic flow falls below 0 and backflow appears.

**TABLE 1 |** D/S of graft flow waveforms in different models.

| Model | D/S |
|---|---|
| lad-40% | Backflow |
| lad-50% | Backflow |
| lad-60% | 3.26 |
| lad-75% | 1.66 |
| lad-90%/g-patent | 1.21 |
| g-25% | 1.33 |
| g-50% | 1.32 |
| g-75% | 1.19 |

**TABLE 2 |** Comparison of clinical factors.

| | Average flow (ml/min) | PI | DF (%) |
|---|---|---|---|
| lad-40% | 33 | 2.7 | 102 |
| lad-50% | 39 | 2 | 93 |
| lad-60% | 50 | 1.4 | 83 |
| lad-75% | 62 | 1 | 75 |
| lad-90%/g-patent | 77 | 1 | 71 |
| g-25% | 70 | 0.9 | 72 |
| g-50% | 67 | 0.9 | 71 |
| g-75% | 39 | 0.6 | 67 |

As can be seen from **Figure 5**, with the increase in the anastomotic stenosis rate, the systolic and diastolic flow in the graft decreases, and the drop scopes are similar. When the anastomotic stenosis rate is 75%, the flow waveform is significantly lower than that of the other three models, but the peak flow ratio of the diastole to systole is basically unchanged. Throughout the process, the waveform maintains a bimodal shape.

In order to quantitatively describe the change of the graft waves, a new index was introduced, which is the ratio of diastolic peak flow to systolic peak flow (D/S). The calculation results are shown in **Table 1**.

As can be seen from the table, with the LAD stenosis rate changing from 90 to 60%, D/S also increases from 1.21 to 3.26, and systolic backflow even occurs after the stenosis rate is lower than 50%. Also, as the stenosis rate of the anastomotic site changes from the patent to 75%, its D/S remains basically unchanged, ranging from 1.2 to 1.3.

## 3.2 The Comparison of Clinical Factors

Average flow, PI, and DF are commonly used in clinical practice to evaluate the quality of the grafts. They were calculated by extracting graft waveforms. The results are shown in **Table 2**.

**TABLE 3 |** FFT ratio of graft flow waveforms.

| | F0/H1 | F0/H2 |
|---|---|---|
| lad-40% | 2.07 | 21.87 |
| lad-50% | 2.39 | 14.89 |
| lad-60% | 4.32 | 5.24 |
| lad-75% | 8.44 | 2.3 |
| lad-90%/g-patent | 1.7 | 1.17 |
| g-25% | 1.85 | 1.45 |
| g-50% | 1.89 | 1.49 |
| g-75% | 1.89 | 1.83 |

**Table 2** shows a comparison of average flow, PI, and DF among different models. As can be seen from the table, for average flow, the maximum flow rate occurs when the LAD stenosis rate is 90% (while the anastomotic site remains patent). As the LAD stenosis rate decreases from 90 to 40%, the average flow rate decreases from 77 ml/min to 33 ml/min. As the anastomosis changes from patent to 75% stenosis, the average flow rate decreases from 77 ml/min to 39 ml/min. For PI, with the decrease of the LAD stenosis rate from 90 to 40%, PI increases from 1 to 2.7. Meanwhile, as the anastomosis changes from patent to 75% stenosis, PI decreases from 1 to 0.6. For DF, DF remains constant in the anastomotic stenosis group, while in the competitive flow group, the LAD stenosis rate reduces from 90 to 40% and DF increases from 70 to 102%. DF reaches 102% due to the presence of systolic backflow, making the total effective flow less than the diastolic flow.

## 3.3 FFT Ratio of Graft Flows

By applying FFT transformation to the abovementioned waveforms, F0/H1 and F0/H2 were calculated, and the results are shown in **Table 3**. To make the results more intuitive, we present the results as line graphs, as shown in **Figure 6**.

As can be seen from **Figure 6**, with the LAD stenosis rate reduced from 90 to 40%, F0/H1 first increases from 1.7 to 8.44 but then decreases to 2.07, and the change in this process is nonlinear. However, F0/H2 increases from 1.17 to 21.87. As the anastomotic site changes from patent to 75% stenosis, the values of F0/H1 and F0/H2 both increase, but these changes are not significant.

Based on the abovementioned results, a method to determine the cause of LIMA instant non-patency is obtained in this study. If it is assumed that the stenosis rate of LAD is less than 50%, the competitive flow has a significant effect (Li L et al., 2017). Under this assumption, when the waveform is single-peak and F0/H2 is greater than 14.89, the competitive flow is significant. However, anastomotic stenosis hardly causes the change of D/S and F0/H2, and its D/S is around 1.21 and F0/H2 is around 1.17.

# 4 DISCUSSION

## 4.1 The Variation of Flow Waveforms in Different Models

Based on the graft flow waveforms obtained by our model calculation, waveforms in the competitive flow and anastomotic stenosis groups are significantly different. The change of the competitive flow group is mainly reflected in the shape of the waveform, while the change of the anastomotic stenosis group is mainly due to amplitude. This allows us to use the shape of the waveform as a key factor in determining the cause of graft instant non-patency. To describe the waveform change quantitatively, a new factor D/S is introduced. It can be seen from the results that with the increase of the competitive flow, D/S increases continuously, and even the graft presents backflow. However, as anastomotic stenosis increases, there are minimal changes in D/S. Therefore, D/S could be considered a key determinant factor.

## 4.2 The Analysis of Average Flow, PI and DF

In the LIMA, the ideal model has the maximum average flow. When the competitive flow increases or the anastomotic

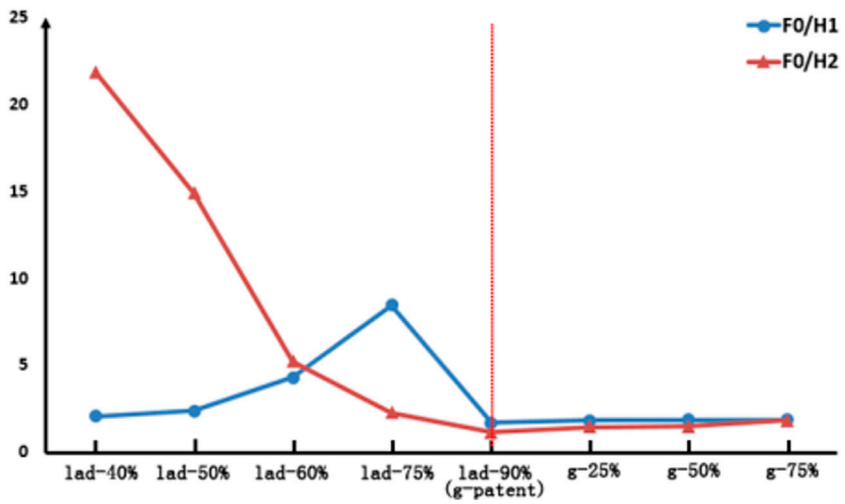


**FIGURE 6 |** Comparison of the FFT ratio results in LIMA. The left of the red dotted line is the competitive flow group and the right is the anastomosis stenosis group.

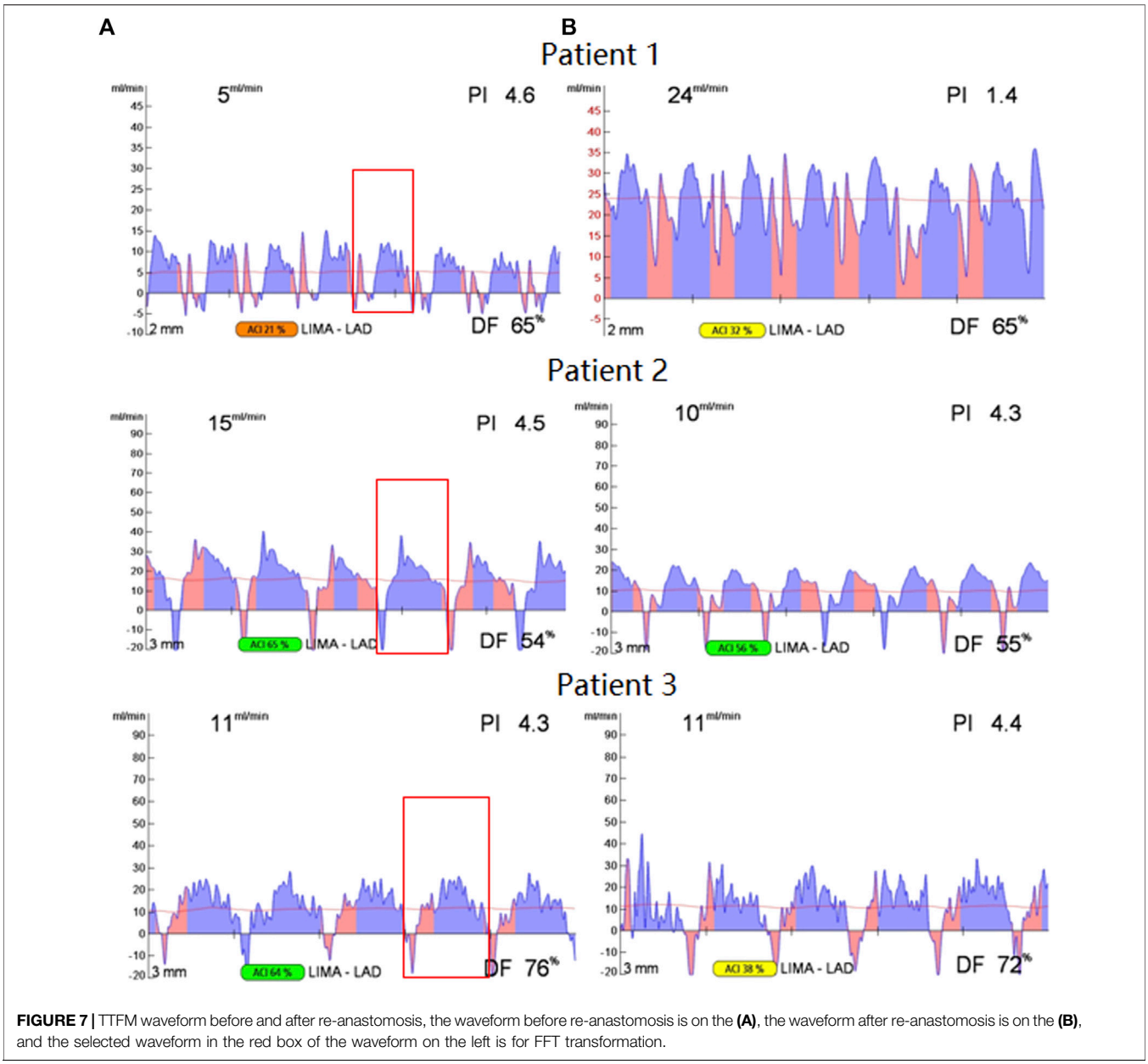


**FIGURE 7 |** TTFM waveform before and after re-anastomosis, the waveform before re-anastomosis is on the **(A)**, the waveform after re-anastomosis is on the **(B)**, and the selected waveform in the red box of the waveform on the left is for FFT transformation.

stenosis increases, the average flow will decrease. This will lead to a challenge in determining the cause using this factor. PI in the competitive flow group is slightly higher than that in the anastomotic stenosis group, and PI increases with the increase of the competitive flow, but it decreases slightly with the increase of the anastomotic stenosis. DF in the competitive flow group increases with the increase of competitive flow, while DF in the anastomotic stenosis group remains constant. However, in general, there is little difference between PI and DF between the two groups, and none of them could be the factor for determining the cause of graft instant non-patency.

## 4.3 The Analysis of FFT Method

After FFT transformation, F0/H1 and F0/H2 have different changing trends. For the anastomotic stenosis group, the change curves of F0/H1 and F0/H2 almost coincide, and the anastomotic stenosis model has no significant change compared with the ideal model. However, for the competitive flow group, not only the model with high competitive flow is very different from the ideal model but also the variation rules of F0/H1 and F0/H2 are different. Compared with the rule that F0/H2 increases monotonically with the increase of competitive flow, F0/H1 is not suitable to be used as a factor in determining the cause of graft instant non-patency due to its non-monotonic characteristics.

Therefore, F0/H2 can be considered a factor in determining the cause of LIMA instant non-patency.

### 4.4 Clinical Graft Flow Waveform Results

In the 132 grafts collected from 60 patients in the previous stage of this study (Mao et al., 2020), a total of 50 LIMA grafts were anastomosed on the LAD branch, and the TTFM waveform of three grafts showed instant non-patency and was re-anastomosed. At present, it is impossible to determine whether the cause of graft instant non-patency is anastomotic stenosis or competitive flow in clinical practice. Therefore, in this study, the grafts with improved flow after re-anastomosis are considered anastomotic stenosis, and the grafts with unimproved flow are considered competitive flow. Based on this principle, one of the three grafts is due to anastomotic stenosis and two are due to competitive flows, as shown in **Figure 7**.

As can be seen from **Figure 7**, for patient 1, the graft flow increases from 5 ml/min to 24 ml/min after re-anastomosis, which is a significant increase. Therefore, it is believed that the cause of graft instant non-patency is anastomotic stenosis. However, for patient 2 and patient 3, it could be seen that flows do not increase after re-anastomosis, so it is believed that the graft's instant non-patency is due to competitive flow.

The left TTFM waveform is observed (before re-anastomosis). A period is selected after the flow waveform is stable, and the selected period is in the red box. The period continuation and FFT transformation of this period waveform are carried out. The waveform of patient 1 basically maintains a double peak in systolic and diastolic periods, while waveforms of patient 2 and patient 3 show a single peak in the diastolic period, and there is obvious negative flow in the systolic stage. After the FFT transformation of the selected waveform, the F0/H2 value is obtained. After calculation, the F0/H2 values of patient 1, patient 2, and patient 3 are 1.99, 15.55, and 13.46, respectively. The difference between patient 1 and the remaining two patients validates the method proposed in this study.

The previous method to determine graft competing for flow and anastomotic stenosis was to clamp the native coronary artery and observe whether graft flow was improved. Our method is to directly use the TTFM waveform through the extraction of waveform features to achieve. Comparatively speaking, the method proposed in this article has the greatest advantage of reducing the possible trauma to patients compared with the previous method because clamping the coronary artery can cause plaque to detach and block the distal coronary artery. However, our method avoids this and achieves a "risk-free" judgment of the cause of graft instant non-patency.

### 4.5 Limitation

Although a method to determine the cause of the graft instant non-patency is obtained in this study, there are still some limitations in the experimental process. Among them, the most important point is that the conclusion of this study was reached through modeling and simulation and variable control, and the sample size was also small in the process of clinical verification, so a clear cut-off value for determining competitive flow or anastomotic stenosis could not be obtained. In addition, rigid walls were used in the 3D modeling process, ignoring the influence of vascular elasticity on the waveforms. The fluid-structure coupling model can be considered to solve this problem in future research.

## 5 CONCLUSION

Based on the abovementioned studies, it is found that for the LIMA graft, when the graft is considered to be non-patent, the waveform shape and FFT ratio results could jointly be used as factors in determining the cause of graft instant non-patency. When backflow occurs during the systolic period and F0/H2 is too high (about 14.89 or higher), it indicates that the cause is competitive flow. When graft flow presents a bimodal state and F0/H2 is at a normal level (about 1.17 or slightly higher), it indicates that the cause is anastomotic stenosis.

## DATA AVAILABILITY STATEMENT

The original contributions presented in the study are included in the article/Supplementary Material; further inquiries can be directed to the corresponding author.

## ETHICS STATEMENT

The studies involving human participants were reviewed and approved by the Peking University people's hospital. The patients/participants provided their written informed consent to participate in this study. Written informed consent was obtained from the individual(s) for the publication of any potentially identifiable images or data included in this article.

## AUTHOR CONTRIBUTIONS

BM is responsible for 3D reconstruction, fluid calculation, and manuscript writing. YF assisted in clinical data analysis and manuscript writing. MD is responsible for data analysis. YD assisted in the 0D/3D model establishment. GL assisted in model optimization. BL assisted in the model calculation. JL assisted in the construction of the 0D model. YG assisted in the fluid calculation. MW assisted in waveform analysis. ZZ is responsible for clinical and experimental data. YL is responsible for supervision.

## FUNDING

This research is supported by the National Natural Science Foundation of China (12102064 and 11832003), and the Fundamental Research Funds for the Central Universities (2021-JYB-XJSJJ022).

## REFERENCES


Beck, C. S. (1935). The Development of a New Blood Supply to the Heart by Operation*. *Ann. Surg.* 102 (5), 801–813. doi:10.1097/00000658-193511000-00001

Beijk, M. A., and Harskamp, R. E. (2013). *Treatment of Coronary Artery Bypass Graft Failure*. London: INTECH Open Access Publisher.

Favaloro, R. G., Effler, D. B., Cheanvechai, C., Quint, R. A., and Sones, F. M. (1971). Acute Coronary Insufficiency (Impending Myocardial Infarction and Myocardial Infarction). *Am. J. Cardiol.* 28 (5), 598–607. doi:10.1016/0002-9149(71)90104-4

Halfwerk, F. R., Spoor, P., Mariani, S., Hagmeijer, R., and Grandjean, J. G. (2021). Intraoperative Transit Time Flow Measurements during Off-pump Coronary Artery Bypass Surgery: The Impact of Coronary Stenosis on Competitive Flow. *J. Cardiac Surg.* 37 (2), 305–313. doi:10.1111/jocs.16103

Iii, J., and Blackstone, E. H. (2008). Coronary Artery Bypass Graft Patency and Competitive Flow. *J. Am. Coll. Cardiol.* 51 (2), 126–128.

Karapanos, N. T., Suddendorf, S. H., Li, Z., Huebner, M., Joyce, L. D., and Park, S. J. (2011). The Impact of Competitive Flow on Distal Coronary Flow and on Graft Flow during Coronary Artery Bypass Surgery. *Interact. Cardiovasc. Thorac. Surg.* 12 (6), 993–997.

Kim, H. J., Vignon-Clementel, I. E., Coogan, J. S., Figueroa, C. A., Jansen, K. E., and Taylor, C. A. (2010). Patient-specific Modeling of Blood Flow and Pressure in Human Coronary Arteries. *Ann. Biomed. Eng.* 38 (10), 3195–3209. doi:10.1007/s10439-010-0083-6

Li, B., Wang, W., Mao, B., Liu, Y., et al. (2018). A Method to Personalize the Lumped Parameter Model of Coronary Artery. *Int. J. Comput. Methods* 16 (3), 1842004.

Li, B., Mao, B., Feng, Y., Liu, J., Zhao, Z., Duan, M., et al. (2021). The Hemodynamic Mechanism of FFR-Guided Coronary Artery Bypass Grafting. *Front. Physiol.* 12, 503687. doi:10.3389/fphys.2021.503687

Li, L., Liu, Y., Zhao, X., Mao, B., and Zhang, H. (2017). Impact of Competitive Flow on Hemodynamics of Lima-Lad Grafting with Different Stenosis: A Numerical Study. *J. Mech. Med. Biol.* 17 (02), 1750040. doi:10.1142/s0219519417500403

Malagón, P., Carrasco, C., Vila, J., Priego, D., Higueras, C., et al. (2020). Intraoperative Hemodynamic Changes in the Arterial Blood Flow Measured by Transit Time Flowmetry (TTFM) during Breast Reconstruction with Free Diep Flap. *J. Plastic, Reconstr. Aesthetic Surg.* 73 (9), 1779–1780.

Mao, B., Feng, Y., Wang, W., Li, B., Zhao, Z., Zhang, X., et al. (2020). The Influence of Hemodynamics on Graft Patency Prediction Model Based on Support Vector Machine. *J. Biomechanics* 98, 109426. doi:10.1016/j.jbiomech.2019.109426

Quin, J. A., Noubani, M., Rove, J. Y., Krstacic, J. E., Hattler, B., Collins, J. F., et al. (2021). Coronary Artery Bypass Grafting Transit Time Flow Measurement: Graft Patency and Clinical Outcomes. *Ann. Thorac. Surg.* 112 (3), 701–707. doi:10.1016/j.athoracsur.2020.12.011

Seki, T., Kitamura, S., Kawachi, K., Morita, R., Kawata, T., Mizuguchi, K., et al. (1992). A Quantitative Study of Postoperative Luminal Narrowing of the Internal Thoracic Artery Graft in Coronary Artery Bypass Surgery. *J. Thorac. Cardiovasc. Surg.* 104 (6), 1532–1538. doi:10.1016/s0022-5223(19)33880-2

Stastny, L., Kofler, M., Zujs, V., Ruttmann, E., Dumfarth, J., Kilo, J., et al. (2021). A New Way to Use Transit-Time Flow Measurement for Coronary Artery Bypass Grafting. *Interact. Cardiovasc. Thorac. Surg.* 32 (5), 711–718. doi:10.1093/icvts/ivaa328

Stergiopulos, N., Meister, J. J., and Westerhof, N. (1996). Determinants of Stroke Volume and Systolic and Diastolic Aortic Pressure. *Am. J. Physiology-Heart Circulatory Physiology* 270 (6), H2050–H2059. doi:10.1152/ajpheart.1996.270.6.h2050

Takami, Y., and Ina, H. (2001). Relation of Intraoperative Flow Measurement with Postoperative Quantitative Angiographic Assessment of Coronary Artery Bypass Grafting. *Ann. Thorac. Surg.* 72 (4), 1270–1274. doi:10.1016/s0003-4975(01)02933-2

Taylor, C. A., Fonte, T. A., and Min, J. K. (2013). Computational Fluid Dynamics Applied to Cardiac Computed Tomography for Noninvasive Quantification of Fractional Flow Reserve. *J. Am. Coll. Cardiol.* 61 (22), 2233–2241. doi:10.1016/j.jacc.2012.11.083

Une, D., Chikazawa, G., Karkhanis, R., Vincent, J., Sever, J., Singh, S., et al. (2011). 611 Can Fast Fourier Transformation (FFT) Analysis of Graft Flow Predict 1 Year Graft Failure after CABG? *Can. J. Cardiol.* 27 (5), S284. doi:10.1016/j.cjca.2011.07.507

Villareal, R. P., and Mathur, V. S. (2000). The String Phenomenon: an Important Cause of Internal Mammary Artery Graft Failure. *Tex Heart Inst. J.* 27 (4), 346–349.

Vineberg, A. M., and Jewett, B. L. (1947). Anastomosis between Coronary Vessels and Internal Mammary Artery. *Can. Med. Assoc. J.* 56 (6), 609–614.

Zhao, X., Liu, Y., Li, L., Wang, W., Xie, J., and Zhao, Z. (2016). Hemodynamics of the String Phenomenon in the Internal Thoracic Artery Grafted to the Left Anterior Descending Artery with Moderate Stenosis. *J. biomechanics* 49 (7), 983–991. doi:10.1016/j.jbiomech.2015.11.044


**Conflict of Interest:** The authors declare that the research was conducted in the absence of any commercial or financial relationships that could be construed as a potential conflict of interest.

frontiers | Frontiers in Physiology

ORIGINAL RESEARCH
published: 13 July 2022
doi: 10.3389/fphys.2022.921764

# Long-Term Inhalation of Ultrafine Zinc Particles Deteriorated Cardiac and Cardiovascular Functions in Rats of Myocardial Infarction

*Yunlong Huo*[1,2]* *and Li Li*[2,3]

[1]Institute of Mechanobiology & Medical Engineering, School of Life Sciences and Biotechnology, Shanghai Jiao Tong University, Shanghai, China, [2]PKU-HKUST Shenzhen-Hong Kong Institution, Shenzhen, China, [3]Department of Mechanics and Engineering Science, College of Engineering, Peking University, Beijing, China

Substantial ultrafine zinc particles exist in air pollutions. The level of Zn concentrations in serum and tissue could affect patients with myocardial infarction (MI). The aim of the study is to investigate the change of cardiac functions and peripheral hemodynamics in MI rats after long-term inhalation of ultrafine Zn particles. Coronary artery ligation surgery was performed to induce MI in Wistar rats. The inhalation of ultrafine Zn particles was carried out for 6 weeks after the operation. Physiological and hemodynamic measurements and computational biomechanics analysis were demonstrated in eight groups of rats at postoperative 4 and 6 weeks. There was no statistical significance between shams and shams with inhalation of ultrafine Zn particles. There were significant impairments of cardiac and hemodynamic functions in MI rats. In comparison with MI rats, the inhalation of ultrafine Zn particles for 4 weeks slowed down the progression from MI to heart failure, but the inhalation for 6 weeks accelerated the process. The long-term inhalation of ultrafine zinc particles induced excessive accumulation of zinc in serum and tissue, which deteriorated cardiac and hemodynamic dysfunctions in MI rats. The findings suggested the importance for regulating Zn intake of MI patients as well as looking at ways to lower zinc concentrations in air pollutions.

**Keywords: myocardium infraction, speckle-tracing echocardiography, strain analysis, ultrafine zinc particle, Womersley analysis**

OPEN ACCESS

***Edited by:***
*Jinseok Lee,*
*Kyung Hee University, South Korea*

***Reviewed by:***
*Mark Russell Miller,*
*University of Edinburgh, United Kingdom*
*Yunyoung Nam,*
*Soonchunhyang University, South Korea*

***Correspondence:**
*Yunlong Huo*
*huoyunlong@sjtu.edu.cn*

***Specialty section:***
*This article was submitted to Computational Physiology and Medicine, a section of the journal Frontiers in Physiology*

***Received:*** *16 April 2022*
***Accepted:*** *23 June 2022*
***Published:*** *13 July 2022*

***Citation:***
*Huo Y and Li L (2022) Long-Term Inhalation of Ultrafine Zinc Particles Deteriorated Cardiac and Cardiovascular Functions in Rats of Myocardial Infarction. Front. Physiol. 13:921764. doi: 10.3389/fphys.2022.921764*

## INTRODUCTION

The American Heart Association reports long-term exposure to particle matters (PMs) in air pollution resulting to cardiovascular morbidity and mortality (Robert, 2004). In comparison with fine particle pollution (PM2.5), ultrafine particles (UFPs) (PM0.1) produced stronger chemical reaction given its small volume and large surface area (Andre 2006; Franck et al., 2011; Karottkiet al., 2014), which could increase vascular tension of systemic circulation resulting in high blood pressure

**Abbreviations:** CO, cardiac output; ESV, end-systolic volume of LV; EDV, end-diastolic volume of LV; EF (%), ejection fraction; FS (%), fractional shortening; HFpEF, heart failure with preserved ejection fraction; HFrEF, heart failure with reduced ejection fraction; LV, left ventricle; LAD, left anterior descending artery; LVAW;s, LV anterior wall in systole; LVAW;d, LV anterior wall in diastole; LVPW;s, LV posterior wall in systole; LVPW;d, LV posterior wall in diastole; LVID;s, LV internal diameter in systole; LVID;d, LV internal diameter in diastole; LVEDP, LV end-diastolic pressure; SV, stroke volume.

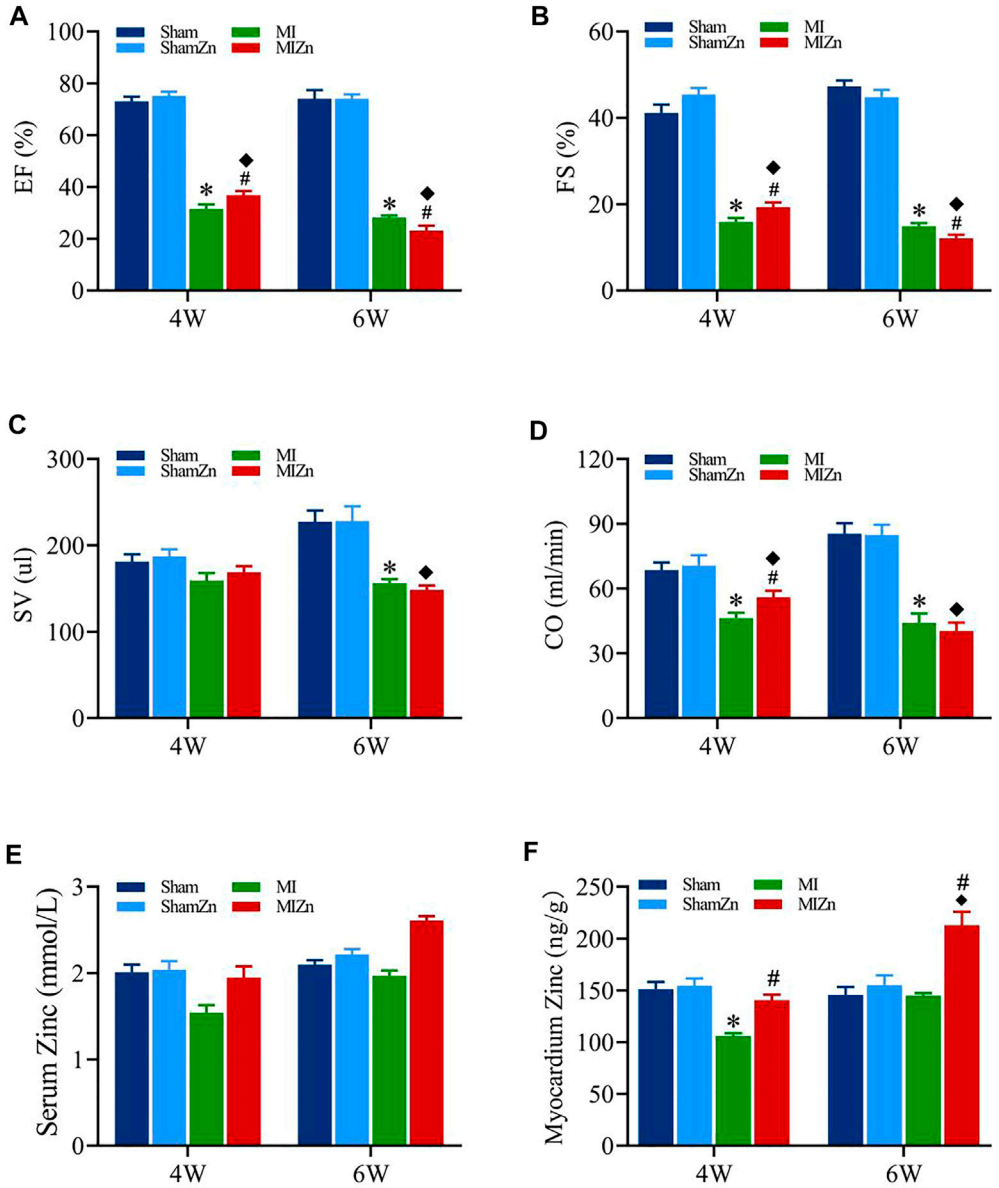


**FIGURE 1 |** Cardiac functions and zinc levels in eight groups. Panels **(A–D)** show the change of EF, FS, SV, CO, respectively. Panels **(E,F)** show the change of serum and myocardium zinc concentrations, respectively. All of the data were shown as Mean ± SEM. *$p < 0.05$, MI vs. Sham; ◆$p < 0.05$, ShamZn vs. MIZn; #$p < 0.05$, MIZn vs. MI.

(Mills et al., 2005; Törnqvist et al., 2007) as well as impair regulation of endogenous fibrinolysis accelerating the process of myocardial remodeling and fibrosis (Wold et al., 2012). Hence, UFPs in air pollution should be more detrimental to patients with myocardial infarction (MI) (Andre, 2006; Franck, et al., 2011; Karottki et al., 2014).

UFPs contained substantial airborne trace metals (Wolfram 2006). The concentrations of trace metals were in the order of Zn > Pb > Cu > Cr > V > Ni in four cities of the Yangtze River Delta (YRD) Metropolitan Area, China, i.e., Shanghai, Nanjing, Hangzhou, Ningbo (Ming et al., 2017). Because of higher concentration of Zn in air pollution, we have investigated the effects of short-term (4 weeks) inhalation of ultrafine Zn particles (wrapped by a layer of ZnO) on MI rats, which was found to alleviate cardiac and hemodynamic dysfunctions in disagreement with the assumption of toxicity hazards (Li et al., 2021). Hence, it is required to further investigate the effects of long-term inhalation of ultrafine zinc particles (wrapped by a layer of ZnO) on MI rats. The words "wrapped by a layer of ZnO" are neglected in the following text unless specifically noted.

The objective of the study is to investigate the change of cardiac functions and peripheral hemodynamics in MI rats after long-term inhalation of ultrafine Zn particles. Here, we hypothesized that the toxic effect of ultrafine Zn particles on

**TABLE 1 |** Morphometric parameters in the LV of eight groups at systole and diastole.

| Groups | LVAW;s (mm) | LVAW;d (mm) | LVPW;s (mm) | LVPW;d (mm) | LVID;s (mm) | LVID;d (mm) | ESV (μL) | EDV (μL) |
|---|---|---|---|---|---|---|---|---|
| Sham4 | 2.69 ± 0.07 | 1.67 ± 0.04 | 2.62 ± 0.04 | 1.71 ± 0.04 | 3.87 ± 0.11 | 6.40 ± 0.08 | 67.00 ± 3.84 | 224.3 ± 13.7 |
| ShamZn4 | 2.74 ± 0.06 | 1.89 ± 0.02 | 2.90 ± 0.09 | 1.90 ± 0.05 | 3.77 ± 0.13 | 6.90 ± 0.16 | 68.62 ± 3.51 | 238.4 ± 12.76 |
| MI4 | 1.07 ± 0.07* *$p < 0.0001$ | 1.05 ± 0.07* *$p < 0.0001$ | 2.61 ± 0.16 *$p > 0.9999$ | 1.91 ± 0.06 *$p = 0.2396$ | 8.02 ± 0.27* *$p < 0.0001$ | 10.06 ± 0.26* *$p < 0.0001$ | 383 ± 10.71* *$p < 0.0001$ | 565 ± 22.77* *$p < 0.0001$ |
| MIZn4 | 1.16 ± 0.04◆ ◆$p < 0.0001$ #$p = 0.9918$ | 1.20 ± 0.10◆ ◆$p < 0.0001$ #$p = 0.8096$ | 2.62 ± 0.11 ◆$p = 0.6435$ #$p > 0.9999$ | 1.93 ± 0.08 ◆$p > 0.9999$ #$p > 0.9999$ | 7.26 ± 0.23◆# ◆$p < 0.0001$ #$p = 0.0467$ | 9.48 ± 0.32◆◆ < $0.0001$ #$p = 0.5974$ | 352 ± 6.81◆# ◆$p < 0.0001$ #$p = 0.0209$ | 493 ± 22.83◆# ◆$p < 0.0001$ #$p = 0.0318$ |
| Sham6 | 2.96 ± 0.18 | 2.01 ± 0.08 | 3.29 ± 0.13 | 2.13 ± 0.08 | 4.17 ± 0.14 | 7.23 ± 0.21 | 75.85 ± 5.76 | 288.00 ± 13.96 |
| ShamZn6 | 3.06 ± 0.04 | 1.95 ± 0.03 | 3.34 ± 0.13 | 2.12 ± 0.07 | 4.45 ± 0.15 | 7.59 ± 0.28 | 75.92 ± 5.29 | 309.70 ± 24.84 |
| MI6 | 0.93 ± 0.07* *$p < 0.0001$ | 1.05 ± 0.11* *$p < 0.0001$ | 2.84 ± 0.11 *$p = 0.1801$ | 2.21 ± 0.07 *$p = 0.9887$ | 8.26 ± 0.23* *$p < 0.0001$ | 10.28 ± 0.38* *$p < 0.0001$ | 402 ± 7.57* *$p < 0.0001$ | 609 ± 12.39* *$p < 0.0001$ |
| MIZn6 | 0.71 ± 0.07◆# ◆$p < 0.0001$ #$p = 0.0485$ | 0.69 ± 0.08◆# ◆$p < 0.0001$ #$p = 0.0323$ | 2.71 ± 0.15◆ ◆$p = 0.0185$ #$p = 0.9908$ | 2.05 ± 0.06 ◆$p = 0.9991$ #$p = 0.7576$ | 9.05 ± 0.18◆# ◆$p < 0.0001$ #$p = 0.0189$ | 10.89 ± 0.24◆ ◆$p < 0.0001$ #$p = 0.7027$ | 438 ± 14.02◆# ◆$p < 0.0001$ #$p = 0.0494$ | 647 ± 10.39◆# ◆$p < 0.0001$ #$p = 0.0319$ |

*All of the data were shown as Mean ± SEM.* *p < 0.05, *MI vs. Sham;* ◆p < 0.05, *ShamZn vs. MIZn;* #p < 0.05, *MIZn vs. MI.*

the progression from MI to heart failure (HF) is associated with time interval of inhaling the particles, i.e., short-term inhalation of ultrafine Zn particles inhibits the progression, but long-term inhalation deteriorates it. To test the hypothesis, Wistar rats were used for coronary artery ligation surgery to induce MI. Partial shams and MI rats underwent inhalation control of ultrafine Zn particles for 6 weeks. Physiological and hemodynamic measurements were demonstrated in the LV and carotid artery for 4 and 6 weeks after the ligation surgery. The speckle tracking echocardiography (STE) was used to analyze LV functions. The Windkessel model was performed for the hemodynamic analysis in the carotid artery.

# METHODS

## Experimental Measurements

Wistar male rats (Beijing Vital River Laboratory Animal Technology) were used in the study. All animals (6 weeks) were housed at standard SPF laboratory and free access to standard rodent chow and water. Myocardial infarction was induced by the left anterior descending (LAD) artery ligation surgery, where a 7-0 suture was ligated at ~1 mm position distal to the LAD artery under the tip of the left auricle (Brenner et al., 2004; Gao et al., 2010), which was considered successful when the LV anterior wall became pale. Alternatively, the ligation suture was placed in the LAD artery, but removed in sham-operated animals. There were four groups: sham group (Sham), sham with inhalation of ultrafine Zn particles (ShamZn), myocardial infarction group (MI), and MI with inhalation of ultrafine Zn particles (MIZn). Three days after the surgery, ShamZn and MIZn groups were exposed in the environment filled with ultrafine zinc particle (diameter of 50 nm and density of 500 μg/$m^3$, Beijing Deke Daojin Science and Technology Co., Ltd.) (Bing et al., 2020). MIZn and ShamZn groups inhaled ultrafine Zn particles for 4 h per day and 4 days per week for 4 and 6 weeks postoperatively (Li et al., 2021). Sixty rats underwent the LAD ligation surgery and eight rats were dead immediately after the surgery, the rest of which were divided into MI and MIZn groups of 26 each. There were four and three dead animals in MI and MIZn groups at postoperative 4 weeks (4W) and subsequently four dead animals in each group at postoperative 6 weeks (6W). There were no dead animals in Sham and ShamZn groups. The four groups were further divided into two subgroups, i.e., postoperative 4 weeks (4W) and 6 weeks (6W): Sham4 ($n$ = 8), ShamZn4 ($n$ = 8), MI4 ($n$ = 10), MIZn4 ($n$ = 11), Sham6 ($n$ = 8), ShamZn6 ($n$ = 8), MI6 ($n$ = 8), and MIZn6 ($n$ = 8). Echocardiographic measurements of animal hearts (all animals) were carried out under anesthesia for 4 and 6 weeks postoperatively, based on which myocardial deformation measurements were demonstrated with advanced STE (Niu et al., 2020). Hemodynamic measurements (all animals) were consistent with those in a previous study (Bing et al., 2020). Histological evaluation and Zn detection ($n$ = 6 in each group) were described in the **Appendix**. All experiments were performed in accordance with Chinese National and Peking University ethical guidelines regarding the use of animals in research, consistent with the NIH guidelines (Guide for the care and use of laboratory animals) on the protection of animals used for scientific purposes. The experimental protocol was approved by the Animal Care and Use Committee of Peking University, China.

## Mathematic Method

Based on pressure and flow waves of carotid artery, the time-averaged pressure and flow over a cardiac cycle ($P_{mean}$ and $Q_{mean}$) are computed consistent with previous studies (Bing et al., 2020). The cardiac output (CO), equal to $Q_{mean} \times 60$ s. The arterial tree was modeled as an elastic chamber (Windkessel) with total compliance, C, and peripheral resistance, R ($\approx P_{ao,mean}/Q_{mean}$, where $P_{ao,mean}$ is the mean aortic pressure). In the diastolic period, the blood pressure decays with a power form:

$$p(t) = p_1 \times e^{-\frac{t}{R \times C}} \quad (1)$$

where $p_1$ is the peak blood pressure at the time $t_1$. Taking the natural log function, **Eq. 1** can be written as:

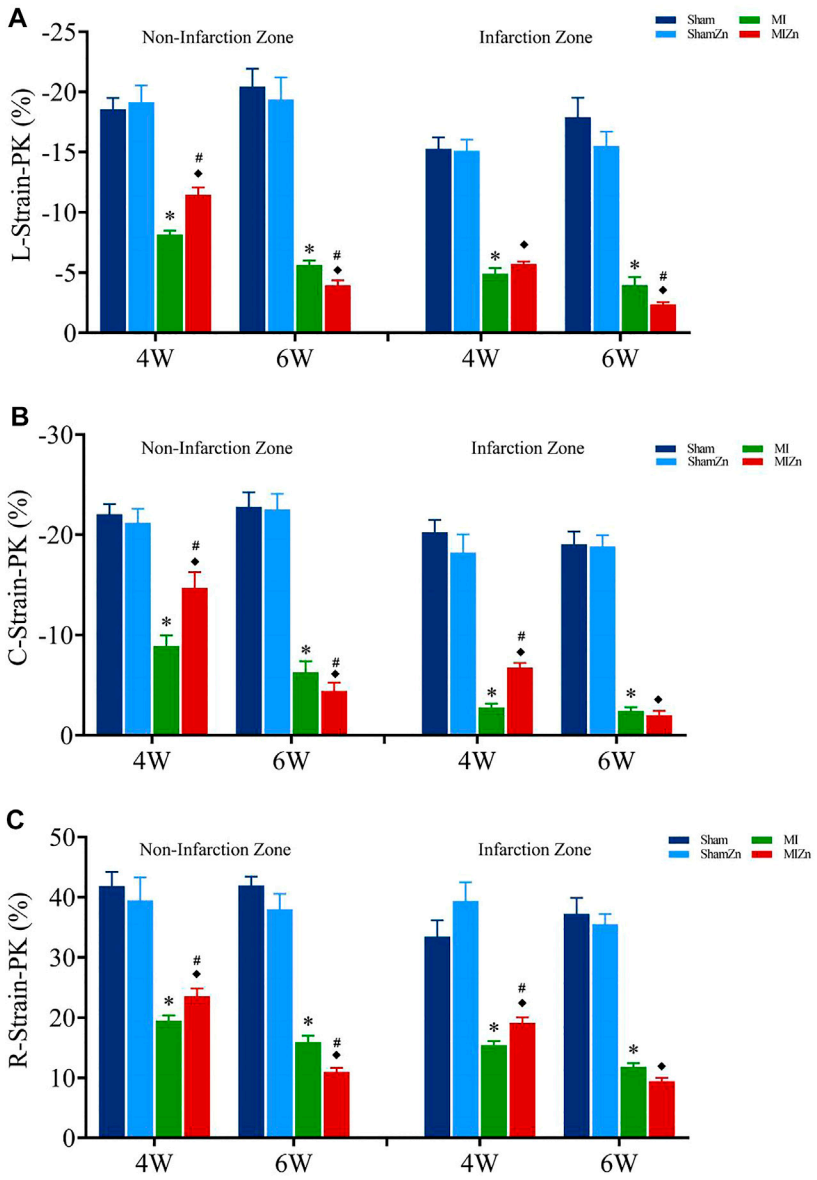


**FIGURE 2 |** Strain peak values in the longitudinal **(A)**, circumferential **(B)** and radial **(C)** directions of myocardial infarction zone and non-infarction zone in eight groups, L: Longitudinal, C: Circumferential, R: Radial. All of the data were shown as Mean ± SEM. *$p < 0.05$, MI vs. Sham; ◆$p < 0.05$, ShamZn vs. MIZn; #$p < 0.05$, MIZn vs. MI.

$$\ln p(t) = -\frac{t}{R \times C} + \ln p_1 \tag{2}$$

Provided the slope of $k$ between $\ln p(t)$ and $t$, total compliance, C, is obtained:

$$C = -\frac{1}{R \times k} \tag{3}$$

These equations are used to solve the total compliance and peripheral resistance.

## Statistical Analysis

Experimental measurements were repeated 3 times and averaged per animal. All parameters were presented as mean ± SEM by averaging over all animals in each group. The two-way ANOVA (SigmaStat3.5) was used to detect the statistical difference of morphometric and hemodynamic parameters between sham and MI groups and between inhalation of zinc particle and no inhalation groups, where $p < 0.05$ was indicative of a significant difference between the two populations.

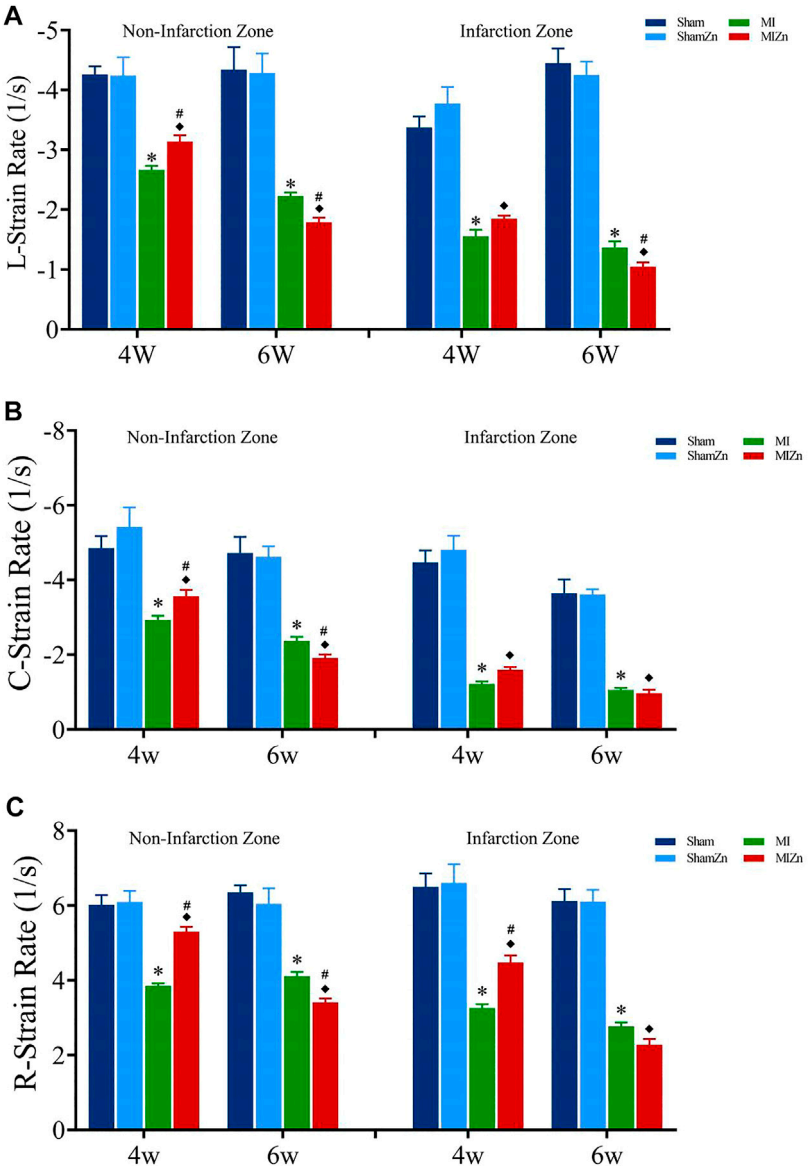


**FIGURE 3 |** Strain rate peak values in the longitudinal **(A)**, circumferential **(B)** and radial **(C)** directions of myocardial infarction zone and non-infarction zone in eight groups, L: Longitudinal, C: Circumferential, R: Radial. All of the data were shown as Mean ± SEM. *$p < 0.05$, MI vs. Sham; ◆$p < 0.05$, ShamZn vs. MIZn; #$p < 0.05$, MIZn vs. MI.

## RESULTS

**Figure 1** shows cardiac functions and zinc levels in eight groups, where EF, FS, SV and CO decrease significantly in MI groups despite of no statistical difference in sham groups. The EF and FS values in the MI4 group are lower than the MIZn4 group (EF/FS: 31.48%/15.87 % vs. 36.76%/19.28%) statistically, but those in the MI6 group are higher than the MIZn6 group (EF/FS: 28.12%/14.85% vs. 23.1%/12.07%) (**Figures 1A,B**). The SV and CO show similar changes (**Figures 1C,D**). The zinc levels are reduced (25%–35% in serum and myocardium) by the MI at post-operative 4 weeks and recover to normal level at post-operative 6 weeks. The inhalation of ultrafine zinc particles retains normal zinc levels in the MIZn4 group and increases the zinc level significantly (25%–35% in serum and myocardium) in the MIZn6 group. The inhalation of ultrafine zinc particles has no effects on cardiac functions and zinc levels in healthy rats, as shown in **Figures 1E,F**. **Table 1** lists morphometric parameters in the LV of eight groups at systole and diastole. The anterior wall of the LV is significantly reduced in MI rats because of myocardial necrosis while the LV volume is increased. The LVAW in the MIZn4 group is higher than the MI4 group, but the LVAW in the MIZn6 group is significantly lower than the MI6 group. In contrast, ESV and EDV in the MIZn4 group are lower than the MI4 group, but the values in the MIZn6 group are significantly higher than the MI6 group.

**TABLE 2 |** Morphological and hemodynamic parameters in the right carotid artery of eight groups.

| Groups | Diameter (mm) | CAS ($mm^2$) | Flow velocity (m/s) | Flow rate (ml/s) | Resistance (mmHg.s/ml) | Compliance ($\times 10^{-4}$) |
|---|---|---|---|---|---|---|
| Sham4 | 1.01 ± 0.02 | 0.80 ± 0.03 | 1.23 ± 0.08 | 0.96 ± 0.04 | 122.49 ± 5.86 | 10.31 ± 0.75 |
| ShamZn4 | 1.08 ± 0.03 | 0.93 ± 0.04 | 1.05 ± 0.07 | 0.95 ± 0.02 | 125.20 ± 6.12 | 9.23 ± 0.69 |
| MI4 | 1.02 ± 0.02 *$p$ > 0.9999 | 0.82 ± 0.03 *$p$ > 0.9999 | 0.48 ± 0.04* *$p$ < 0.0001 | 0.38 ± 0.03* *$p$ < 0.0001 | 280 ± 22.82* *$p$ < 0.0001 | 4.35 ± 0.44* *$p$ < 0.0001 |
| MIZn4 | 1.03 ± 0.02 ◆$p$ = 0.8314 #$p$ = 0.9998 | 0.84 ± 0.04 ◆$p$ = 0.8369 #$p$ > 0.9999 | 0.66 ± 0.05◆ ◆$p$ = 0.0005 #$p$ = 0.2388 | 0.55 ± 0.03◆# ◆$p$ < 0.0001 #$p$ = 0.0169 | 196 ± 14.83◆# ◆$p$ = 0.0099 #$p$ = 0.0008 | 5.55 ± 0.42◆ ◆$p$ = 0.0014 #$p$ = 0.2290 |
| Sham6 | 1.12 ± 0.02 | 0.98 ± 0.04 | 0.93 ± 0.06 | 0.91 ± 0.05 | 119.18 ± 9.38 | 9.85 ± 0.155 |
| ShamZn6 | 1.10 ± 0.02 | 0.95 ± 0.03 | 0.91 ± 0.05 | 0.87 ± 0.06 | 134.95 ± 6.93 | 9.75 ± 1.18 |
| MI6 | 1.15 ± 0.04 *$p$ = 0.9995 | 1.05 ± 0.07 *$p$ = 0.9804 | 0.29 ± 0.04* *$p$ < 0.0001 | 0.29 ± 0.02* *$p$ < 0.0001 | 339 ± 22.86* *$p$ < 0.0001 | 3.60 ± 0.642* *$p$ < 0.0001 |
| MIZn6 | 1.09 ± 0.03 ◆$p$ > 0.9999 #$p$ = 0.8324 | 0.94 ± 0.06 ◆$p$ > 0.9999 #$p$ = 0.7857 | 0.24 ± 0.03◆ ◆$p$ < 0.0001 #$p$ = 0.9997 | 0.22 ± 0.02◆ ◆$p$ < 0.0001 #$p$ = 0.9622 | 409 ± 38.14◆# ◆$p$ < 0.0001 #$p$ = 0.0228 | 0.96 ± 0.168◆# ◆$p$ < 0.0001 #$p$ = 0.0010 |

*All of the data were shown as Mean ± SEM.* *p < 0.05, MI vs. Sham; ◆p < 0.05, ShamZn vs. MIZn; #p < 0.05, MIZn vs. MI.

**Figures 2**, **3** show peak values of strains and strain rates, respectively, in the longitudinal, circumferential and radial directions of myocardial infarction and non-infarction zones in eight groups. There is no statistical difference between Sham and ShamZn groups at postoperative 4 and 6 weeks. In comparison with Sham and ShamZn groups, peak values of strains and strain rates in both infarction and normal regions are significantly reduced in MI and MIZn groups. Peak values in the three directions in the MIZn4 group are higher than those in the MI4 group. In contrast, peak values of strains and strain rates in the MIZn6 group are lower than those in the MI6 group.

Morphological and hemodynamic parameters of the right carotid artery are listed in **Table 2**. There is no statistical difference between Sham and ShamZn groups at postoperative 4 and 6 weeks. Myocardial infarction deteriorates hemodynamic environment in peripheral arteries significantly. The short-term (4 weeks) inhalation of ultrafine zinc particles inhibits the impairments caused by the MI (Resistances in MI4 vs. MIZn4: 280 vs. 196, $p < 0.005$). On the other hand, the long-term (6 weeks) inhalation of ultrafine zinc particles accelerates the impairments (Resistances in MI6 vs. MIZn6: 339 vs. 409, $p < 0.005$).

**Figures 4A,B** show representative diagrams of WGA + DAPI redyeing and statistical results of myocyte number per unit area. The myocyte number per unit area in the MIZn4 group is higher than the MI4 group (18.0 vs. 16.5) with no statistical significance, but that in the MIZn6 group is lower than the MI6 group (11.0 vs. 15.3, $p < 0.05$). **Figures 4C–E** show representative diagrams of Sirius red staining and statistical results of type I (yellow) and type III (green) collagens. The content of type I collagen in the MIZn4 group is lower than the MI4 group (87% vs. 92%, $p < 0.05$), but that in MIZn6 group is higher than the MI6 group (97% vs. 93%, $p < 0.05$). The content of type III collagen in the MIZn4 group is higher than MI4 group (10% vs. 7%, $p < 0.05$), but that in MIZn6 group is lower than MI6 group (3% vs. 6%, $p < 0.05$). **Figures 4F,G** show schematic panoramas of Masson staining and statistical results of myocardium fibrosis. Myocardial infarction significantly increases collagens of types I and results in myocardium fibrosis. In comparison with the MI groups, the inhalation of ultrafine Zn particles inhibits the deuteriation of myocardial fibrosis in the MIZn4 group (MI4 vs. MIZn4: 42% vs. 36%, $p < 0.05$), but accelerates the impairments in the MIZn6 group (MI6 vs. MIZn6: 45% vs. 51%, $p < 0.05$).

## DISCUSSION

The present study investigated the changes of cardiac functions and hemodynamics in MI rats at the end of long period of inhaling ultrafine Zn particles. The long-term (6 weeks) inhalation of ultrafine Zn particles is found to impair cardiac functions and hemodynamics in MI rats while the short-term (4 weeks) inhalation has a protective effect.

Zinc has the highest concentration in the trace metals of air pollution in the YRD Metropolitan Area, China (Ming et al., 2017). Exposure to UFPs in air pollution leads to cardiovascular morbidity and mortality (Brook et al., 2010). As a logistic starting point, we investigated the effects of inhaling ultrafine Zn particles in the rat MI model. Monse et al. found that controlled exposures to ZnO nanoparticles caused both airway and systemic inflammations in human subjects, which were observed at a concentration of 0.5 $mg/m^3$ and higher (Monsé et al., 2018; Monsé et al., 2019). Since molecular weight of Zn is five times higher than that of O, we selected ultrafine Zn particles (wrapped by a layer of ZnO) of 0.5 $mg/m^3$ in the rat model. The Zn level in both serum and heart tissue gradually increased over time after MI rats inhaled ultrafine Zn particles.

Myocardial infarction activated atrial natriuretic peptide, which resulted in an increase of urinary Zn excretion and a decrease of Zn concentrations in plasma and erythrocytes. The significant decrease of Zn concentrations in serum and heart tissue led to myocardial structural and functional disorders (Ripa et al., 1998). The short-term inhalation of ultrafine Zn particles was found to retain the Zn level to a normal range in serum and heart tissue and slow down LV dysfunctions and remodeling in MI rats, consistent with a previous study (Li et al., 2021). On the other hand, there were higher Zn concentrations in the MIZn6 group than others. The higher Zn accumulation is deleterious to MI rats, which accelerates the progression from MI to heart failure. Substantial studies have shown the important

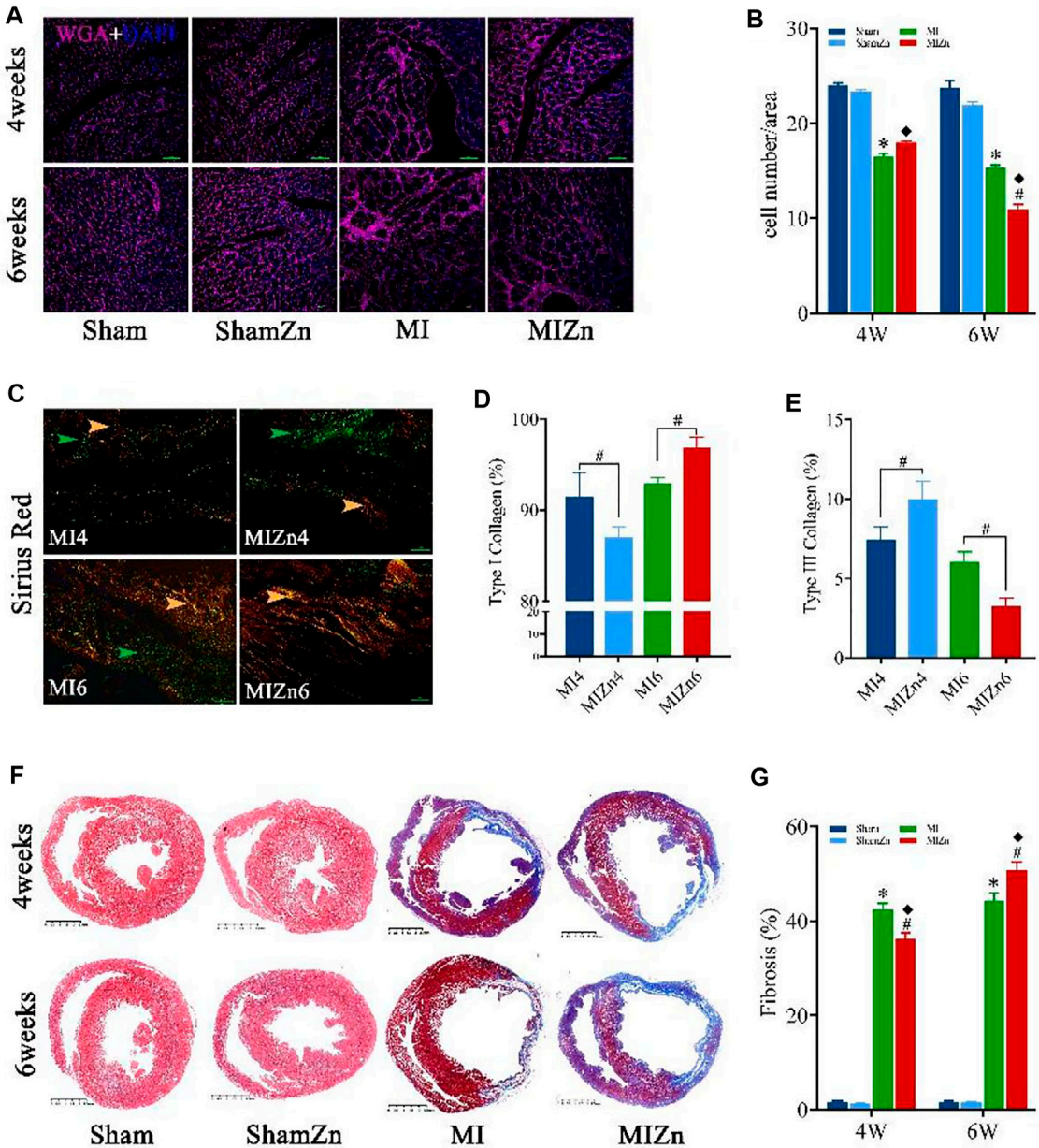


**FIGURE 4 |** Representative diagrams of WGA + DAPI redyeing **(A)** and statistical results of myocyte number per unit area (image magnification: × 200 and scales: 50 μm) **(B)**; Representative diagrams of Sirius red staining **(C)** and statistical results of type I collagen (yellow) **(D)** and type III collagen (green) **(E)**. Schematic panoramas of Masson staining **(F)** and statistical results of myocardium fibrosis (scales: 2.5 mm) **(G)**. All of the data were shown as Mean ± SEM. $^{*}p < 0.05$, MI vs. Sham; $^{\blacklozenge}p < 0.05$, ShamZn vs. MIZn; $^{\#}p < 0.05$, MIZn vs. MI.

role of Zn in redox signaling pathway and antioxidant biological process (Korichneva 2006; Foster and Samman 2010; Maret, 2019), which showed that pro-oxidation due to low or high Zn concentrations is a risk factor for myocardial structural and functional disorders. Excessive Zn concentrations can also inhibit the key enzymes of phosphorylation and redox (Maret, 2019) and induce the inflammation (De Paula et al., 2014).

In the STE analysis, peak myocardial strains and strain rates show the shortening of working myocardial fibers and the relaxation of working myocardial fibers, respectively, which characterize cardiac functions (Niu et al., 2020; Li et al., 2021). The peak values decreased with time after the occurrence of MI in rats. The MI-induced decrease of strains and strain rates denoted the deterioration of systolic and diastolic functions. The short-term inhalation of ultrafine Zn particles inhibited the MI-induced decrease of strains and strain rates while the long-term inhalation accelerated the deterioration of systolic and diastolic functions, which mainly results from myocardium fibrosis. The UFPs-induced change of Zn concentrations affected the content and proportion of types I and III collagen in myocardium of MI rats. Type I collagen is coarse fiber with low ductility and elasticity and

high stiffness while type III collagen is fine fiber with mechanical properties opposite to type I collagen. Myocardial infarction stimulated the growth of type I and type III collagen fibers. There was an increase of type III collagens in a week after the MI surgery and then a significant increase of type I collagens after the first week. The increase of type I collagens can create cardiac scarring (Cleutjens et al., 1995) and impair systolic and diastolic functions in MI rats. In comparison with the MI rats, there was lower and higher ratios of type I collagens in MIZn4 and MIZn6, respectively. Matrix metalloproteinases (MMPs) are a family of Zn-dependent endopeptidases involving in the breakdown of extracellular matrix and basement membrane components such as collagen, elastin, fibronectin, gelatin, and laminin (Murphy et al., 1991; Roy and Carey 1997; Page-Mccaw et al., 2007). The decrease of Zn-dependent MMPs is a risk factor for the increase of type I collagens (Tian et al., 2015), which still requires more investigations.

The increased stiffness and resistance in peripheral arteries of MI rats can contribute to the incidence and progression of heart failure (Wu et al., 2017; Huo et al., 2018; Bing et al., 2020; Niu et al., 2020; Li et al., 2021). The MIZn6 group had higher vascular stiffness and resistance than the MI6 group, but the MIZn4 group had the opposite change. The stiffness index in peripheral arteries is associated with the high level of type I collagen in serum (Chatzikyriakou et al., 2014), which was caused by the increased Zn concentrations in serum in the MIZn6 group. Moreover, high Zn concentrations induce oxidative stress and inflammation as well as disrupt the autonomic nervous system (Brook et al., 2010; Cutrufello et al., 2011), which can increase arterial stiffness and resistance. Hence, Zn-regulated changes of arterial stiffness and resistance, in conjunction with cardiac changes, affected the development of heart failure in MI rats.

## Implications of the Study

Previous studies showed the highest concentrations of trace metal Zn, but did not measure its chemical and physical forms in air pollutions in the YRD region, China (Shen et al., 2014; Ming et al., 2017). The emissions of trace metals resulted from various sources, such as vehicle emissions. In order to test the proposed hypothesis, we selected ultrafine Zn particles wrapped by a layer of ZnO. The concentration of Zn is about 193–1,360 ng/m$^3$ in air pollutions in China. Human respiratory capacity is about 70–100 times higher than rats. Based on the formula of drug dose conversion between humans and animals, the drug dose of rats should be about 56 times higher than human. Hence, we selected a relative biosafety dose of 500 ug/m$^3$, similar to previous studies (Monsé et al., 2018; Monsé et al., 2019). The cardiac and hemodynamic dysfunctions caused by the long-term inhalation of ultrafine Zn particles suggest that we should be looking at ways to lower zinc concentrations in air pollutions, for example, using electric vehicles to reduce the emissions. On the other hand, zinc is a nutrient to improve immune system and metabolism function in human. The results from the short-term inhalation of ultrafine Zn particles suggest that MI patients should obtain enough zinc from food sources of zinc, e.g., chicken, red meat and so on.

## Critique of the Study

This study investigated the toxic effect of ultrafine Zn particles on the progression from MI to heart failure in the rat model. Although cardiac strains and strain rates were analyzed by the STE measurement, myocardial stresses are needed to be studied similar to previous studies (Yin et al., 2020; Zhao et al., 2020). Although we measured blood inflammation factors CRP/IL8/TNF-α and biomarker of heart failure BNP in some animals, which showed that Zn deficiency could increase oxidative stress and promote inflammation in MI rats, the molecular and cellular analysis is still required to find the mechanisms relevant to the effect of Zn. This study only used ultrafine Zn particles with the concentration of 500 ug/m$^3$. We will investigate different doses of ultrafine Zn particles as well as other metal constituents in the MI rat model in the following studies.

# CONCLUSION

Zinc is a main metal component in air pollutions and an essential trace element in the body. The high and low Zn concentrations in serum and tissue have different effects on MI rats. This study carried out the analysis of cardiac functions, histomorphology, and hemodynamics in peripheral arteries in the Sham4, ShamZn4, MI4, MIZn4, Sham6, ShamZn6, MI6, and MIZn6 groups. In comparison with the MI rats, the short-term (4 weeks) inhalation of ultrafine Zn particles supplied the zinc deficiency state and slowed down the progression from MI to heart failure, but the long-term (6 weeks) inhalation induced accumulation of zinc and accelerated the development. Hence, it is of importance for MI patients to regulate Zn intake to slow down the MI progression.

# DATA AVAILABILITY STATEMENT

The original contributions presented in the study are included in the article/supplementary material, further inquiries can be directed to the corresponding author.

# ETHICS STATEMENT

The animal study was reviewed and approved by Animal Care and Use Committee of Peking University.

# AUTHOR CONTRIBUTIONS

YH wrote the manuscript and LL carried out experiments and computation.

# FUNDING

This work is supported by the National Key Research and Development Program of China 2021YFA1000200 and 2021YFA1000203 (YH), Shenzhen Science and Technology R&D Grant KQTD20180411143400981 (YH), and National Natural Science Foundation of China Grant 11732001 (YH).

## REFERENCES


Andre, N. (2006). Toxic Potential of Materials at the Nanolevel. *Science* 311 (5761), 622–627. doi:10.1126/science.1114397

Bing, F., Wang, X., Shen, W., Li, L., Niu, P., Chen, Y., et al. (2020). Inhalation of Ultrafine Zinc Particles Impaired Cardiovascular Functions in Hypertension-Induced Heart Failure Rats with Preserved Ejection Fraction. *Front. Bioeng. Biotechnol.* 8, 13. doi:10.3389/fbioe.2020.00013

Brenner, W., Aicher, A., Eckey, T., Massoudi, S., Zuhayra, M., Koehl, U., et al. (2004). 111In-labeled CD34+ Hematopoietic Progenitor Cells in a Rat Myocardial Infarction Model. *J. Nucl. Med.* 45 (3), 512–518.

Brook, R. D., Rajagopalan, S., Pope, C. A., 3rd, Brook, J. R., Bhatnagar, A., Diez-Roux, A. V., et al. (2010). Particulate Matter Air Pollution and Cardiovascular Disease. *Circulation* 121 (21), 2331–2378. doi:10.1161/cir.0b013e3181dbece1

Chatzikyriakou, S. V., Tziakas, D. N., Chalikias, G. K., Stakos, D. A., Thomaidi, A. K., Mitrousi, K., et al. (2014). Serum Levels of Collagen Type-I Degradation Markers Are Associated with Vascular Stiffness in Chronic Heart Failure Patients. *Eur. J. Heart Fail* 10 (12), 1181–1185. doi:10.1016/j.ejheart.2008.09.007

Cleutjens, J. P., Verluyten, M. J., Smiths, J. F., and Daemen, M. J. (1995). Collagen Remodeling after Myocardial Infarction in the Rat Heart. *Am. J. Pathol.* 147 (2), 325–338.

Cutrufello, P. T., Rundell, K. W., Smoliga, J. M., and Stylianides, G. A. (2011). Inhaled Whole Exhaust and its Effect on Exercise Performance and Vascular Function. *Inhal. Toxicol.* 23 (11), 658–667. doi:10.3109/08958378.2011.604106

De Paula, R. C. S., Aneni, E. C., Costa, A. P. R., Figueiredo, V. N., Moura, F. A., Freitas, W. M., et al. (2014). Low Zinc Levels Is Associated with Increased Inflammatory Activity but Not with Atherosclerosis, Arteriosclerosis or Endothelial Dysfunction Among the Very Elderly. *BBA Clin.* 2, 1–6. doi:10.1016/j.bbacli.2014.07.002

Foster, M., and Samman, S. (2010). Zinc and Redox Signaling: Perturbations Associated with Cardiovascular Disease and Diabetes Mellitus. *Antioxidants Redox Signal.* 13 (10), 1549–1573. doi:10.1089/ars.2010.3111

Franck, U., Odeh, S., Wiedensohler, A., Wehner, B., and Herbarth, O. (2011). The Effect of Particle Size on Cardiovascular Disorders - the Smaller the Worse. *Sci. Total Environ.* 409 (20), 4217–4221. doi:10.1016/j.scitotenv.2011.05.049

Gao, E., Lei, Y. H., Shang, X., Huang, Z. M., Zuo, L., Boucher, M., et al. (2010). A Novel and Efficient Model of Coronary Artery Ligation and Myocardial Infarction in the Mouse. *Circ. Res.* 107 (12), 1445–1453-+. doi:10.1161/circresaha.110.223925

Huo, Y., Chen, H., and Kassab, G. S. (2018). Acute Tachycardia Increases Aortic Distensibility, but Reduces Total Arterial Compliance up to a Moderate Heart Rate. *Front. Physiol.* 9, 1634. doi:10.3389/fphys.2018.01634

Karottki, D. G., Bekö, G., Clausen, G., Madsen, A. M., Andersen, Z. J., Massling, A., et al. (2014). Cardiovascular and Lung Function in Relation to Outdoor and Indoor Exposure to Fine and Ultrafine Particulate Matter in Middle-Aged Subjects. *Environ. Int.* 73, 372–381. doi:10.1016/j.envint.2014.08.019

Korichneva, I. (2006). Zinc Dynamics in the Myocardial Redox Signaling Network. *Antioxid. Redox Signal* 8 (9-10), 1707–1721. doi:10.1089/ars.2006.8.1707

Li, L., Niu, P., Wang, X., Bing, F., Tan, W., and Huo, Y. (2021). Short-Term Inhalation of Ultrafine Zinc Particles Could Alleviate Cardiac Dysfunctions in Rats of Myocardial Infarction. *Front. Bioeng. Biotechnol.* 9, 646533. doi:10.3389/fbioe.2021.646533

Maret, W. (2019). The Redox Biology of Redox-Inert Zinc Ions. *Free Radic. Biol. Med.* 134, 311–326. doi:10.1016/j.freeradbiomed.2019.01.006

Mills, N. L., Tǒrnqvist, H., Robinson, S. D., Gonzalez, M., Darnley, K., MacNee, W., et al. (2005). Diesel Exhaust Inhalation Causes Vascular Dysfunction and Impaired Endogenous Fibrinolysis. *Circulation* 112 (25), 3930–3936. doi:10.1161/circulationaha.105.588962

Ming, L., Jin, L., Li, J., Fu, P., Yang, W., Liu, D., et al. (2017). PM2.5 in the Yangtze River Delta, China: Chemical Compositions, Seasonal Variations, and Regional Pollution Events. *Environ. Pollut.* 223, 200–212. doi:10.1016/j.envpol.2017.01.013

Monsé, C., Hagemeyer, O., Raulf, M., Jettkant, B., van Kampen, V., Kendzia, B., et al. (2018). Concentration-dependent Systemic Response after Inhalation of Nano-Sized Zinc Oxide Particles in Human Volunteers. *Part Fibre Toxicol.* 15 (1), 8. doi:10.1186/s12989-018-0246-4

Monsé, C., Raulf, M., Hagemeyer, O., van Kampen, V., Kendzia, B., Gering, V., et al. (2019). Airway Inflammation after Inhalation of Nano-Sized Zinc Oxide Particles in Human Volunteers. *BMC Pulm. Med.* 19 (1), 266. doi:10.1186/s12890-019-1026-0

Murphy, G. J., Murphy, G., and Reynolds, J. J. (1991). The Origin of Matrix Metalloproteinases and Their Familial Relationships. *FEBS Lett.* 289 (1), 4–7. doi:10.1016/0014-5793(91)80895-a

Niu, P., Li, L., Yin, Z., Du, J., Tan, W., and Huo, Y. (2020). Speckle Tracking Echocardiography Could Detect the Difference of Pressure Overload-Induced Myocardial Remodelling between Young and Adult Rats. *J. R. Soc. Interface.* 17 (163), 20190808. doi:10.1098/rsif.2019.0808

Page-Mccaw, A., Ewald, A. J., and Werb, Z. (2007). Matrix Metalloproteinases and the Regulation of Tissue Remodelling. *Nat. Rev. Mol. Cell. Biol.* 8 (3), 221–233. doi:10.1038/nrm2125

Ripa, S., Ripa, R., and Giustiniani, S. (1998). Are Failured Cardiomyopathies a Zinc-Deficit Related Disease? A Study on Zn and Cu in Patients with Chronic Failured Dilated and Hypertrophic Cardiomyopathies. *Minerva Med.* 89 (11-12), 397–403.

Robert, D. B. (2004). Air Pollution and Cardiovascular Disease: a Statement for Healthcare Professionals from the Expert Panel on Population and Prevention Science of the American Heart Association. *Circulation* 109 (21), 2655–2671. doi:10.1161/01.CIR0000128587.30041.C8

Roy, M. K., and Carey, P. D. (1997). Matrix Metalloproteinases. *Br. J. Surg.* 84 (8), 1171–1171. doi:10.1002/bjs.1800840842

Shen, G. F., Yuan, S. Y., Xie, Y. N., Xia, S. J., Li, L., Yao, Y. K., et al. (2014). Ambient Levels and Temporal Variations of PM2.5and PM10at a Residential Site in the Mega-City, Nanjing, in the Western Yangtze River Delta, China. *J. Environ. Sci. Health, Part A* 49 (2), 171–178. doi:10.1080/10934529.2013.838851

Tian, T., Huang, Z., Xiaojing, C., Jie, W., Tianyu, W., and Zongzhen, N. (2015). Effects of Puerarin on MMP-2 and Col1A1 in HFSF Cells under Extremely Low Frequency Electromagnetic Radiation. *Adv. Mod. Biomed.* 36, 7001–7003. 7008.

Törnqvist, H., Mills, N. L., Gonzalez, M., Miller, M. R., Robinson, S. D., Megson, I. L., et al. (2007). Persistent Endothelial Dysfunction in Humans after Diesel Exhaust Inhalation. *Am. J. Respir. Crit. Care Med.* 176 (4), 395–400. doi:10.1164/rccm.200606-872OC

Wold, L. E., Ying, Z., Hutchinson, K. R., Velten, M., Gorr, M. W., Velten, C., et al. (2012). Cardiovascular Remodeling in Response to Long-Term Exposure to Fine Particulate Matter Air Pollution. *Circ. Heart Fail.* 5 (4), 452–461. doi:10.1161/circheartfailure.112.966580

Wolfram, B. (2006). Trace Metal Concentrations and Water Solubility in Size-Fractionated Atmospheric Particles and Influence of Road Traffic. *Environ. Sci. Technol.* 4 (40), 1144–1153. doi:10.1021/es0486925

Wu, H., Li, L., Niu, P., Huang, X., Liu, J., Zhang, F., et al. (2017). The Structure-Function Remodeling in Rabbit Hearts of Myocardial Infarction. *Physiol. Rep.* 5 (12), e13311. doi:10.14814/phy2.13311

Yin, Z., Zhang, W., Zhao, D., Sulejmani, F., Feng, Y., Huo, Y., et al. (2020). Cardiac Wall Mechanics Analysis in Hypertension-Induced Heart Failure Rats with Preserved Ejection Fraction. *J. biomechanics* 98, 109428. doi:10.1016/j.jbiomech.2019.109428

Zhao, D., Niu, P., Sun, X., Yin, Z., Tan, W., and Huo, Y. (2020). Mechanical Difference of Left Ventricle between Rabbits of Myocardial Infarction and Hypertrophy. *J. Biomechanics* 111, 110021. doi:10.1016/j.jbiomech.2020.110021


**Conflict of Interest:** The authors declare that the research was conducted in the absence of any commercial or financial relationships that could be construed as a potential conflict of interest.

## APPENDIX

Histological evaluation: Animals were terminated for histological analysis at postoperative 4 or 6 weeks. After hearts were harvested, plugs of myocardial tissues were removed from different positions of the LV. These plugs were fixed in 4% paraformaldehyde (PFA)/PBS solution overnight at room temperature and processed for paraffin sectioning. Masson's trichrome and Picro-Sirius Red (PSR) staining was carried out according to standard procedures. Sections were also detected *via* wheat germ agglutinin (WGA) conjugated to Alexa Fluor 594 (50 ug $ml^{-1}$, Invitrogen), similar to a previous study (Wu et al., 2017). Moreover, nuclear morphology was assessed by Hoechst 33,258 dye (Molecular Probes).

Zinc detection: Fresh heart tissue (50 mg) was cut into pieces and dissolved with 65% concentrated nitric acid (1 ml) in a beaker, which was heated for about 30 min until the tissue was completely dissolved. Distilled water with 1 ml 65% concentrated nitric acid was added to the beaker for the 5 ml solution, which was filtrated to obtain the clear liquid. The ICP-OES (iCapRQ, Thermal Fisher Scientific) was used to determine the zinc concentration in the sample solution. The zinc concentration in the serum were also detected using the previous method (Li et al., 2021).

frontiers | Frontiers in Physiology

TYPE Original Research
PUBLISHED 29 September 2022
DOI 10.3389/fphys.2022.1010862



OPEN ACCESS

EDITED BY
Shaun Gregory,
Monash University, Australia

REVIEWED BY
Michael Neidlin,
RWTH Aachen University, Germany
Socrates Dokos,
University of New South Wales, Australia

*CORRESPONDENCE
Mojgan Ghodrati-Misek,
mojgan.ghodrati-misek@meduniwien.ac.at

SPECIALTY SECTION
This article was submitted to Computational Physiology and Medicine, a section of the journal Frontiers in Physiology

RECEIVED 03 August 2022
ACCEPTED 01 September 2022
PUBLISHED 29 September 2022

CITATION
Ghodrati-Misek M, Schlöglhofer T, Gross C, Maurer A, Zimpfer D, Beitzke D, Zonta F, Moscato F, Schima H and Aigner P (2022), Left atrial appendage occlusion in ventricular assist device patients to decrease thromboembolic events: A computer simulation study. *Front. Physiol.* 13:1010862. doi: 10.3389/fphys.2022.1010862



# Left atrial appendage occlusion in ventricular assist device patients to decrease thromboembolic events: A computer simulation study

Mojgan Ghodrati-Misek[1]*, Thomas Schlöglhofer[1,2,3], Christoph Gross[2,3], Alexander Maurer[1,2], Daniel Zimpfer[3], Dietrich Beitzke[4], Francesco Zonta[5], Francesco Moscato[1,2], Heinrich Schima[1,2,3] and Philipp Aigner[1,2]

[1]Center for Medical Physics and Biomedical Engineering, Medical University of Vienna, Vienna, Austria, [2]Ludwig Boltzmann Institute for Cardiovascular Research, Vienna, Austria, [3]Department of Cardiac Surgery, Medical University of Vienna, Vienna, Austria, [4]Department of Biomedical Imaging and Image Guided Therapy, Medical University of Vienna, Vienna, Austria, [5]Institute of Fluid Dynamics and Heat Transfer, Technical University of Vienna, Vienna, Austria

Atrial fibrillation (AF) is a common comorbidity in left ventricular assist device (LVAD) patients and has been identified as a risk factor for thromboembolic stroke. Blood stagnation within the left atrial appendage (LAA) is considered a possible major source of thrombosis and clinical studies have shown reduced thromboembolic risk after LAA occlusion (LAAO). Therefore, this study aims to investigate the effect of LAAO on thrombosis-related parameters using patient-specific simulations. Left ventricular and left atrial geometries of an LVAD patient were obtained from computed tomography and combined with hemodynamic data with either sinus rhythm (SR) or AF generated by a lumped parameter model. In four simulations applying contractile walls, stagnation volume and blood residence times were evaluated with or without AF and with or without LAAO. Reduced atrial contraction in AF resulted in unfavorable flow dynamics within the left atrium. The average atrial velocity was lower for the AF simulation when compared to SR, resulting in a 55% increase in the atrial stagnation volume (from 4.2 to 6.5 $cm^3$). Moreover, blood remained in the LAA for more than 8 cardiac cycles. After LAAO the atrial stagnation decreased from 4.2 to 1.4 $cm^3$ for SR and from 6.5 to 2.3 $cm^3$ for the AF simulation. A significant stagnation volume was found in the LAA for both SR and AF, with larger values occurring with AF. These regions are known as potential sources for thrombus formation and can be diminished by LAAO. This significantly improved the thrombus-related flow

**Abbreviations:** AF, Atrial fibrillation; CFD, Computational Fluid Dynamics; CT, Computed tomography; LA, Left atrium; LAA, Left atrial appendage; LAAO, Left atrial appendage occlusion; LV, Left ventricle; LVAD, Left ventricular assist device; SR, Sinus rhythm; WSS, Wall shear stress.

parameters and may also lower the risk of thromboembolic events from the appendage.

KEYWORDS

atrial fibrillation, sinus rhythm, left atrial appendage occlusion, thromboembolic risk, ventricular assist device, computational fluid dynamics

# 1 Introduction

Left ventricular assist device (LVAD) therapy is considered a treatment for patients with end-stage heart failure and is used either as a bridge to transplant or as destination therapy (Mancini and Colombo, 2015). Despite the success of this treatment (Molina et al., 2021), a high risk for thrombosis and, consequently, stroke related mortality persists (Acharya et al., 2017; DeVore and Stewart, 2017).

The left atrial appendage (LAA) has been considered as a potential source of thrombus formation for atrial fibrillation (AF) patients because of their reduced atrial contractility, which can lead to blood stasis and platelet deposition (Blackshear and Odell, 1996). AF has also been shown to be a significant risk factor for thromboembolic events (Stulak et al., 2013; Deshmukh et al., 2017) affecting up to 54% of patients undergoing LVAD implantation (Deshmukh et al., 2017).

Occlusion of the LAA has been associated with a lower risk of thromboembolic events in AF patients undergoing cardiac surgery (Friedman et al., 2018). For the LVAD population, LAAO has been recommended to reduce the prevalence of thromboembolic events, even for patients free from AF (Deshmukh et al., 2019), however the rationale remains hypothetical.

Computational Fluid Dynamics (CFD) has the potential to provide some insight into the changes occurring within the heart chambers after LAAO. Individual CFD simulations can be performed with patient-specific models of LVAD patient's hearts, which can be used to investigate the influence of both AF and LAAO on haemodynamics and blood flow. While in several computational studies, the intraventricular flow pattern during LVAD support was modeled without including the essential motion of the heart wall (Chivukula et al., 2018, 2019; Liao et al., 2018a; Liao et al., 2018b; Ghodrati et al., 2020; Ghodrati and Khienwad, 2021; Ghodrati and Schlöglhofer, 2021), To date, no CFD simulation study has examined the effects of AF on the contractile left heart or of LAAO in patients with LVAD support.

In this study, a patient-specific flow-field simulation was performed in which the contraction of the left atrium and left ventricle was implemented by moving the endocardial wall of these two chambers. This was used to 1) evaluate the blood flow patterns for an LVAD patient with sinus rhythm (SR) and with AF and 2) to investigate the post-procedure blood flow dynamics to quantify the efficacy of LAA occlusion on thrombus-related flow parameters.

# 2 Materials and methods

## 2.1 Patient models

The left atrium and the left ventricle of an LVAD patient were segmented from computed tomography (CT) images using Mimics Research 20.0 and 3-matic Research 13.0 (Materialise, Belgium NV). The end systolic volume of the atrium and ventricle of this patient were 169 and 295 $cm^3$, respectively (Figure 1). The left atrial appendage geometry was occluded virtually (Ansys, SpaceClaim 19.3, Pennsylvania, United States) (Figure 1).

A mitral valve model (Domenichini and Pedrizzetti, 2015) was defined using the following parametric equations:

$$x_v(\theta, s) = R\cos\theta\left(1 - s\cos\varphi\right) - \varepsilon Rs\cos\varphi$$

$$y_v(\theta, s) = R\sin\theta\left(1 - sk\cos\varphi\right)$$

$$z_v(\theta, s) = -s^2\left(\frac{1+k}{2} + \varepsilon\cos\theta + \frac{1-k}{2}\cos 2\theta\right)R\sin\varphi$$

In which $\theta$ is 100 points from $0$ to $2\pi$ and $s$ is 40 points from 0 to 1. $\varepsilon = 0.35$ shows the symmetry ratio between anterior and posterior leaflet. $k = 0.6$, shows the ellipticity of the valvular edge. $\varphi = 60$, shows the opening angle of the mitral valve.

The created valve geometry was placed at the position and matching the orientation of the mitral valve as defined via the CT images.

The mitral valve was considered in the open status with a rigid wall and the flow rate over the mitral valve was controlled using the volume change of the left atrium and left ventricle, leading to zero flow rate over the mitral valve during systole.

## 2.2 Meshing

An unstructured tetrahedral mesh with a total of 1.5 million cells was created (Ansys Meshing, 19.3, Pennsylvania, United States). All of the mesh elements showed a skewness factor below 0.84 and orthogonal quality above 0.16, which is in the recommended ranges of the Ansys Meshing User Guide (Baker, 2016). A suitable mesh size was chosen based on a mesh independence study, which can be found in the Supplementary Material.

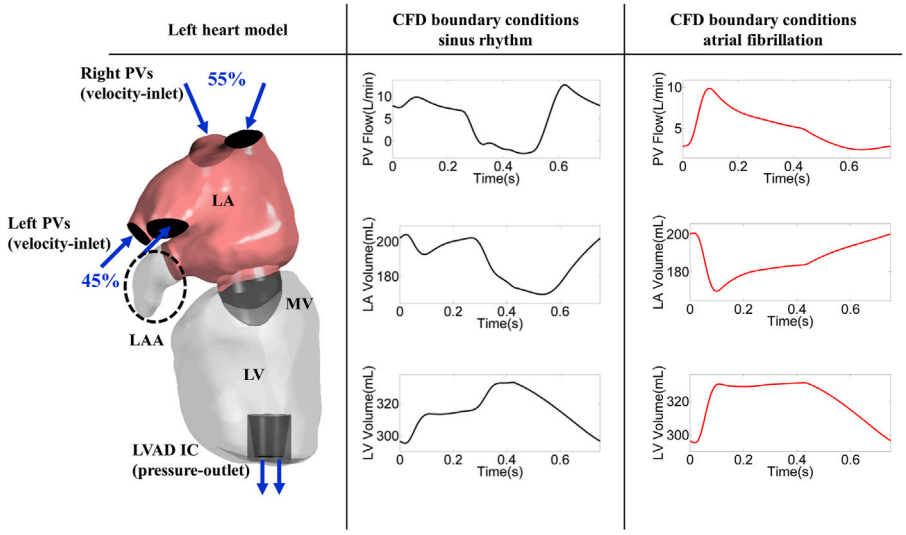


FIGURE 1
Left heart model (encircled dashed ellipse marks LAAO) and CFD boundary conditions; PV: pulmonary vein, LA: left atrium, LV: left ventricle, MV: mitral valve, LAA: left atrial appendage, SR: sinus rhythm, AF: atrial fibrillation, LVAD: left ventricular assist device, IC: inflow cannula.

## 2.3 Haemodynamics

The haemodynamics values for a typical LVD patient under full support were determined based on previous studies, in which the mass flow rate over LVAD inflow cannula was 5.2 L/min, blood pressure was equal to 83.8 ± 10.5 mmHg and heartrate was 79.3 ± 17.0 bpm (Jacquet et al., 2011; Martina et al., 2013; Muthiah, 2015; Burrell et al., 2015; Haft et al., 2007). Moreover, the left ventricular inflow filling pattern, E/A ratio of 1.2 ± 0.7 was chosen from (Estep et al., 2014).

The haemodynamics were simulated using the previously developed and published lumped parameter model (Moscato et al., 2012). Briefly, the LPM of the circulatory system consists of active ventricles and atria, simulated by a non-linear elastance function, with heart valves to prevent backflow, compliant vessels and resistances for the pulmonary and systemic vascular bed (arterioles). The pump characteristics (pump head, pump speed and pump output) of the HVAD (Medtronic) were implemented with the inlet of the pump connected to the LV and the outlet of the pump in the aorta.

To simulate the hemodynamics for a typical LVAD patient, the following parameters in the original lumped parameter model were adjusted: 1) Heartrate was set to 80 bpm, LV peak iso-volumic pressure was reduced from 100 to 80 mmHg, 2) right ventricular peak iso-volumic pressure was reduced from 80 to 50 mmHg, 3) mean circulatory pressure was reduced from 12.5 to 10 mmHg, 4) arterial systemic resistance was reduced by 6%, and 5) To adapt the E/A ratio, the constant (alpha) for the calculation of the end-diastolic pressure-volume relation was increased by 70%.

For the atrial fibrillation scenario, the only change compared to the typical LVAD patients was the deactivated LA active contraction. The stroke volume for the AF simulation was a result of the passive contraction of the atrium (Figure 1).

## 2.4 Boundary conditions and solver setup

The Navier-Stokes equations were solved with a finite volume approach in the CFD solver (FLUENT, Ansys 19.3, Pennsylvania, United States) and blood flow was modeled using the Laminar method and Newtonian fluid with a density of 1,060 kg/m$^3$ and a dynamic viscosity of 0.0035 Pa s was considered. The incoming flow was delivered over the right and left pulmonary veins with a distribution of 55 and 45%, respectively (Wong et al., 2014). The velocity and pressure boundary conditions were imposed at both the inlet and outlet.

The atrial and ventricular volume waveforms (Figure 1) were assigned through user-defined functions (UDFs) to implement the dynamics of the atrium and the ventricle. The atrial and ventricular volume waveforms were divided in 750 equal time-steps in one cardiac cycle. Combination of shape optimization algorithm and dynamic mesh was used to model the contraction of the LA and LV. The shape optimization is a feature in Ansys Fluent in which the geometry is changed in order to reach a specific criterion. The shape optimization algorithm was utilized to calculate the geometry deformation based on the volume difference between two consecutive time-steps. The calculated value then was used to move the mesh vortices using dynamic mesh in which a combination of smoothing and re-meshing methods. The

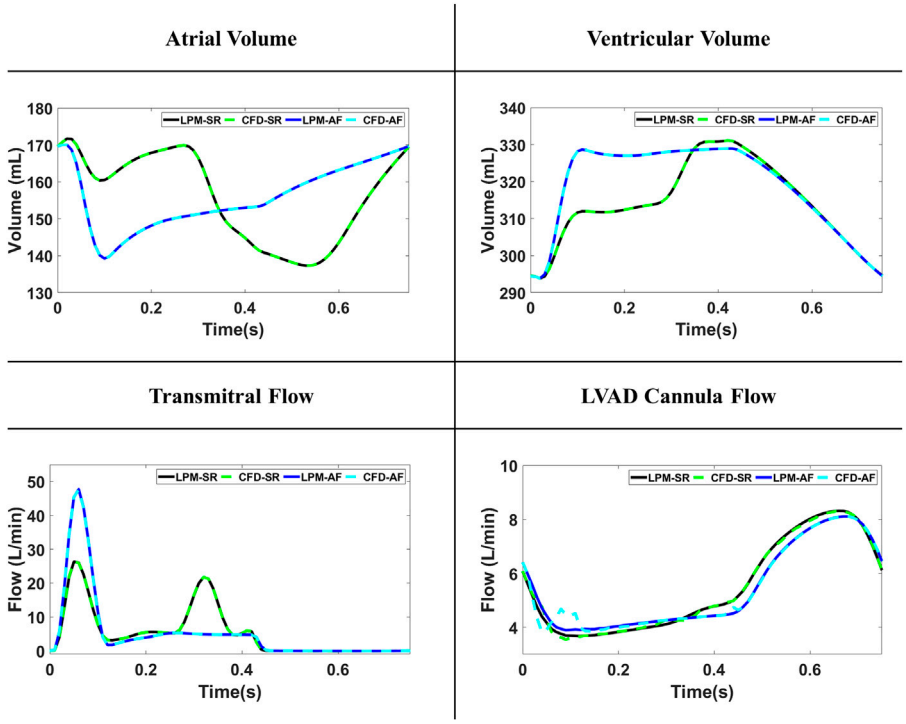


FIGURE 2
The volume and flow curves comparison between the lumped-parameter model (LPM) and computational fluid dynamics (CFD) models for simulations with sinus rhythm (SR) and atrial fibrillation (AF).

dynamic mesh approach in ANSYS (Ansys Fluent, 19.3, Pennsylvania, United States) applies a form of smoothing in which the size of the existing elements is modified until the size/quality of the elements exceed the user defined thresholds (skewness below 0.84, size below 2 mm). In case of a large deformation, the solver relies on re-meshing, with which new mesh elements will be added to keep the size/quality in the defined range. The inlet and outlet boundaries as well as the mitral valve were considered rigid.

The PISO (pressure implicit with splitting of operators) algorithm was employed along with a second order upwind scheme. Simulations were performed for duration of 12 cardiac cycles with a temporal resolution of 0.001 s. The first four cardiac cycles were defined as the initialization phase to ensure fully developed atrial and ventricular flow after this time and were not considered in the final data evaluation. Convergence was observed in each time step when the residuals were below $10^{-3}$ for continuity, $x$-velocity, $y$-velocity and $z$-velocity. All simulations were performed on the Vienna Scientific Cluster using 2,500 core-hours for each simulation.

## 2.5 Flow parameter evaluation

The atrial and ventricular flow variation over time was determined using the standard deviation of velocity.

Wall shear stress (WSS) within the atrium and the ventricular surface was categorized in a low non-physiological range (0–0.2 Pa) (Rayz et al., 2010) and physiological range (0.2–9 Pa) (Ghodrati et al., 2020). Volumes with a time-averaged velocity of less than 1 mm/s were defined as stagnation volumes to highlight stasis regions (Dintenfass, 1964; Rayz et al., 2008).

Atrial and ventricular blood washout was quantified using a virtual ink technique (Rayz et al., 2010; Prisco et al., 2017) in which all fluid domains were initialized with an ink concentration of 0, with a value of 1 at the inlets representing flow of fresh blood. The rate of atrial and ventricular washout was calculated by the percentage of old blood in the atrium and ventricle, normalized by the atrial and ventricular volume.

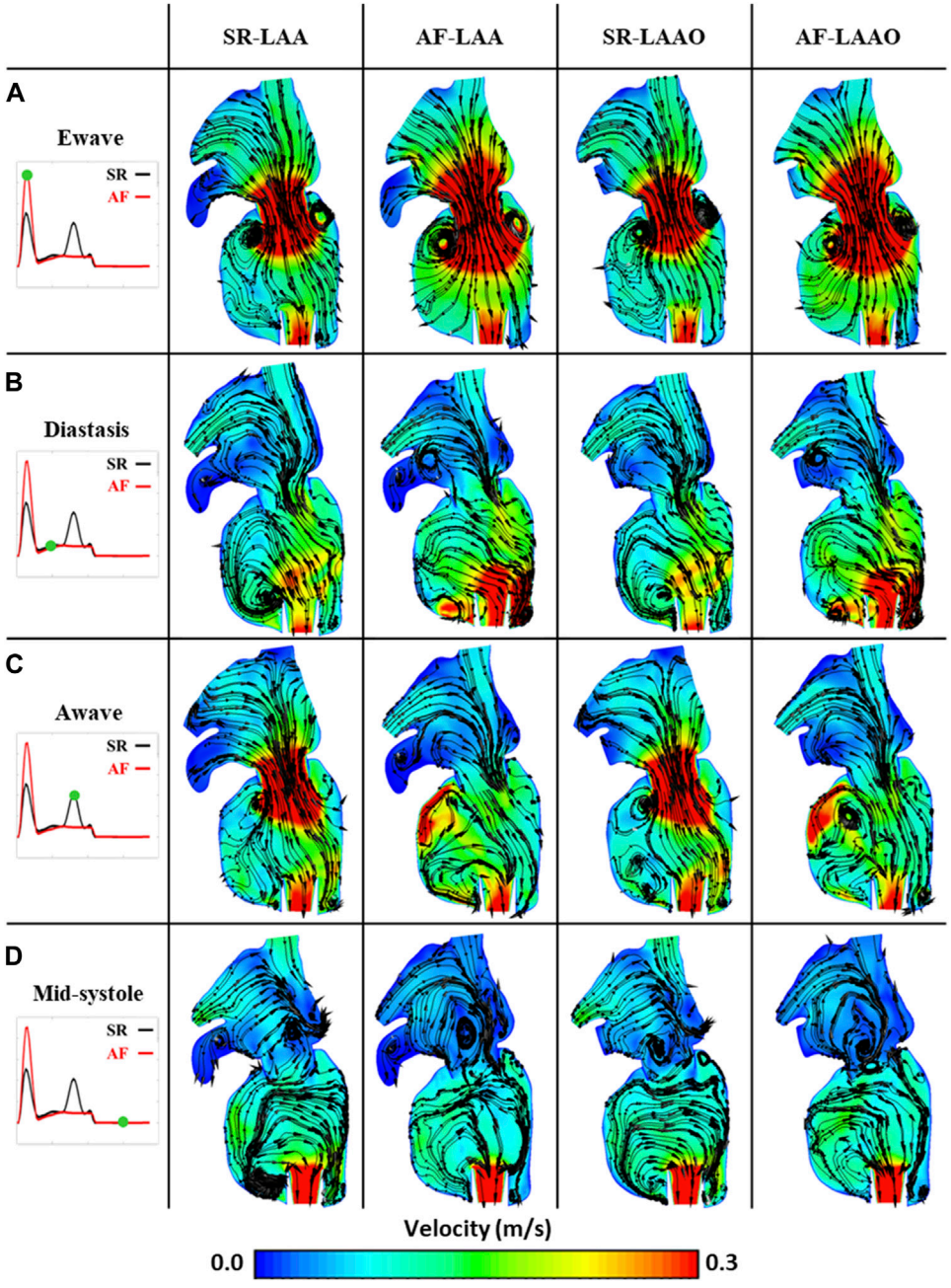


FIGURE 3
Phasic average flow fields at Ewave **(A)**, Diastasis **(B)**, Awave **(C)** and Mid-systole **(D)** in a coronal plane for SR-LAA, SR-LAAO, AF-LAA and AF-LAAO.

# 3 Results

## 3.1 Volume and flow curves

The volume changes of the LA and LV were accurately implemented by CFD simulation leading to identical flow over the mitral valve and LVAD cannula between CFD simulations and LPN model. A comparison of the volume changes and flow rate values between CFD and LPM results for the SR-LAA and AF-LAA simulation can be seen in Figure 2. Similar results were observed for two other simulations (SR-LAAO and AF-LAAO).

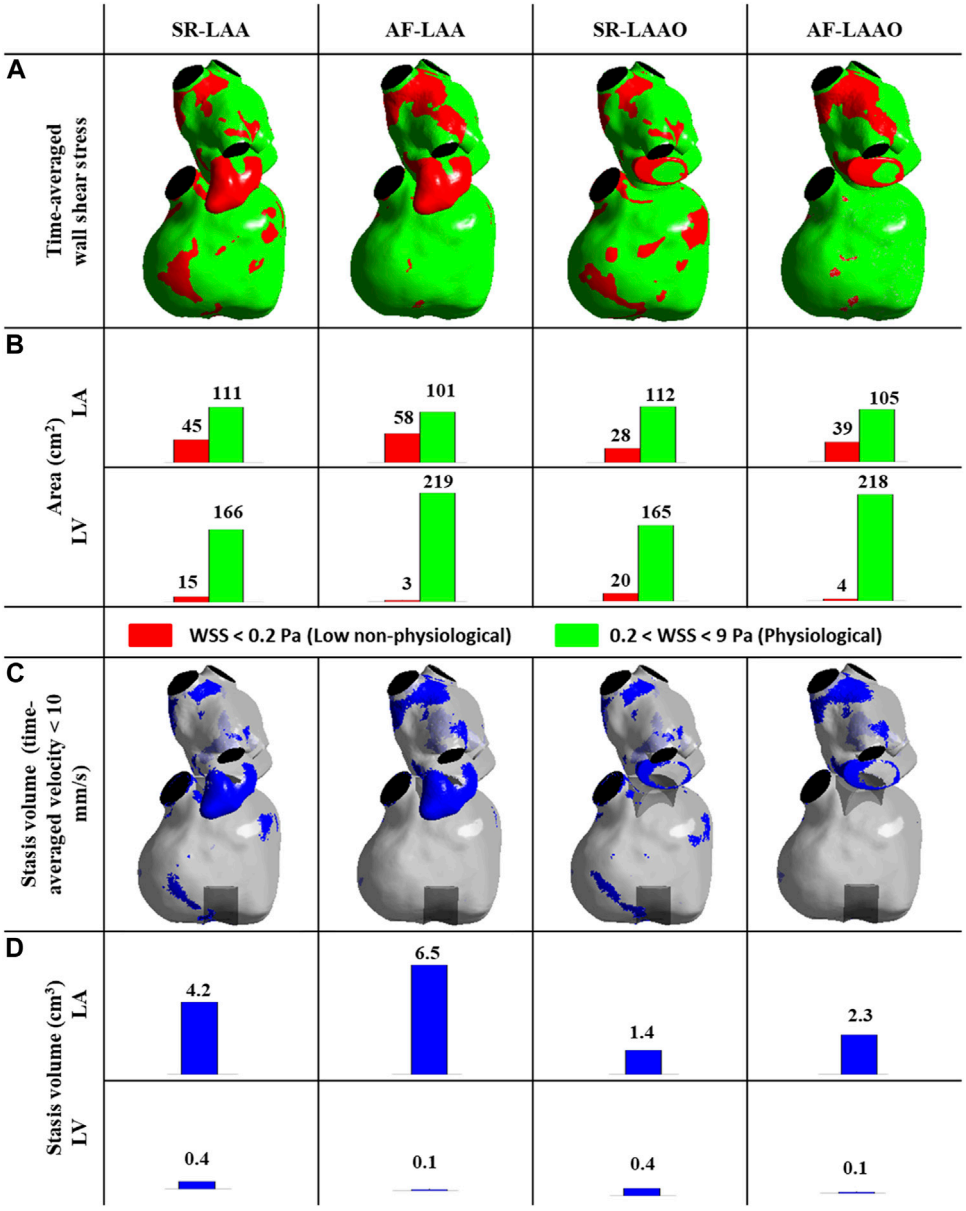


FIGURE 4
**(A,B)** Time-averaged wall shear stress distribution at the atrial and ventricular wall **(A,B)**, time-averaged stagnation volume within the atrium and ventricle **(C,D)**.

## 3.2 Blood flow patterns

Blood flow patterns with and without atrial fibrillation and with/without appendage occlusion were successfully simulated and on the first view showed similar results, however the detailed evaluation of the flow fields showed significant differences in thrombus-related flow parameters.

### 3.2.1 SR versus AF

Atrial fibrillation led to a 10% (from 6.8 cm/s to 6.1 cm/s) reduction of the blood velocity within the atrium. At the E-wave, due to the passive contraction of the atrium, high blood velocity was created at the mitral valve, leading to rapid filling of the ventricle (Figure 3A). With the onset of the diastasis phase, formation of a recirculation zone was observed within the LAA for both SR and AF simulations (Figure 3B). During the A-wave

this region diminished for the simulation with the sinus rhythm due to the left atrial kick (Figure 3C). In the AF simulation, persistence of the recirculation zone inside the LAA could be observed until the end of the cardiac cycle (Figures 3C,D).

### 3.2.2 SR (LAA versus LAAO)

Occlusion of the appendage, which is a source of recirculation zones and stasis areas, improved the atrial haemodynamics. The average blood velocity within the atrium increased by 5%. The standard deviation of velocity in the LAA was five times lower than in the LA chamber (LAA: 1.1, LA: 6.2 cm/s).

### 3.2.3 AF (LAA versus LAAO)

The results of the AF simulation pre and post LAAO were similar to the simulation with SR. A 6% increase in mean atrial velocity over one cardiac cycle was observed due to the LAAO. For the AF simulation, a six times lower standard deviation was observed within the LAA compared to LA (LAA: 1.1, LA: 7.3 cm/s).

## 3.3 Wall shear stress and stagnation volume

### 3.3.1 SR versus AF

With either SR or AF with intact LAA, thrombosis-related parameters, mainly at the LAA, were found to be significant i.e., low WSS values and high stasis volumes. These parameters however had lower values for the simulation with SR. Atrial fibrillation leads to an increase of 29% (from 45 to 58 $cm^2$) on the low WSS area (Figures 4A,B) and 55% (from 4.2 to 6.5 $cm^3$) on the stasis volume (Figures 4C,D) compared to the SR simulation.

### 3.3.2 SR (LAA versus LAAO)

Appendage occlusion resulted in a reduction of low WSS areas and stasis volumes; the reduction of 37% (from 45 to 28 $cm^2$) in areas with low WSS (Figures 4A,B) and 66% reduction (from 4.2 to 1.4 $cm^3$) in stasis volume was observed post-LAAO for SR (Figures 4C,D). The values within the ventricle remained similar pre- and post-LAAO for both SR and AF (Figure 4).

### 3.3.3 AF (LAA versus LAAO)

Comparable results were also observed with AF; with a 32% (from 58 to 39 $cm^2$) reduction in low WSS areas (Figures 3A,B) and 64% reduction (from 6.5 to 2.3 $cm^3$) in stasis volume (Figures 4C,D). The LAAO did not influence the areas with low WSS or stagnation volume within the ventricle (Figure 4).

The effect of atrial fibrillation on thrombosis-related flow parameters (low WSS, stagnation volume) was mainly observed within the left atrium. These parameters were increased with atrial fibrillation, but were significantly decreased by occlusion of the atrial appendage leading to more favorable condition.

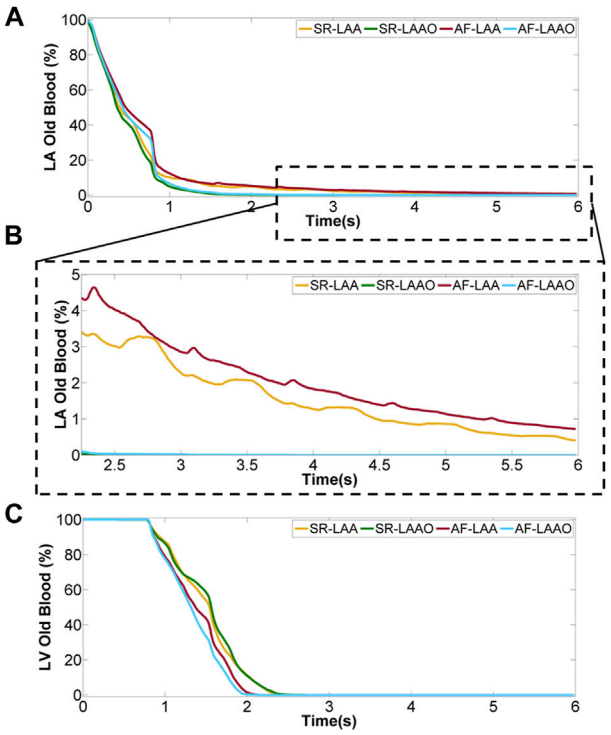


FIGURE 5
Percentage of old blood remaining within the atrium **(A)**, a close-up for last 5 cycles **(B)** and ventricle **(C)** over 8 cardiac cycles.

## 3.4 Blood washout

### 3.4.1 SR versus AF

The blood washout which was calculated using virtual-ink method showed similar behaviour within the left atrium for SR and AF simulations before LAAO, after 3 cardiac cycles around 95% of the old blood was replaced with new blood. However, the ventricular washout was slightly different. The complete replacement of the old blood with fresh blood in the LV took 2.5 s in the SR simulation and 2.2 s in the AF simulation (Figures 5A,B).

### 3.4.2 SR (LAA versus LAAO)

Occlusion of the appendage significantly accelerated the replacement of the old blood with new blood within the atrium (Figures 5A,B), while the blood volume exchange within the ventricle remained similar for pre- and post-LAAO (Figure 5C). After 2.5 s the old blood within the atrium was replaced with new blood for LAAO while without the occlusion 3% (5 ml) of the old blood entering the LA on the first cycle remained in the LAA.

The evaluation of the blood washout only within the appendage showed that after 8 cardiac cycles, 8% of the old blood entering the LAA in the first cardiac cycle remains there.

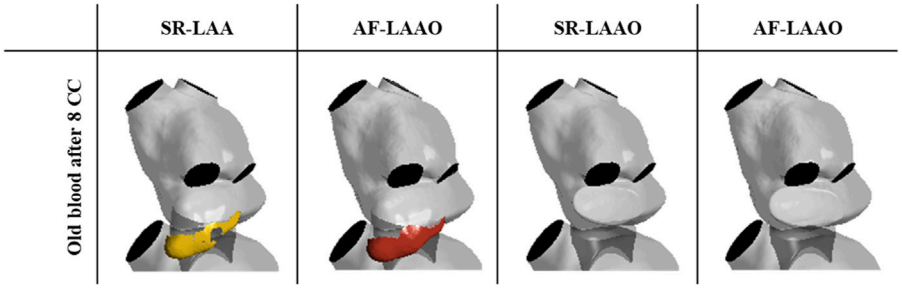


FIGURE 6
Volume of the old blood remaining in the LAA after 8 cardiac cycles.

### 3.4.3 AF (LAA versus LAAO)

A similar behaviour as with sinus rhythm was observed for the atrial fibrillation after LAAO (Figure 5). After 3.2 s the replacement of the old blood with fresh blood within the atrium was observed for the LAAO simulation while without the occlusion 4% (6 ml) of the old blood remained in the LAA. Evaluation of the washout within the appendage showed that from the 9 ml of blood entering the LAA on the first cycle, 14% of 9 ml resides there after 8 cardiac cycles (Figure 6).

## 4 Discussion

Clinical studies show high prevalence of AF for LVAD patients. AF was diagnosed in 26–54% of patients before LVAD implantation (Stulak et al., 2013; Deshmukh et al., 2017) and 13–28% post-LVAD implantation (Hickey et al., 2016; Deshmukh et al., 2018). Preoperative AF is associated with an increased risk for thromboembolic events after LVAD implantation (Stulak et al., 2013; Enriquez et al., 2014), while postoperative AF increases the risk of ischemic stroke, and device thrombosis in the long term after LVAD implantation (Deshmukh et al., 2018). Surgical LAAO at the time of LVAD implantation was linked to a decrease in thromboembolic events which has been shown to be true with and without AF (Deshmukh et al., 2019), however, no clinical trial data is currently available on this issue to support the decision making process with respect to left atrial appendage procedures (Deshmukh et al., 2017).

This is the first study in which numerical simulations show the effect of LAAO on flow patterns in the left heart under LVAD support. Four simulations were performed in total: two with normal sinus rhythm (with and without LAA) and two with AF (with and without LAA). The hemodynamic differences and various thrombosis-related parameters including stasis volume, low WSS and blood residence time were computed (Rayz et al., 2010). Since fluid dynamical parameters and its influence on the mechanism for thrombus formation are still poorly understood, various parameters with complementary roles were considered to evaluate the risk of thrombosis. Low wall shear stresses show the areas on the wall where the blood in their vicinity experiences very low velocities and could be the origin of the thrombus formation. However, defining a sharp threshold bears the risk to oversimplify mechanisms and consequently on detecting the size of stasis regions. Therefore, the stagnation volume was used for complementary evaluation of the high-risk regions which shows the high-risk areas within the cavity. Also, the residence time was used to demonstrate the locations where blood resides there for a long time, which in combination with low blood velocity, might lead to platelet aggregation.

Reduction in the flow velocities of the left atrium and LAA were observed for AF when compared to SR. This behavior was also observed in 4D flow MRI analysis and was associated with an elevated risk of stroke for AF patients (Markl et al., 2016). A flow recirculation zone was observed in the LAA with low velocity, leading to the formation of a stagnation volume for both SR and AF simulations. The WSS also remained abnormally low along the LAA wall during the entire simulation and part of the initially injected fluid remained within the LAA for more than 8 cardiac cycles. An increased flow residence time in a region with low shear stresses and low velocity values may promote blood clot formation and subsequent adhesion to the LAA wall, since the formed clot is not transported away by the flow. The results of this study highlight the risk of clot formation in the LAA for LVAD patients independent of AF. This could be the reason for the lower prevalence of thromboembolic events for patients who received surgical LAAO at the time of LVAD implantation (Deshmukh et al., 2019). This finding is consistent with findings of clinical studies performed for patients with AF who were scheduled to undergo cardiac surgery. In this study LAAO showed larger influence than antithrombotic therapy among high-risk AF patients with regards to risk reduction of ischemic strokes and systemic embolism (Chen et al., 2021; Whitlock et al., 2021).

The distribution of low WSS at the ventricular wall and thus the formation of stagnant volume within the ventricular cavity was unchanged for both SR and AF, for both occluded and unoccluded LAAs. These results show that thrombosis-related parameters are important in the LAA, but play a minor role in the left ventricle.

### 4.1 Limitation

The evaluation was performed for one patient geometry that allows us comparison between the sinus rhythm and atrial fibrillation with and without LAA for LVAD patients in the same geometry. However, There are other forms and shapes of the LAA (Cactus, Chicken Wing, Windsock, and Cauliflower) which likely influence the hemodynamics within the LA (Beigel et al., 2014). Since the quality of CT scans for LVAD patients was not sufficient for segmentation of the mitral valve and papillary muscles, a standardized parametric mitral valve was used which allows comparison with other studies (Liao et al., 2018a; Liao et al., 2018b).

## 5 Conclusion

To conclude, this is the first study that applies moving walls and realistic hemodynamics in order to quantitatively analyze the effects of AF and LAAO in the LVAD population. The findings of this study highlight the unfavorable hemodynamics at the LAA for LVAD patients with both SR and AF. Occlusion of the LAA significantly reduced the thrombus related flow mechanical parameters. This procedure could be performed concomitant with LVAD implantation and might lower the risk of thromboembolic events caused by the appendage.

## Data availability statement

The original contributions presented in the study are included in the article/Supplementary Material, further inquiries can be directed to the corresponding author.

## Author contributions

MG-M, TS, HS, and PA developed the concept and design of the study. MG-M was responsible for performing CFD simulation, post-processing of the CFD results and drafting article. CG was responsible for providing the haemodynamics. Data analysis and interpretation was performed by MG-M, TS, PA, and HS. The clinical overview was provided by TS and HS. All authors contributed to manuscript revision, read, and approved the submitted version.

## Funding

This work was partially founded by the Austrian Research Promotion Agency (FFG): M3dRES Project No. 858060. This work was supported by the Vienna Scientific Cluster (VSC) Computer Network.

## Conflict of interest

DZ has served as a proctor, advisor, and speaker for Medtronic Inc., Abbott Inc., Berlin Heart, Edwards, Abiomed, and has received research and travel grants from Medtronic Inc. and Abbott Inc. HS has served as an advisor for Medtronic Inc. and has received research grants from Medtronic Inc. TS has served as a consultant and advisor for Medtronic Inc. and Abbott Inc. and received research grants from Abbott, Medtronic and CorWave.

The remaining authors declare that the research was conducted in the absence of any commercial or financial relationships that could be construed as a potential conflict of interest.

## Publisher's note



## Supplementary material

The Supplementary Material for this article can be found online at: https://www.frontiersin.org/articles/10.3389/fphys.2022.1010862/full#supplementary-material

# References


Acharya, D., Loyaga-Rendon, R., Morgan, C. J., Sands, K. A., Pamboukian, S. V., Rajapreyar, I., et al. (2017). INTERMACS analysis of stroke during support with continuous-flow Left Ventricular assist devices: Risk factors and outcomes. *JACC. Heart Fail.* 5 (10), 703–711. doi:10.1016/j.jchf.2017.06.014

Baker, T. J. (2016). *'ANSYS fluent meshing user's Guide'*, 372.

Beigel, R., Wunderlich, N. C., Ho, S. Y., Arsanjani, R., and Siegel, R. J. (2014). The left atrial appendage: Anatomy, function, and noninvasive evaluation. *JACC. Cardiovasc. Imaging* 7 (12), 1251–1265. doi:10.1016/j.jcmg.2014.08.009

Blackshear, J. L., and Odell, J. A. (1996). Appendage obliteration to reduce stroke in cardiac surgical patients with atrial fibrillation. *Ann. Thorac. Surg.* 61 (2), 755–759. doi:10.1016/0003-4975(95)00887-X

Burrell, A., Hayward, C., Mariani, J., Leet, A., and Kaye, D. M. (2015). Clinical utility of invasive exercise hemodynamic evaluation in LVAD patients. *J. Heart Lung Transplant.* 34 (12), 1635–1637. doi:10.1016/j.healun.2015.06.004

Chen, S., Chun, K. R. J., Ling, Z., Liu, S., Zhu, L., Wang, J., et al. (2021). Comparison of left atrial appendage occlusion versus non-vitamin-K antagonist oral anticoagulation in high-risk atrial fibrillation: An update. *J. Cardiovasc. Dev. Dis.* 8 (6), 69. doi:10.3390/jcdd8060069

Chivukula, V. K., Beckman, J. A., Prisco, A. R., Dardas, T., Lin, S., Smith, J. W., et al. (2018). Left ventricular assist device inflow cannula angle and thrombosis risk. *Circ. Heart Fail.* 11 (4), e004325. doi:10.1161/CIRCHEARTFAILURE.117.004325

Chivukula, V. K., Beckman, J. A., Prisco, A. R., Lin, S., Dardas, T. F., Cheng, R. K., et al. (2019). Small left ventricular size is an independent risk factor for ventricular assist device thrombosis. *ASAIO J.* 65 (2), 152–159. doi:10.1097/MAT.0000000000000798

Deshmukh, A., Bhatia, A., Anyanwu, E., Ota, T., Jeevanandam, V., Uriel, N., et al. (2018). Incidence and outcomes of postoperative atrial fibrillation after left ventricular assist device. *ASAIO J.* 64 (5), 581–585. doi:10.1097/MAT.0000000000000763

Deshmukh, A., Bhatia, A., Sayer, G. T., Kim, G., Raikhelkar, J., Imamura, T., et al. (2019). Left atrial appendage occlusion with left ventricular assist device decreases thromboembolic events. *Ann. Thorac. Surg.* 107 (4), 1181–1186. doi:10.1016/j.athoracsur.2018.09.004

Deshmukh, A., Kim, G., Burke, M., Anyanwu, E., Jeevanandam, V., Uriel, N., et al. (2017). Atrial arrhythmias and electroanatomical remodeling in patients with left ventricular assist devices. *J. Am. Heart Assoc.* 6 (3), e005340. doi:10.1161/JAHA.116.005340

DeVore, A. D., and Stewart, G. C. (2017). The risk of stroke on left ventricular assist device support. *JACC. Heart Fail.* 5 (10), 712–714. :. doi:10.1016/j.jchf.2017.08.002

Dintenfass, L. (1964). Viscosity and clotting of blood in venous thrombosis and coronary occlusions. *Circ. Res.* 14 (1), 1–16. doi:10.1161/01.RES.14.1.1

Domenichini, F., and Pedrizzetti, G. (2015). Asymptotic model of fluid–tissue interaction for mitral valve dynamics. *Cardiovasc. Eng. Technol.* 6 (2), 95–104. doi:10.1007/s13239-014-0201-y

Enriquez, A. D., Calenda, B., Gandhi, P. U., Nair, A. P., Anyanwu, A. C., and Pinney, S. P. (2014). Clinical impact of atrial fibrillation in patients with the HeartMate II left ventricular assist device. *J. Am. Coll. Cardiol.* 64 (18), 1883–1890. doi:10.1016/j.jacc.2014.07.989

Estep, J. D., Vivo, R. P., Krim, S. R., Cordero-Reyes, A. M., Elias, B., Loebe, M., et al. (2014). Echocardiographic evaluation of hemodynamics in patients with systolic heart failure supported by a continuous-flow LVAD. *J. Am. Coll. Cardiol.* 64 (12), 1231–1241. Available at:. doi:10.1016/j.jacc.2014.06.1188

Friedman, D. J., Piccini, J. P., Wang, T., Zheng, J., Malaisrie, S. C., Holmes, D. R., et al. (2018). Association between left atrial appendage occlusion and readmission for thromboembolism among patients with atrial fibrillation undergoing concomitant cardiac surgery. *JAMA* 319 (4), 365–374. Available at:. doi:10.1001/jama.2017.20125

Ghodrati, M., Khienwad, T., Maurer, A., Moscato, F., Zonta, F., Schima, H., et al. (2021). Validation of numerically simulated ventricular flow patterns during left ventricular assist device support. *Int. J. Artif. Organs* 44 (1), 30–38. Available at:. doi:10.1177/0391398820904056

Ghodrati, M., Maurer, A., Schloglhofer, T., Khienwad, T., Zimpfer, D., Beitzke, D., et al. (2020). The influence of left ventricular assist device inflow cannula position on thrombosis risk. *Artif. Organs* 44 (9), 939–946. Available at:. doi:10.1111/aor.13705

Ghodrati, M., Schlöglhofer, T., Maurer, A., Khienwad, T., Zimpfer, D., Beitzke, D., et al. (2021). Effects of the atrium on intraventricular flow patterns during mechanical circulatory support. *Int. J. Artif. Organs* 45, 421–430. Available at:. doi:10.1177/03913988211056018

Haft, J., Armstrong, W., Dyke, D. B., Aaronson, K. D., Koelling, T. M., Farrar, D. J., et al. (2007). Hemodynamic and exercise performance with pulsatile and continuous-flow left ventricular assist devices. *Circulation* 116 (11 Suppl), I8–15. doi:10.1161/CIRCULATIONAHA.106.677898

Hickey, K. T., Garan, H., Mancini, D. M., Colombo, P. C., Naka, Y., Sciacca, R. R., et al. (2016). Atrial fibrillation in patients with Left Ventricular assist devices: Incidence, predictors, and clinical outcomes. *JACC. Clin. Electrophysiol.* 2 (7), 793–798. Available at:. doi:10.1016/j.jacep.2016.03.009

Jacquet, L., Vancaenegem, O., Pasquet, A., Matte, P., Poncelet, A., Price, J., et al. (2011). Exercise capacity in patients supported with rotary blood pumps is improved by a spontaneous increase of pump flow at constant pump speed and by a rise in native cardiac output. *Artif. Organs* 35 (7), 682–690. doi:10.1111/j.1525-1594.2011.01227.x

Liao, S., Neidlin, M., Li, Z., Simpson, B., and Gregory, S. D. (2018a). Ventricular flow dynamics with varying LVAD inflow cannula lengths: *In-silico* evaluation in a multiscale model. *J. Biomech.* 72, 106–115. Available at:. doi:10.1016/j.jbiomech.2018.02.038

Liao, S., Wu, E. L., Neidlin, M., Li, Z., Simpson, B., and Gregory, S. D. (2018b) The influence of rotary blood pump speed modulation on the risk of intraventricular thrombosis. *Artif. Organs* 42 (10), 943–953. doi:10.1111/aor.13330

Mancini, D., and Colombo, P. C. (2015). Left ventricular assist devices: A rapidly evolving alternative to transplant. *J. Am. Coll. Cardiol.* 65 (23), 2542–2555. Available at:. doi:10.1016/j.jacc.2015.04.039

Markl, M., Lee, D. C., Furiasse, N., Carr, M., Foucar, C., Ng, J., et al. (2016). Left atrial and left atrial appendage 4D blood flow dynamics in atrial fibrillation. *Circ. Cardiovasc. Imaging* 9 (9), e004984. Available at:. doi:10.1161/CIRCIMAGING.116.004984

Martina, J., de Jonge, N., Rutten, M., Kirkels, J. H., Klopping, C., Rodermans, B., et al. (2013). Exercise hemodynamics during extended continuous flow left ventricular assist device support: The response of systemic cardiovascular parameters and pump performance. *Artif. Organs* 37 (9), 754–762. doi:10.1111/aor.12151

Molina, E. J., Shah, P., Kiernan, M. S., Cornwell, W. K., 3rd, Copeland, H., Takeda, K., et al. (2021). The society of thoracic surgeons intermacs 2020 annual report. *Ann. Thorac. Surg.* 111 (3), 778–792. Available at:. doi:10.1016/j.athoracsur.2020.12.038

Moscato, F., Granegger, M., Naiyanetr, P., Wieselthaler, G., and Schima, H. (2012). Evaluation of left ventricular relaxation in rotary blood pump recipients using the pump flow waveform: A simulation study. *Artif. Organs* 36 (5), 470–478. Available at:. doi:10.1111/j.1525-1594.2011.01392.x

Muthiah, K., Robson, D., Prichard, R., Walker, R., Gupta, S., Keogh, A. M., et al. (2015). Effect of exercise and pump speed modulation on invasive hemodynamics in patients with centrifugal continuous-flow left ventricular assist devices. *J. Heart Lung Transpl.* 34 (4), 522–529. doi:10.1016/j.healun.2014.11.004

Prisco, A. R., Aliseda, A., Beckman, J. A., Mokadam, N. A., Mahr, C., and Garcia, G. J. M. (2017). Impact of LVAD implantation site on ventricular blood stagnation. *ASAIO J.* 63 (4), 392–400. Available at:. doi:10.1097/MAT.0000000000000503

Rayz, V. L., BousseL, L., Ge, L., Leach, J. R., Martin, A. J., Lawton, M. T., et al. (2010). Flow residence time and regions of intraluminal thrombus deposition in intracranial aneurysms. *Ann. Biomed. Eng.* 38 (10), 3058–3069. Available at:. doi:10.1007/s10439-010-0065-8

Rayz, V. L., BousseL, L., Lawton, M. T., Acevedo-Bolton, G., Ge, L., Young, W. L., et al. (2008). Numerical modeling of the flow in intracranial aneurysms: Prediction of regions prone to thrombus formation. *Ann. Biomed. Eng.* 36 (11), 1793–1804. Available at:. doi:10.1007/s10439-008-9561-5

Stulak, J. M., Deo, S., Schirger, J., Aaronson, K. D., Park, S. J., Joyce, L. D., et al. (2013). Preoperative atrial fibrillation increases risk of thromboembolic events after left ventricular assist device implantation. *Ann. Thorac. Surg.* 96 (6), 2161–2167. Available at:. doi:10.1016/j.athoracsur.2013.07.004

Whitlock, R. P., Belley-Cote, E. P., Paparella, D., Healey, J. S., Brady, K., Sharma, M., et al. (2021). Left atrial appendage occlusion during cardiac surgery to prevent stroke. *N. Engl. J. Med.* 384 (22), 2081–2091. Available at:. doi:10.1056/NEJMoa2101897

Wong, D. T. H., Lee, K. J., Yoo, S. J., Tomlinson, G., and Grosse-Wortmann, L. (2014). Changes in systemic and pulmonary blood flow distribution in normal adult volunteers in response to posture and exercise: A phase contrast magnetic resonance imaging study. *J. Physiol. Sci.* 64 (2), 105–112. Available at:. doi:10.1007/s12576-013-0298-z

# Frontiers in Physiology

**Understanding how an organism's components work together to maintain a healthy state**

The second most-cited physiology journal, promoting a multidisciplinary approach to the physiology of living systems - from the subcellular and molecular domains to the intact organism and its interaction with the environment.

---

## Discover the latest Research Topics

See more →

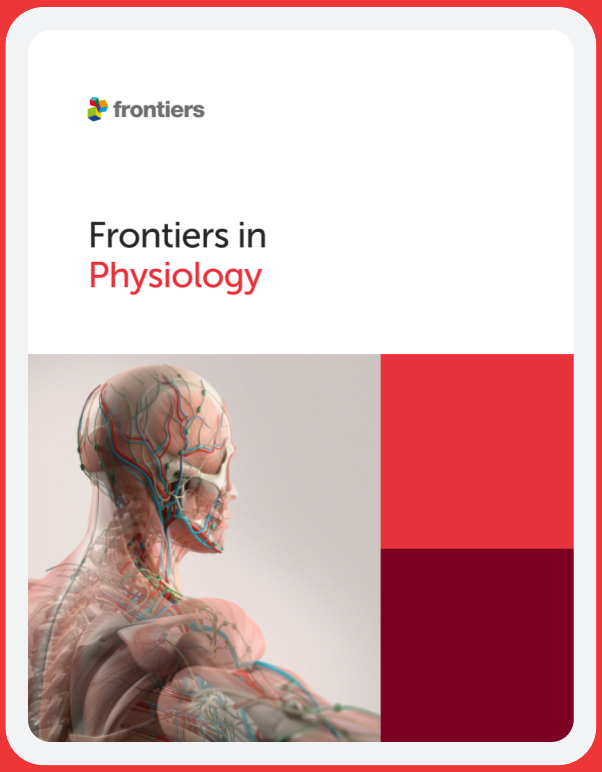


**Frontiers**

Avenue du Tribunal-Fédéral 34
1005 Lausanne, Switzerland
frontiersin.org

**Contact us**

+41 (0)21 510 17 00
frontiersin.org/about/contact